2003-09-08

Low-order coupled map lattices for estimation of wake patterns behind vibrating flexible cables

Ganapathi Raman Balasubramanian
Worcester Polytechnic Institute

Low-Order Coupled Map Lattices for Estimation of Wake Patterns Behind Vibrating Flexible Cables

by

Ganapathi Raman Balasubramanian

A Dissertation

Submitted to the Faculty

of the

WORCESTER POLYTECHNIC INSTITUTE

In partial fulfillment of the requirements for the

Degree of Doctor of Philosophy

in

Mechanical Engineering

by

August 2003

APPROVED:

Professor David Olinger, Major Advisor

Professor Michael Demetriou, Co-advisor

Professor Nikos Gatsonis, Committee Member

Professor Homer Walker, Committee Member

Professor George Karniadakis, Committee Member

Professor John Sullivan, Graduate Committee Representative

Abstract

Fluid-structure interaction arises in a wide array of technological applications including naval and marine hydrodynamics, civil and wind engineering and flight vehicle aerodynamics. When a fluid flows over a bluff body such as a circular cylinder, the periodic vortex shedding in the wake causes fluctuating lift and drag forces on the body. This phenomenon can lead to fatigue damage of the structure due to large amplitude vibration. It is widely believed that the wake structures behind the structure determine the hydrodynamic forces acting on the structure and control of wake structures can lead to vibration control of the structure. Modeling this complex non-linear interaction requires coupling of the dynamics of the fluid and the structure. In this thesis, however, the vibration of the flexible cylinder is prescribed, and the focus is on modeling the fluid dynamics in its wake. Low-dimensional iterative circle maps have been found to predict the universal dynamics of a two-oscillator system such as the rigid cylinder wake. Coupled map lattice (CML) models that combine a series of low-dimensional circle maps with a diffusion model have previously predicted qualitative features of wake patterns behind freely vibrating cables at low Reynolds number. However, the simple nature of the CML models implies that there will always be unmodelled wake dynamics if a detailed, quantitative comparison is made with laboratory or simulated wake flows. Motivated by a desire to develop an improved CML model, we incorporate self-learning features into a new CML that is trained to precisely estimate wake patterns from target numerical simulations and experimental wake flows. The eventual goal is to have the CML learn from a laboratory flow in real time. A real-time self-learning CML capable of estimating experimental wake patterns could serve as a wake model in a future anticipated feedback control system designed to produce desired wake patterns.

A new convective-diffusive map that includes additional wake dynamics is developed. Two different self-learning CML models, each capable of precisely estimating

complex wake patterns, have been developed by considering additional dynamics from the convective-diffusive map. The new self-learning CML models use adaptive estimation schemes which seek to precisely estimate target wake patterns from numerical simulations and experiments. In the first self-learning CML, the estimator scheme uses a multi-variable least-squares algorithm to adaptively vary the spanwise velocity distribution in order to minimize the state error (difference between modeled and target wake patterns). The second self-learning model uses radial basis function neural networks as online approximators of the unmodelled dynamics. Additional unmodelled dynamics not present in the first self-learning CML model are considered here. The estimator model uses a combination of a multi-variable normalized least squares scheme and a projection algorithm to adaptively vary the neural network weights.

Studies of this approach are conducted using wake patterns from spectral element based NEKTAR simulations of freely vibrating cable wakes at low Reynolds numbers on the order of 100. It is shown that the self-learning models accurately and efficiently estimate the simulated wake patterns within several shedding cycles.

Next, experimental wake patterns behind different configurations of rigid cylinders were obtained. The self-learning CML models were then used for off-line estimation of the stored wake patterns.

With the eventual goal of incorporating low-order CML models into a wake pattern control system in mind, in a related study control terms were added to the simple CML model in order to drive the wake to the desired target pattern of shedding. Proportional, adaptive proportional and non-linear control techniques were developed and their control efficiencies compared.

Acknowledgements

I would like to acknowledge the support and guidance of my advisors, Professors David J. Olinger and Michael A. Demetriou throughout my graduate study at WPI. It is impossible to even think of attempting a rigorous journey through higher studies without their constant encouragement and advise. They convinced me to pursue my PhD and very early in my PhD I had a clear-cut idea of the work ahead of me until its completion . I strongly believe that this has helped me maintain my focus and sustain my motivation.

I would also like to thank Professors Gatsonis, Walker, Sullivan and Karniadakis for agreeing to serve in the dissertation committee. Thanks also go to Professor Hermanson who served earlier in this committee and also in my MS thesis committee.

I would like to acknowledge the Office of Naval Research (Grant No. N00014-96-1-0004) for supporting this research as well as my earlier research at WPI. I also gratefully acknowledge the financial support from WPI.

I thank Professor Alexandrou who initially encouraged me to apply to WPI for my graduate studies. I have had the previlege of taking some courses under Professors Olinger, Demetriou, Gatsonis, Johari, Hermanson, Hou and Dimentberg. I simply cannot thank them enough.

The NEKTAR simulations were conducted on Cray T3E and IBM SP supercomputers at the San Diego Supercomputer Cenetr with support from the National Partnership for Advanced Computational Infrastructure (NPACI), and on the IBM SP supercomputer. I thank Prof. Karniadakis for providing access to and help with the NEKTAR code.

I thank all my friends (list is too long to name individually) at WPI for their intellectual company. Some of them have helped me maintain my focus during tough times. I thank Jim for helping me with my experimental work.

Finally, I would like to thank all the ME Secretaries (past and present) for all their help in completing my degree requirements.

I dedicate this thesis to my family for their encouragement and support throughout my academic career.

Contents

List of Figures

Chapter 1

Introduction

Flow induced vibration of an elastic structure is an important problem with numerous practical engineering applications. These include naval and marine hydrodynamics, underwater acoustics, surveillance and detection technology, offshore exploration and drilling, and flight vehicle aerodynamics. One classic example of flow induced vibration is the collapse of the Tacoma Narrows bridge. Such problems are also encountered in nuclear and conventional power generation, and electric power transmission.

However, progress in understanding the interaction between an elastic structure and the fluid flowing over it has accelerated in the last two decades, largely due to improved experimental and computational studies. Flow induced vibration is a long standing problem with early published works date to the late 19th century. The intellectual challenge continues to be daunting, and a theoretical solution to this problem for structures of practical importance is currently impossible. Therefore, before even attempting to model complex applications listed previously, a fundamental understanding of problems involving simple geometries such as an oscillating circular cylinder, is essential.

The wake of a circular cylinder is characterized by a vortex street, where vortices are shed alternatively from both sides of the cylinder. This arrangement of vortices causes an alternating pressure force and periodically fluctuating lift and drag forces leading to bluff body vibration. It is now well understood that flows past circular

cylinders or cables can yield large vibration amplitudes due to periodic vortex shedding in the flow. This happens at resonance, when the dominant wake frequencies happen to coincide with one of the natural frequencies of the cable. This phenomenon is one of the main reasons for failure of structures in the marine environment. This problem has been experimentally and numerically investigated for more than a century (Bearman, (1984), Blevins, (1977)) but many fundamental questions still need to be addressed, even in the low Reynolds number regime studied in this work.

The main question addressed in this thesis is whether simple models can be developed to predict the salient fatures of the vortex formation process. Recently, there has been an increased interest in the use of low dimensional models such as coupled circle map lattices, Ginzburg-Landau or van der Pol equations to model the spatio-temporal dynamics of the cylinder wake. All these models use spanwise diffusive coupling of the temporal dynamics of each oscillator on the cylinder. The current work is an extension of earlier work by Olinger (1988, 1993, 1998) on coupled map lattices to model vortex shedding patterns behind a cylinder wake. A review of existing literature pertaining to this work follows.

Our review of wakes behind circular cylinders includes previous investigations on low Reynolds number cylinder wake, cylinder vibration and vortex lock-on, three dimensional wake structures in the low Reynolds number regime, and a summary of work which has applied the dynamical systems approach to cylinder wakes. This chapter then concludes with a section outlining the objectives of this research work.

1.1 Low Reynolds number Cylinder Wake

In this section, a brief outline of the various wake phenomena observed with changes in Reynolds number is provided. The Reynolds number is given by $Re = U_\infty D/\nu$, where U_∞ is the freestream velocity, D is the diameter of the cylinder, and ν is the viscosity of the fluid. When $Re < 4$, the flow is steady and goes over the cylinder. No vortices are formed behind the cylinder. Such a flow is termed Stokes flow and

the solution is found in standard texts (Batchelor, 1967).

For $4 < Re < 40$, a pair of vortices is formed behind the cylinder. The size of the vortices increase with the Reynolds number. The wake is still laminar, and the vortices act like rollers over which the main stream flows. Tritton (1959) showed that a vortex street first appears behind the cylinder at a Re near 40. It arises due to the instability of the vortex pair. Karman gave his first theory of the vortex street in 1911. Since then, numerous review articles on subsequent work have been written by Roshko (1954), Marris (1964) and more recently Griffin *et al.* (1991).

When the Reynolds number approaches 100, the flow becomes more complex giving rise to three-dimensional wake structures. We will discuss these later in this chapter. In the case of a fixed cylinder, the shedding frequency, f_{so}, (and hence the Strouhal number, $St = f_{so}D/U_\infty$) for a fluid flow is a function of the Reynolds number only. Roshko's experiments (1954) on fixed cylinders were summarized in the form of a Strouhal-Reynolds number relationship (Figure 1.1). Even today, the Strouhal-Reynolds curve is used as a benchmark for experimental or computational studies.

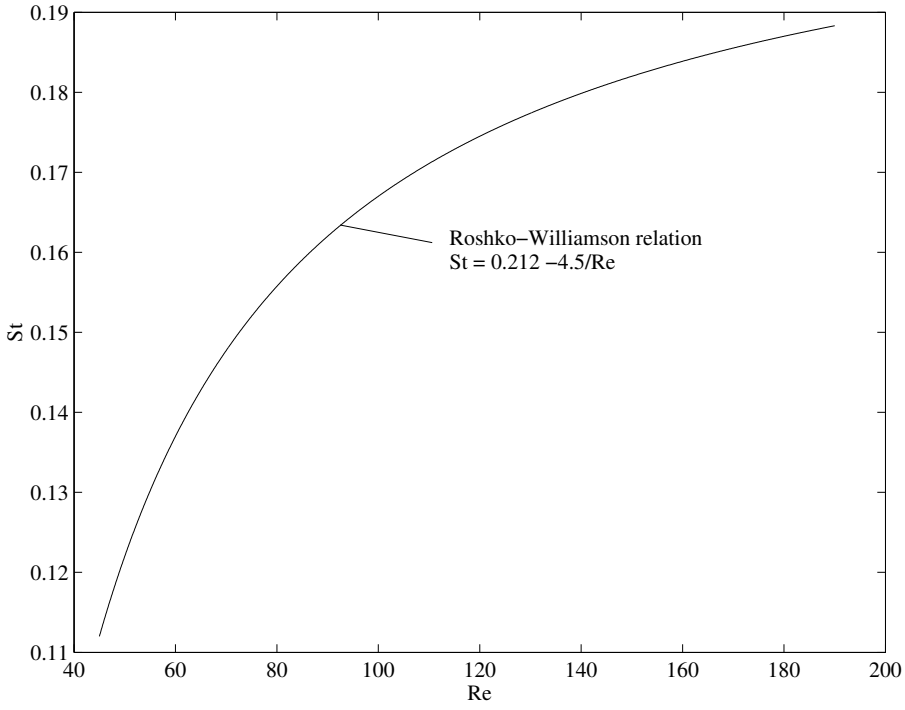

Figure 1.1: $St - Re$ relationship in laminar shedding regime.

1.2 Cylinder Vibration and Vortex Lock-on

A cylinder can either be forced externally to oscillate in a flow or induced to vibrate freely by the oncoming flow. In the latter case, the cylinder is excited by the periodic shedding of vortices in the wake. Here, the alternate shedding of vortices creates a fluctuating lift force on the cylinder which results in cylinder motion. This force attains a maximum when the shedding frequency is in the vicinity of the structural natural frequency of the cylinder. Koopman (1967) studied an elastically mounted rigid cylinder, forced externally at a certain frequency, and found that the shedding frequency of the wake changed to match the cylinder's excitation frequency under certain conditions. This phenomenon of vortex lock-on occurred when the natural shedding frequency of the cylinder was within 25-30 % of the excitation frequency of the cylinder. Tanida *et al.* (1973) showed evidence of lock-on due to cross-stream and in-line vibrations of a cylinder. The extent of lock-on region was found to be related to the reduced amplitude, A/D (where A is the amplitude of oscillation and D is the cylinder diameter). Similar results were reported by Stansby (1976) for transverse oscillations and Griffin and Ramberg (1974) for in-line oscillations. Extensive reviews on vortex-induced oscillations and vortex lock-on can be found in Sarpkaya (1979) and Bearman (1984). More recently, Griffin and Hall (1991) have given a detailed review of vortex shedding lock-on and flow control in bluff body wakes. This introduction is a very brief summary of the large number of classical investigations into vortex shedding phenomena in the last century.

1.3 Three-dimensional wake structures

We have seen that the fundamental wake instability results in the formation of the classical von Karman street configuration for $Re > 49$. However, only recently have a large number of investigations have been concerned with the development of three-dimensional structure in cylinder wakes. Recent developments have been reviewed

comprehensively by Williamson (1996). The three-dimensional transition of the wake starts at $Re \approx 190$ with the formation of modes A and B in Williamson's nomenclature; mode B dominates after $Re \approx 250$ and results in the formation of streamwise vortices with a typical distance of one diameter from each other. The bulk of the recent experimental efforts has focused on low Reynolds numbers, where smaller scales have not yet developed. The possibility of control on the shedding pattern has corresponding implications for the control of unsteady fluid forces experienced by the body.

Some of the commonly observed three-dimensional wake structures such as *parallel shedding, oblique shedding, cellular shedding* and *vortex dislocations* are illustrated in Figures 1.2- 1.5.

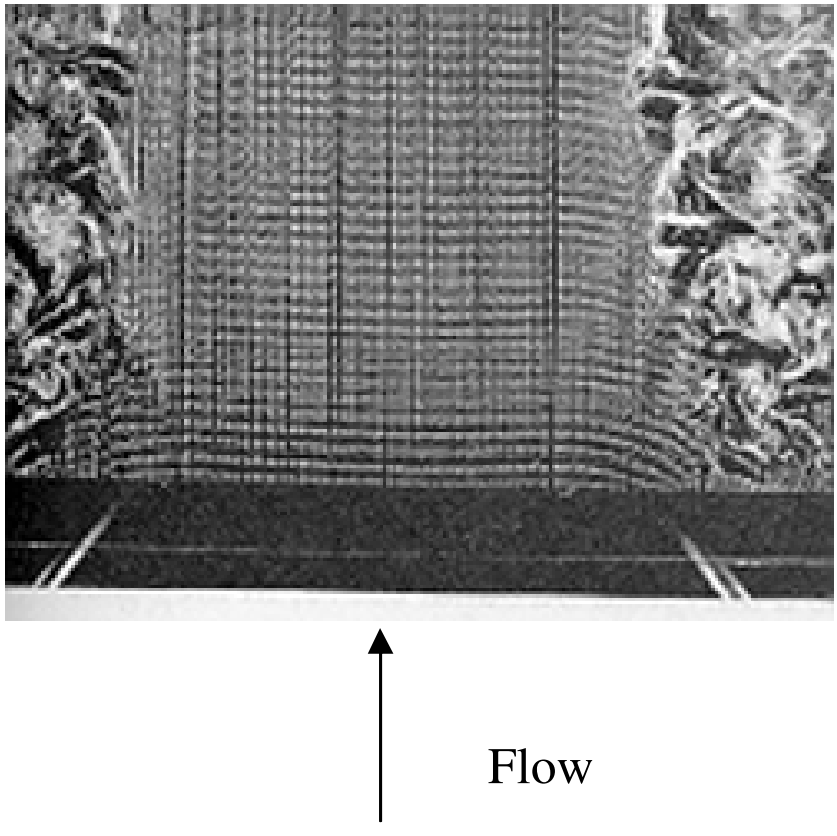

Figure 1.2: Illustration of parallel vortex shedding, from Williamson (1997).

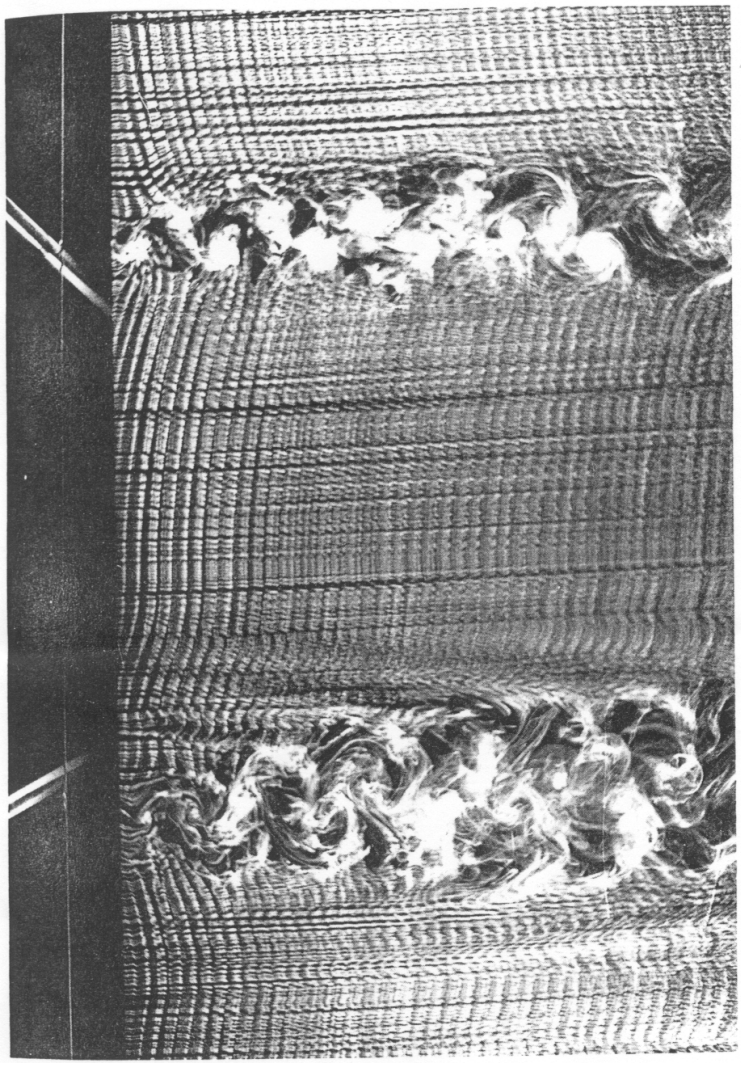

Figure 1.3: Illustration of oblique vortex shedding, from Williamson (1997).

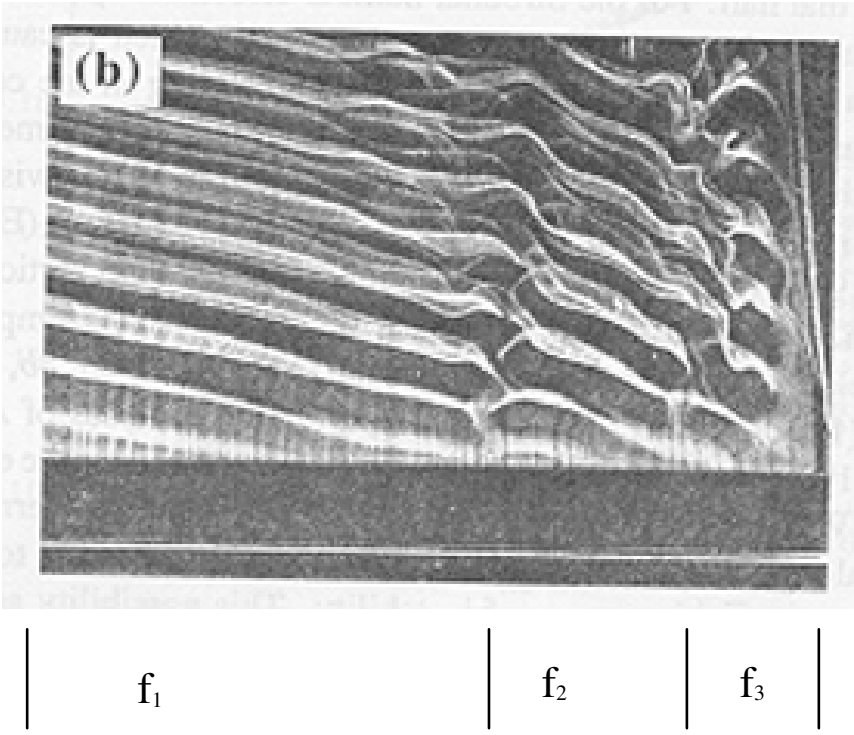

Figure 1.4: Illustration of cellular shedding, from Williamson (1997). Three distinct cells with shedding frequencies f_1, f_2, f_3 are observed.

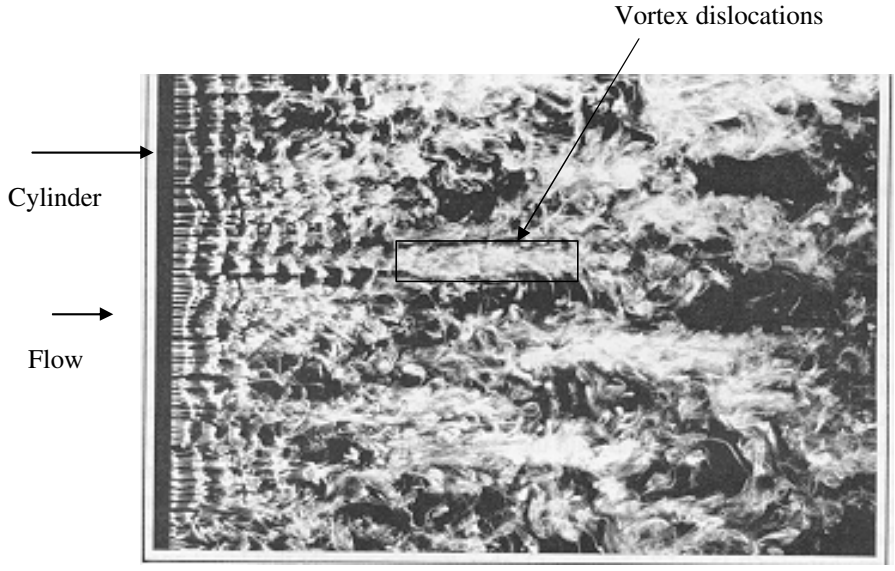

Figure 1.5: Illustration of vortex dislocations, from Williamson (1997).

Gerrard (1966) was one of the first to study in detail the three-dimensional aspects of the cylinder wakes. He identified three ways in which vortex shedding would deviate from a two-dimensional form: *oblique shedding* in which the vortices are shed at an angle to the cylinder axis, the *splitting* or *dislocation* of vortices of similar sign and the *looping* of vortices to the other side of the wake. Vortex dislocations (vortex splitting), i.e. the strong localized distortions of a spanwise vortex and its connection with two or more vortices, have also been studied by Gerrard (1978), Eisenlohr and Eckelmann (1989), Williamson (1992) and Zhang *et al.* (1995). Williamson (1992) has shown that vortex dislocations account for intermittent low-frequency oscillations in the wake. Such vortex dislocations are generated between adjacent spanwise cells of different frequency and cause a momentary difference in shedding phase of the primary vortices between cells (spanwise regions of constant shedding frequency). Cells are caused, for example, by cylinder inhomogeneities and by end conditions.

Gaster's work (1971) on weakly tapered cylinders introduced the possibility of spanwise cells of different frequency by forcing the flow to be non-uniform across the cylinder span. Maull and Young (1973) observed similar spanwise frequency cells in the wake of a circular cylinder placed in a spanwise freestream shear flow. Gerich and Ecklemann (1982) observed spanwise cell structures with frequencies 10-15 % lower than the Strouhal frequency near the cylinder endplates in the range of 10-20 cylinder diameters. Extensive investigation has been done on three-dimensional effects for Reynolds numbers greater than 100. Most of the recent advances in understanding the three-dimensional aspects of wake flows behind cylinders are discussed in review papers of Roshko (1993) and Williamson (1996). For $Re < 64$, Williamson (1988) observed spanwise cells of different frequency caused by oblique shedding from cylinder endplates and hence a quasi-periodic wake spectra. He concluded that this transition in the mode of oblique shedding from the cylinder endplates could be responsible for the discontinuity in the Strouhal-Reynolds number curve. Williamson (1988, 1989) also found that the oblique vortices formed a periodic chevron pattern in his towing tank and wind tunnel experiments.

To summarize, the current understanding on oblique vs parallel shedding in the wake behind a uniform cylinder is as follows; parallel shedding occurs in the absence of side-wall influences or by manipulation of end conditions, and oblique shedding is naturally induced by end effects (no slip condition) due to parallel side walls.

The end conditions have been altered in different ways in order to control vortex shedding patterns. Williamson (1988) showed that end plates suitably angled with respect to the incoming flow can be used to induce parallel shedding. Eisenlohr and Eckelmann (1989) used end plates combined with large diameter cylinders inserted at the ends of the main cylinder to control the wake. Miller and Williamson (1994) used a non-mechanical technique using suction tubes from downstream to achieve parallel vortex shedding. Hammache and Gharib (1989,1991) developed a "transverse control cylinders technique" where two larger circular "control cylinders" were positioned upstream of and normal to the shedding cylinder. Their study revealed that a non-symmetric pressure distribution, which induced a spanwise flow in the base region of the cylinder, was responsible for slantwise shedding and that a symmetric pressure distribution with zero spanwise component of velocity was responsible for parallel vortex shedding.

Valles *et al.* (2002) numerically investigated wake phenomena caused by a discontinuity in the cylinder diameter. The vortex linkage and half-loop formation, originally observed experimentally by Lewis and Gharib (1992) were reproduced numerically.

Wake structures behind oscillating cylinders

Most of recent work on understanding three-dimensional wake structures has focussed on stationary cylinders. However, Griffin and Ramberg (1992) studied the wake behind a vibrating flexible cable and proposed that the near wake at any point could be sensibly represented by the near wake of a rigid cylinder under the same conditions of frequency, amplitude, and Reynolds number. The numerical simulation work of Newman (1996) and Newman and Karniadakis (1996,1997) provided a quantitative comparison of forced and flow-induced cable vibrations at Reynolds numbers 100, 200

and 300 and aspect ratios 12.6 and 45. They used a parallel spectral element/Fourier method developed by Henderson and Karniadakis (1995). For the lower aspect ratio case, at the low Reynolds number ($Re = 100$) they observed a staggered pattern of vorticity connected in a "lace-like" pattern for a standing wave cable vibration. A travelling wave cable response produced oblique shedding of spanwise vorticity. When the Reynolds number was increased to 200, in the free vibration case they observed indications of oblique shedding due to the travelling wave response of the cable. In the forced vibration case, they noted that the pattern does not show the strong staggered pattern as in the $Re = 100$ case. The vortex structures were also analyzed at $Re = 300$ for the higher aspect ratio cylinder. They noticed a more three-dimensional wake with no staggered patterns or symmetric shedding patterns as was observed in the short wavelength case. They concluded that the forced and flow-induced vibration responses may not be similar, and that these differences increase at higher Reynolds numbers.

Newman (1996) also studied sheared inflow with Reynolds numbers ranging between 50 and 100 along the span of a cable of aspect ratio of 100. For the free vibration case, the cable crossflow displacement showed a mixed standing wave/travelling wave response forming an overall chevron pattern. A higher frequency of shedding was observed at the location of maximum spanwise inflow (cable midspan) as compared to the cable end. This difference in shedding frequency along the span causes vortex dislocation. Newman observed a more turbulent wake when the maximum Reynolds number was increased to 200. For the forced vibration case he reported relatively similar results for the two Reynolds numbers.

1.4 Nonlinear Dynamics Approach for Modeling Cylinder Wakes

Experiments and computational fluid dynamics (CFD) techniques remain the classical tools in the study of cylinder wakes and other complex fluid dynamical systems. In addition to these techniques, a new approach to modeling complex systems using tools from nonlinear dynamics has been pursued in the last two decades. The heart of this approach is the concept of universality, the notion that there might be some fundamental physics that applies to a wide range of systems. By utilizing this concept complex fluid systems can be efficiently studied using low dimensional models.

In the case of forced cylinder wakes, the universal phenomenon of lock-on is applicable. This concept was utilized by Olinger (1998) in his modeling of the cylinder wake as a coupled system of circle map oscillators. The basis for this wake oscillator model (termed Coupled Map Lattice, CML in short) came from his earlier success in the use of a circle map (Olinger, 1988,1993) to model the two-dimensional wake behind an externally forced, rigid cylinder. He showed that a circle map could be developed using a Landau-Stuart equation as a starting point. The Landau-Stuart equation can be deduced from the Navier-Stokes equations, and is known to describe the wake evolution near the critical Reynolds number for vortex shedding. A comprehensive discussion on coupled map lattices follows in Chapter 2.

The success of Olinger's CML model in describing the wake evolution behind freely vibrating cables provided the motivation for establishing the next class of models based on CMLs. These models incorporate additional unmodelled dynamics and provide for improved wake description. The accuracy comes from self-learning adaptive features introduced in the model. The present work largely deals with the development of the self-learning CML models, and therefore further discussion on this will be presented in the later chapters.

Several other investigators have proposed phenomenological models based on wake oscillators. Diffusively coupled models for wake flows, based on Ginzburg-Landau

(Albarede and Monkewitz, 1992) and van der Pol oscillators (Facchinetti *et al.*, 2002) have also been studied. Aamo and Krstic (2003) developed a backstepping control for a non-linear Ginzburg-Landau model (Roussopoulos and Monkewitz, 1996) of vortex shedding. Therefore, it is believed that in addition to describing the wake evolution, these models could also be developed for purposes of flow control. In this context, Balasubramanian (1998) added control terms to Olinger's CML model and explored the controlled dynamics of the CML. Proportional control and discontinuous nonlinear control methods were used to develop the control laws and the control efficiencies were compared. Such preliminary works will help establish a class of real-time flow control models for laboratory wake flows.

1.5 Coupled Map Lattice: Review

In a previous section we reviewed experimental and computational approaches to the study of three-dimensional wake structures. As we have just seen, the use of start-of-the-art flow visualization techniques has resulted in numerous observations of three-dimensional wake phenomena such as oblique and parallel shedding, cellular shedding, vortex dislocations, small scale three-dimensional instabilities (mode A-B) at transitional Reynolds numbers etc. Numerical simulations have so far mainly been used to confirm what has already been experimentally observed. However, a thorough physical understanding of the origin of the wake structures and their coupling effect on structural vibration is still unavailable. We also reviewed some studies based on the nonlinear dynamical systems approach in the previous section. In this section, a low-dimensional iterative model, the circle map, which forms the basis of the class of coupled map lattice (CML) models developed in this thesis, and the basic CML model are briefly reviewed.

The circle map

The circle map (Ostlund *et al.*, (1983), Feigenbaum *et al.*, (1982), Shenker, (1982)) is a standard universal model describing the non-linear dynamics of two coupled oscillators on a Poincaré section. In the context of a rigid cylinder, the temporal circle map,

$$X_{n+1} = X_n + \Omega - \frac{K}{2\pi}\sin(2\pi X_n), \tag{1.1}$$

was used to study a cylinder wake subjected to an imposed oscillation of controlled amplitude and frequency. The parameters in the circle map are related to the wake situation as follows: The system variable X_n represents the phase of the vortex shedding event at discrete times $t = n\Delta t = n/f_e$. The periodic vortex shedding from a stationary cylinder (at frequency) f_{so} and the imposed cylinder oscillation (at frequency f_e) yield the unforced frequency ratio, $\Omega = f_{so}/f_e$. The forcing term K is analogous to the imposed cylinder oscillation amplitude, A/D, where A is the amplitude and D is the cylinder diameter. The dynamics of the circle map are studied by determining the forced frequency ratio, $\omega = f_s/f_e = \lim_{n\to\infty} \dfrac{X_n - X_0}{n}$, where f_s is the vortex shedding frequency for the forced cylinder wake. Lock-on or resonance states are correlated with rational values of $\omega = p/q = f_s/f_e$, where p and q are integers. Irrational values of ω correspond to quasi-periodic states outside the lock-on regions. A summary of results, representing contours of ω were shown on the $K - \Omega$ plane. Multiple lock-on regions at fractional p/q ratios of the forcing frequency predicted by the circle map (Olinger, 1988) were also confirmed experimentally (see Stansby, (1976), Olinger, (1988), Bernhardt *et al.*, (1996)).

The coupled map lattice

As seen already, in case of a rigid cylinder forced to oscillate in a lock-on region represented on the $K - \Omega$ plane, periodic structures parallel to the axis of the cylinder are shed in the wake. The absence of any spanwise variation in the wake structure meant that a purely temporal model such as the circle map was sufficient to describe

the wake. However, the spatially varying wake flow, such as the flow-induced vibration of a flexible cable results in three-dimensional wake structures. In this case, the purely temporal circle map model is insufficient. Therefore, by combining the highly successful circle map with a spatial diffusion model, a spatio-temporal model capable of modeling three-dimensional wakes was developed. This model, known as the coupled map lattice (CML), utilized a series of circle map oscillators placed at the lattice points along the cylinder span. The coupling among the spatial oscillators was provided by a diffusion model. The vorticity transport equation:

$$\frac{\partial \omega}{\partial t} = \underbrace{-\mathbf{u}\cdot\nabla\omega + \omega\cdot\nabla\mathbf{u}}_{\text{convective}} + \underbrace{\nu\nabla^2\omega}_{\text{diffusive}}\ , \tag{1.2}$$

where ω and $\mathbf{u}$ are the vorticity and velocity vectors, is used as the starting point. If we now consider the spanwise (z) component of (1.2), we have:

$$\frac{\partial w_z}{\partial t} = -u\,\frac{\partial w_z}{\partial x} - v\,\frac{\partial w_z}{\partial y} - w\,\frac{\partial w_z}{\partial z} + w_x\,\frac{\partial w}{\partial x} + w_y\,\frac{\partial w}{\partial y} + w_z\,\frac{\partial w}{\partial z} + \nu\,\nabla^2 w_z\,. \tag{1.3}$$

Neglecting streamwise and transverse vorticity ($\omega_x = 0, \omega_y = 0$), streamwise and transverse variations in spanwise vorticity ($\frac{\partial w_z}{\partial x} = \frac{\partial w_z}{\partial y} = 0$), and the spanwise velocity component ($w = 0$), (essentially neglecting the convective terms) yields

$$\frac{\partial w_z}{\partial t} = \nu\frac{\partial^2 \omega_z}{\partial z^2}\,. \tag{1.4}$$

In order to obtain the diffusion map, we set $\mathrm{X} \equiv \omega_z$, where X is the state variable representing the phase of vortex shedding event. This will be justified if we understand that the vortex shedding event ($X = 1$, see figure 1.6) corresponds to attainment of a critical level of spanwise vorticity. Application of a simple explicit finite difference technique to (1.4) then results in,

$$\mathrm{X}_{n+1}^{k} = \epsilon\left(\mathrm{X}_{n}^{k+1} + \mathrm{X}_{n}^{k-1}\right) + (1-2\epsilon)\,\mathrm{X}_{n}^{k}, \tag{1.5}$$

where

$$\epsilon = \frac{\nu \Delta t}{\Delta z^2}.$$

We now consider the modified circle map which is combined with the diffusion model to form the CML model:

$$f_n^k = \mathrm{X}_n^k + \Omega^k - \frac{\mathrm{K}^k}{2\pi}\left(\sin\left(2\pi \mathrm{X}_n^k - \phi_1^k - \frac{\pi}{2}\right)\right). \tag{1.6}$$

In (1.6), the additional input parameter, ϕ_1^k represents the phase angle between the vortex shedding event and the cylinder motion at a given k location in a two-dimensional wake. The dependence of ϕ_1^k with cable vibration amplitude was discussed by Olinger (1998).

In order to combine the modified circle map with the diffusion model, we set $\mathrm{X}_n^k = f_n^k$ on the right hand side of (1.5). The diffusion model (1.7) along with (1.6) forms the coupled map lattice:

$$\mathrm{X}_{n+1}^k = \epsilon\left(f_n^{k+1} + f_n^{k-1}\right) + (1 - 2\epsilon) f_n^k. \tag{1.7}$$

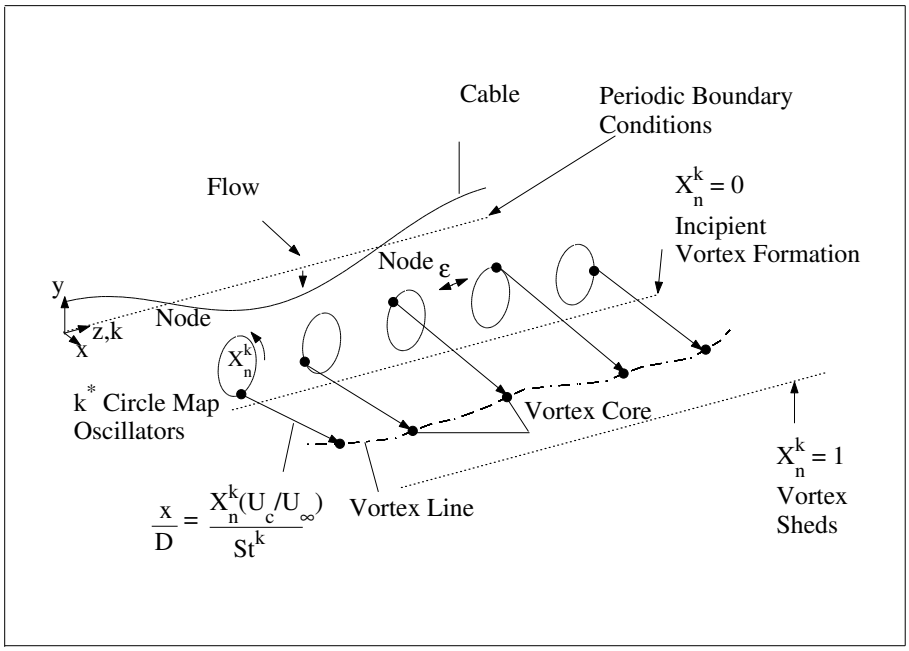

Figure 1.6: Schematic of the coupled map lattice. Adapted from Olinger, (1998).

Inputs for basic CML

The imposed cable oscillation is studied using the forcing term K^k in (1.6). For example,

$$\mathrm{K}^k = \mathrm{K}_0 \cos\left(2\pi(k - nk_t)/k_{wave}\right), \tag{1.8}$$

can model both standing wave cable mode shapes ($k_t = 0$) and traveling wave cable mode shapes ($k_t \neq 0$). The unforced frequency ratio, ($\Omega^k = f^k_{so}/f_e$) can be varied along the span in order to model shear flow effects arising from freestream flow conditions or spanwise variations in geometry. Other input parameters such as the Reynolds number, Re, the number of lattice points, k^*, the aspect ratio or the spanwise wavelength, $AR = L/D$ are required to determine the diffusion coefficient

$$\epsilon = \frac{\nu \Delta t}{(\Delta z)^2} = \frac{\Omega^k (k^* - 1)^2}{StReAR^2}$$

in the diffusion model.Further details can be obtained in Olinger (1998). Specification of Ω^k and K^k in the CML implies that externally forced, as opposed to self-excited cable wakes are modeled in the present study.

Freely vibrating CML

However, using the same dynamical systems framework adopted in the current work, Davis *et al.*(2003) developed a coupled cable-wake model for studying freely vibrating (self-excited) cables. He combined a CML wake model with a linear wave equation cable model to study the free response of the wake and the resulting wake structures. Results showed that the freely vibrating CML predicted cross-flow amplitudes comparable to numerical predictions (Newman and Karniadakis, 1997) as the cable mass-damping parameter was varied over an order of magnitude.

Basic CML output

The primary output of the CML model is vortex shedding patterns. The *phase of vortex shedding*, X_n^k in the CML model, is converted to a downstream vortex core location, x/D, (1.9) through a linear transformation to determine these patterns (see Figure 1.6);

$$\left(\frac{x}{D}\right)_n^k = \mathrm{X}_n^k \, x^* = \frac{\mathrm{X}_n^k \, U_c}{St \, U_\infty} \, . \tag{1.9}$$

Here, x^* represents a characteristic non-dimensional vortex spacing in the streamwise direction, $St = f_{so}D/U_\infty$ is the *Strouhal number*, f_{so} is the *vortex shedding frequency*, U_c is the *vortex convection velocity* and U_∞ is the *uniform freestream velocity*. Both $(x/D)_n^k$ and X_n^k outputs will be used interchangeably throughout this thesis as convenient to present the results.

In addition to the vortex shedding patterns, the phase of the vortex shedding, X_n^k, is also used to determine the forced frequency ratio, $\omega^k = f_s^k/f_e$, in order to determine the lock-on regions (see Olinger 1998).

Basic CML limitations

In Figure 1.7 the resultant wake patterns due to K_o variation are compared to a wake pattern (phase of vortex shedding event) determined from a direct numerical simulation of the Navier-Stokes equations using the NEKTAR simulation. The simulation of Figure 1.7 will serve as a sample NEKTAR run throughout the present work. Figure 1.7(a),(b) show vortex shedding patterns for one shear layer viewed by an observer looking in the transverse (y direction) observing the x-z plane (see Figure 1.6). The cable and flow direction (left to right) are included to orient the reader. The methods used to determine the NEKTAR simulation wake pattern shown here will be detailed in subsequent sections.

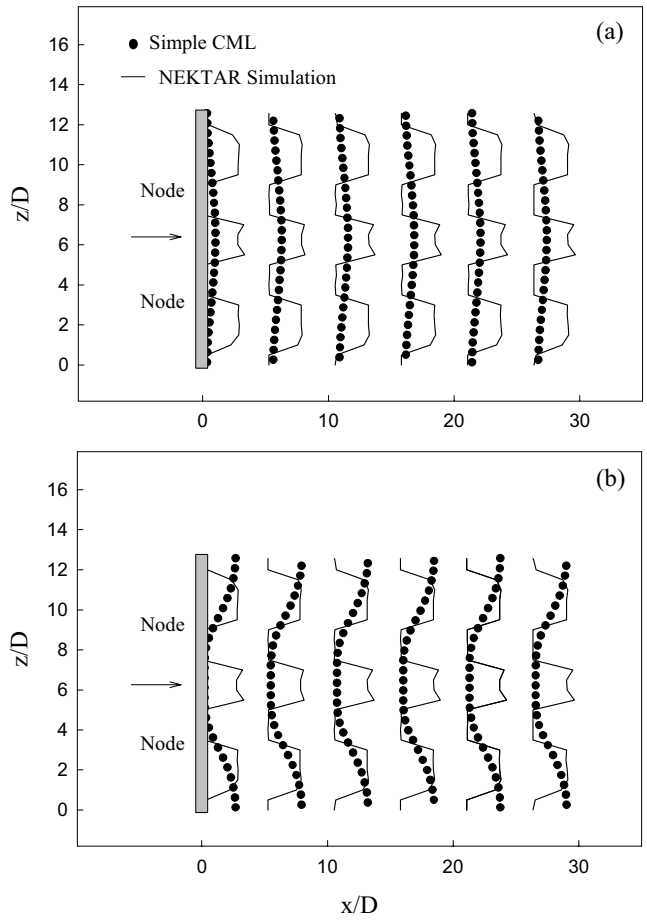

Figure 1.7: Comparison of vortex shedding wake patterns from the simple CML and the NEKTAR simulation. $Re = 100, \Omega = 1.0, AR = 4\pi, k^* = 26, A/D = 0.68$ at anti-nodes in NEKTAR simulation. (a) $K_o = 0.01$. (b) $K_o = 0.1$.

It can be clearly seen that simple variation of the free parameters in the CML model ((1.7), (1.6)) cannot yield wake patterns which precisely match the NEKTAR simulation patterns. The simple nature of our previous CML models means that there will always be unmodelled wake dynamics if a detailed comparison is made between an actual wake flow and the CML wake patterns. These unmodelled dynamics result in the difference between the wake patterns from the CML model and the actual wake flow in Figure 1.7.

Other studies on coupled maps

We will briefly mention other investigators who have studied couple map oscillators. Kaneko (1989,1991) investigated coupled map lattices as a model for spatiotemporal chaos and made some connections with the Navier-Stokes equations. Kaneko also studied transitions among coherent, ordered, partially ordered and turbulent states in circle maps. Alstrom and Ritala (1987) studied mode locking in coupled circle maps with random phases and found very different behavior compared to a single circle map. Sinha and Gupte (1998) investigated two-dimensional coupled map lattices and targeted spatio-temporal patterns using adaptive control techniques. Balasubramanian *et al.* (2002) introduced control terms into the basic CML model in their effort to modify complex wake patterns behind vibrating flexible cables. Three different control techniques were developed and applied to a modeled vortex dislocation structure. The desired parallel shedding patterns were targeted and the control efficiencies of the different schemes were compared. A complete summary of this work is given in Chapter 6.

1.6 Motivation and goals of current work

In our discussion of the limitations of the basic CML model, we came to the conclusion that the limited free parameters do not permit accurate modeling of complex wake structures observed, for example, in NEKTAR simulations. A number of simpli-

fying assumptions were made in order to derive the simplest possible diffusion model from the vorticity transport equation. These simplifying assumptions meant that some essential dynamics were not modeled. These unmodelled dynamics result in the difference between actual and modeled wake structures.

However, the low-order models are computationally efficient and therefore preferred over computational or experimental approaches. The computationally intensive Navier Stokes solvers are not suitable for an observer based feedback control of wake flows. This fact merits the continued development of highly accurate and efficient low-order models for on-line estimation and control of vortex shedding patterns. It must be emphasized here that control of vortex shedding patterns eventually helps in the suppression of vortex induced vibrations. The vortex patterns determine the fluid loadings which in turn help determine the amplitude of vibration of the structure. Therefore, suitable manipulation of fluid loadings by controlling wake patterns can lead to suppression of vortex induced vibration. We believe that use of low-dimensional models is the best approach to solving this highly important problem.

With this eventual goal of incorporating low-order CML models into a wake control system established, the current study focuses on achieving the following goals:

1. Overcome the limitations of the simple diffusive CML model by considering additional dynamics in a new convective diffusive CML model (see Chapter 2). In this new model, an additional spanwise velocity parameter can be varied across the cable span.

2. Establish a class of self-learning CML models based on the new convective diffusive model by incorporating adaptive estimation techniques. These techniques have been widely applied in signal processing, speech recognition and control systems. Adaptive estimation is a modeling technique in which certain parameters of the system model are adaptively varied in time based on a stable learning process (estimation model) derived for the system. A stable estimation model ensures that the error between the modeled and the actual system does not grow unbounded. The new self-learning CML will be useful for making quantitative comparisons between the

modeled wake flows and wake flows from numerical simulations or experiments.

3. Compare the modeling efficiencies of two different self-learning CML models. The first model is based on a newly developed multi-variable least-squares algorithm (see Chapter 3). For the first time in this thesis, convergence of the multi-variable least-squares algorithm is addressed. The second model based on neural networks is discussed in Chapter 4. The two models are used to predict wake patterns from NEKTAR simulations at $Re = 100$.

4. Apply the self-learning CML models to estimate data from laboratory experiments (Chapter 5) to develop the capability of an off-line estimation scheme. In this scheme, the wake data are measured and the stored data are used for estimation. This is opposed to an on-line (real-time) scheme in which the generation and estimation of wake data occur simultaneously with no time delay. The development of self-learning CML models capable of off-line estimation of wake data is the goal of this thesis.

5. In a parallel theoretical study, incorporate control strategies into the simple CML model (see Chapter 6) . Such flow control models could eventually model an experimental wake flow in a feedback control system designed to produce desired wake patterns behind vibrating cables.

The self-learning CML model extends the earlier simple basic CML model with the introduction of self-learning features which adaptively estimate unmodelled dynamics. These unmodelled dynamics result in the difference between the estimated wake patterns and simulated or experimentally observed wake patterns. The adaptive estimation schemes are developed to eliminate the differences in observed and predicted wake patterns. The current work focuses on offline estimation of wake patterns using self-learning CML models. However, the extension of this work towards on-line estimation of laboratory wake flow patterns should be pursued in the near future. This can be accomplished if the estimation of wake patterns occur within a sampling interval (period of vortex shedding). Currently, the self-learning CML models require $O(10^{-}2)$ wall-clock seconds per shedding cycle. Therefore, if the sampling intervals are of the same order, such timing issues can be easily addressed by the current

self-learning CML models and on-line capabilities can be immediately realized.

The on-line self-learning CML models would then serve as wake models in flow control experiments. Methods developed for controlling wake patterns of the simple CML model can similarly be pursued for the self-learning CML models. However, we still need to address control actuation issues and interfacing CML models with the control actuator in an on-line scheme.

Chapter 2

Convective-Diffusive CML

In this chapter, we discuss the development of the convective-diffusive CML. This new CML model is capable of modeling additional dynamics not previously considered in the basic CML model discussed in Chapter 1. In order to motivate the development of a new CML model, it is worth mentioning again that the goal of this thesis is to develop highly efficient estimation models for identification of complex cylinder wake dynamics obtained from numerical simulations, or laboratory wake flow experiments. As a first step in realizing this goal, numerical simulation from a highly accurate NEKTAR code was chosen for a proof-of-concept study. Simulations of uniform freestream flow and sheared freestream flow over a uniform cylinder were carried out. The cylinder was forced to vibrate in the standing wave mode at Reynolds number of the order of 100. More details of the simulations will follow in Chapters 3 and 4. We will now provide a brief introduction to the NEKTAR solver.

2.1 Introduction to NEKTAR

The NEKTAR code (see Warburton, 1998) is used to solve the three-dimensional Navier-Stokes equations governing the coupled fluid-structure interaction. It is based on hierarchical spectral/hp expansions on hybrid subdomains. The spectral element method uses the same form of approximate solution as the (traditional) Galerkin

method (Fletcher, 2000). Like the (traditional) Galerkin method the approximating functions are non-zero throughout the computational domain. The main difference is that spectral element method uses orthogonal functions for the approximating functions. Two-dimensional elements (triangles and quadrilaterals) are used to discretize the (x-y) planes, while a Fourier expansion is used in the spanwise (z) direction along the cylinder axis. The code is written in C + + and MPI (Message Passing Interface) is employed in all simulations. For parallel implementation, each Fourier mode is assigned to a separate processor (see Crawford *et al.* 1996).

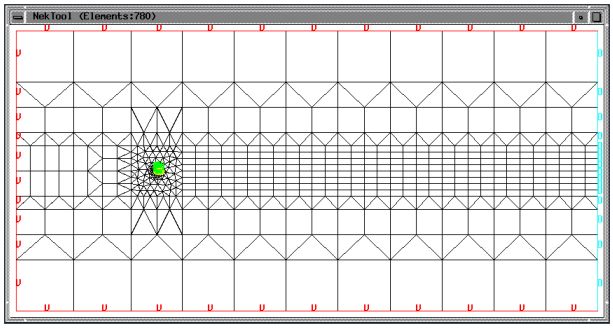

Figure 2.1: Hybrid grid used for the numerical simulations.

The computational domain for the (x,y)-plane used for the Re = 100 simulations extends 69 cylinder diameters downstream and 22 diameters in front, above and below the cylinder. The spanwise wavelength (also referred to as aspect ratio, AR in this thesis) = 4π. A hybrid mesh (see Figure 2.1) consisting of 780 elements was used for the simulations. An 8^{th} order polynomial was considered for the entire domain. 16 z-planes or 8 independent Fourier modes were used and a $\frac{3}{2}$ de-aliasing rule was applied. The cylinder was forced to vibrate in the standing wave mode, $y(z,t) = A\cos(f_e t)\cos(2\pi z/L)$. The amplitude was chosen as $A = 0.7D$, and the frequency as $f_e = 2\pi * 0.167 = 1.05$, giving rise to an unforced frequency ratio, $\Omega = f_{so}/f_e = 1.0$. Simulations of this lock-on case were carried out on an IBM SP supercomputer at San Diego Supercomputer Center. A non-dimensional time step of $\Delta tU/d = 0.001$ was used giving rise to approximately 5800 time steps per shedding cycle and a computational time close to 5 seconds per time step.

2.2 Development of the convective-diffusive CML

The convective-diffusive CML includes additional convective dynamics in the vorticity transport equation not considered in the basic CML.

$$\frac{\partial \omega}{\partial t} = \underbrace{-\mathbf{u}\cdot\nabla\omega + \omega\cdot\nabla\mathbf{u}}_{\text{convective}} + \underbrace{\nu\nabla^2\omega}_{\text{diffusive}} \ , \tag{2.1}$$

where ∇ is the vector differential operator, $\mathbf{u} = (u, v, w)$ and $\omega = (\omega_\mathbf{x}, \omega_\mathbf{y}, \omega_\mathbf{z}) = \nabla\times\mathbf{u}$, and x, y, z represent the streamwise, crossflow and spanwise directions respectively, ν is the kinematic viscosity of the fluid. The first two terms on the right hand side of (2.1) are the added convective terms. The additional convective terms allow for modeling the spanwise variations in spanwise velocity, $w(z)$, and streamwise vorticity, $\omega_z(z)$. We now consider the z component of the vorticity transport equation to get,

$$\frac{\partial w_z}{\partial t} = -u\,\frac{\partial w_z}{\partial x} - v\,\frac{\partial w_z}{\partial y} - w\,\frac{\partial w_z}{\partial z} + w_x\,\frac{\partial w}{\partial x} + w_y\,\frac{\partial w}{\partial y} + w_z\,\frac{\partial w}{\partial z} + \nu\,\nabla^2 w_z\,. \tag{2.2}$$

We make the following assumptions;

$$\frac{\partial w_z}{\partial x} = \frac{\partial w_z}{\partial y} = 0,\ O(w_x) \ll O(w_z),\ O(w_y) \ll O(w_z).$$

These assumptions are reasonable for the cylinder wake flow which is modeled by the CML. The vorticity transport equation in the z direction now simplifies to,

$$\frac{\partial w_z}{\partial t} = -w\,\frac{\partial w_z}{\partial z} + w_z\,\frac{\partial w}{\partial z} + \nu\,\frac{\partial^2 w_z}{\partial z^2}. \tag{2.3}$$

The convective-diffusive CML is obtained by combining the modified circle map with a discrete diffusion map derived from the simplified vorticity transport equation (2.3). In order to obtain the diffusion map, define $\mathrm{X} \equiv w_z$. We apply simple explicit finite differencing (forward in time, centered in space) derived from Taylor series expansion

of X at time $n\Delta t$ and spanwise location $k\Delta z$ as follows:

$$\begin{aligned}
\left(\frac{\partial \mathrm{X}}{\partial t}\right)_n^k &= \frac{(\mathrm{X}_{n+1}^k - \mathrm{X}_n^k)}{\Delta t} + O(\Delta t) \\
\left(\frac{\partial \mathrm{X}}{\partial z}\right)_n^k &= \frac{(\mathrm{X}_n^{k+1} - \mathrm{X}_n^{k-1})}{2\Delta z} + O((\Delta z)^2) \\
\left(\frac{\partial^2 \mathrm{X}}{\partial z^2}\right)_n^k &= \frac{(\mathrm{X}_n^{k+1} - 2\mathrm{X}_n^k + \mathrm{X}_n^{k-1})}{(\Delta z)^2} + O((\Delta z)^2)
\end{aligned}$$

Here, Δt and Δz represent the spacing in time and space respectively. If we apply the Taylor series expansions in (2.2), then replacing w_z by X we get,

$$\left(\frac{\partial \mathrm{X}}{\partial t}\right)_n^k = -\left(w\,\frac{\partial \mathrm{X}}{\partial z}\right)_n^k + \left(\mathrm{X}\,\frac{\partial w}{\partial z}\right)_n^k + \nu\left(\frac{\partial^2 \mathrm{X}}{\partial z^2}\right)_n^k.$$

Now, omitting the $O(\Delta t)$ and $O((\Delta z)^2)$ terms in the finite difference representation of (2.3) with the understanding that the simple explicit scheme is of $O(\Delta t, (\Delta z)^2)$ we get,

$$\begin{aligned}
\mathrm{X}_{n+1}^k &= \mathrm{X}_n^k + \frac{\Delta t}{2\Delta z}\left(w_n^k(\mathrm{X}_n^{k-1} - \mathrm{X}_n^{k+1}) + \mathrm{X}_n^k(w_n^{k+1} - w_n^{k-1})\right) \\
&+ \frac{\nu \Delta t}{(\Delta z)^2}\left(\mathrm{X}_n^{k-1} - 2\mathrm{X}_n^k + \mathrm{X}_n^{k+1}\right).
\end{aligned} \tag{2.4}$$

We will now make a further assumption that the convection is of Burger's type. With this assumption, the temporal variation of the spanwise velocity w_n^k is ignored and a spatially varying spanwise velocity $c^k \equiv w^k$ is introduced. As one can see in the latter steps of the development of the convective-diffusive CML, the relaxation of temporal variation of spanwise velocity can be removed without any change in the form of the equations in the model. The importance of a spatial-temporal spanwise velocity is re-established in Chapter 3. However, the current objective of the development of the convective-diffusive CML is the inclusion of additional convective dynamics in the simplest form (Burgers type). So, we will omit w_n^k in favor of c^k in (2.4).

Using non-dimensional parameters,

$$\overline{c}^k = \frac{c^k}{U_\infty}, \quad \gamma^k = \frac{c^k \Delta t}{2\Delta z} = \frac{\overline{c}^k \Omega(k^*-1)}{2StAR}, \quad \epsilon = \frac{\nu \Delta t}{\Delta z^2} = \frac{\Omega(k^*-1)^2}{StReAR^2},$$

we can rewrite (2.4) in non-dimensional form as,

$$\begin{aligned} \mathrm{X}_{n+1}^k = & \underbrace{\left(-\mathrm{X}_n^k \gamma^{k-1} + (\mathrm{X}_n^{k-1} - \mathrm{X}_n^{k+1})\gamma^k + \mathrm{X}_n^k \gamma^{k+1}\right)}_{\text{convective}} \\ & + \underbrace{\left(\epsilon\, \mathrm{X}_n^{k-1} + (1-2\epsilon)\mathrm{X}_n^k + \epsilon \mathrm{X}_n^{k+1}\right)}_{\text{diffusive}}. \end{aligned} \tag{2.5}$$

The coupling between (2.5) and the modified circle map (1.6) requires $f_n^k = \mathrm{X}_n^k$ so that,

$$\begin{aligned} X_{n+1}^k = & \Big(- f_n^k \gamma^{k-1} + (f_n^{k-1} - f_n^{k+1})\gamma^k + f_n^k \gamma^{k+1} \Big) \\ & + \Big(\epsilon f_n^{k-1} + (1-2\epsilon) f_n^k + \epsilon f_n^{k+1} \Big). \end{aligned} \tag{2.6}$$

Equation (2.6) can be written in vector form as:

$$\begin{aligned} \mathbf{X}_{n+1} &= \mathbf{A}(\epsilon)\mathbf{F}(\mathbf{X}_n) + \mathbf{G}(\mathbf{X}_n)\mathbf{\Gamma} \\ &= \underbrace{\mathbf{A}(\epsilon)\mathbf{F}(\mathbf{X}_n)}_{\text{diffusive}} + \underbrace{\mathbf{Y}_{n+1}}_{\text{convective}}, \end{aligned} \tag{2.7}$$

where $\mathbf{X}_n = \left(\mathrm{X}_n^1\ \mathrm{X}_n^2\ \cdots\ \mathrm{X}_n^{k^*}\right)^T$, $k^* = 1 + \frac{L}{D\Delta z}$ is the number of spanwise oscillators,

$$\mathbf{A}(\epsilon) = \begin{bmatrix} 1+\epsilon & -2\epsilon & \epsilon & 0 & \cdots & 0 \\ \epsilon & 1-2\epsilon & \epsilon & 0 & \cdots & 0 \\ 0 & \ddots & \ddots & \ddots & \ddots & \vdots \\ \vdots & \ddots & \ddots & \ddots & \ddots & 0 \\ 0 & \cdots & 0 & \epsilon & 1-2\epsilon & \epsilon \\ 0 & \cdots & 0 & \epsilon & -2\epsilon & 1+\epsilon \end{bmatrix},$$

$$\mathbf{G}(\mathbf{X}_n) = \begin{bmatrix} f_n^{k^*-1} - f_n^2 & f_n^1 & 0 & \cdots & 0 & -f_n^1 \\ -f_n^2 & f_n^1 - f_n^3 & f_n^2 & 0 & \cdots & 0 \\ 0 & \ddots & \ddots & \ddots & \ddots & \vdots \\ \vdots & \ddots & \ddots & \ddots & \ddots & 0 \\ 0 & \cdots & 0 & \ddots & \ddots & f_n^{k^*-1} \\ f_n^{k^*} & 0 & \cdots & 0 & -f_n^{k^*} & f_n^{k^*-1} - f_n^2 \end{bmatrix},$$

$\mathbf{F}(\mathbf{X}_n) = \begin{pmatrix} f_n^1 & f_n^2 & \dots & f_n^{k^*} \end{pmatrix}^T$ and $\mathbf{\Gamma} = \begin{pmatrix} \gamma^1 & \gamma^2 & \dots & \gamma^{k^*} \end{pmatrix}^T$.

In (2.7) $\mathbf{X}_n$ is available and $\mathbf{\Gamma}$, i.e., the w term in the vorticity diffusion equation (2.4) is the unknown. It is desired to estimate $\mathbf{\Gamma}$ from experimental data. It is observed that the convective-diffusive CML predicts a more complex wake structure compared to the diffusive CML due to the additional dynamics modeled in the vorticity equation.

It has been shown earlier in Balasubramanian *et al.* (2001,2002) that a simple variation of the two input parameters, unforced frequency ratio, $\Omega = f_{so}/f_e$, where f_e is the excitation frequency, and the forcing term, K^k, in the basic CML model cannot yield wake patterns that precisely match wake patterns determined from a numerical simulation of the Navier-Stokes equation using the NEKTAR code. The unmodelled dynamics result in the difference between the CML wake patterns and the actual wake flow. In order to overcome this limitation, self-learning features are incorporated into the basic CML model. The unmodelled dynamics in the convective-diffusive CML are described by the $\mathbf{G}(\mathbf{X}_n)$ term in (2.7).

Typical wake patterns from the diffusive CML of (1.7), (1.6) and the convective-diffusive CML ((2.5),(1.6)) are compared in Figure 2.2. A sinusoidal variation in the spanwise velocity distribution, γ^k, is assumed to qualitatively match the NEKTAR simulation prediction for this quantity. The spatial wavelength of γ^k is set at half the value of the cable vibration wavelength given in (1.8), again consistent with the NEKTAR simulation. It is observed that the convective-diffusive CML predicts a more complex wake structure compared to the diffusive CML due to the additional

dynamics modeled in the vorticity equation. For the self-learning CML developed later in Chapter 3, the spanwise velocity distribution is adaptively estimated.

Next, in Figure 2.3 the wake patterns shown in Figure 2.2 are then compared with the NEKTAR wake patterns (shown in Figure 1.7). We can observe that the convective-diffusive CML (with its increased modeling capabilities in the form of the spanwise velocity parameter) performs better in predicting complex NEKTAR wake patterns than the basic CML. We now logically seek to extend the modeling capabilities of the convective-diffusive CML by introducing self-learning features. With this goal in mind, the assumption of temporal invariance of the spanwise velocity parameter is removed and spatio-temporal spanwise velocity, Γ_n^k is established. The increased dimension of the spanwise velocity, $\mathbf{\Gamma}$, means that it can no longer be an input parameter. But, by suitably varying $\mathbf{\Gamma}$, increased modeling capabilities are achieved. Chapters 3 and 4 are devoted to the development of a class of self-learning CML models suitable for quantitative comparison with experimental and NEKTAR wake patterns.

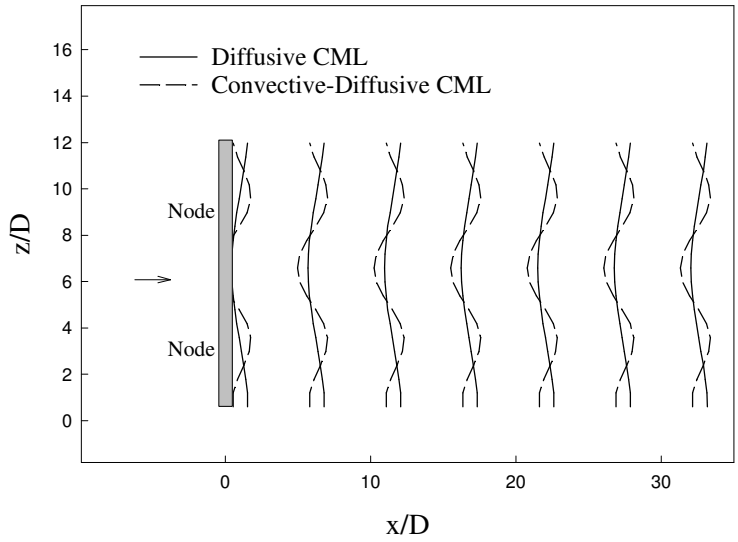

Figure 2.2: Comparison of vortex shedding patterns for the simple diffusive CML and the convective-diffusive CML. $Re = 100, \Omega = 1, \mathrm{K}_o = 0.01, w_o = 0.001$.

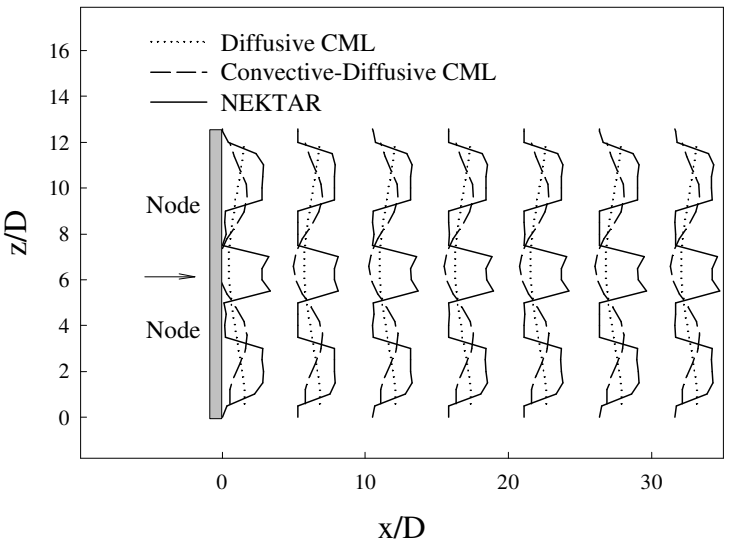

Figure 2.3: Comparison of NEKTAR vortex shedding patterns with the simple diffusive CML and the convective-diffusive CML. $Re = 100, \Omega = 1, \mathrm{K}_o = 0.01, w_o = 0.001$.

Chapter 3

Self-Learning CML

In this chapter, we discuss the development of the self-learning CML which seeks to accurately estimate unmodelled dynamics in wake flows. A schematic of the self-learning CML is shown in Figure 3.1. It is worth mentioning once again that X_n^k, the phase of the vortex shedding event, will be used to represent the wake patterns, x_n^k. This was justified in Chapter 1 by the assumption of constant vortex convection velocities without dissipation in the near wake. The self-learning CML is required to precisely match wake patterns from NEKTAR simulation (as shown in Figure 3.1. To this end, target wake patterns using cross-correlation methods detailed in this Chapter are obtained from NEKTAR (experimental) wake velocity signatures (Figure 3.1a). The self-learning CML model computes estimated wake patterns, $\widehat{X}_n^k$. The difference between the estimated and target wake patterns is called the state error. The state error is fed into the adaptive estimation models which form the core of the self-learning CML (Figure 3.1b). The objective is to drive the state error to zero, resulting in accurate prediction of target wake patterns (Figure 3.1c).

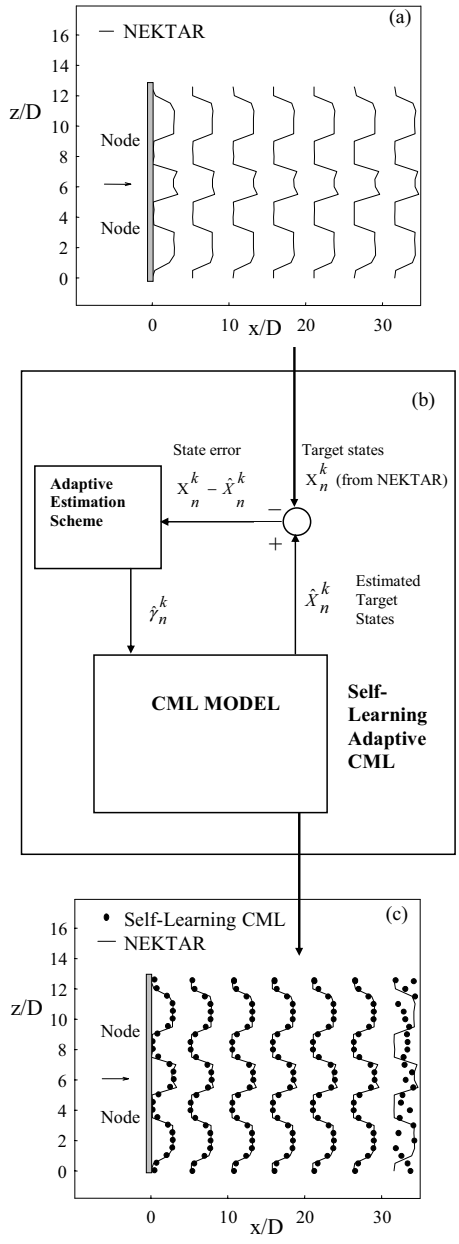

Figure 3.1: Diagram of the self-learning coupled map lattice. (a) Vortex shedding pattern form the NEKTAR simulation that serves as target states for the self-learning CML. (b) Schematic of the self-learning CML model. (c) Desired vortex pattern match between the self-learning CML and the NEKTAR simulation.

3.1 Self-learning CML based on convective-diffusive CML and MVLS algorithm

The self-learning CML mimics the dynamics of the convective-diffusive CML (2.7). It is assumed that the diffusion process is modeled exactly as in the convective-diffusive CML. The diffusion and convection processes are uncoupled in the convective-diffusive CML and also in the self-learning CML. In the first stage of model development, it is assumed that the convective process is accurately modeled by the spanwise velocity distribution alone. So, the only unknown term to be estimated is $w(z)$, spanwise distribution of the spanwise velocity, i.e. $\mathbf{\Gamma}$ term in (2.7). Now, the self-learning CML (adaptive observer) can be written as:

$$\begin{aligned} \widehat{\mathbf{X}}_{n+1} &= \mathbf{A}(\epsilon)\mathbf{F}(\mathbf{X}_n) + \mathbf{G}(\mathbf{X}_n)\widehat{\mathbf{\Gamma}}_n \\ &= \mathbf{A}(\epsilon)\mathbf{F}(\mathbf{X}_n) + \widehat{\mathbf{Y}}_{n+1} \end{aligned}, \tag{3.1}$$

where $\widehat{\mathbf{\Gamma}}_n$ is the estimator (on-line estimate) of the time invariant, unknown spanwise velocity distribution, $\mathbf{\Gamma}$. It is our objective to find a recursive estimation procedure for $\widehat{\mathbf{\Gamma}}_n$. Therefore, let us define the *state error* as:

$$\begin{aligned} \mathbf{e}_{n+1} &\equiv \widehat{\mathbf{X}}_{n+1} - \mathbf{X}_{n+1} \\ &= \mathbf{G}(\mathbf{X}_n)(\widehat{\mathbf{\Gamma}}_n - \mathbf{\Gamma}) \\ &= \mathbf{G}(\mathbf{X}_n)\widetilde{\mathbf{\Gamma}}_n \\ &= \mathbf{G}(\mathbf{X}_n)\widehat{\mathbf{\Gamma}}_n - \mathbf{Y}_{n+1}, \end{aligned} \tag{3.2}$$

where $\widetilde{\mathbf{\Gamma}}$ denotes the *parameter error*, $\widetilde{\mathbf{\Gamma}}_n = \widehat{\mathbf{\Gamma}}_n - \mathbf{\Gamma}$. Our goal is to drive the state error to zero in the shortest possible time for efficient estimation of wake patterns. We use a *multi-variable least-squares* algorithm (Goodwin and Sin, 1984) to minimize the state error after each time step. Goodwin and Sin (1984) also address convergence and boundedness issues for similar adaptive schemes. The following equations illustrate the steps in the derivation of the adaptation scheme for the state error. The

multi-variable least-squares algorithm involves the minimization of a positive definite function (cost function), suitably chosen to represent the accuracy of estimation. In our case, the cost function is defined as

$$\begin{aligned} J_n &= (\overline{\mathbf{\Gamma}} - \widehat{\mathbf{\Gamma}}_0)^T \mathbf{P}_0^{-1} (\overline{\mathbf{\Gamma}} - \widehat{\mathbf{\Gamma}}_0) \\ &\quad + \tfrac{1}{2} \sum_{j=1}^{n} \left(\mathbf{Y}_{j+1} - \mathbf{G}(\mathbf{X}_j)\overline{\mathbf{\Gamma}} \right)^T \mathbf{R}^{-1} \left(\mathbf{Y}_{j+1} - \mathbf{G}(\mathbf{X}_j)\overline{\mathbf{\Gamma}} \right) , \end{aligned} \tag{3.3}$$

where $\overline{\mathbf{\Gamma}}$ is a dummy variable used for analysis purposes, the first term is the cost associated with parameter estimation, and the second term is the cost associated with state estimation. The parameters $\mathbf{P}_0$ and $\mathbf{R}$ are input weighting matrices and can be varied to achieve optimal parameter estimation.

When the parameter $\widehat{\mathbf{\Gamma}}_0$ is chosen as some finite valued vector, then minimizing the cost function J_n with respect to the dummy variable $\overline{\mathbf{\Gamma}}$ yields the solution, $\widehat{\mathbf{\Gamma}}_{n+1}$ as:

$$\begin{aligned} &\frac{\partial J_n}{\partial \overline{\mathbf{\Gamma}}} = \mathbf{0} \implies \\ &\mathbf{P}_0^{-1}(\overline{\mathbf{\Gamma}} - \widehat{\mathbf{\Gamma}}_0) - \sum_{j=1}^{n} \mathbf{G}(\mathbf{X}_j)^T \mathbf{R}^{-1} \left(\mathbf{Y}_{j+1} - \mathbf{G}(\mathbf{X}_j)\overline{\mathbf{\Gamma}} \right) = 0 \cdot \end{aligned} \tag{3.4}$$

Solving (3.4) for $\widehat{\mathbf{\Gamma}}_{n+1}$, one obtains

$$\widehat{\mathbf{\Gamma}}_{n+1} = \left(\mathbf{P}_0^{-1} + \sum_{j=1}^{n} \mathbf{G}(\mathbf{X}_j)^T \mathbf{R}^{-1} \mathbf{G}(\mathbf{X}_j) \right)^{-1} \left(\mathbf{P}_0^{-1} \widehat{\mathbf{\Gamma}}_0 + \sum_{j=1}^{n} \mathbf{G}(\mathbf{X}_j)^T \mathbf{R}^{-1} \mathbf{Y}_{j+1} \right) \cdot \tag{3.5}$$

Now, define the *covariance matrix* $\mathbf{P}_n$ and get a recurrence relation using the Matrix Inversion Lemma (Harville, 1997) as follows:

$$\begin{aligned} &\mathbf{P}_n^{-1} = \mathbf{P}_0^{-1} + \sum_{j=1}^{n} \mathbf{G}(\mathbf{X}_j)^T \mathbf{R}^{-1} \mathbf{G}(\mathbf{X}_j), \\ &\implies \mathbf{P}_n^{-1} = \mathbf{P}_{n-1}^{-1} + \mathbf{G}(\mathbf{X}_n)^T \mathbf{R}^{-1} \mathbf{G}(\mathbf{X}_n), \\ &\mathbf{P}_n = \mathbf{P}_{n-1} - \mathbf{P}_{n-1} \mathbf{G}(\mathbf{X}_n)^T \overline{\mathbf{R}}_n^{-1} \mathbf{G}(\mathbf{X}_n) \mathbf{P}_{n-1} \cdot \end{aligned} \tag{3.6}$$

In (3.6) we introduced an intermediate variable

$$\overline{\mathbf{R}}_n = \left(\mathbf{R} + \mathbf{G}(\mathbf{X}_n)\mathbf{P}_{n-1}\mathbf{G}(\mathbf{X}_n)^T\right). \tag{3.7}$$

The matrix $\overline{\mathbf{R}}_n$ in (3.7) is positive definite (as $\mathbf{R} > \mathbf{0}, \mathbf{P}_{n-1} > \mathbf{0}$ and $\mathbf{G}(\mathbf{X}_n)$ is invertible) and is used frequently for analysis purposes. Substituting (3.6) in (3.5) and simplifying, we get a recurrence relation for $\widehat{\mathbf{\Gamma}}_n$ as,

$$\begin{aligned} \widehat{\mathbf{\Gamma}}_{n+1} &= \widehat{\mathbf{\Gamma}}_n + \mathbf{P}_{n-1}\mathbf{G}(\mathbf{X}_n)^T\overline{\mathbf{R}}_n^{-1}\mathbf{G}(\mathbf{X}_n)(\mathbf{\Gamma} - \widehat{\mathbf{\Gamma}}_n) \\ &= \widehat{\mathbf{\Gamma}}_n - \mathbf{P}_{n-1}\mathbf{G}(\mathbf{X}_n)^T\overline{\mathbf{R}}_n^{-1}\mathbf{e}_{n+1}. \end{aligned} \tag{3.8}$$

Another simple recurrence relation for $\widetilde{\mathbf{\Gamma}}_n$ that will be useful later in the stability analysis can be obtained from (3.6) and (3.8) as:

$$\widetilde{\mathbf{\Gamma}}_{n+1} = \mathbf{P}_n\mathbf{P}_{n-1}^{-1}\widetilde{\mathbf{\Gamma}}_n. \tag{3.9}$$

We now present the main result on the application of multi-variable least-squares algorithm for the adaptive parameter estimation as it pertains to the fluid systems under consideration. While (3.8) is implemented from available signals, (3.9) is used for analysis purposes.

Before implementing an adaptive observer for a given system, it is essential to study its applicability by considering issues of convergence. We will now derive results for convergence of the state error and also state conditions for the same.

Lemma 3.1.1 *Given the algorithm* (3.6) *and* (3.8) *for the parameter updates* $\widehat{\mathbf{\Gamma}}$ *of the unknown vector of convective terms* $\mathbf{\Gamma}$ *in* (2.7) *along with the adaptive observer*

(3.1) *for the plant* (2.7), *it follows that*

$$(i)\ \|\widehat{\mathbf{\Gamma}}_{n+1} - \mathbf{\Gamma}\|^2 \ \leq\ \kappa_1 \|\widehat{\mathbf{\Gamma}}_1 - \mathbf{\Gamma}\|^2;\ \ n \geq 1$$

where (3.10)

$\kappa_1 =$ *condition number of* $[\mathbf{P}_0^{-1}] \triangleq \dfrac{\lambda_{\max} \mathbf{P}_0^{-1}}{\lambda_{\min} \mathbf{P}_0^{-1}}$

$$(ii)\ \lim_{n\to\infty} \sum_{j=1}^{n} \mathbf{e}_{j+1}^T \overline{\mathbf{R}}_j^{-1} \mathbf{e}_{j+1} \ <\ \infty \tag{3.11}$$

and this implies

$$(iii)\ \lim_{n \to \infty} \left(\lambda_{min} \overline{\mathbf{R}}_n^{-1}\right)^{1/2} \mathbf{e}_{n+1} = \mathbf{0} \tag{3.12}$$

$$(iv)\ \lim_{n\to\infty} \sum_{j=1}^{n} \left(\overline{\mathbf{R}}_j^{-1} \mathbf{e}_{j+1}\right)^T \mathbf{G}(\mathbf{X}_j) \mathbf{P}_{j-1} \mathbf{G}(\mathbf{X}_j)^T \left(\overline{\mathbf{R}}_j^{-1} \mathbf{e}_{j+1}\right) \ <\ \infty \tag{3.13}$$

$$(v)\ \lim_{n\to\infty} \sum_{j=1}^{n} \|\widehat{\mathbf{\Gamma}}_{j+1} - \widehat{\mathbf{\Gamma}}_j\|^2 \ <\ \infty \tag{3.14}$$

$$(vi)\ \lim_{n\to\infty} \sum_{j=k}^{n} \|\widehat{\mathbf{\Gamma}}_{j+1} - \widehat{\mathbf{\Gamma}}_{j+1-k}\|^2 \ <\ \infty \tag{3.15}$$

$$(vii)\ \lim_{n\to\infty} \|\widehat{\mathbf{\Gamma}}_{n+1} - \widehat{\mathbf{\Gamma}}_{n+1-k}\| \ =\ 0 \ \textit{for any finite } k. \tag{3.16}$$

Proof : (i) *Define a nonnegative scalar Lyapunov function*

$$V_{n+1} = \widetilde{\mathbf{\Gamma}}_{n+1}^T \mathbf{P}_n^{-1} \widetilde{\mathbf{\Gamma}}_{n+1},$$

we have

$$\begin{aligned} V_{n+1} - V_n &= \widetilde{\mathbf{\Gamma}}_{n+1}^T \mathbf{P}_n^{-1} \widetilde{\mathbf{\Gamma}}_{n+1} - \widetilde{\mathbf{\Gamma}}_n^T \mathbf{P}_{n-1}^{-1} \widetilde{\mathbf{\Gamma}}_n \\ &= \left(\widetilde{\mathbf{\Gamma}}_{n+1} - \widetilde{\mathbf{\Gamma}}_n\right)^T \mathbf{P}_{n-1}^{-1} \widetilde{\mathbf{\Gamma}}_n \quad \textit{using}\,(3.9) \\ &= -\mathbf{e}_{n+1}^T \overline{\mathbf{R}}_n^{-1} \mathbf{G}(\mathbf{X}_n) \widetilde{\mathbf{\Gamma}}_n \qquad \textit{from}\,(3.8) \\ &= -\mathbf{e}_{n+1}^T \overline{\mathbf{R}}_n^{-1} \mathbf{e}_{n+1} \qquad \textit{from}\,(3.2) \\ &\leq 0. \end{aligned} \tag{3.17}$$

Thus V_n is a non-negative, non-increasing function and hence

$$\widetilde{\mathbf{\Gamma}}_{n+1}^T \mathbf{P}_n^{-1} \widetilde{\mathbf{\Gamma}}_{n+1} \leq \widetilde{\mathbf{\Gamma}}_1^T \mathbf{P}_0^{-1} \widetilde{\mathbf{\Gamma}}_1. \tag{3.18}$$

Now from (3.6) *it follows that,*

$$\begin{aligned} \mathbf{P}_n^{-1} &\geq \mathbf{P}_{n-1}^{-1} \\ \Rightarrow \quad \lambda_{\min}\left(\mathbf{P}_n^{-1}\right) &\geq \lambda_{\min}\left(\mathbf{P}_{n-1}^{-1}\right) \\ &\geq \lambda_{\min}\left(\mathbf{P}_0^{-1}\right). \end{aligned} \tag{3.19}$$

Equation (3.19) *implies that*

$$\begin{aligned} \lambda_{\min}\left(\mathbf{P}_0^{-1}\right) \left\|\widetilde{\mathbf{\Gamma}}_{n+1}\right\|^2 &\leq \lambda_{\min}\left(\mathbf{P}_n^{-1}\right) \left\|\widetilde{\mathbf{\Gamma}}_{n+1}\right\|^2 \\ &\leq \widetilde{\mathbf{\Gamma}}_{n+1}^T \mathbf{P}_n^{-1} \widetilde{\mathbf{\Gamma}}_{n+1} \\ &\leq \widetilde{\mathbf{\Gamma}}_1^T \mathbf{P}_0^{-1} \widetilde{\mathbf{\Gamma}}_1 \ \textit{using}\,(3.18) \\ &\leq \lambda_{\max}\left(\mathbf{P}_0^{-1}\right) \left\|\widetilde{\mathbf{\Gamma}}_1\right\|^2 \\ \Rightarrow \quad \left\|\widetilde{\mathbf{\Gamma}}_{n+1}\right\|^2 &\leq \frac{\lambda_{\max}\left(\mathbf{P}_0^{-1}\right)}{\lambda_{\min}\left(\mathbf{P}_0^{-1}\right)} \left\|\widetilde{\mathbf{\Gamma}}_1\right\|^2. \end{aligned} \tag{3.20}$$

This establishes part (i). (*ii*) *Going back to* (3.17) *and summing from* 1 *to* n *gives*

$$\lim_{n\to\infty} V_{n+1} = V_1 - \lim_{n\to\infty} \sum_{j=1}^{n} \mathbf{e}_{j+1}^T \overline{\mathbf{R}}_j^{-1} \mathbf{e}_{j+1}\ . \tag{3.21}$$

Since V_n is nonnegative, we immediately have (3.11).

(*iii*) *Since* $\overline{\mathbf{R}}_j^{-1} > \mathbf{0}$

$$\lambda_{\min}\left(\overline{\mathbf{R}}_j^{-1}\right)\mathbf{e}_{j+1}^T\mathbf{e}_{j+1} < \mathbf{e}_{j+1}^T\overline{\mathbf{R}}_j^{-1}\mathbf{e}_{j+1}.$$

Using (3.11) *we can write*

$$\lim_{n\to\infty}\sum_{j=1}^{n}\left(\lambda_{\min}\overline{\mathbf{R}}_j^{-1}\right)\mathbf{e}_{j+1}^T\mathbf{e}_{j+1} < \infty \tag{3.22}$$

Equation (3.12) *follows immediately from* (3.22).

(*iv*) *Using* (3.11) *we can write*

$$\begin{aligned}&\lim_{n\to\infty}\sum_{j=1}^{n}\left(\overline{\mathbf{R}}_j^{-1}\mathbf{e}_{j+1}\right)^T\overline{\mathbf{R}}_j\left(\overline{\mathbf{R}}_j^{-1}\mathbf{e}_{j+1}\right) < \infty \Rightarrow\\ &\lim_{n\to\infty}\sum_{j=1}^{n}\left(\overline{\mathbf{R}}_j^{-1}\mathbf{e}_{j+1}\right)^T\left(\mathbf{R}+\mathbf{G}(\mathbf{X}_n)\mathbf{P}_{n-1}\mathbf{G}(\mathbf{X}_n)^T\right)\left(\overline{\mathbf{R}}_j^{-1}\mathbf{e}_{j+1}\right) < \infty.\end{aligned} \tag{3.23}$$

Equation (3.13) *follows immediately as* $\mathbf{R} > \mathbf{0}$.

(*v*) *From the algorithm* (3.8),

$$\begin{aligned}\|\widehat{\mathbf{\Gamma}}_{j+1}-\widehat{\mathbf{\Gamma}}_j\|^2 &= \left(\widehat{\mathbf{\Gamma}}_{j+1}-\widehat{\mathbf{\Gamma}}_j\right)^T\left(\widehat{\mathbf{\Gamma}}_{j+1}-\widehat{\mathbf{\Gamma}}_j\right)\\ &= \mathbf{e}_{j+1}^T\overline{\mathbf{R}}_j^{-1}\mathbf{G}(\mathbf{X}_j)\mathbf{P}_{j-1}\mathbf{P}_{j-1}\mathbf{G}(\mathbf{X}_j)^T\overline{\mathbf{R}}_j^{-1}\mathbf{e}_{j+1}\\ &= \left(\overline{\mathbf{R}}_j^{-1}\mathbf{e}_{j+1}\right)^T\mathbf{G}(\mathbf{X}_j)\mathbf{P}_{j-1}\mathbf{P}_{j-1}\mathbf{G}(\mathbf{X}_j)^T\left(\overline{\mathbf{R}}_j^{-1}\mathbf{e}_{j+1}\right)\\ &\le \left(\overline{\mathbf{R}}_j^{-1}\mathbf{e}_{j+1}\right)^T\mathbf{G}(\mathbf{X}_j)\mathbf{P}_{j-1}\mathbf{G}(\mathbf{X}_j)^T\left(\overline{\mathbf{R}}_j^{-1}\mathbf{e}_{j+1}\right)\lambda_{\max}\left(\mathbf{P}_{j-1}\right)\\ &\le \left(\overline{\mathbf{R}}_j^{-1}\mathbf{e}_{j+1}\right)^T\mathbf{G}(\mathbf{X}_j)\mathbf{P}_{j-1}\mathbf{G}(\mathbf{X}_j)^T\left(\overline{\mathbf{R}}_j^{-1}\mathbf{e}_{j+1}\right)\lambda_{\max}\left(\mathbf{P}_0\right)\ \textit{using}\,(3.6).\end{aligned} \tag{3.24}$$

Equation (3.14) follows immediately from (3.13).

(*vi*) It is clear that,

$$\|\widehat{\mathbf{\Gamma}}_{j+1}-\widehat{\mathbf{\Gamma}}_{j+1-k}\|^2 = \|\widehat{\mathbf{\Gamma}}_{j+1}-\widehat{\mathbf{\Gamma}}_j+\widehat{\mathbf{\Gamma}}_j-\widehat{\mathbf{\Gamma}}_{j-1}\cdots\widehat{\mathbf{\Gamma}}_{j+1-(k-1)}-\widehat{\mathbf{\Gamma}}_{j+1-k}\|^2 \tag{3.25}$$

Then, using the Schwarz inequality,

$$\|\widehat{\mathbf{\Gamma}}_{j+1} - \widehat{\mathbf{\Gamma}}_{j+1-k}\|^2 \;\leq\; k\left(\|\widehat{\mathbf{\Gamma}}_{j+1} - \widehat{\mathbf{\Gamma}}_{j}\|^2 + \cdots + \|\widehat{\mathbf{\Gamma}}_{j+1-(k-1)} - \widehat{\mathbf{\Gamma}}_{j+1-k}\|^2\right) \tag{3.26}$$

Equation (3.15) follows immediately from (3.14) since k is finite.

(*vii*) Equation (3.16) follows immediately from (3.15).

Parameter convergence can be similarly established by imposing a richness-like condition and thus we have the following result.

Lemma 3.1.2 *The multi-variable least-squares algorithm* (3.6) *and* (3.8) *for* $\widehat{\mathbf{\Gamma}}_n$ *is convergent to* $\mathbf{\Gamma}$ *provided that*

$$\lim_{n\to\infty} \lambda_{min}\left(\sum_{j=1}^{n} \mathbf{G}(\mathbf{X}_j)^T \mathbf{R}^{-1} \mathbf{G}(\mathbf{X}_j)\right) = \infty\,. \tag{3.27}$$

Proof : *It is clear from* (3.6) *and the definitions of* $\widetilde{\mathbf{\Gamma}}_n$ *and* V_n *that* $\widetilde{\mathbf{\Gamma}}_n$ *will converge to zero provided that*

$$\lim_{n\to\infty} \lambda_{\min} \mathbf{P}_n^{-1} = \infty$$

and this is guaranteed provided that (3.27) *is satisfied.* ∎

Remark 3.1.1 *Equation* (3.27) *is a form of condition for persistence of excitation (Goodwin and Sin, 1984).*

In the following section, we apply the multi-variable estimation scheme to estimate complex NEKTAR wake patterns from varying flow situations.

3.2 Results

In this section, we present a detailed summary of the results obtained from the simulation of the self-learning CML model based on the multi-variable least-squares algorithm. The target wake patterns are obtained from the NEKTAR code. Three different flow situations are considered. First, we study the uniform flow over a flexible cable forced to vibrate in the cross-flow direction at a frequency coinciding with the natural vortex shedding frequency behind a stationary rigid cylinder. We use the term lock-on periodic case ($\Omega = f_e/f_{so} = 1.0$) to describe the flow situation. The objective of this study is to generate complex wake structures such as lace-like patterns, vortex dislocations etc. observed in the study of Newman and Karniadakis (1996,1997). As we have seen before, the development of a new self-learning CML model was required because the basic CML model was not successful in achieving quantitative prediction of the complex wake structures.

The non-periodic case ($\Omega = 0.9$) of uniform flow over flexible cable is considered in the second study. As we will see later, this study will be useful in determining the effectiveness of the self-learning CML to model transient effects (i.e. rapidly changing wake structures within a few shedding cycles), and also more complex wake effects than in the first study.

In the third study, we generate target wake patterns from a sheared freestream flow over a forced flexible cable under lock-on conditions ($\Omega = 1.0$). Studies of Newman (1996,1997) and others show that the vortices are shed at an oblique angle with respect to an axis parallel to the longitudinal axis of the cylinder. Therefore, this study is useful in analyzing the ability of the self-learning CML model to model oblique shedding patterns.

We will first select the input parameters for NEKTAR simulations, then discuss the various methods of generating wake patterns. Later, we apply the MVLS algorithm for each of the three cases. Finally, we discuss prediction of these patterns and also convergence of the state error. An optimization study is also done in order to choose

the input parameters for the self-learning CML model. The evolution in time of the wake patterns as well as the vortex shedding phase angles for the NEKTAR wake and the self-learning CML is also considered.

3.2.1 Input parameters for NEKTAR simulation

The mesh used for the low-Reynolds number (=100) NEKTAR simulations, and the required computational times were already given in Chapter 2. For all three flow situations described above, the parameters, $AR = 4\pi$, $A/D = 0.69$, are kept the same. The freestream Reynolds number, Re was set to 100 for the uniform flow cases, and to one period of a cosine distribution, with antinodal value = $Re_{max} = 100$, and the nodal value = $Re_{min} = 75$ for the shear flow case.

3.2.2 Generation of NEKTAR wake patterns

The low-dimensional CML model approach considers the vortex shedding phase angles, X_n^k, in order to quantify the wake patterns. Therefore the generation of the NEKTAR wake patterns based on this approach is first considered in this section. In order to obtain X_n^k, time-traces of streamwise (u) velocities at sampled locations, uniformly distributed along the spanwise (z) direction are first generated from the NEKTAR simulation. In order to consider the time evolution of wake structures at a particular streamwise (x/D) location, the spanwise sampling of the u-velocities is conducted. For example, in Figure 3.2 the u-velocities from the NEKTAR simulation at 26 equispaced locations are shown.

Four near wake x/D locations, $x/D = 0.5, 1, 3, 5$ and a far wake location $x/D = 10$ are chosen for estimation of wake structures at these locations. The spanwise vorticity (representing the wake structure) from the NEKTAR simulation at a specific time instant is shown in Figure 3.3. One observes a lace-like structure in the near wake of the cable ($x/D < 2$), characteristic of standing wave mode forcing of the cable. Further downstream, ($2 < x/D < 6$), more complex vortex structures with

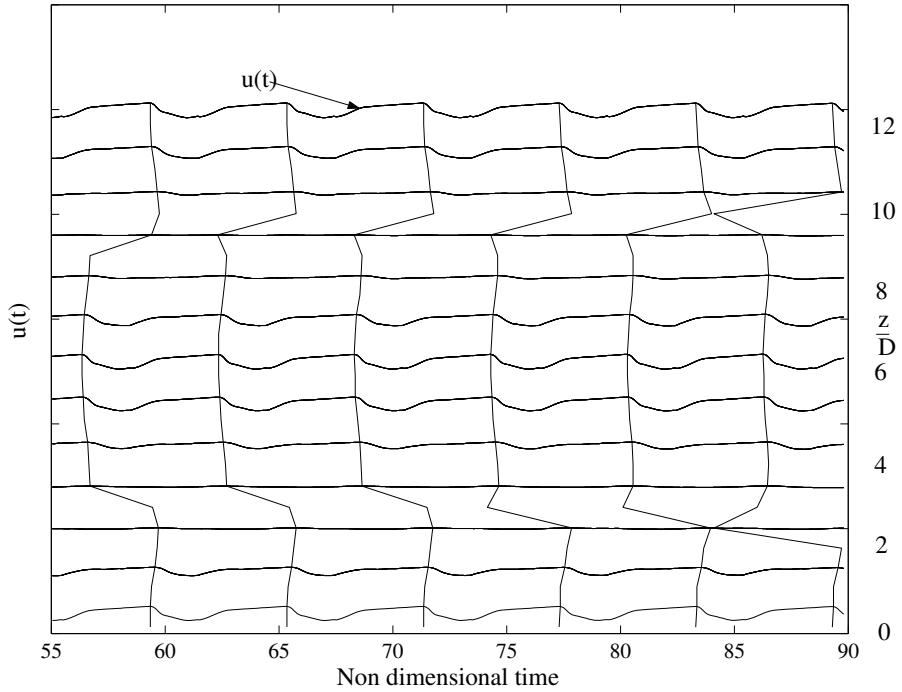

Figure 3.2: Streamwise velocity traces providing a schematic for visualizing wake patterns: $\Omega = 1.0, x/D = 1.0$

decreased spanwise wavelengths evolve. So the choice of x/D locations provide a wide complexity of wake structures for estimation purposes.

Cross-correlation algorithm

The vortex shedding phase angles, X_n^k at the various z/D locations are generated using a cross-correlation algorithm. The idea is based on standard signal processing theory. The phase difference between two signals corresponds to the phase of the dominant frequency of the cross-power spectrum between the two signals. The cross-power spectrum is calculated using

$$C_{u_1 u_2}(f) = U_1(f) \cdot U_2^*(f)$$

where $U_1(f)$ and $U_2(f)$ are the Fourier transforms of the individual time traces, $u_1(t)$ and $u_2(t)$, respectively. The cross-power spectrum is interpreted in polar form (magnitude, angle) to determine the phase difference, X_n^k, between the two time histories within each shedding cycle. A typical phase angle distribution resulting

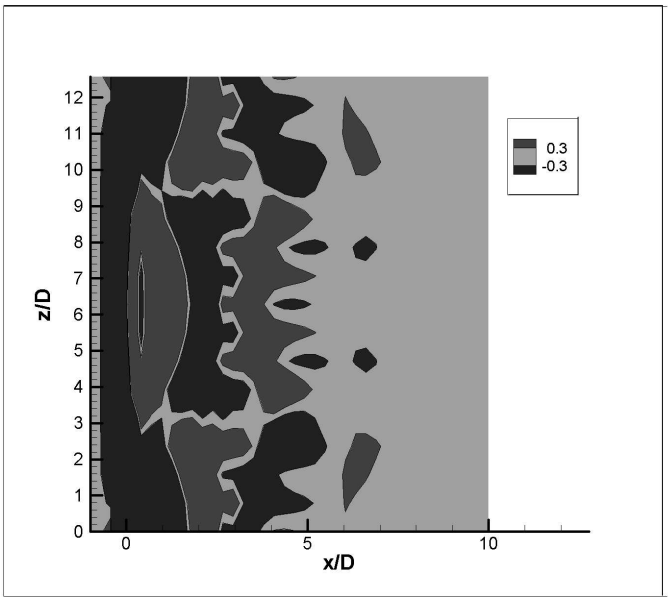

Figure 3.3: Contours of spanwise vorticity in the x-z plane from NEKTAR simulation

from these correlation methods at one time instance is shown in Figure 3.4 for the near wake, $x/D = 1.0$.

To illustrate the phase angle extraction from the cross-power spectrum, we consider the tenth shedding cycle ($n = 10$). The magnitude of FFTs of u-velocities at $x/D = 3$ and $z/D = 3, 6, 9, 12$ are shown in Figure 3.5. Also, in Figure 3.6 the magnitude of the cross-power spectrum between u-velocities at $x/D = 1$ and $z/D = 0, 5$ (or) $k = 1, 11$ for the tenth shedding cycle, shows a peak at a frequency = 0.35 Hz and a corresponding phase angle, $X_{n=10}^{k=11} = 0.5$. Repeating this procedure for pairs of u-velocities, one being a reference velocity considered at $z/D = 0$ throughout, we generate vortex shedding phase angles, X_n^k for every spanwise location (k) and shedding cycle (n) as can be seen in Figure 3.7.

We repeat the above procedure for streamwise locations $x/D = 0.5, 3, 5, 10$ in order to generate the corresponding vortex shedding phase angles. The FFTs of the streamwise velocities at representative spanwise locations, ($z/D = 3, 6, 9, 12$) for $x/D = 0.5$ and 10 are shown in Figures 3.8- 3.9. In both the figures, we can identify peaks at the Strouhal frequency, indicating that the cable is oscillating at the lock-on condition.

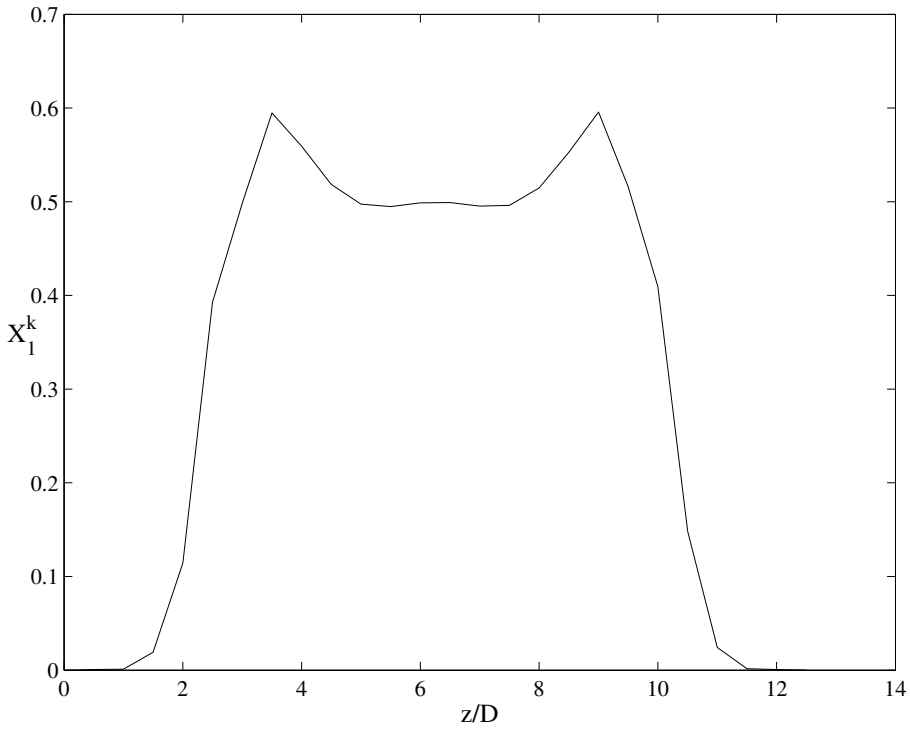

Figure 3.4: Typical vortex shedding phase distribution that serves as a target state for the self-learning CML: $\Omega = 1.0, x/D = 1.0, n = 10$

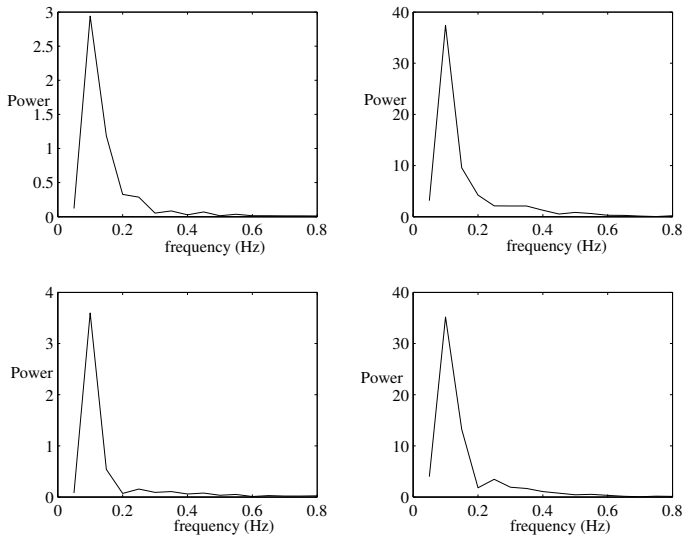

Figure 3.5: Sample FFTs of $u(x/D = 1, z/D = 3, 6, 9, 12)$ for generating cross-power spectrum

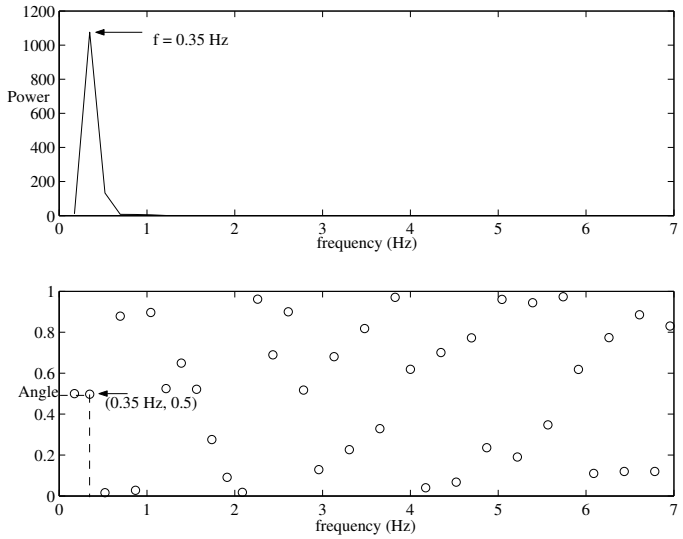

Figure 3.6: Magnitude and phase of cross-power spectrum interpreted to get vortex shedding phase angle, $X_{n=10}^{k=11} : \Omega = 1.0, z/D = 5$

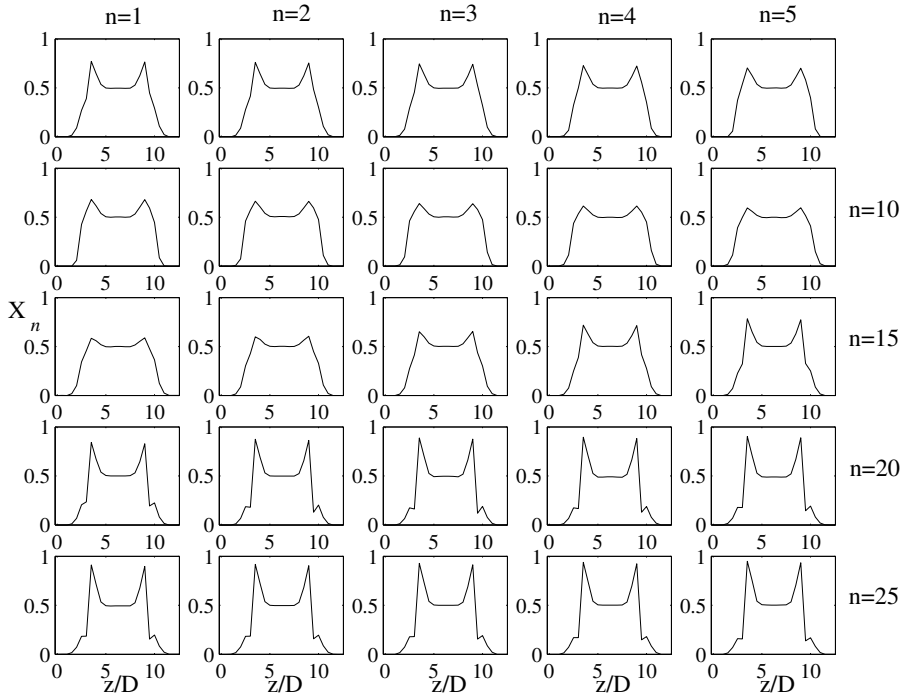

Figure 3.7: Illustration of vortex shedding phase angles, $X_n^k : \Omega = 1.0, x/D = 1$

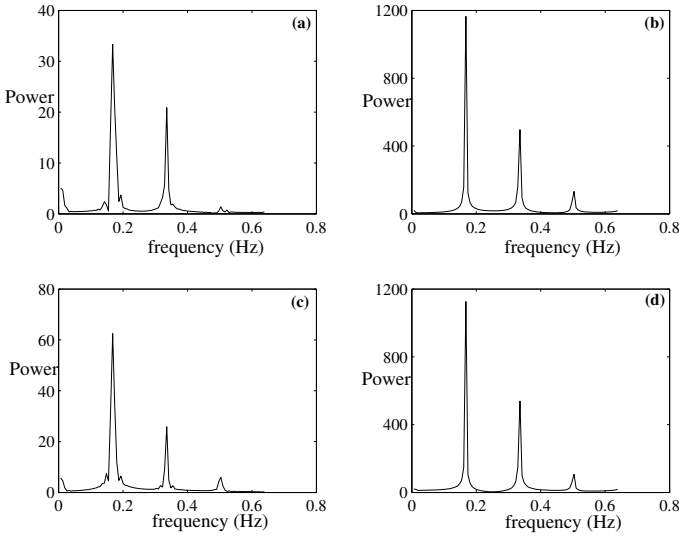

Figure 3.8: Sample FFTs of $u(x/D = 0.5, z/D = 3, 6, 9, 12)$ for generating cross-power spectrum

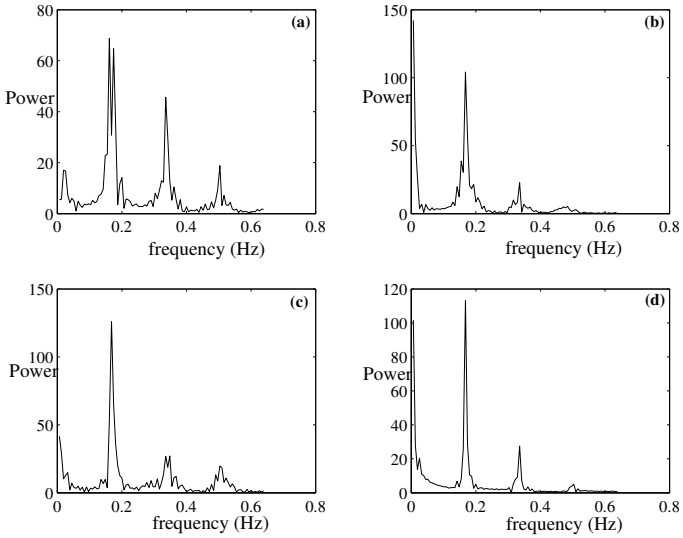

Figure 3.9: Sample FFTs of $u(x/D = 10, z/D = 3, 6, 9, 12)$ for generating cross-power spectrum

The cross-correlation technique for extracting phase angles is then applied to 3 other near wake locations ($x/D = 0.5, 3, 5$), and one far wake location ($x/D = 1$). The state of the wake becomes progressively more complex with increase in downstream distance, x/D (see Figures 3.10 - 3.13). These states are then used as target states, $\mathbf{X}_n$, for the estimation methods used in Chapters 3 and 4.

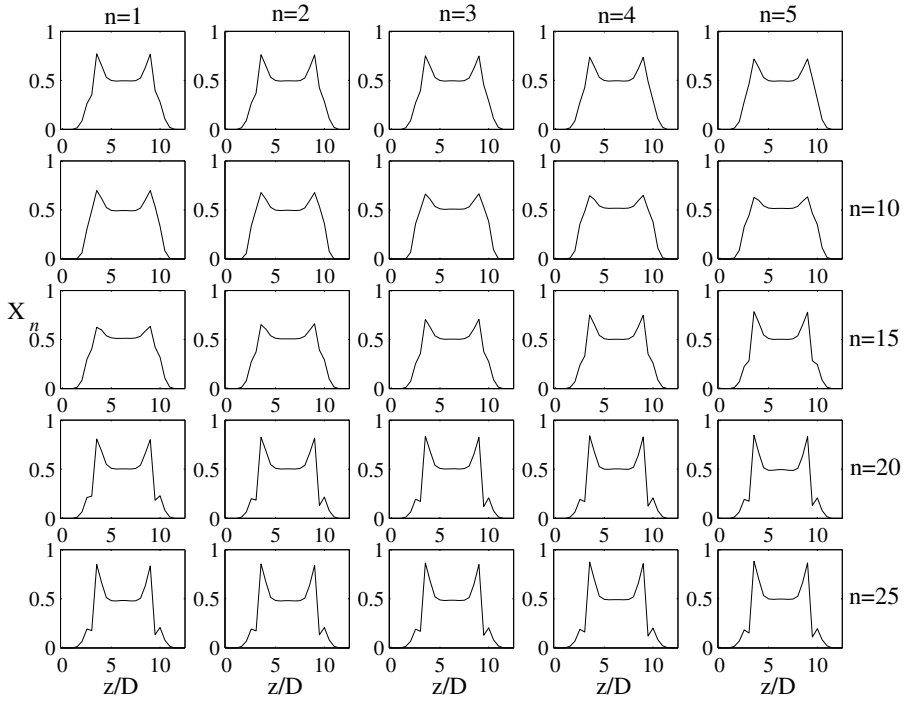

Figure 3.10: Illustration of vortex shedding phase angles, $X_n^k : \Omega = 1.0, x/D = 0.5$

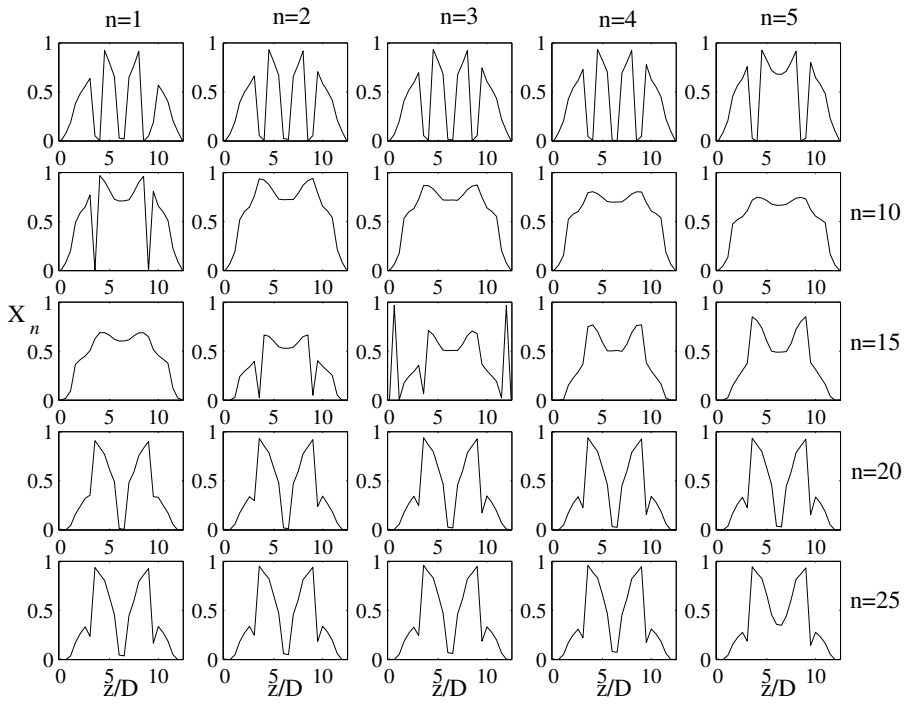

Figure 3.11: Illustration of vortex shedding phase angles, $X_n^k : \Omega = 1.0, x/D = 3$

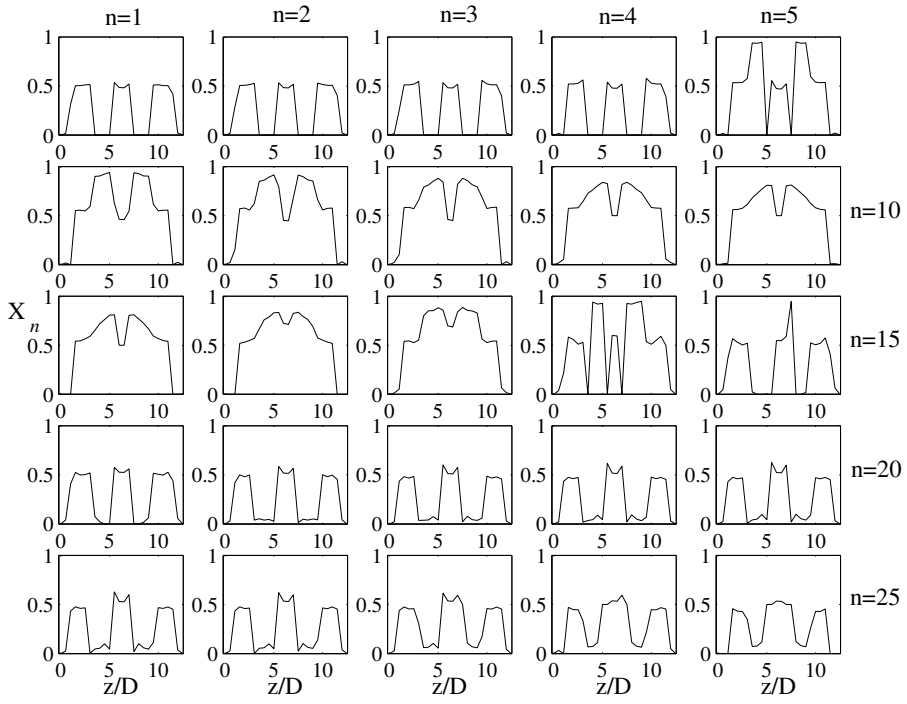

Figure 3.12: Illustration of vortex shedding phase angles, $X_n^k : \Omega = 1.0, x/D = 5$

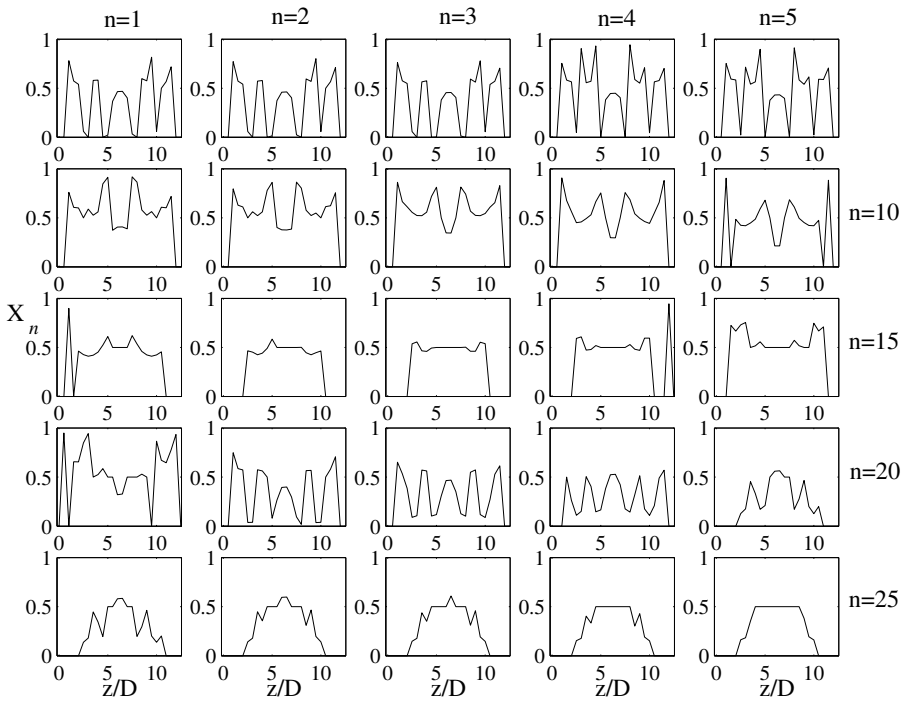

Figure 3.13: Illustration of vortex shedding phase angles, $X_n^k : \Omega = 1.0, x/D = 10$

Wake patterns from vortex shedding phase angles

In chapter 1, we discussed the methods of plotting wake patterns from vortex shedding angles, see Figure 1.6. One of the assumptions of the current CML model is that the spanwise oscillators are effectively moved to the streamwise location under consideration. Then, the vortices convect downstream at a constant velocity without any dissipation. This assumption led to the definition of a characteristic streamwise distance, x^*, for vortex convection in a shedding cycle, $x^* = U_c/(U_\infty St)$. With this definition, a simple equation (3.28) for the location of the vortex core of the n^{th} shedding cycle is given by:

$$\left(\frac{x}{D}\right)_n^k = (\mathrm{X}_n^k + n_{final} - n) * U_c/(U_\infty St)\,. \tag{3.28}$$

We now apply (3.28) to the X_n^k values computed at $x/D = 0.5, 1, 3, 5, 10$ to generate the wake patterns (see Figures 3.15- 3.17). We will use these as target patterns for estimation using the methods in Chapters 3 and 4.

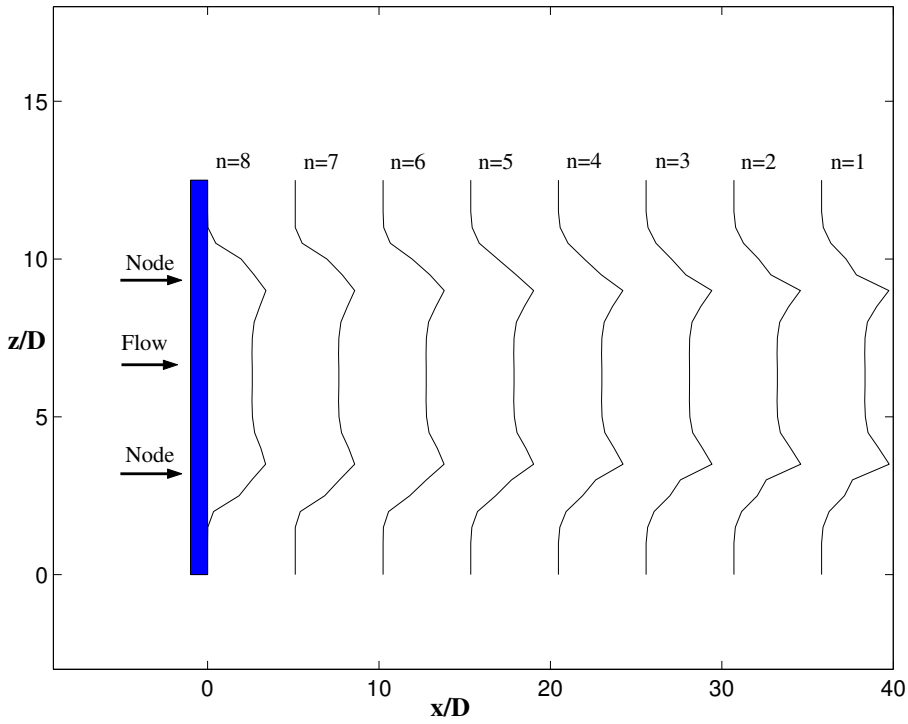

Figure 3.14: First 8 shedding cycles showing wake patterns at $x/D = 0.5$ for lock-on case: $\Omega = 1.0$

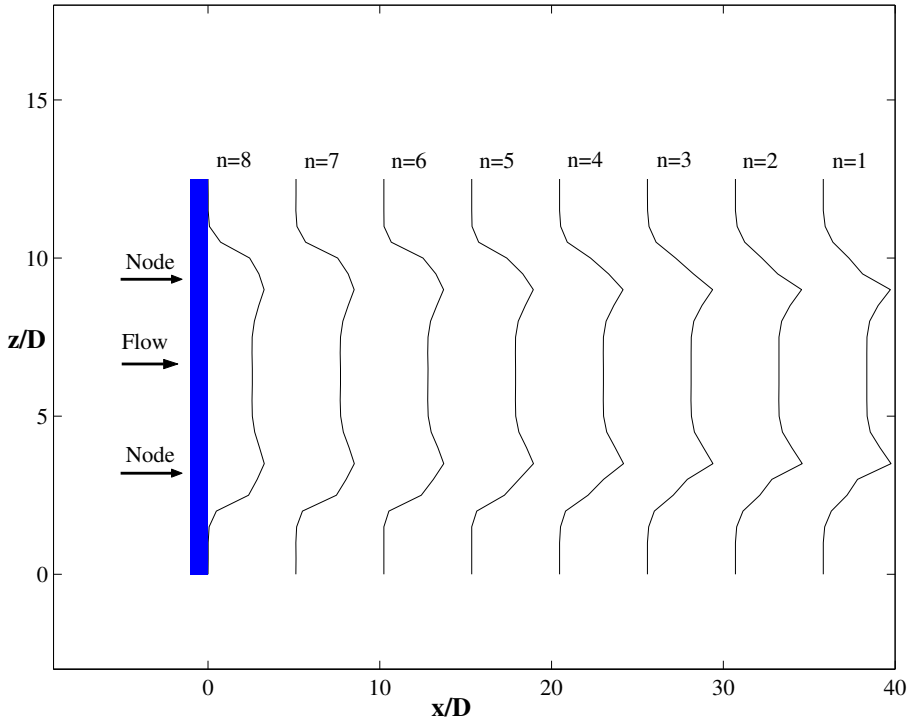

Figure 3.15: First 8 shedding cycles showing wake patterns at $x/D = 1.0$ for lock-on case: $\Omega = 1.0$

Wake patterns from time history

We will now present an alternative method for drawing wake patterns using wake velocity signatures. While this method is not used for analysis purposes, it gives us an idea of how these wake patterns are interpreted visually. For each shedding cycle, the peaks or troughs (easily identifiable points) in u of the adjacent spanwise locations are joined together to form the wake pattern. Peaks (or troughs) in the velocity trace at $z/D = 0$ are used as reference states. We illustrate this method for all the x/D locations in Figures 3.18- 3.21. We can easily verify that the wake becomes increasingly more complex with downstream distance.

Quasi-periodic case: $\Omega = 0.9$

In this study, the cable oscillates at a frequency further removed from the natural shedding frequency of the wake at that Reynolds number, so that $\Omega = f_e/f_{so} = 0.9$. All other parameters are retained from the lock-on case. We can see more complex

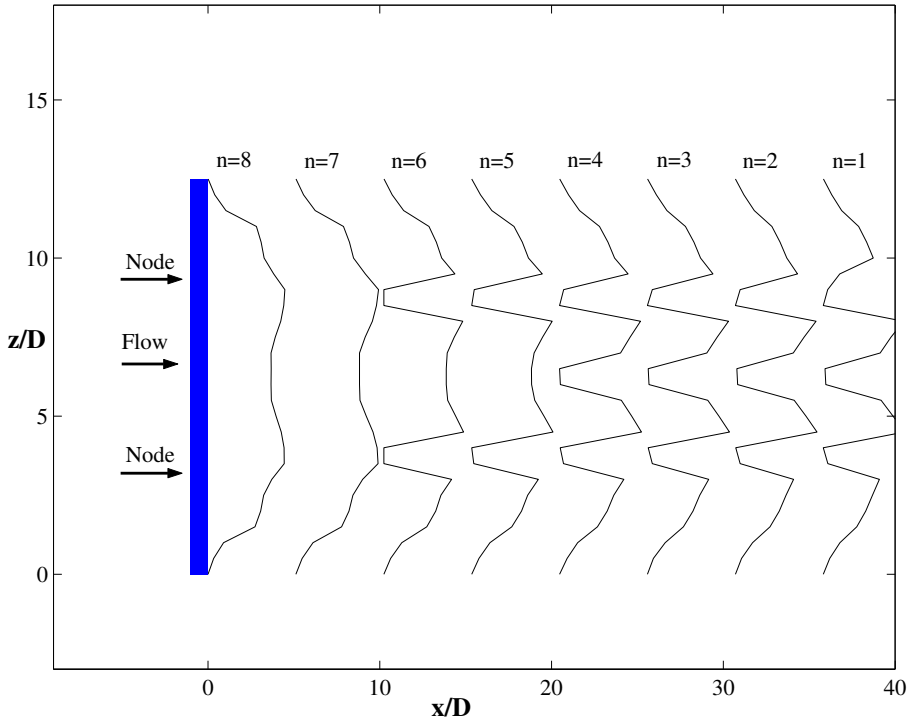

Figure 3.16: First 8 shedding cycles showing wake patterns at $x/D = 3.0$ for lock-on case: $\Omega = 1.0$

wake structures including vortex dislocations in Figure 3.22. These structures are more difficult to estimate and are also commonly observed in experiments. So the target states, $\mathbf{X}_n$, obtained from this study are correspondingly highly complex with sudden changes in phase angles in successive shedding cycles, indicative of vortex dislocations (see Figure 3.23). The transient states, for $1 \leq n \leq 4$, are highly complex and the steady state behavior ($n > 20$) also exhibits decreased spanwise wavelengths compared to the lock-on case at the same x/D location. A plot of the first 8 shedding cycles, corresponding to $1 \leq n \leq 8$ in Figure 3.23 is shown in Figure 3.24. The vortex dislocations near the node ($z/D = 9.5$) are labeled. It is our goal to estimate these wake structures accurately using the self-learning CML models. We will apply the estimation methods in Chapters 3 and 4 as part of a study of applicability of these methods to varied flow-structure interaction situations.

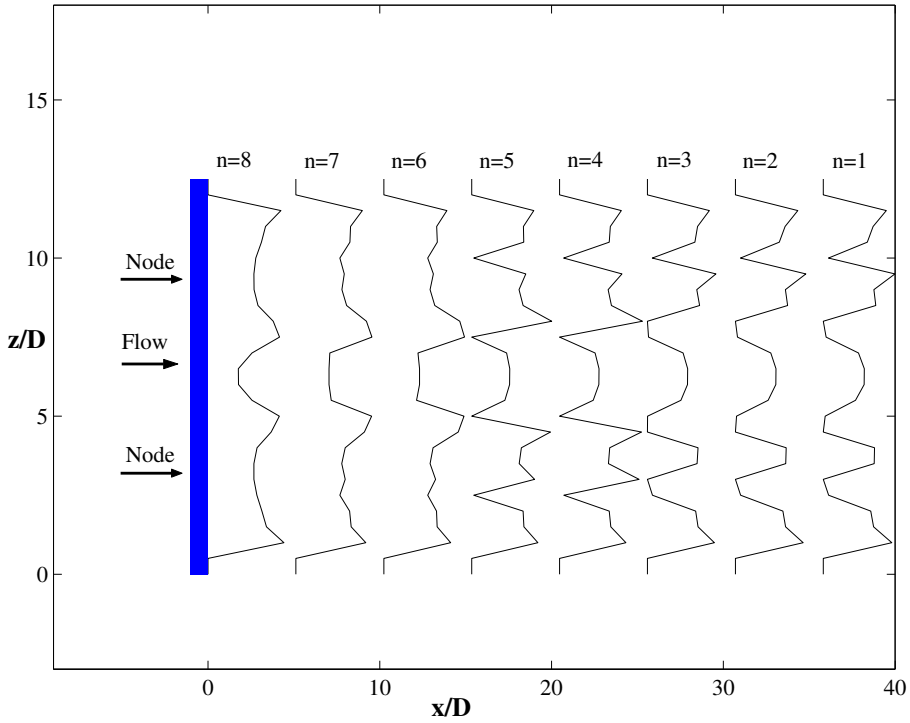

Figure 3.17: First 8 shedding cycles showing wake patterns at $x/D = 10$ for lock-on case: $\Omega = 1.0$

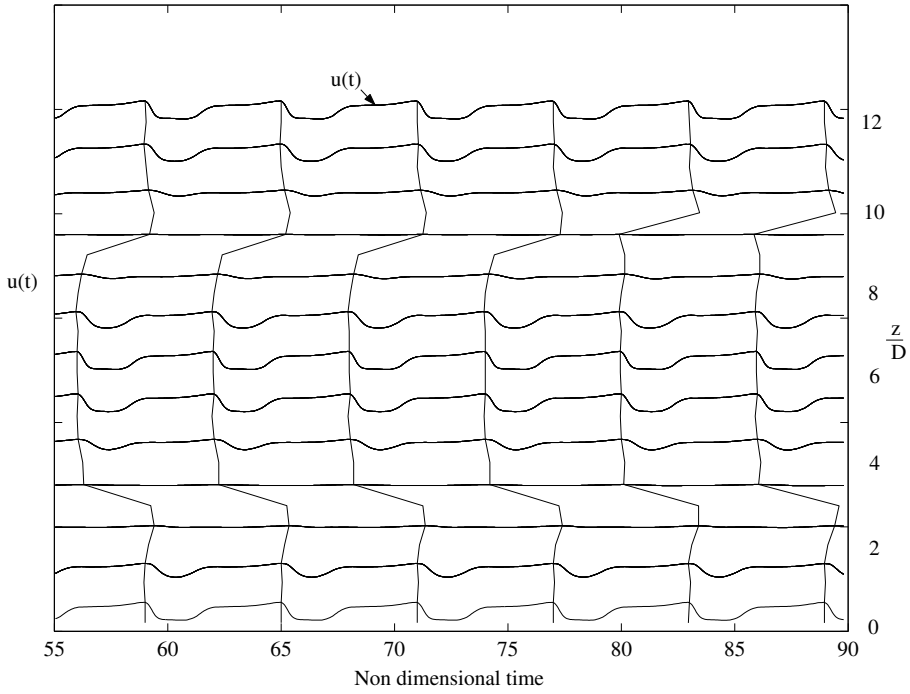

Figure 3.18: Streamwise velocity traces providing a schematic for visualizing wake patterns: $\Omega = 1.0, x/D = 0.5$

Sheared freestream flow: $\Omega_{max} = 1.0$

The quasi-periodic case was used to study the effect of changes in excitation frequency of the cable on vortex shedding. In this section, we study the wake of a

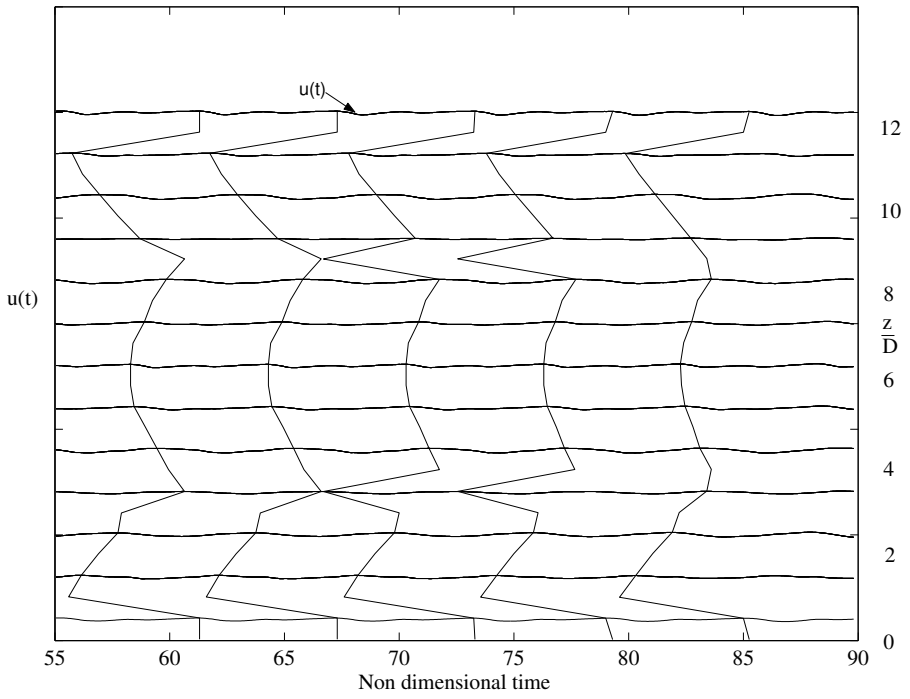

Figure 3.19: Streamwise velocity traces providing a schematic for visualizing wake patterns: $\Omega = 1.0, x/D = 3$

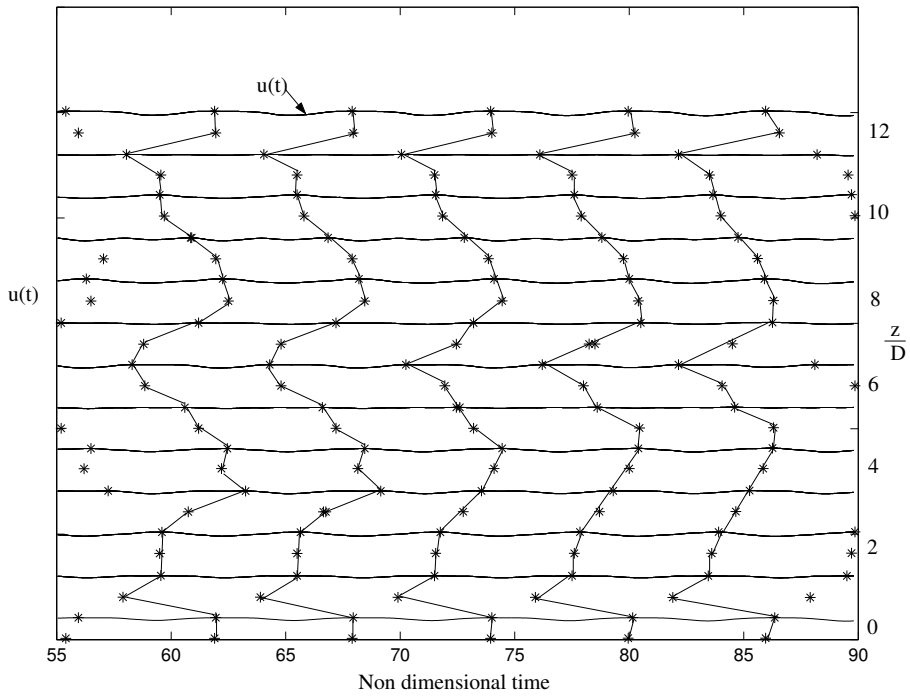

Figure 3.20: Streamwise velocity traces providing a schematic for visualizing wake patterns: $\Omega = 1.0, x/D = 5$

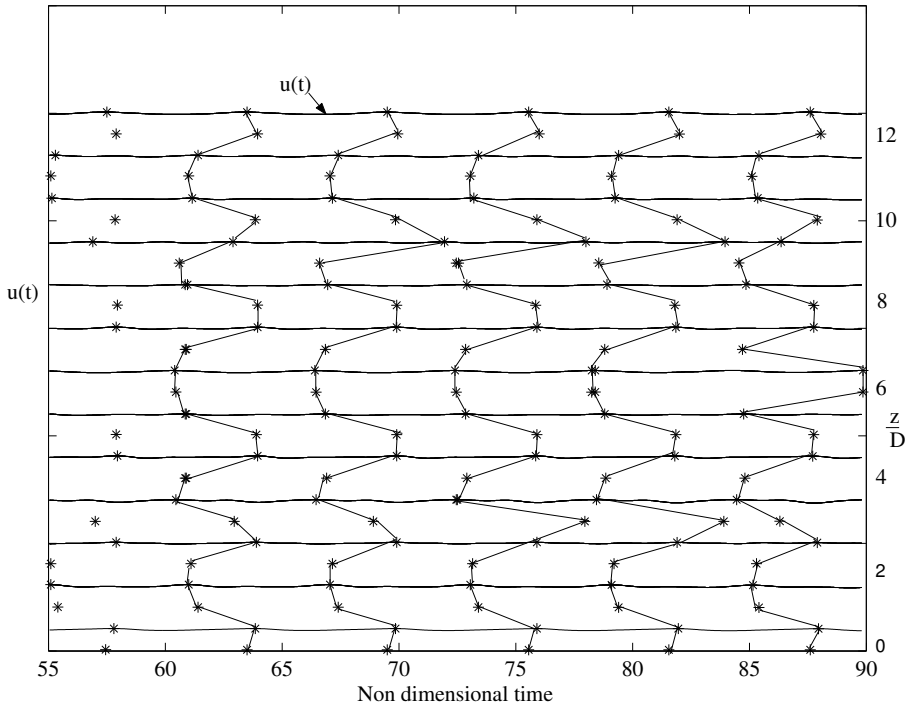

Figure 3.21: Streamwise velocity traces providing a schematic for visualizing wake patterns: $\Omega = 1.0, x/D = 10$

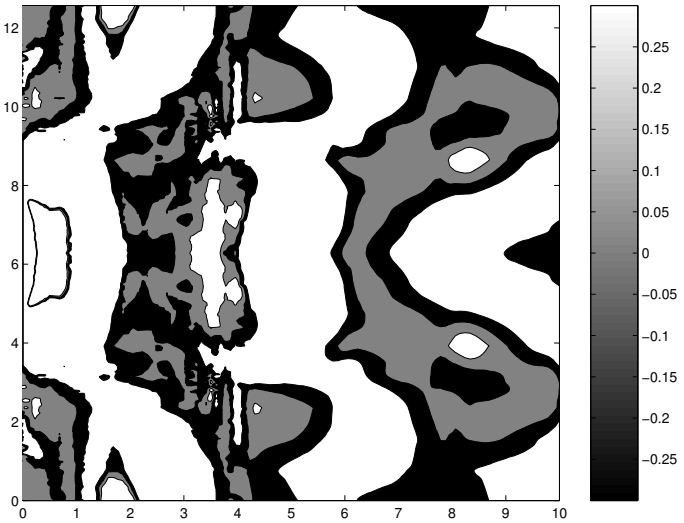

Figure 3.22: Contours of spanwise vorticity in the x-z plane from NEKTAR simulation

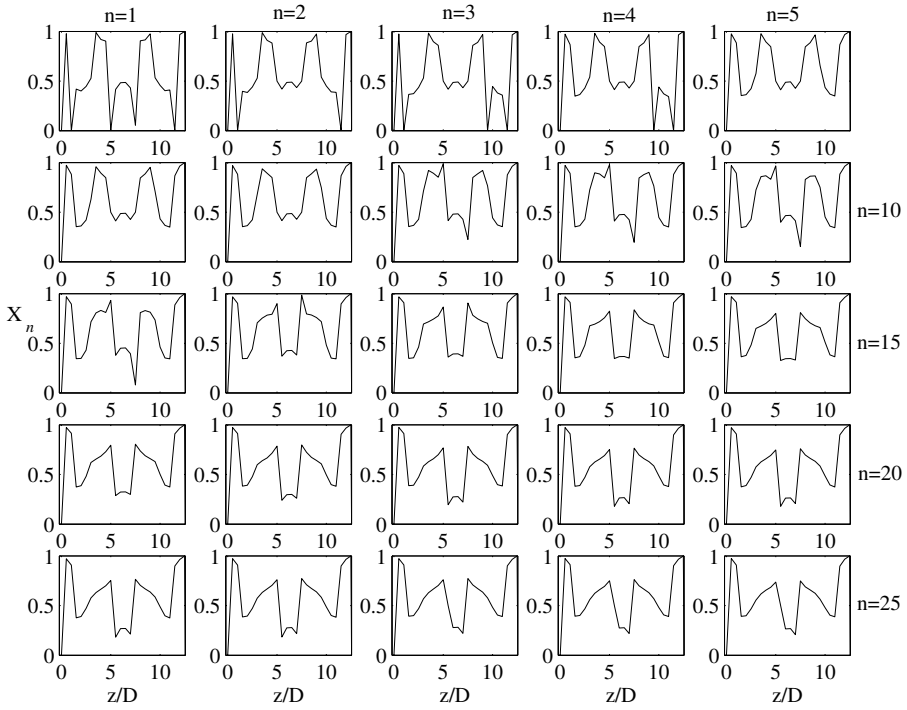

Figure 3.23: Illustration of vortex shedding phase angles, $X_n^k : \Omega = 0.9, x/D = 5$

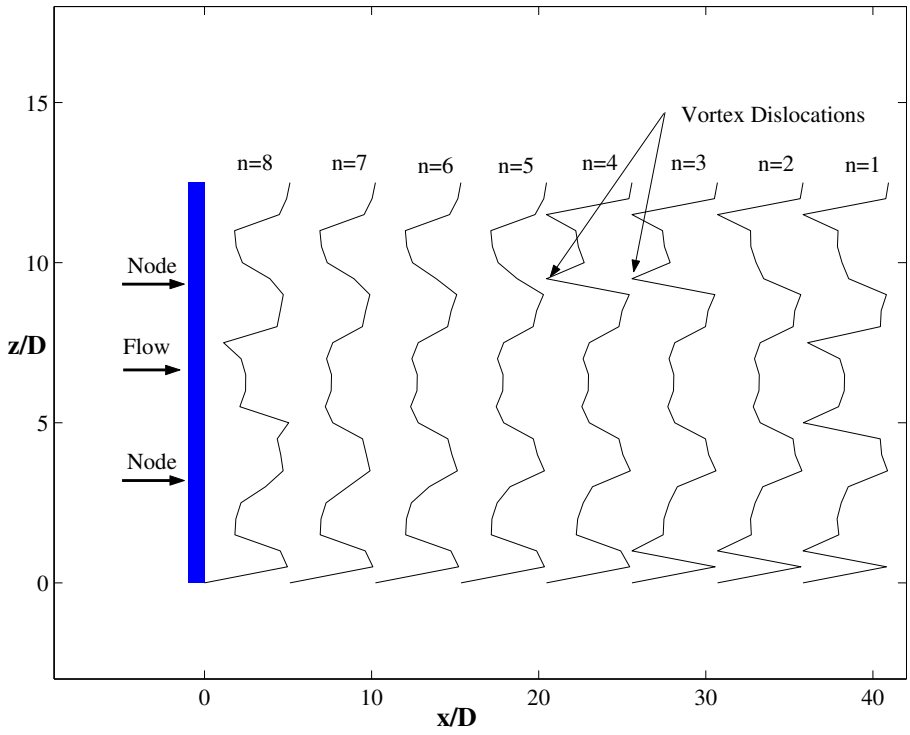

Figure 3.24: First 8 shedding cycles showing wake patterns at $x/D = 5.0$ for quasi-periodic case: $\Omega = 0.9$

sheared freestream flow interacting with a cable forced to vibrate at the Strouhal frequency based on the maximum freestream Reynolds number, i.e. $\Omega_{max} = 1.0$. This flow can also be used to model spanwise changes in diameter (example: a tapered cylinder). However, we retain the spanwise uniformity in the diameter of the cable in the current study and create a shear flow by varying the freestream velocity. The Reynolds number, as a function of the spanwise distance is given by: $Re(z) = 12.5(7 + cos(2\pi z/AR))$. The cosine distribution gives rise to $Re_{max} = 100$ at the ends and $Re_{min} = 75$ at the midspan. All other parameters are unchanged. Streamwise wake velocities are measured at $x/D = 5.0$ and the cross-correlation method is used to obtain the vortex shedding phase angles for $1 \leq n \leq 23$ in Figure 3.25. The corresponding wake patterns are then shown in Figure 3.26. Once the transients die out, the wake exhibits a chevron like pattern in the midspan, not seen in the uniform flow cases. Therefore, this study will be further helpful in determining the efficiency of the estimation methods in Chapter 3 and 4 in predicting varied wake patterns.

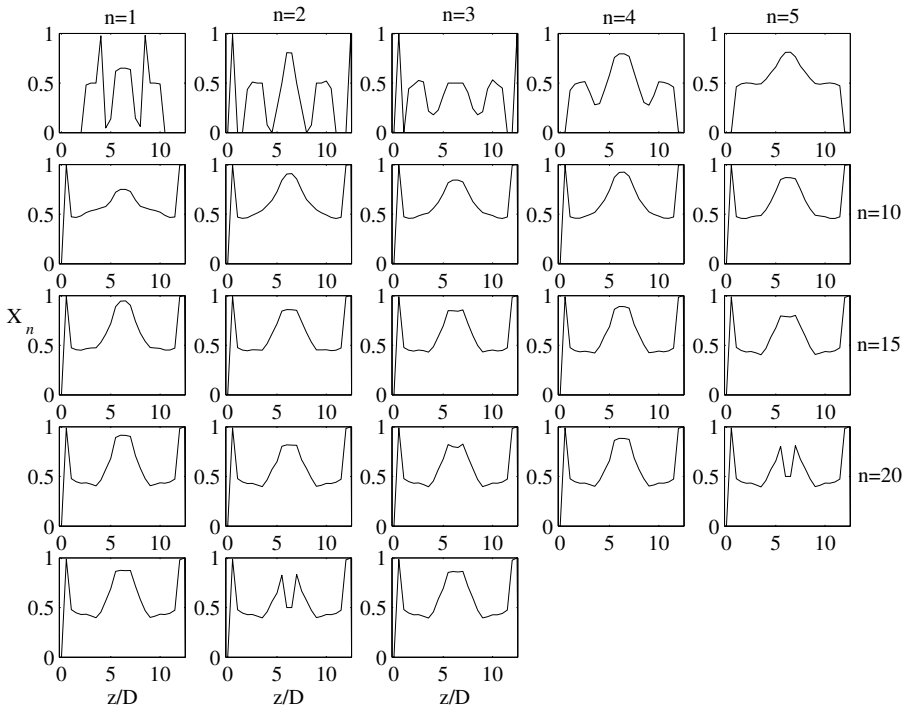

Figure 3.25: Sheared freestream flow case: Illustration of vortex shedding phase angles, X_n^k; $\Omega_{max} = 1.0, Re_{max} = 100, Re_{min} = 75, x/D = 5$

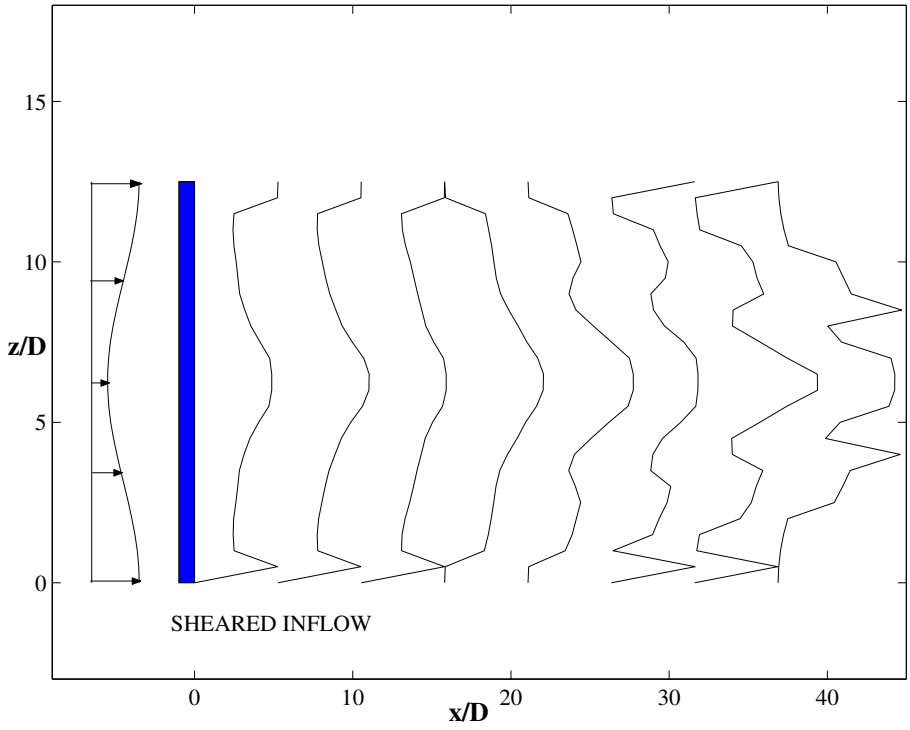

Figure 3.26: Sheared freestream flow: First 8 shedding cycles showing wake patterns at $x/D = 5.0$; $Re_{max} = 100, Re_{min} = 90, \Omega_{max} = 1.0$

3.2.3 MVLS algorithm for estimation

In this section we study the effectiveness of the MVLS algorithm based self-learning model in estimating vortex shedding wake patterns from the NEKTAR simulations. We study 3 different flow situations: Uniform flow and lock-on, uniform flow and quasi-periodic, and shear flow and lock-on. Before going into the results of the estimation procedure, we will summarize the input parameters used for the estimation model ((3.1), (3.6), (3.8)). The input weighting matrices $\mathbf{P}_0$ and $\mathbf{R}$ are chosen to be diagonal matrices with constant entries P_0 and R respectively. With this choice, it can be shown analytically that the ratio P_0/R is relevant in the estimation study. Therefore, an optimization study was conducted to determine an optimal value of $\mathrm{P}_0/\mathrm{R} = 0.001$. This value was uniformly applied for all 3 flow situations. The additional input parameters are $\widehat{X}_1^k$ and $\widehat{\Gamma}_1^k$, initial guesses for the vortex shedding phase angle and the spanwise velocity respectively. A random distribution was chosen for $\widehat{X}_1^k$ and $\widehat{\Gamma}_1^k$ was set uniformly to zero.

First, the wake patterns are estimated for the different flow cases in Figures 3.27-3.32. The estimation of the vortex shedding phase angles as a function of the number of shedding cycles is shown in Figures 3.34- 3.39. Next, the *state error* is used to highlight the efficiency of the self-learning CML in estimating these wake patterns. The evolution in time of the estimator of the spanwise velocity is then considered.

Estimation of NEKTAR wake patterns

In all the flow cases (Figures 3.27- 3.32) , a random wake pattern (phase angle distribution) is used as the initial condition for the self-learning CML. From the near wake studies ($x/D = 0.5, 1$) of the uniform flow, lock-on case, we see that the wake patterns from the self-learning scheme quickly evolve from the random distribution, and successfully estimate the lace-like patterns of the NEKTAR simulation within a single shedding cycle. For the same flow, at $x/D = 3.0$ we see that the self-learning scheme successfully captures the transient states ($1 \leq n \leq 6$) involving a transition from an initial "M-like" pattern in the midspan to the lace-like pattern observed in the near wake. Several other wake patterns ($x/D = 5, 10$) with increasing complexity are also efficiently estimated.

Successful estimation of the quasi-periodic wake evolution at $x/D = 5$ is shown in Figure 3.32. Unlike the lock-on (periodic) cases discussed in Figures 3.27- 3.32, we see that there is no periodicity in the evolution of the wake. This feature represents additional challenges in modeling using the self-learning CML. The wake shows some standing wave features of the cable oscillation, however with decreased wavelengths along the span. This feature is captured accurately by the estimation scheme for some shedding cycles.

Finally, in Figure 3.33 we plot the wake patterns for the NEKTAR simulation and the self-learning CML for the shear flow case. Once the initial transients die out, ($1 \leq n \leq 4$), we see oblique shedding patterns emerge from either end of the cylinder, consistent with the symmetrical freestream velocity distribution. An initial random wake pattern is used for the self-learning CML just as in the other cases.

The estimation is good for $n \geq 6$, everywhere except at one end of the cylinder. This result suggests that further improvements in the self-learning model in future. A possible alternative for modeling such complex features in the wake is suggested in Chapter 4. We can then directly compare the efficiency of the two methods.

For all the cases, the computational time in seconds per shedding cycle was of the order of 10^{-2} wall clock seconds on a Pentium PC. This included both the generation of target patterns from velocity data and the the estimation of the target wake patterns. The generation of NEKTAR wake data required 10^4 wall clock seconds per shedding cycle on an IBM supercomputer. This highlights the computational efficiency of the self-learning CML. Implications for future flow control studies using CML models is discussed later.

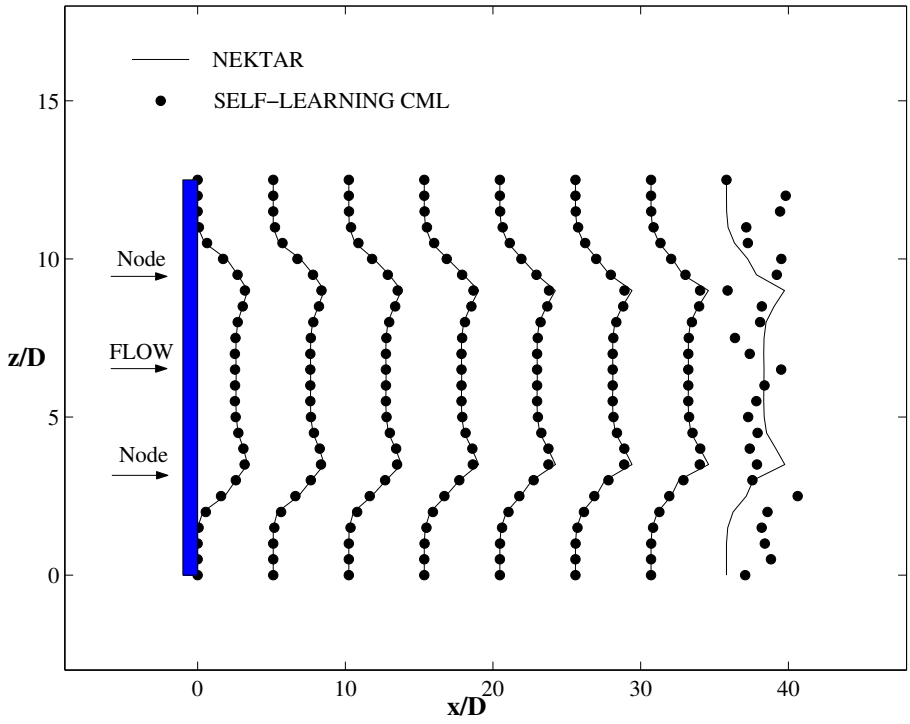

Figure 3.27: Estimation of first 8 shedding cycles showing wake patterns at $x/D = 0.5$ for lock-on case: $\Omega = 1.0$

Estimation of vortex shedding phase angles

We plot the vortex shedding phase angles (Figures 3.34- 3.39) which were used to generate the target and estimated wake patterns just considered. We use these to

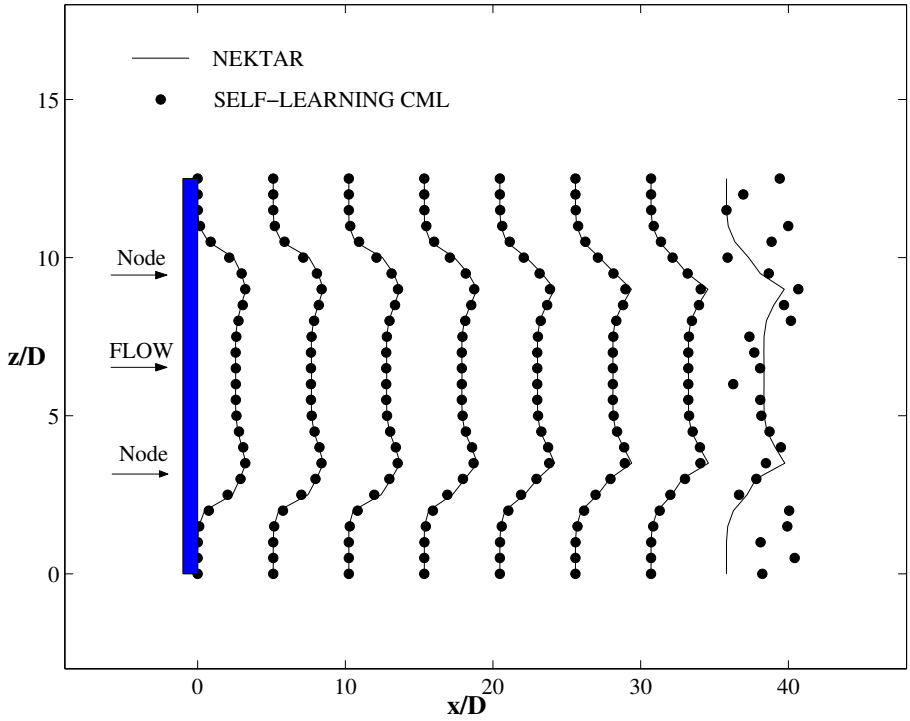

Figure 3.28: Estimation of first 8 shedding cycles showing wake patterns at $x/D = 1.0$ for lock-on case: $\Omega = 1.0$

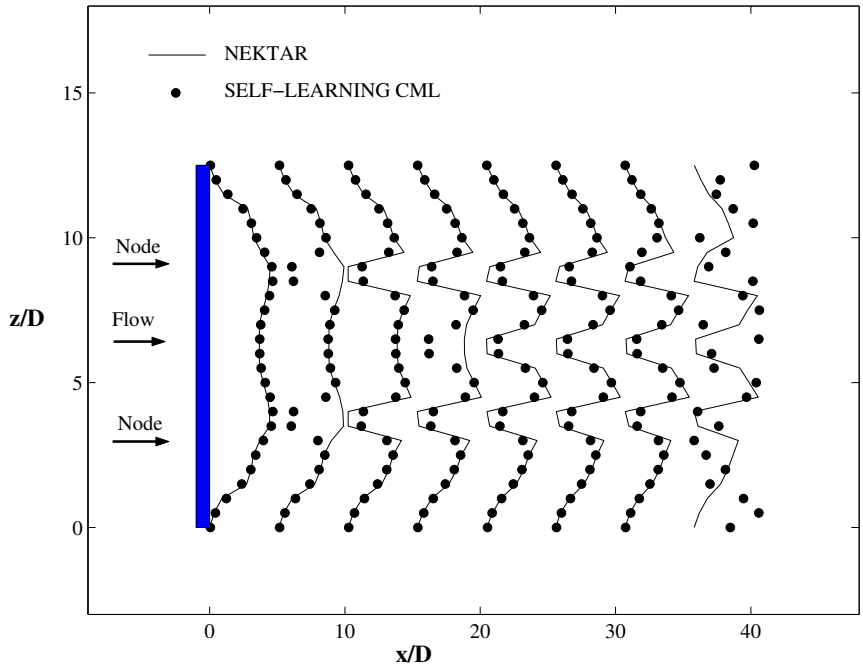

Figure 3.29: Estimation of first 8 shedding cycles showing wake patterns at $x/D = 3.0$ for lock-on case: $\Omega = 1.0$

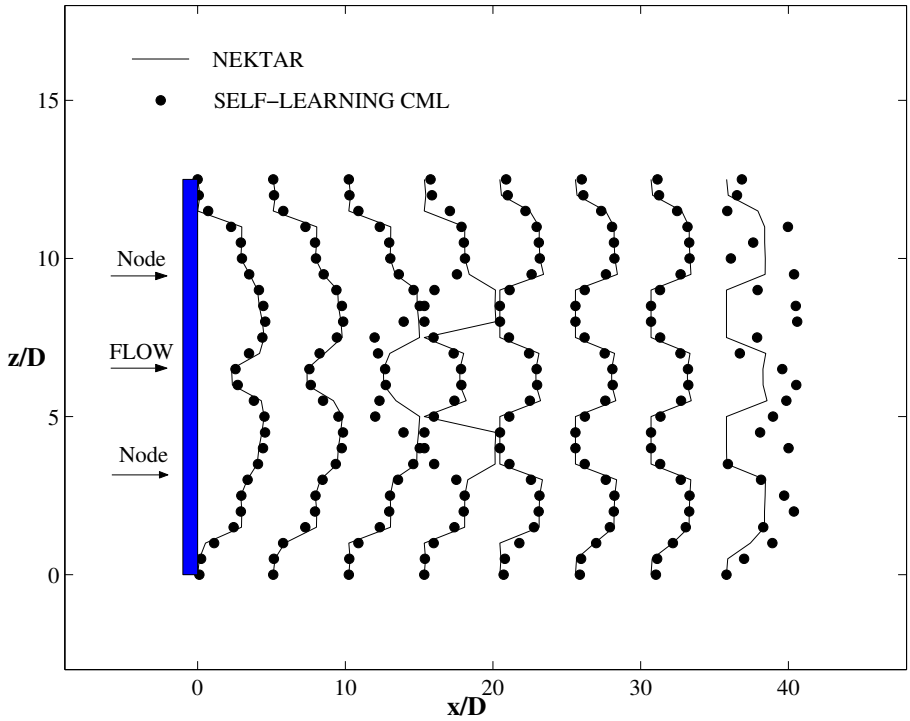

Figure 3.30: Estimation of first 8 shedding cycles showing wake patterns at $x/D = 5.0$ for lock-on case: $\Omega = 1.0$

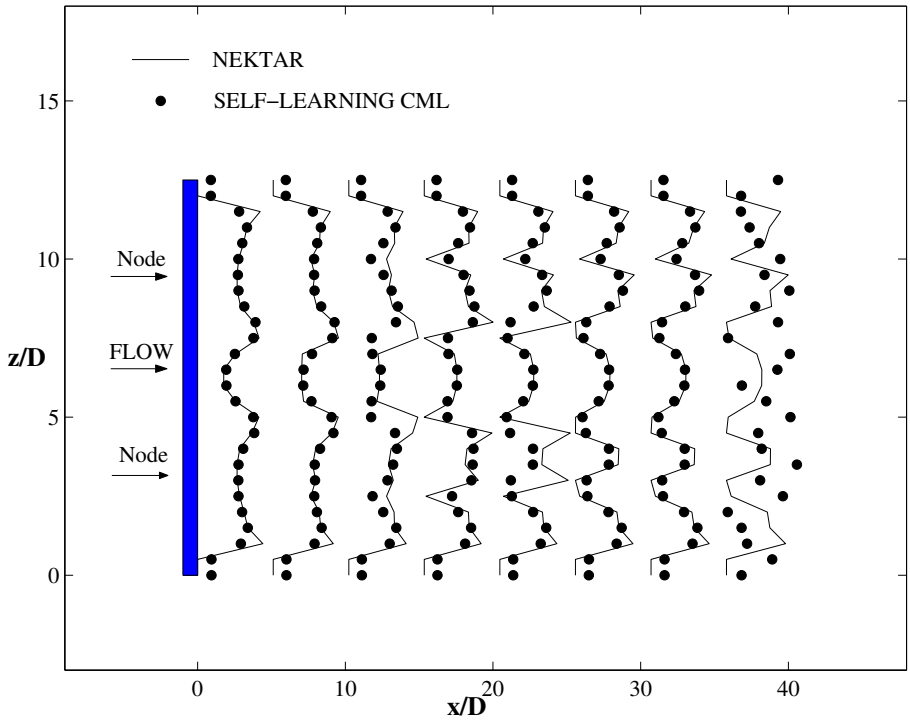

Figure 3.31: Estimation of first 8 shedding cycles showing wake patterns at $x/D = 10$ for lock-on case: $\Omega = 1.0$

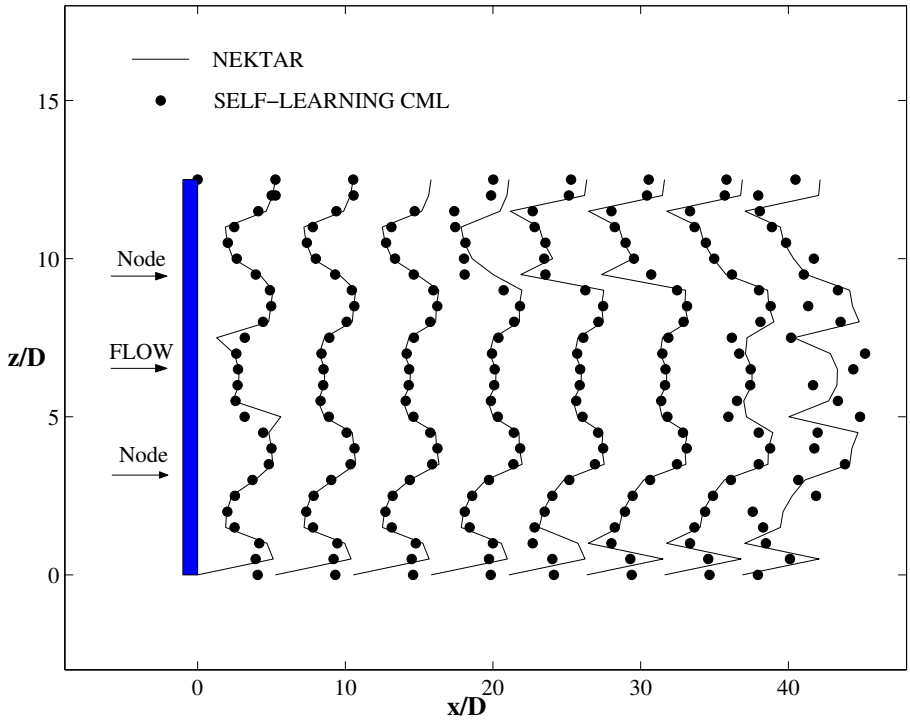

Figure 3.32: Estimation of first 8 shedding cycles showing wake patterns at $x/D = 5.0$ for quasi-periodic case: $\Omega = 0.9$

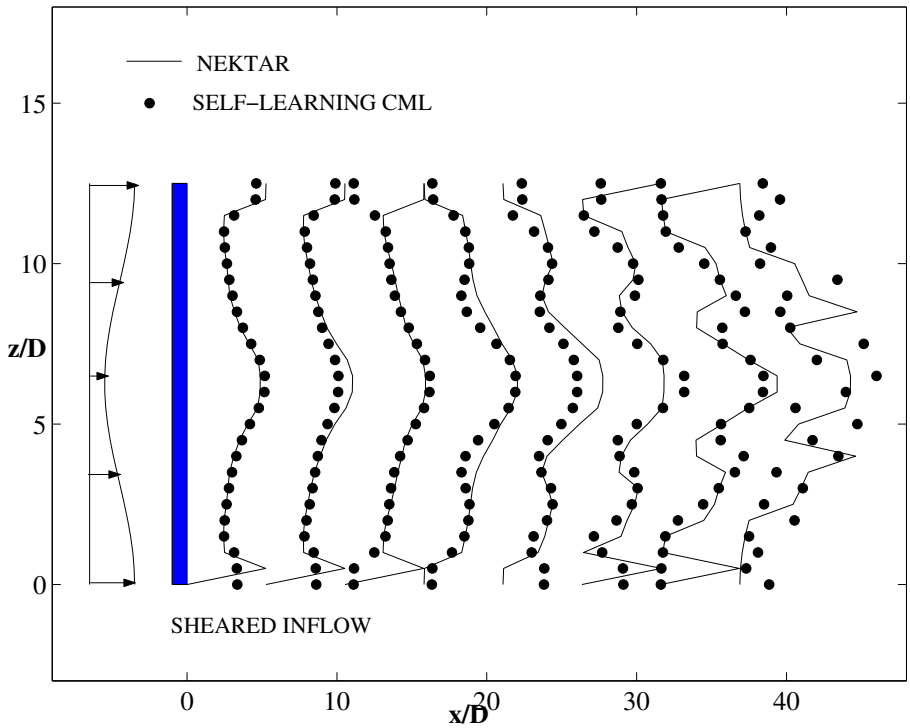

Figure 3.33: Estimation of first 8 shedding cycles showing wake patterns at $x/D = 5.0$ for shear flow case: $Re_{max} = 100, Re_{min} = 75, \Omega_{max} = 1.0$

summarize the results of estimation by comparing directly the state, X_n^k, with the adaptive estimator, $\widehat{X}_n^k$, for all values of n and k. In Figures 3.34,3.35, we show that the self-learning CML is highly accurate in predicting the periodic lace-like patterns in the near wake. It is also efficient in estimating several transients in the wake (see Figures 3.36- 3.39)

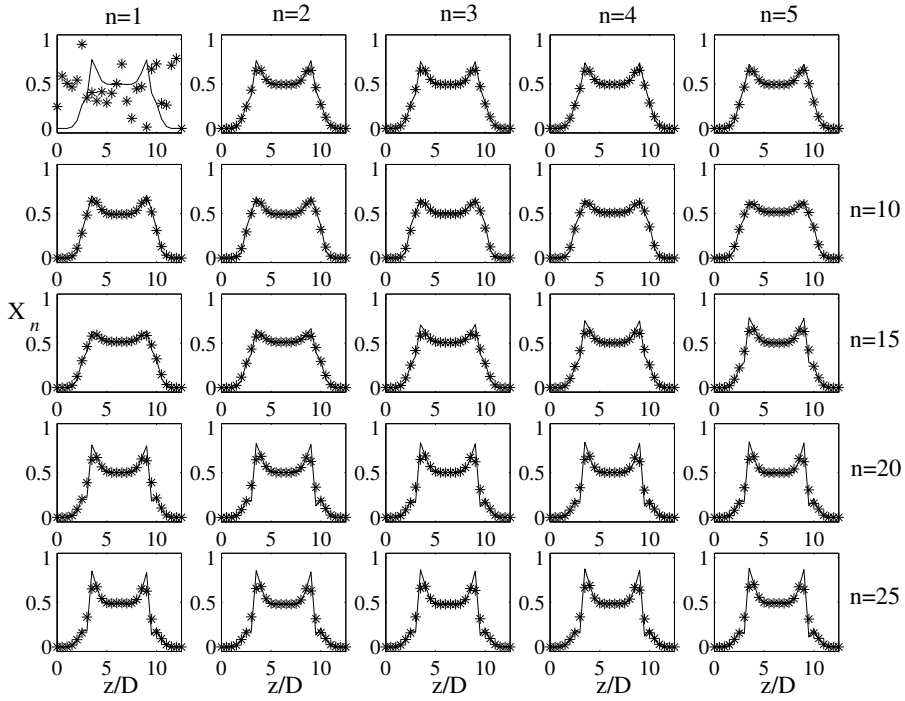

Figure 3.34: Temporal evolution of vortex shedding phase angles at $x/D = 0.5$ for uniform flow, lock-on case, $\Omega = 1.0$

Spatio-temporal evolution of the state error

The state error, e_n^k, is the difference between the target vortex shedding phase angle (state), X_n^k, and its estimator, $\widehat{X}_n^k$. We can use the state error to quantify the accuracy of the self-learning CML. In Figure 3.41, we plot the evolution of the state error in time n and spanwise distance z/D for the uniform flow, lock-on case at $x/D = 5$. For purposes of clarity, the complete results (up to $n = 25$) are not presented. We can see that the state error starts off high (as we have assumed a random initial distribution for the estimator) and within a couple of shedding cycles settles down to a low value of the order of 0.1. However, at certain discrete z/D locations, we see large values

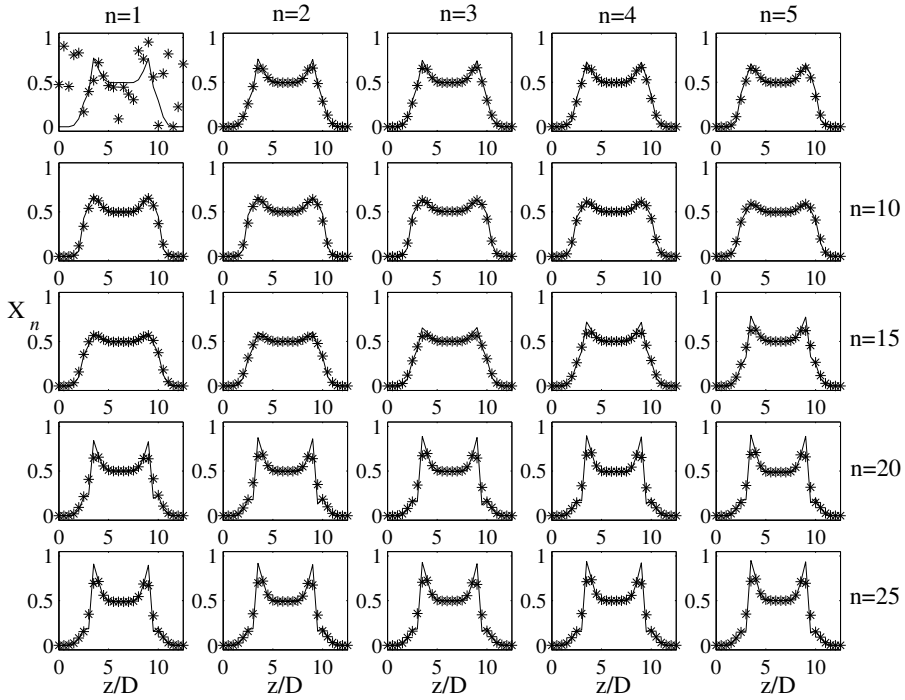

Figure 3.35: Temporal evolution of vortex shedding phase angles at $x/D = 1.0$ for uniform flow, lock-on case, $\Omega = 1.0$

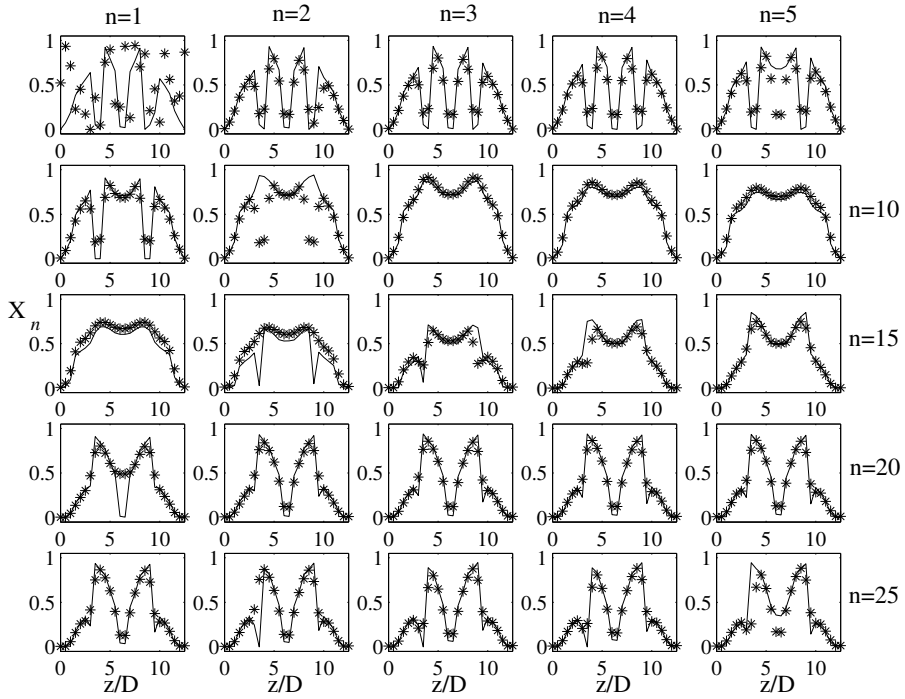

Figure 3.36: Temporal evolution of vortex shedding phase angles at $x/D = 3.0$ for uniform flow, lock-on case, $\Omega = 1.0$

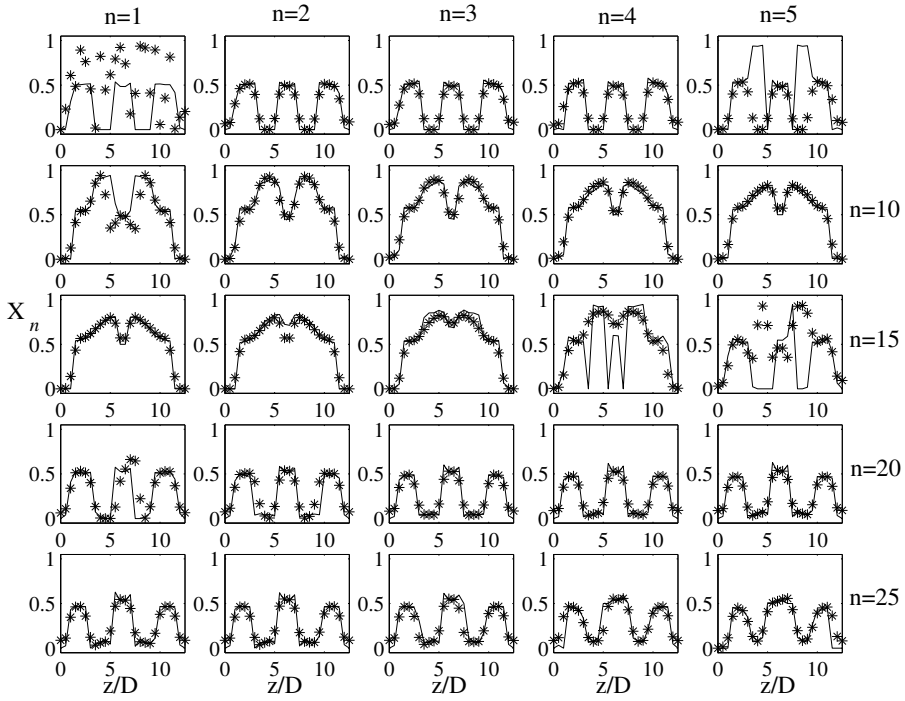

Figure 3.37: Temporal evolution of vortex shedding phase angles at $x/D = 5.0$ for uniform flow, lock-on case, $\Omega = 1.0$

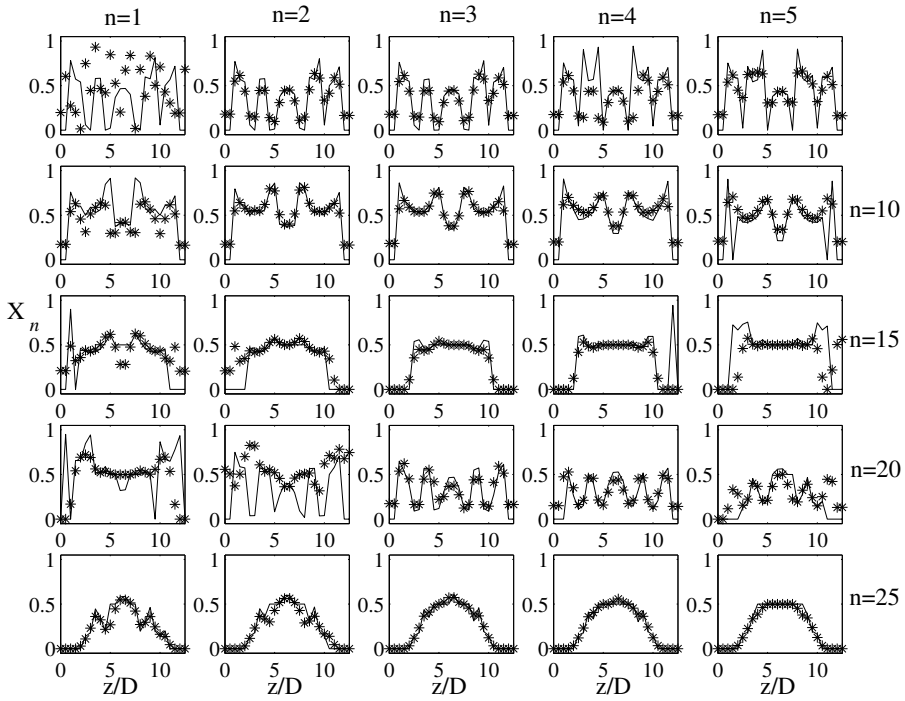

Figure 3.38: Temporal evolution of vortex shedding phase angles at $x/D = 10$ for uniform flow, lock-on case, $\Omega = 1.0$

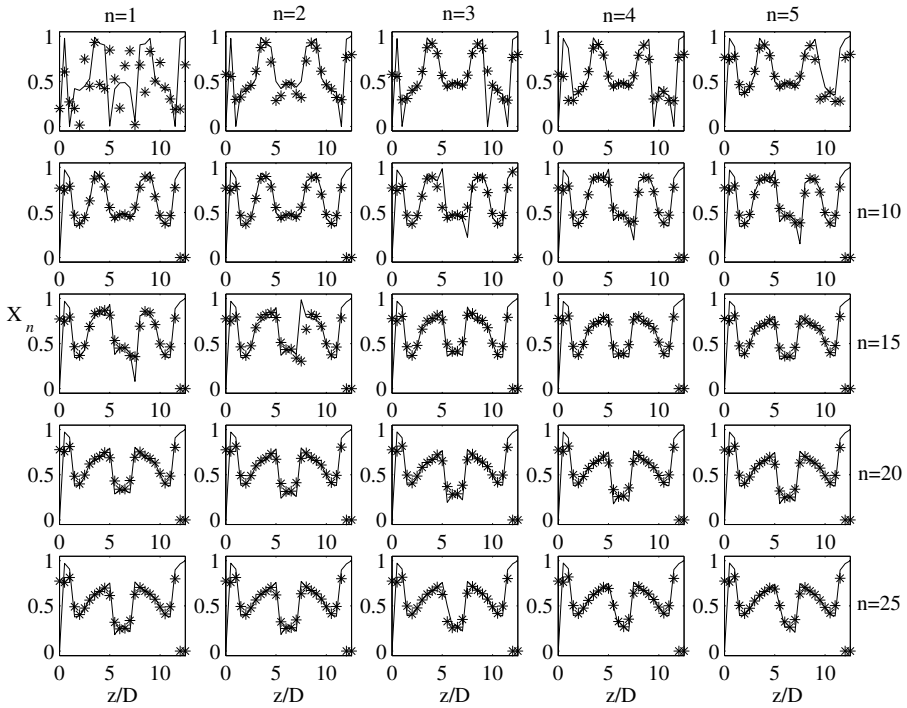

Figure 3.39: Temporal evolution of vortex shedding phase angles at $x/D = 3.0$ for uniform flow, quasi-periodic case, $\Omega = 0.9$

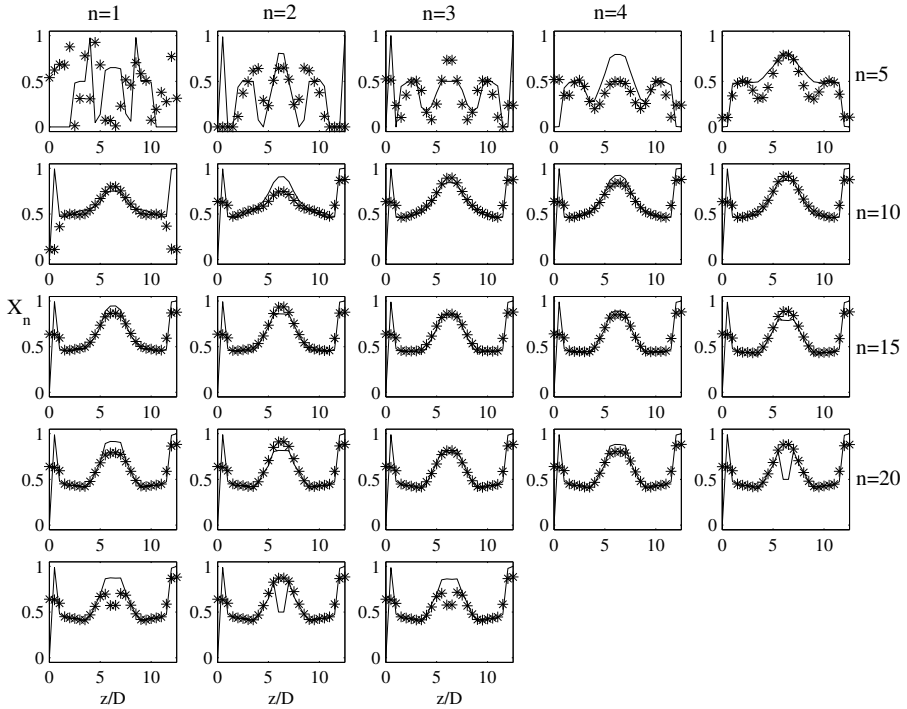

Figure 3.40: Temporal evolution of vortex shedding phase angles at $x/D = 5$ for shear flow case, $Re_{max} = 100, Re_{min} = 75, \Omega_{max} = 1.0$

of the state error. We believe that this discrepancy can be removed by considering additional spanwise oscillators especially in the mid-span regions where large errors are encountered. We specifically considered the $x/D = 5$ case in order to highlight the deficiencies of the current estimator. For the near wake cases (see Figure 3.42), we do not encounter such difficulties and the self-learning CML estimates the target wake patterns efficiently.

We will now consider the state error for the uniform flow, quasi-periodic case at the same $x/D = 5$ location in Figure 3.43. Features similar to the observations in Figure 3.41 are obtained. In addition, large errors are also encountered at the ends of the cable. This suggests that optimal placement of sensors depends on the type of flow situation, the type of forcing of the cable and the eventual interaction between the flow and the cable.

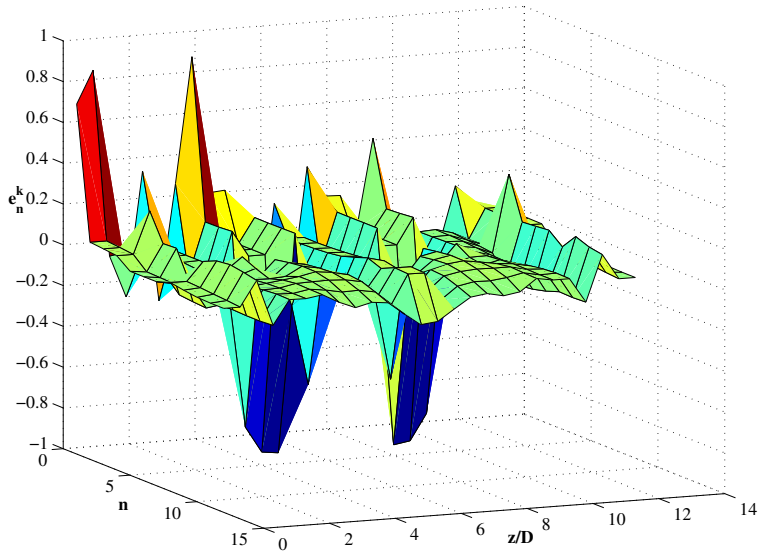

Figure 3.41: Local state error vs. spanwise location and time, for uniform flow, lock-on case, $x/D = 5$, $\Omega = 1.0$

Temporal evolution of the RMS error

We now present another measure to quantify the accuracy of the self-learning scheme. The root-mean-square (RMS) value of the state error, $\|e_n\|$ is defined for each shedding

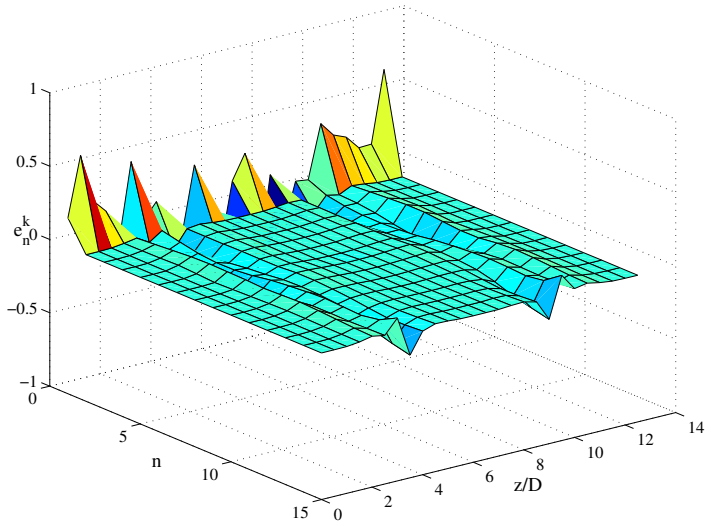

Figure 3.42: Local state error vs. spanwise location and time, for uniform flow, lock-on case, $x/D = 1$, $\Omega = 1.0$

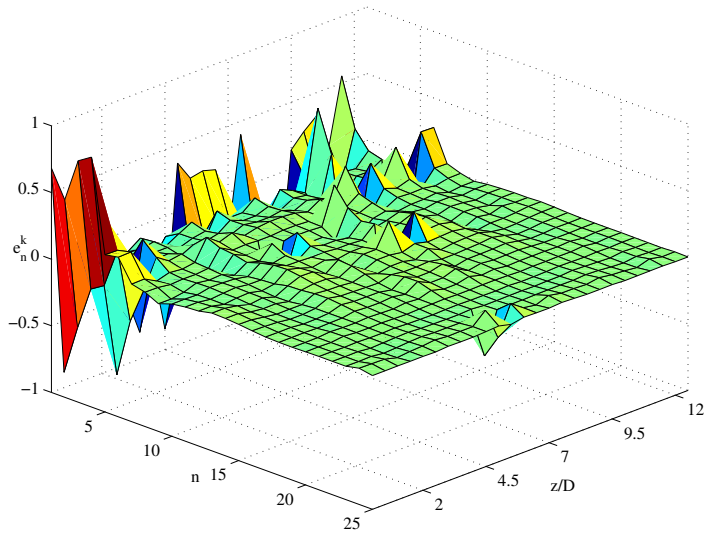

Figure 3.43: Local state error vs. spanwise location and time, for uniform flow, quasi-periodic case, $x/D = 5$, $\Omega = 0.9$

cycle n as:

$$\|e_n\| = \sqrt{\sum_{k=1}^{k^*} \frac{(\mathrm{X}_n^k - \widehat{X}_n^k)^2}{k^*}}. \tag{3.29}$$

The RMS value represents a global measure of the state error. We plot the RMS value of the state error, $\|e_n\|$, for all the 5 cases considered in Figure 3.44. The corresponding values for the quasi-periodic and shear flow cases are plotted in Figure 3.45. We can see that lock-on cases are efficiently estimated than the quasi-periodic case. Estimation of wake patterns generated from near-wake u-velocities, $x/D = 0.5, 1, 3$ are more efficiently estimated compared to the far-wake cases, $x/D = 5, 10$. Also, the periodic reduction and increase in $\|e_n\|$ observed for all the cases is due to the transients that are encountered in the wake. This was seen in the form of sudden change in wake patterns from one shedding cycle to the next. However, the MVLS algorithm certainly brings down the values of $\|e_n\|$ as soon as the estimation scheme "recognizes" the evolution of the wake patterns.

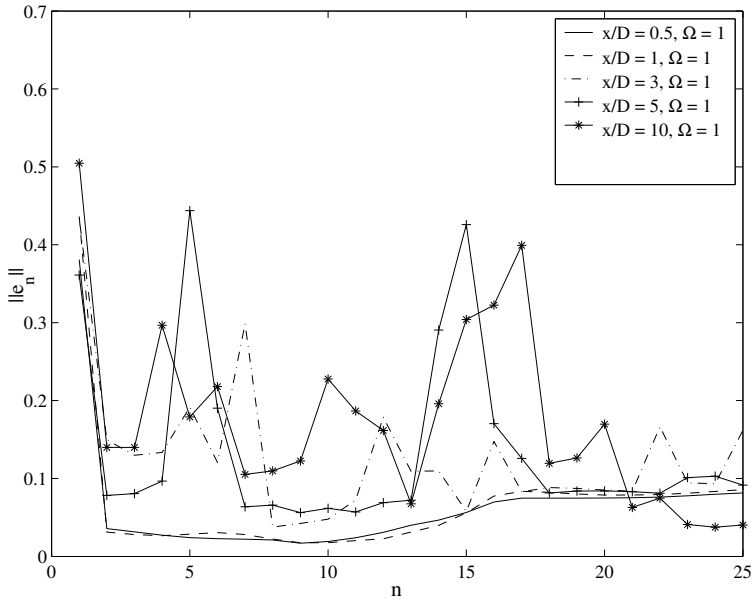

Figure 3.44: Time evolution of the root-mean-square of the state error, $\|e_n\|$, for the self-learning CML.

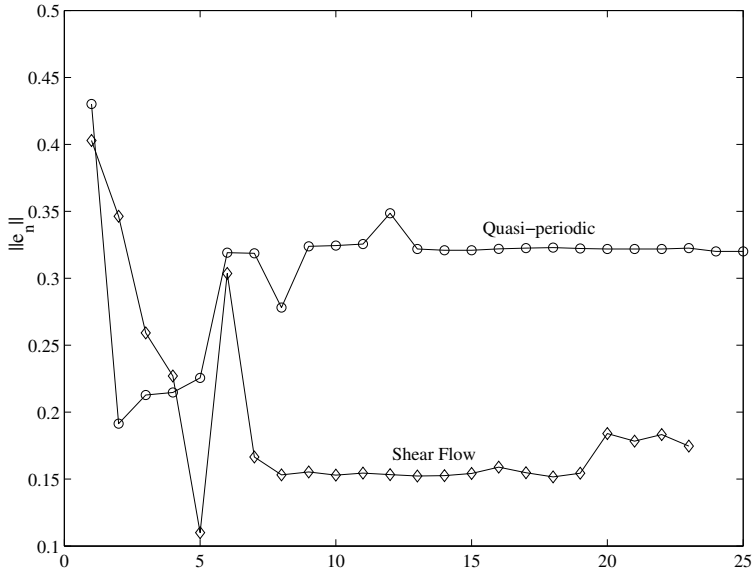

Figure 3.45: Time evolution of the root-mean-square of the state error, $\|e_n\|$, for the self-learning CML.

Temporal evolution of estimator of spanwise velocity

As we have seen before, the MVLS algorithm is used to adaptively estimate the spanwise velocity in order to minimize the state error, the difference between the NEKTAR wake patterns and the self-learning CML wake patterns. In Figure 3.46, the spanwise distribution of this parameter, $\widehat{\Gamma}_1^k$ to $\widehat{\Gamma}_5^k$, for the uniform flow, lock-on case, $x/D = 5$, is shown for the first 5 shedding cycles. Starting with zero values for $\widehat{\Gamma}_1^k$, we see that the self-learning scheme quickly estimates a complex distribution of spanwise velocities, $\widehat{\Gamma}_2^k$ to $\widehat{\Gamma}_5^k$ which are used to obtain the estimates of the vortex shedding phase angles shown in Figure 3.37. Notice the sharp change in the NEKTAR shedding phase angle distribution, between X_4^k and X_5^k, from $n = 4$ to $n = 5$, and the corresponding change in the spanwise velocity estimates, $\widehat{\Gamma}_4^k$ to $\widehat{\Gamma}_5^k$ in Figure 3.46.

The spanwise velocity distributions show spatial oscillations from positive to negative values near cable anti-nodes (z/D = 2) where the spanwise velocity becomes precisely zero. The opposite signed values correspond physically to a reversal in direction of spanwise velocity in the near wake as one moves along the cable span. The zero spanwise velocity implies that no fluid crosses the cable anti-nodes. Spanwise

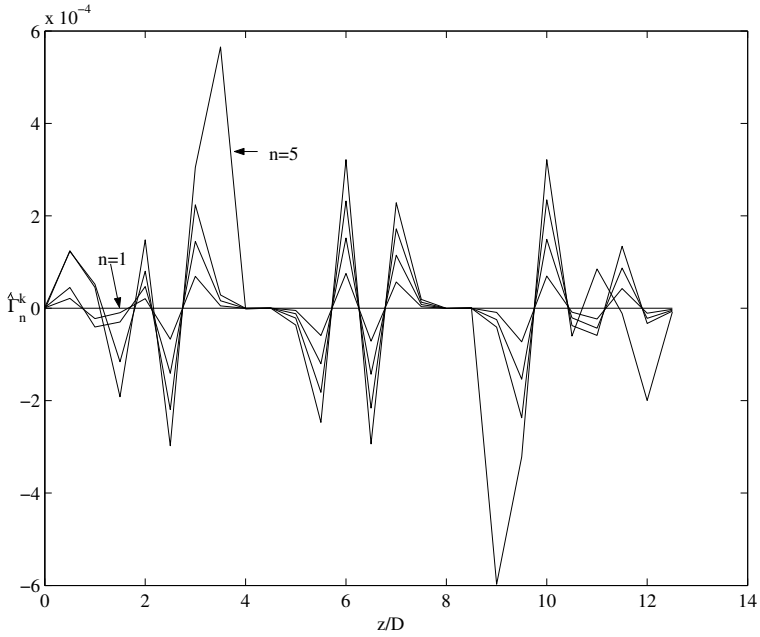

Figure 3.46: Time evolution of the estimate of spanwise velocity distribution, $\widehat{\Gamma}_n^k$, uniform flow, lock-on case, $x/D = 5$.

flow reversals and stagnation points such as these have also been observed in the simulations of Newman and Karniadakis (1997), and in experiments on oscillating tapered cylinders at low Reynolds numbers (Lin, Vorobieff and Rockwell, 1996), a flow with many of the characteristics of oscillating cable flows. It is also observed that the spatial wavelength of the spanwise velocity oscillations is approximately one to two cable diameters, similar to the results of Lin et al (1996).

This study completes the use of the MVLS algorithm based self-learning CML in targeting NEKTAR wake patterns. In Chapter 5, we will apply this model to estimate wake patterns from laboratory wake flows.

Chapter 4

Self-Learning CML based on Neural Networks

Neural networks represent a class of universal approximators that are used in the estimation and control of non-linear dynamical systems (Narendra *et al.*, 1990). In this study, radial basis functions are used as on-line approximators of the coupled map lattice. We choose a large number of radial basis functions and vary the associated weighting parameters suitably to estimate the dynamics of the coupled map lattice. This scheme is developed to further improve upon the MVLS algorithm based scheme discussed in Chapter 3. We no longer assume that the convection process of the vorticity transport equation is completely described by the spanwise velocity distribution. This relaxation is useful in modeling additional unmodelled dynamics from the self-learning CML described in Chapter 3. A schematic of the neural networks based self-learning CML is shown in Figure 4.1. We use recurrent neural networks in order to adaptively vary the neural network weights associated with a single layer of radial basis functions. The *state error* is progressively reduced leading to efficient estimation of target wake patterns. First, the self-learning CML is developed to estimate target wake patterns. Later, the results of the current scheme are presented for the same 7 cases considered in Chapter 3.

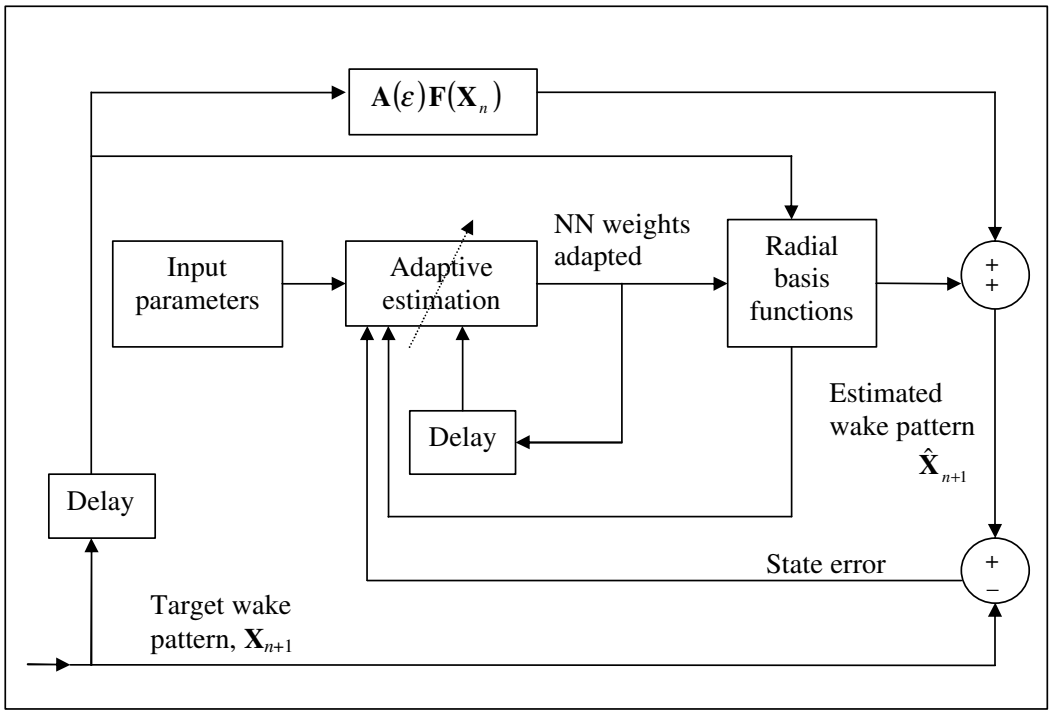

Figure 4.1: Schematic of the neural networks based self-learning CML. A single layer recurrent neural network is used for estimation of wake patterns.

4.1 Development of the neural network based CML

The starting point for this method is the vorticity diffusion equation (2.1). However, unlike the self-learning CML of Chapter 3, we consider all terms in the z component of the vorticity diffusion equation (2.1) in our model development. Equation (2.2) is repeated below with the diffusive and convective terms separated for analysis purposes:

$$\frac{\partial w_z}{\partial t} = \underbrace{\nu \nabla^2 w_z}_{\text{diffusive}} \underbrace{-u \frac{\partial w_z}{\partial x} - v \frac{\partial w_z}{\partial y} - w \frac{\partial w_z}{\partial z} + w_x \frac{\partial w}{\partial x} + w_y \frac{\partial w}{\partial y} + w_z \frac{\partial w}{\partial z}}_{\text{convective}}. \quad (4.1)$$

Equation (4.1) is then rewritten as:

$$\frac{\partial w_z}{\partial t} = \nu \frac{\partial^2 w_z}{\partial z^2} + h(\mathbf{u}, \omega, t), \quad (4.2)$$

where $h(\mathbf{u}, \omega, t)$ represents the difference in the right hand side of (4.1) and (4.2).

The first term in the right hand side of (4.2) is used to model the z-diffusion exactly as in the basic CML model. The unknown term, $h(\mathbf{u}, \omega, t)$, is modeled with neural networks.

We now use the analogy between the vortex shedding event and the magnitude of the w_z to define $\mathrm{X} \equiv w_z$ as before. Now, applying Simple Explicit Finite Differencing (forward in time, centered in space) to the above PDE we get,

$$\frac{\mathrm{X}_{n+1}^k - \mathrm{X}_n^k}{\Delta t} = \frac{\nu}{(\Delta z)^2} \left(\mathrm{X}_n^{k-1} - 2\mathrm{X}_n^k + \mathrm{X}_n^{k+1} \right) + h_n^k \quad (4.3)$$

We now use the diffusion coefficient, $\epsilon = \nu \Delta t / (\Delta z)^2$ and the non-dimensional term, $\overline{h}_n^k = h_n^k \Delta t$, to rewrite (4.3) as:

$$\mathrm{X}_{n+1}^k = \underbrace{\left(\epsilon \, \mathrm{X}_n^{k-1} + (1 - 2\epsilon) \mathrm{X}_n^k + \epsilon \mathrm{X}_n^{k+1} \right)}_{\text{diffusive}} + \underbrace{\overline{h}_n^k}_{\text{convective}} \quad (4.4)$$

The coupling between the above finite difference equation (4.4) and the modified circle map (1.6) requires $f_n^k = \mathrm{X}_n^k$ so that:

$$\mathrm{X}_{n+1}^k = \underbrace{\left(\epsilon\, f_n^{k-1} + (1-2\epsilon) f_n^k + \epsilon f_n^{k+1}\right)}_{\text{diffusive}} + \underbrace{\widehat{h}_n^k}_{\text{convective}} \quad , \ \widehat{h}_n^k = f(\overline{h}_n^k). \tag{4.5}$$

Equation (4.5) is written in vector form as:

$$\mathbf{X}_{n+1} = \mathbf{A}(\epsilon)\mathbf{F}(\mathbf{X}_n) + \mathbf{H}(\mathbf{X}_n), \ \mathbf{X} \in \Psi \subset \Re^{k^*}. \tag{4.6}$$

The set Ψ is such that it contains all possible "trajectories" of $\mathbf{X}$. While being aware of its existence, in our analysis we do not need to know the region Ψ. Equation (4.6) represents the true dynamics of the system obtained by simple explicit finite differencing of the vorticity diffusion equation and coupling of the resulting equation with the modified circle map. We will assume that $\mathbf{H}(\mathbf{X}_n)$ in (4.6) can be modeled by linearly parametrized approximators, $\mathbf{Y}(\mathbf{X}_n; \theta^*)$ such that

$$\mathbf{X}_{n+1} = \mathbf{A}(\epsilon)\mathbf{F}(\mathbf{X}_n) + \mathbf{Y}(\mathbf{X}_n; \theta^*) + \mathbf{N}_n. \tag{4.7}$$

The optimal parameter matrix $\theta^* \in \mathbb{R}^{k^* \times p}$ is chosen to minimize the distance between $\mathbf{H}(\mathbf{X}_n)$ and $\mathbf{Y}(\mathbf{X}_n; \theta^*)$ over all $\mathbf{X} \in \Psi$ in some compact learning domain, subject to the restriction that θ^* belongs to a compact, convex region $\mathcal{M}_\theta \subset \mathbb{R}^{k^* \times p}$; i.e.,

$$\theta^* :\equiv \arg\min_{\theta \in \mathcal{M}_\theta} \left\{ \sup_{\mathbf{X} \in \Psi} \left| \mathbf{H}(\mathbf{X}_n) - \mathbf{Y}(\mathbf{X}_n; \theta^*) \right| \right\}. \tag{4.8}$$

The modeling error $\mathbf{N}_n$ occurs due to the (possible) inadequacy of the approximator $\mathbf{Y}(\mathbf{X}_n; \theta)$ to match exactly the non-linear function $\mathbf{H}(\mathbf{X}_n)$ even if an optimal set of parameters $\theta = \theta^*$ were to be chosen.

4.1.1 Estimation model

Based on (4.7), we consider the estimation model

$$\widehat{\mathbf{X}}_{n+1} = \mathbf{A}(\epsilon)\mathbf{F}(\mathbf{X}_n) + \mathbf{Y}(\mathbf{X}_n; \widehat{\theta}_n), \tag{4.9}$$

where $\widehat{\theta}_n \in \mathbb{R}^{k^* \times p}$ is the estimator of θ^* at the discrete-time n, and $\widehat{\mathbf{X}}_n$ is the output of the estimator at time n. It is our objective to find a recursive estimation procedure for $\widehat{\theta}_n$. Therefore, let us define the *state error* as

$$\begin{aligned} \mathbf{E}_{n+1} &:\equiv \widehat{\mathbf{X}}_{n+1} - \mathbf{X}_{n+1} \\ &= \mathbf{Y}(\mathbf{X}_n; \widehat{\theta}_n) - \mathbf{Y}(\mathbf{X}_n; \widehat{\theta}^*) - \mathbf{N}_n. \end{aligned} \tag{4.10}$$

Linear Parametrization

Here, the unknown function to be approximated, $\mathbf{H}(\mathbf{X}_n)$, is modeled as a linear function of the elements of the parameter estimation matrix, that is,

$$\underset{k^* \times 1}{\mathbf{Y}(\mathbf{X}_n; \widehat{\theta}_n)} :\equiv \underset{k^* \times p}{\widehat{\theta}_n} \; \underset{p \times 1}{\mathbf{W}(\mathbf{X}_n)}, \tag{4.11}$$

where $\mathbf{W} \in \mathbb{R}^{p \times 1}$ are the sigmoidal neural networks. Based on the above definition, the state error is a linear function of the parameter estimator,

$$\mathbf{E}_{n+1} = (\widehat{\theta}_n - \theta^*)\, \mathbf{W}(\mathbf{X}_n) - \mathbf{N}_n. \tag{4.12}$$

Let us define $\widehat{\theta}_n :\equiv \left(\widehat{\theta_n^1}, \widehat{\theta_n^2}, \ldots, \widehat{\theta_n^{k^*}}\right)^T$, where $\theta_n^j \in \mathbb{R}^{p \times 1}$ is the j^{th} column of $\widehat{\theta}_n^T$. Now, define a new parameter estimator vector, $\widehat{\mathbf{Q}}_n \in \mathbb{R}^{k^* p \times 1}$ so that,

$$\widehat{\mathbf{Q}}_n :\equiv \left((\widehat{\theta_n^1})^T, (\widehat{\theta_n^2})^T, \ldots, (\widehat{\theta_n^{k^*}})^T\right)^T. \tag{4.13}$$

The j^{th} element of $\mathbf{Y}(\mathbf{X}_n;\widehat{\theta}_n)$, $y_j(\mathbf{X}_n;\widehat{\theta}_n)$ is given by:

$$\begin{aligned} y_j(\mathbf{X}_n;\widehat{\theta}_n) &= \left[\mathbf{0}_{1\times(j-1)p} \,|\, \mathbf{W}(\mathbf{X}_n)^T \,|\, \mathbf{0}_{1\times(k^*-j)p}\right]\widehat{\mathbf{Q}}_n \\ &= \overline{\mathbf{W}}_j(\mathbf{X}_n)\widehat{\mathbf{Q}}_n, \end{aligned} \tag{4.14}$$

where $\mathbf{0}_{1\times m}$ is the standard notation for a zero vector of m columns. The on-line approximator (4.11) can now be written as:

$$\begin{aligned} \mathbf{L}(\mathbf{X}_n;\widehat{\mathbf{Q}}_n) &:\equiv \mathbf{Y}(\mathbf{X}_n;\widehat{\theta}_n) \\ &= \overline{\mathbf{W}}(\mathbf{X}_n)\widehat{\mathbf{Q}}_n, \quad \overline{\mathbf{W}} \in \mathbb{R}^{k^*\times k^*p}. \end{aligned} \tag{4.15}$$

We can define the optimal parameter vector $\mathbf{Q}^*$ in the same way θ^* was defined in (4.8). Now, the state error can be written as:

$$\begin{aligned} \mathbf{E}_{n+1} &= \mathbf{L}(\mathbf{X}_n;\widehat{\mathbf{Q}}_n) - \mathbf{L}(\mathbf{X}_n;\mathbf{Q}^*) - \mathbf{N}_n \\ &= \overline{\mathbf{W}}(\mathbf{X}_n)\left(\widehat{\mathbf{Q}}_n - \mathbf{Q}^*\right) - \mathbf{N}_n. \end{aligned} \tag{4.16}$$

In order to minimize the state error after each timestep, we consider the following adaptive law which is based on a multi-variable normalized least squares scheme and a projection algorithm (Polycarpou *et al.*, 1992, Johnson, 1988):

$$\widehat{\mathbf{Q}}_{n+1} = \begin{cases} \mu_{n+1} & \text{if } \|\mu_{n+1}\| \le M_\theta \\ \mathbf{P}(\mu_{n+1}) & \text{if } \|\mu_{n+1}\| > M_\theta \end{cases}, \tag{4.17}$$

where M_θ defines the size of the hypersphere $\mathcal{M}_p = \{\widehat{\theta} : |\widehat{\theta}| < M_\theta\}$ with

$$\mu_{n+1} :\equiv \widehat{\mathbf{Q}}_n - \frac{\gamma_0 \overline{\mathbf{W}}(\mathbf{X}_n)^T \mathbf{E}_{n+1}}{\beta_0 + \|\overline{\mathbf{W}}(\mathbf{X}_n)\|^2}, \beta_0 > 0, 0 < \gamma_0 < 2, \tag{4.18}$$

where we use the Frobenius norm, defined as $\|\mathbf{A}\| = \left(\text{trace}(\mathbf{A}\mathbf{A}^T)\right)^{\frac{1}{2}} = \left(\sum_i \sum_j a_{ij}^2\right)^{\frac{1}{2}}$. The projection operator $\mathbf{P}(\cdot)$ which constrains the parameter $\widehat{\theta}_n$ to the compact, con-

vex region $\mathcal{M}_p$, is defined as

$$\mathbf{P}(\mu_{n+1}) :\equiv \frac{\mathrm{M}_\theta}{\|\mu_{n+1}\|}\,\mu_{n+1}. \tag{4.19}$$

The neural network based CML is then comprised of (4.17),(4.18), (4.19) and the estimation model repeated here for convenience.

$$\widehat{\mathbf{X}}_{n+1} = \mathbf{A}(\epsilon)\mathbf{F}(\mathbf{X}_n) + \overline{\mathbf{W}}(\mathbf{X}_n)\widehat{\mathbf{Q}}_n.$$

Theorem 4.1.1 *The parameter adaptive law* (4.17) *to* (4.19) *guarantees that* $\mathbf{E}_{n+1}$ *and* $\widehat{\mathbf{Q}}_{n+1}$ *are uniformly bounded and there exists constants* λ_1, λ_2 *such that for any finite integer* N

$$\sum_{n=0}^{N-1} \|\mathbf{E}_{n+1}\|^2 < \lambda_1 + \lambda_2 \sum_{n=0}^{N-1} \|\mathbf{N}_n\|^2 \ , \ \lambda_1,\, \lambda_2 > 0 \tag{4.20}$$

where $\mathbf{N}_n$ *is given by* (4.7). *Furthermore, if* $\mathbf{N}_n \in \ell_2$, *that is,* $\sum_{n=1}^{\infty} \|\mathbf{N}_n\|^2 < \infty$, *then* $\mathbf{E} \in \ell_2$ *and* $\lim_{n\to\infty} \mathbf{E}_n \to \mathbf{0}$.

The proof is very long and is therefore included in the Appendix. In essence, one constructs a positive definite Lyapunov function for the estimation model and the parameter adaptive law (4.17) - (4.19) forces its time derivative to be negative. According to Theorem 1, in any discrete-time interval $[0, N]$, the "energy" of the state error is (at most) of the same order as the "energy" of the modeling error.

Having discussed the convergence issues of the neural network based self-learning CML, we will now apply this model to target the same NEKTAR wake patterns considered in Chapter 3.

4.2 Results

We have applied the neural network based CML to predict wake patterns from 7 different NEKTAR simulations. First, we study a lock-on case of uniform flow over a cable forced to vibrate in standing wave mode shape at the Strouhal frequency. The relevant parameters are $Re = 100, AR = 4\pi, A/D = 0.69, \Omega = f_o/f_e = 1.0, x/D = 0.5, 1, 3, 5, 10$. Second, a quasi-periodic case with frequency ratio $\Omega = 0.9$ studies the sensitivity of the scheme to variations in cable oscillation frequency. We consider only one $x/D = 5$ case for this study. Third, we study a sheared inflow which, in the context of a spanwise periodic model such as the NEKTAR/CML, is simulated by specifying a sinusoidal inflow. Therefore, we set the inflow velocity to

$$u(-\infty, y, z) = \frac{7 + \cos(2\pi z/L)}{8}$$

resulting in a corresponding range of local Reynolds numbers from $Re = 100$ to $Re = 75$. Once again, the NEKTAR wake patterns are obtained from u-velocities sampled at $x/D = 5$.

Optimization of input parameters

The input parameters for the neural network based CML (apart from the basic input parameters used for the basic CML model) are $\widehat{X}^k_{n=0}, \gamma_0, \beta_0$, p- the number of radial basis functions, type of the neural network function, and the initial guess for parameter, $\widehat{Q}^k_{n=0}$. A random vortex shedding phase angle distribution, $\widehat{X}^k_{n=0}$, is considered as in Chapter 3. The acceleration parameter, $\gamma_0 = 1.9$, is chosen in the required stable range of 0 to 2. The parameter β_0 is typically set to a very small value, set to 0.001 here. Radial basis functions are used to represent the neural networks as they are proven as universal approximators. The initial guess of the distribution of estimates of the neural network weights, $\widehat{Q}^k_0 = 0$.

We next present an optimization study to determine the number of neural net-

works required for successful estimation. We consider the quasi-periodic case, $\Omega = 0.9$, to illustrate the optimization study. We define the summed squared state error, V_n,

$$V_n = \mathbf{E}_n^T \mathbf{E}_n,$$

for this purpose and observe from Figure 4.2 that V_n decreases with an increase in the number of neural networks as expected. The neural network based CML also outperforms the previous self-learning CML with V_n values several orders of magnitude lower at all the discrete times.

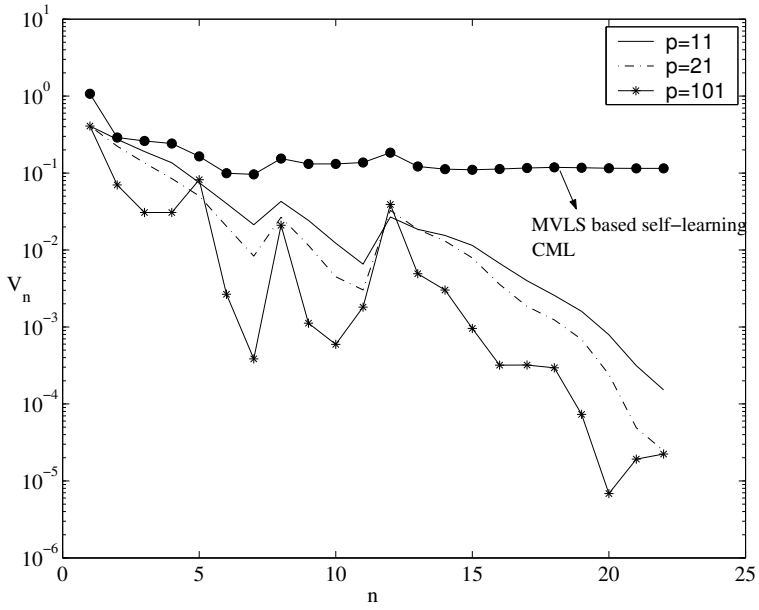

Figure 4.2: Optimization of the number of neural networks using the mean summed squared error criterion, quasi-periodic case.

Estimation of NEKTAR wake patterns

In this section, we apply the neural network adaptive scheme to target NEKTAR wake patterns estimated by the MVLS algorithm based self-learning CML in Chapter 3. The input parameters for the neural network scheme were discussed previously. We will compare the effectiveness of the two self-learning CML models by studying the same NEKTAR flow situations. First, we consider the case of uniform flow over a cable forced externally to oscillate in a standing wave motion at the Strouhal frequency.

For this lock-on case, $\Omega = 1.0$, lace-like flow structures are observed in NEKTAR simulations in the near wake, $(0 \leq x/D \leq 2)$ (Figure 3.3). We consider two x/D locations, $x/D = 0.5, 1$, in the near wake to illustrate estimation of the lace-like wake patterns as in Chapter 3. In Figure 4.3, an initial random wake pattern is used for the neural network model. Successful estimation of the lace-like patterns is observed within a single shedding cycle. There is little to compare the effectiveness of the self-learning CML models in estimating these periodic near wake patterns (see Figures 4.3, 3.27). On closer observation, the neural network method is more accurate in estimating the vortex cores at the nodes $(z/D \approx \pi, z/d \approx 3\pi)$ for every shedding cycle. A similar observation can be made for the near wake case, $x/D = 1.0$ (Figures 4.4, 3.27).

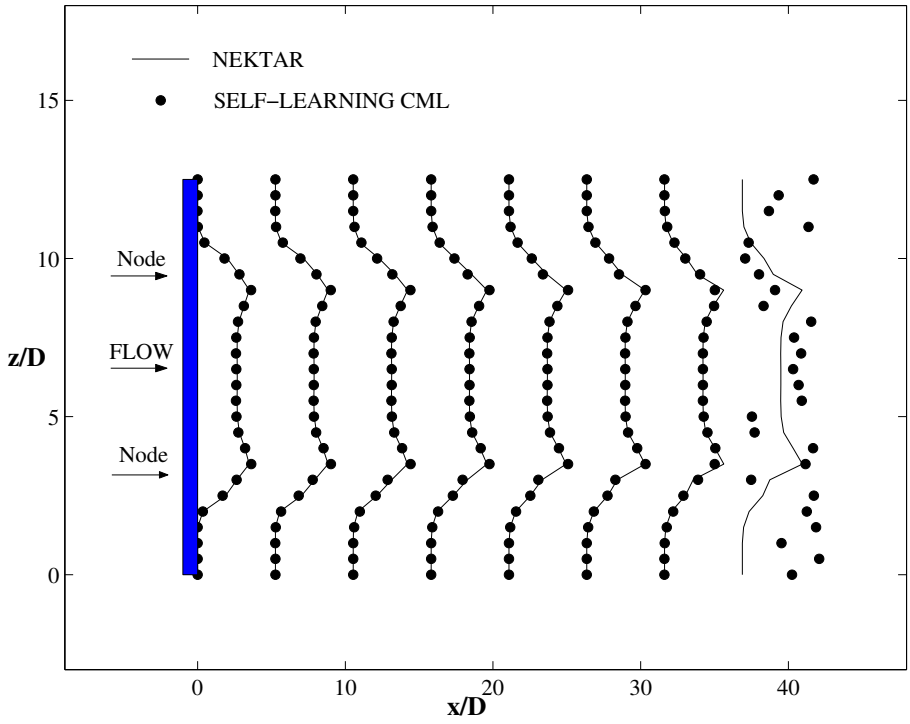

Figure 4.3: Estimation of first 8 shedding cycles showing wake patterns at $x/D = 0.5$ for lock-on case: $\Omega = 1.0$

The flow structures at $x/D = 3.0$ begin to show the transition from the near wake lace-like patterns to structures with decreased spanwise lengths. In Figure 4.5, we observe intermediate "M-like" patterns which are more difficult to estimate because of transient effects. The neural network estimation is very good for $n = 3, 4$, and the

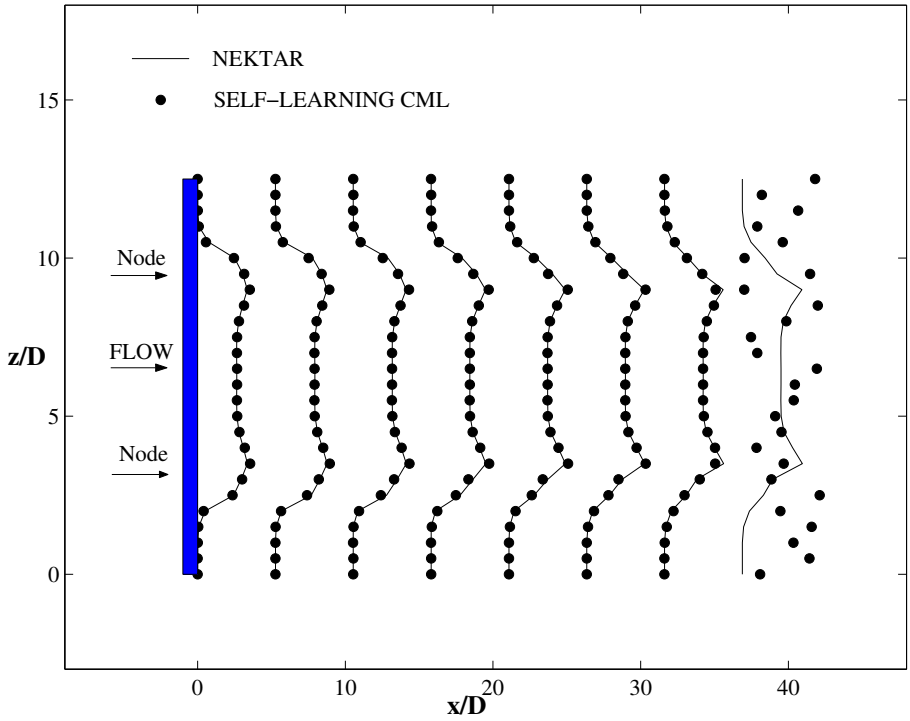

Figure 4.4: Estimation of first 8 shedding cycles showing wake patterns at $x/D = 1.0$ for lock-on case: $\Omega = 1.0$

local minima and maxima of the vortex cores are more accurately predicted by this scheme (Figure 4.5, 3.29). However, the MVLS algorithm based self-learning CML predicts the sixth and eighth patterns more accurately. We can say that the MVLS algorithm models transient wake effects more accurately than the neural network scheme. This observation is quite useful when we consider the application of these methods to target experimental wake flow patterns in Chapter 5.

Next, we consider an intermediate location, $x/D = 5.0$ to further consider modeling of complex transient and steady state vortex shedding patterns. In Figure 4.6, we observe a sudden change in the NEKTAR vortex shedding pattern from $n = 4$ to $n = 5$. These are vortex dislocations and are commonly observed in experiments. These are more difficult to estimate with the current neural network model. However, there are limited data provided to the neural network for the adaptive estimation to be highly accurate. If more such instances are provided for the neural network model, successful estimation of these dislocations is possible. Comparison of the estimated wake patterns from Figures 4.6, 3.30 shows that the neural network scheme is more

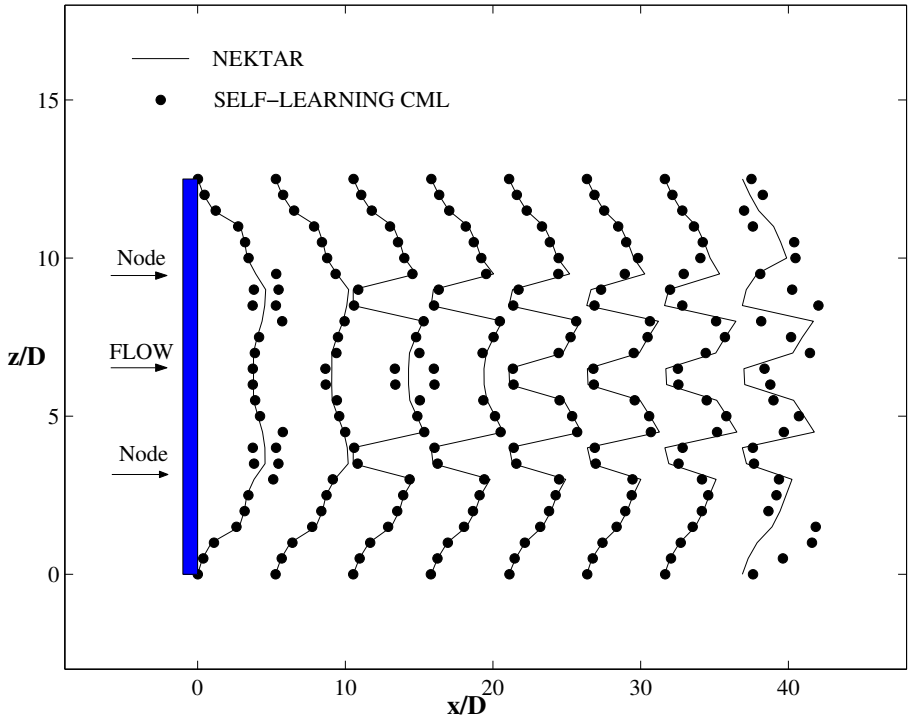

Figure 4.5: Estimation of first 8 shedding cycles showing wake patterns at $x/D = 3.0$ for lock-on case: $\Omega = 1.0$

efficient than the MVLS algorithm based self-learning CML.

We now consider the far wake location, $x/D = 10$, uniform flow, lock-on case, for estimation of the NEKTAR wake patterns using the neural network model (Figure 4.7). The NEKTAR wake patterns are highly complex with decreased spanwise lengths, rapidly changing spanwise lengths and also vortex dislocations. The neural network model quickly and successfully predicts the second and third wake patterns, and also gradually predicts the transition to a more uniform pattern with increased spanwise lengths. Once again, comparison of the estimated wake patterns from Figures 4.7, 3.31 shows that the neural network scheme is more efficient than the MVLS algorithm based self-learning CML.

In the next study, the cable is forced to oscillate at a frequency greater than the Strouhal frequency (quasi-periodic case) so that $\Omega = 0.9$. This interaction results in further degradation in the periodicity of the wake. Estimation of quasi-periodic or non-periodic wakes are important because such flow situations are often encountered in reality. The neural network scheme is used to estimate NEKTAR wake patterns

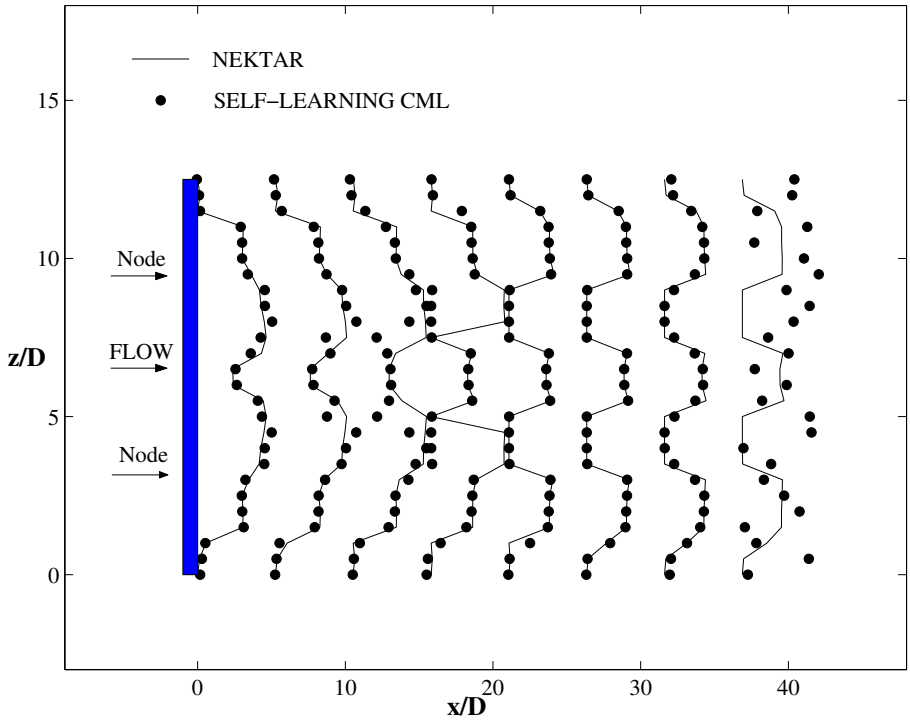

Figure 4.6: Estimation of first 8 shedding cycles showing wake patterns at $x/D = 5.0$ for lock-on case: $\Omega = 1.0$

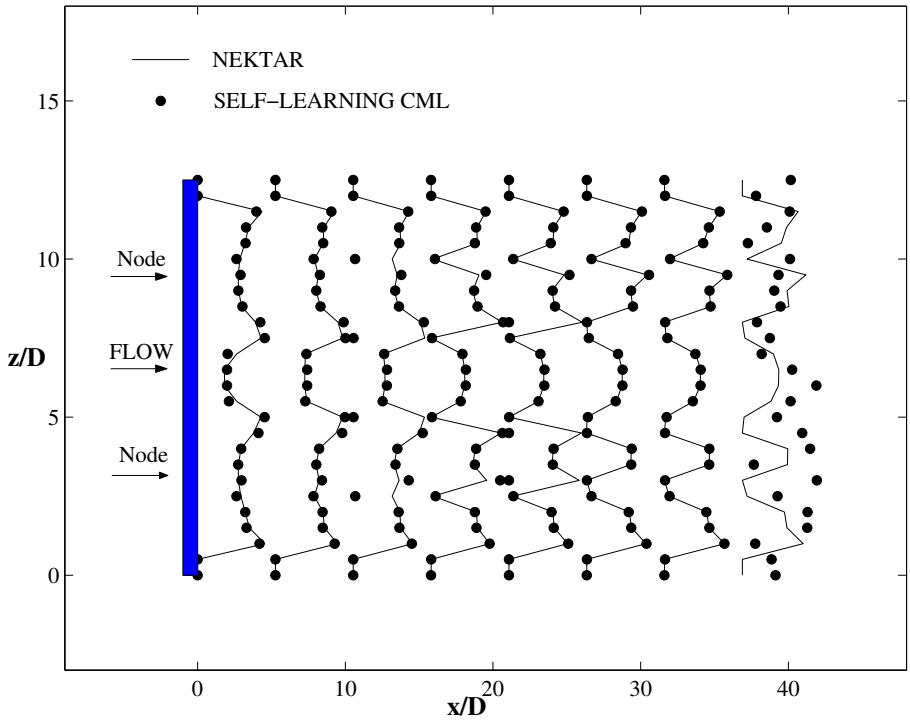

Figure 4.7: Estimation of first 8 shedding cycles showing wake patterns at $x/D = 10$ for lock-on case: $\Omega = 1.0$

(Figure 4.8) for this flow at $x/D = 5.0$ and accurate prediction is observed for $n = 4, 5$ and 7. Comparison of the estimated wake patterns from Figures 4.8, 3.32 shows that the neural network scheme is more accurate than the MVLS algorithm based self-learning CML.

Similar results are obtained for the shear flow case considered in Figures 4.9, 3.33. Oblique vortex shedding patterns are a common feature in the wake of a sheared freestream flow. The two self-learning CML models are quite capable of modeling these flow structures (see $n = 6, 7, 8$). We will also consider estimation of oblique shedding patterns from laboratory wake flows in Chapter 5.

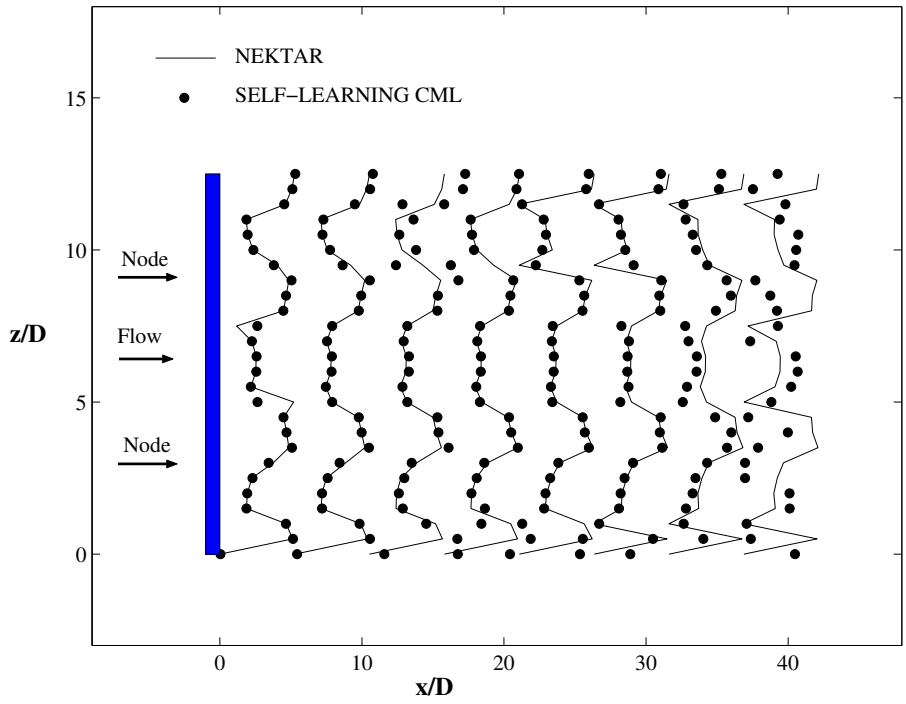

Figure 4.8: Estimation of first 8 shedding cycles showing wake patterns at $x/D = 5.0$ for quasi-periodic case: $\Omega = 0.9$

Estimation of vortex shedding phase angles

The vortex shedding phase angles are used to plot the target and estimated wake patterns considered previously. Only the first 8 wake patterns were shown for the purpose of clarity. In this section, we plot vortex shedding phase angles, $\mathrm{X}_n^k, \widehat{X}_n^k$, for 25 successive shedding cycles, corresponding to approximately 145 seconds of flow

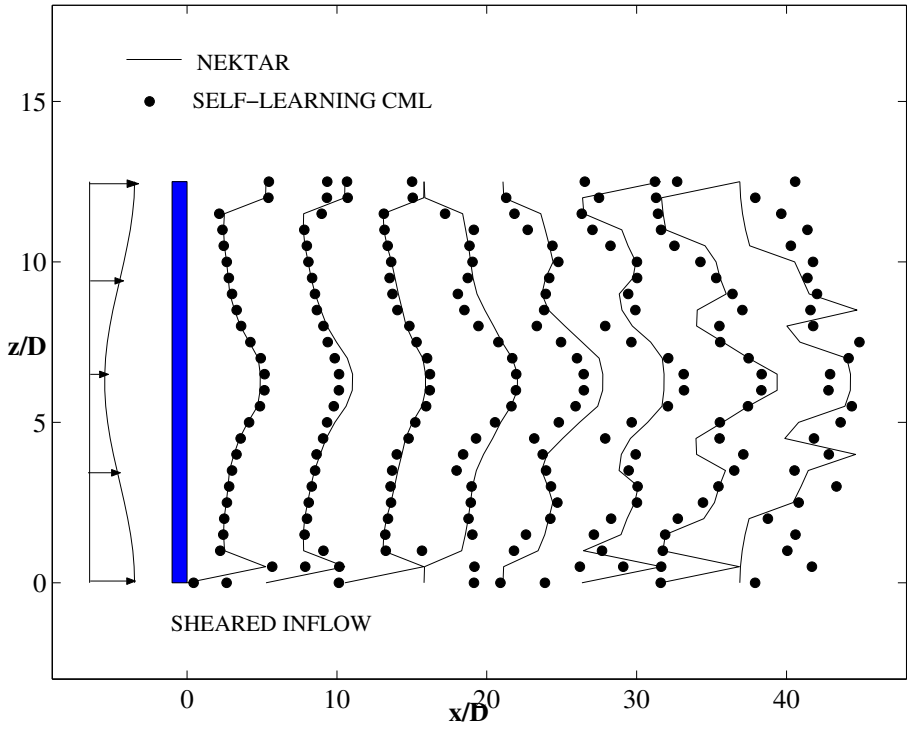

Figure 4.9: Estimation of first 8 shedding cycles showing wake patterns at $x/D = 5.0$ for shear flow, lock-on case: $Re_{max} = 100, Re_{min} = 75, \Omega_{max} = 1.0$

simulation. First we consider uniform freestream flow at $Re = 100$ over a cable (aspect ratio $= L/D = 4\pi$) oscillating at the lock-on frequency ($\Omega = 1.0$). The vortex shedding phase angles are highly periodic (Figures 4.10, 4.11) in the near wake ($x/D = 0.5, 1$) and are accurately estimated by the neural network based self-learning CML. Later, the accuracy of estimation is quantified using the state error, e_n^k. For all the 3 NEKTAR flow cases considered in this study, a random vortex shedding phase angle distribution, $\widehat{X}_1^k$, is used as an input to this scheme. The neural network based self-learning CML predicts the peaks near the nodes ($z/D = \pi, 3\pi$) more accurately than the MVLS algorithm based self-learning CML (Figures 3.34, 3.38). Transient wake effects are observed for further downstream locations, $x/D = 3, 5, 10$, and the degradation in the periodicity of the wake with increasing downstream distance is clearly observed. As a consequence, the vortex shedding phase angle distributions are highly complex with high transients and rapidly changing spanwise wavelengths (Figures 4.12 - 4.14). For the most part, the neural network based self-learning CML predicts these complex distributions and the predictions are comparable to those of

the MVLS algorithm based self-learning CML.

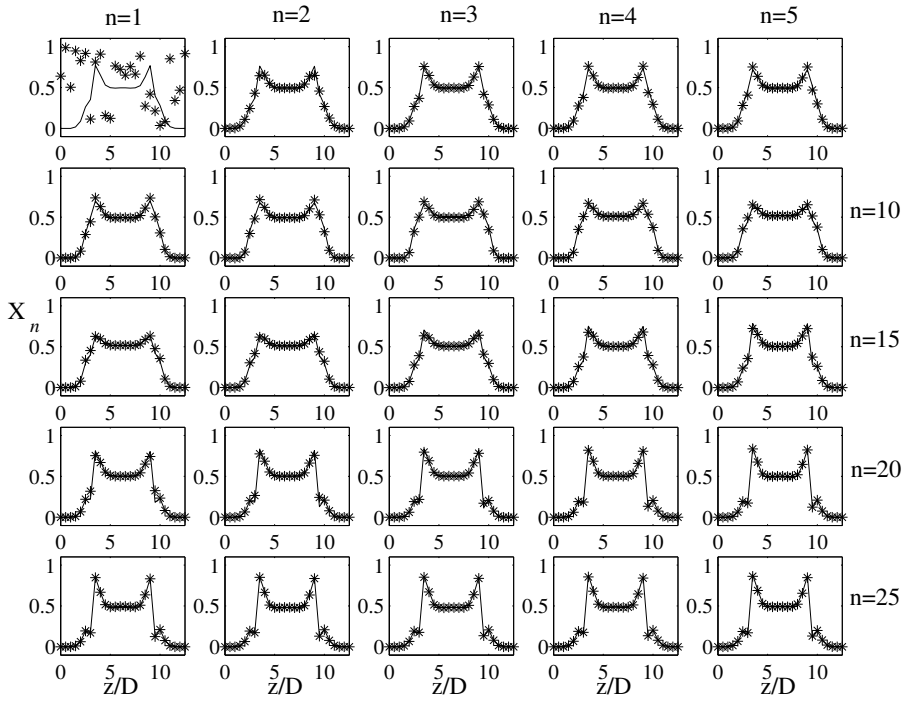

Figure 4.10: Temporal evolution of vortex shedding phase angles at $x/D = 0.5$ for uniform flow, lock-on case, $\Omega = 1.0$

We now consider the quasi-periodic wake for freestream $Re = 100$. The vortex shedding phase angles for this case are shown in Figure 4.15. The neural network prediction of these phase angles are highly accurate for $n \geq 13$. This model is also more efficient than the MVLS based self-learning CML in predicting these highly complex but somewhat periodic vortex shedding phase angle distributions (Figures 4.15, 3.39).

Finally, the case of sheared freestream flow at a lock-on situation ($\Omega_{max} = 1.0$) is considered. Once the transients die out, a bell shaped vortex shedding phase angle distribution is observed in the midspan. This distribution as well as the spikes at the cable ends are predicted by the neural network based self-learning CML more accurately than the MVLS algorithm based self-learning CML (Figures 4.16, 3.40).

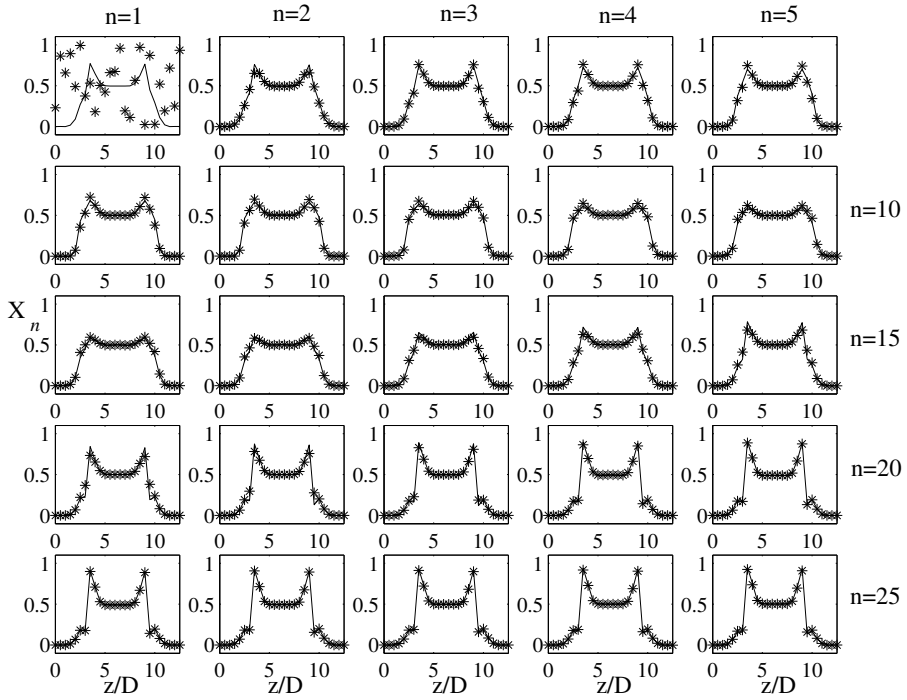

Figure 4.11: Temporal evolution of vortex shedding phase angles at $x/D = 1.0$ for uniform flow, lock-on case, $\Omega = 1.0$

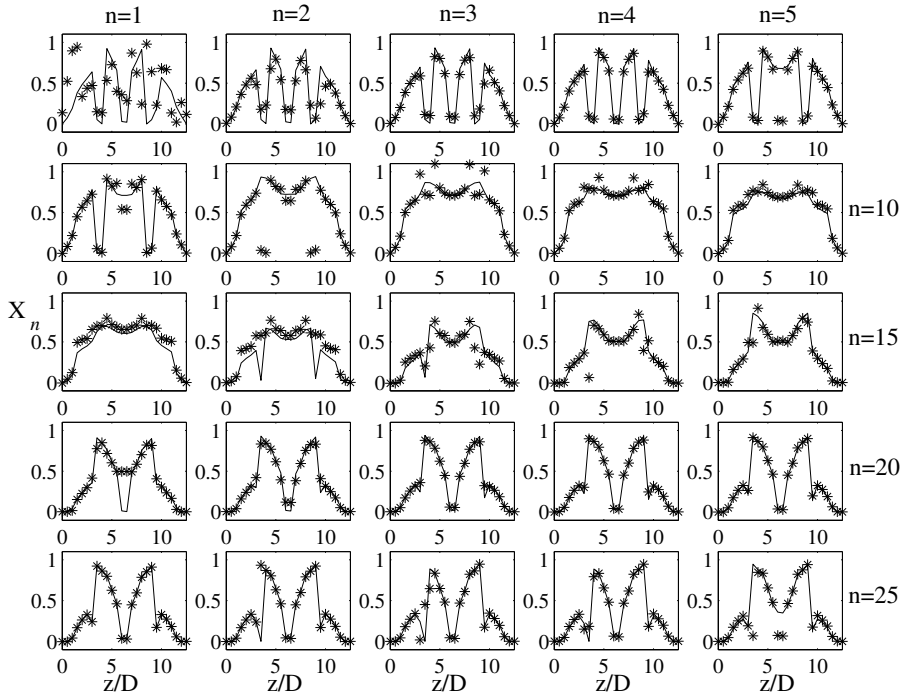

Figure 4.12: Temporal evolution of vortex shedding phase angles at $x/D = 3.0$ for uniform flow, lock-on case, $\Omega = 1.0$

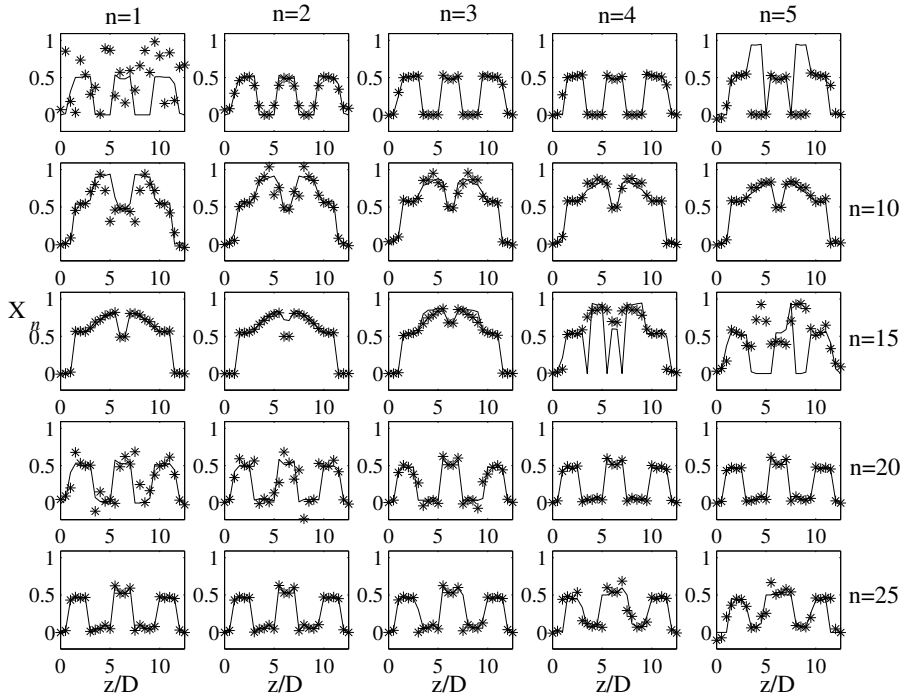

Figure 4.13: Temporal evolution of vortex shedding phase angles at $x/D = 5.0$ for uniform flow, lock-on case, $\Omega = 1.0$

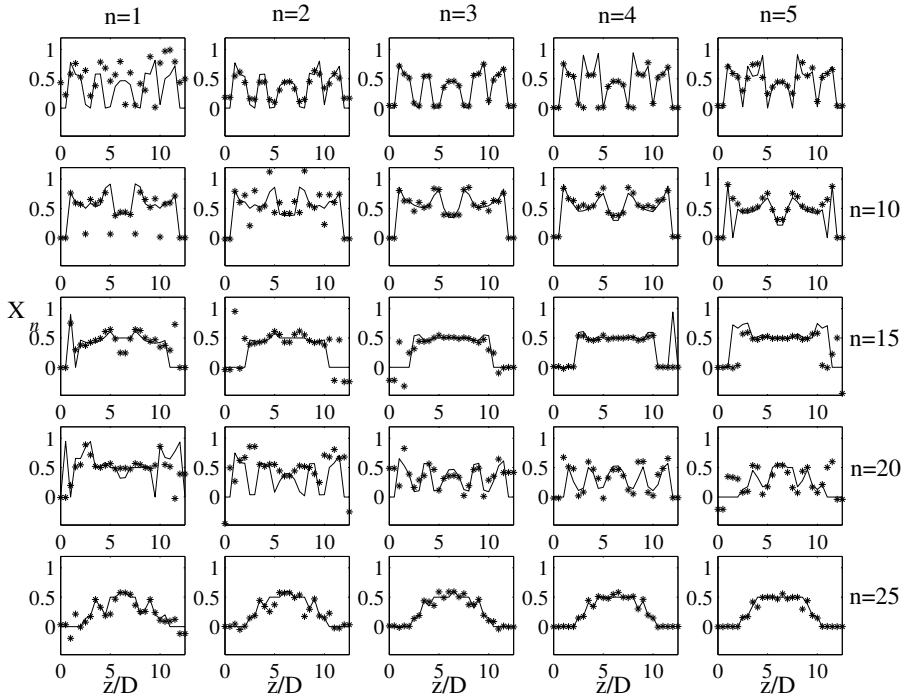

Figure 4.14: Temporal evolution of vortex shedding phase angles at $x/D = 10$ for uniform flow, lock-on case, $\Omega = 1.0$

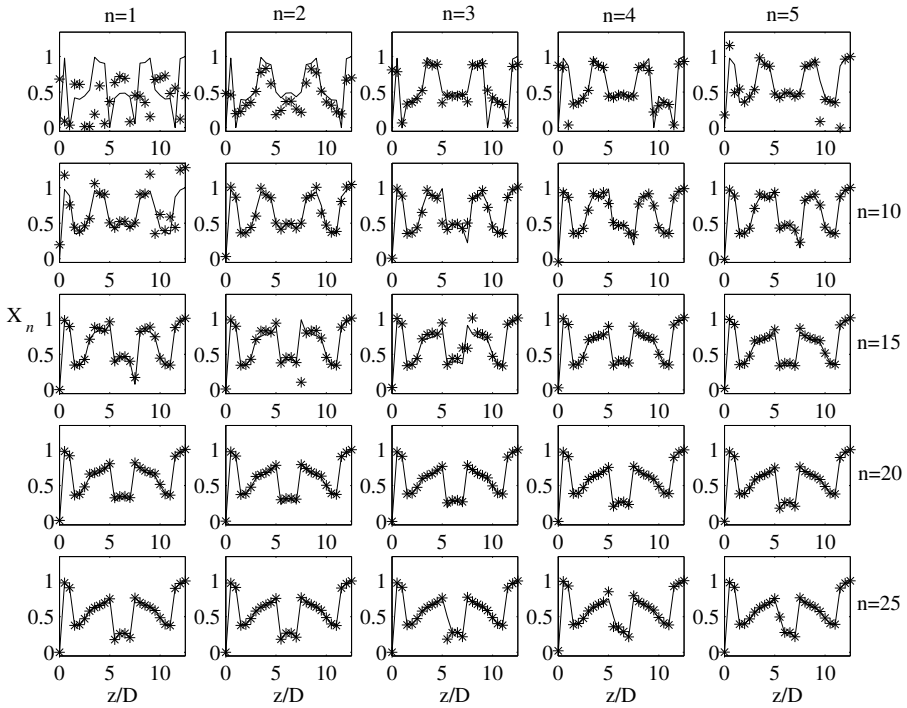

Figure 4.15: Temporal evolution of vortex shedding phase angles at $x/D = 5.0$ for uniform flow, quasi-periodic case, $\Omega = 0.9$

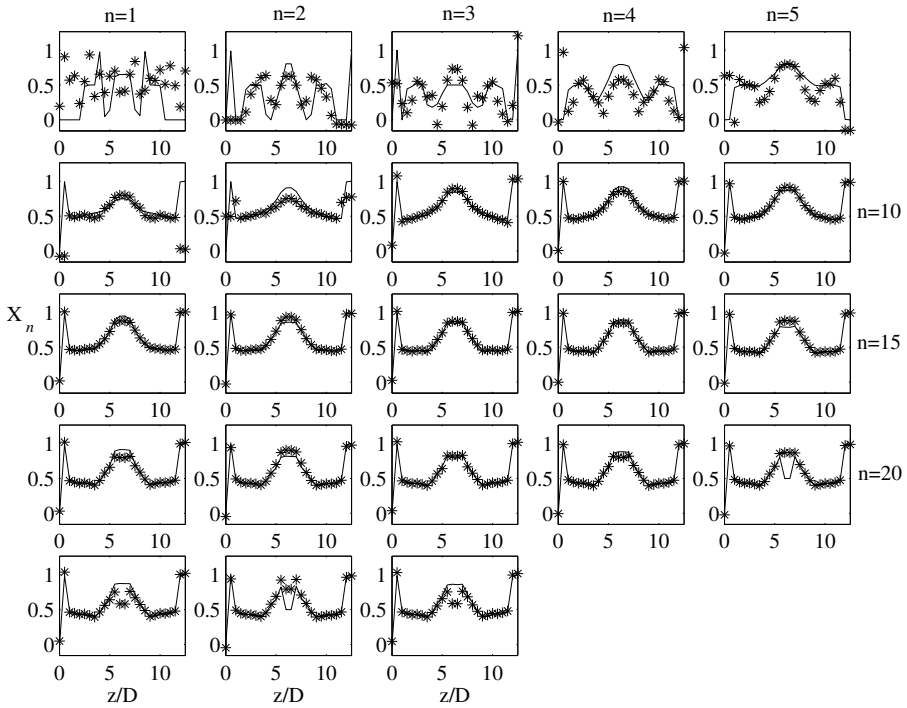

Figure 4.16: Temporal evolution of vortex shedding phase angles at $x/D = 10$ for shear flow, lock-on case, $Re_{max} = 100, Re_{min} = 75, \Omega_{max} = 1.0$

Spatio-temporal variation of state error

We will now quantify the efficiency of the neural network based self-learning CML using the state error. The downstream location $x/D = 5$ is common for all the three flow situations considered. We choose this x/D value to make comparisons in the efficiency of neural estimation for the different flows. For the uniform flow, lock-on case (Figure 4.17), deviations in wake patterns of the order of $O(0.1)$ are obtained. Some instances of high magnitudes of state error are also observed for $14 \leq n \leq 17$ coinciding with the formation of vortex dislocations. The steady state ($n > 17$) values of the state error are of the order of $O(0.01)$. For the uniform flow, quasi-periodic case, we saw a marked improvement in the prediction of the vortex shedding phase angle distributions. Correspondingly, the spatio-temporal variation of the state error in Figure 4.18 shows exponential decrease in values within a few shedding cycles. Some spikes in the magnitude of state error are observed for $n = 4, 5, 12$ at certain spanwise locations. These are believed to be due to vortex dislocations. Finally, for the shear flow, lock-on case, we observe relatively high values in magnitude of state error in the midspan region (Figure 4.19).

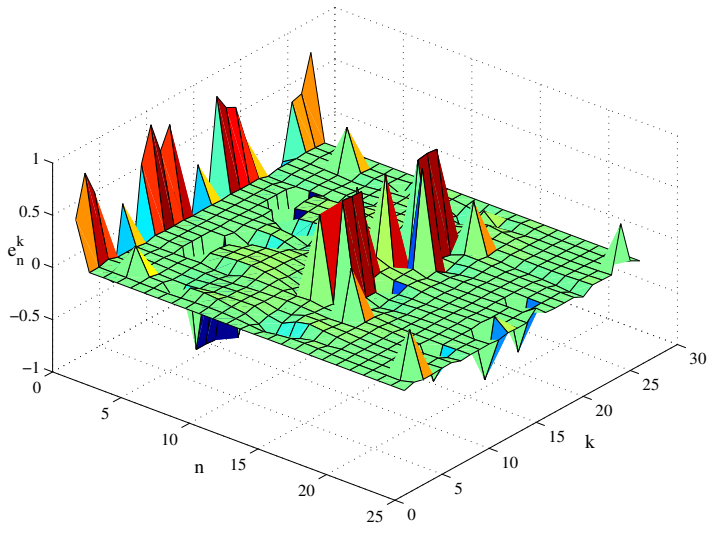

Figure 4.17: Local state error vs. spanwise location and time, for uniform flow, lock-on case, $x/D = 5$, $\Omega = 1.0$

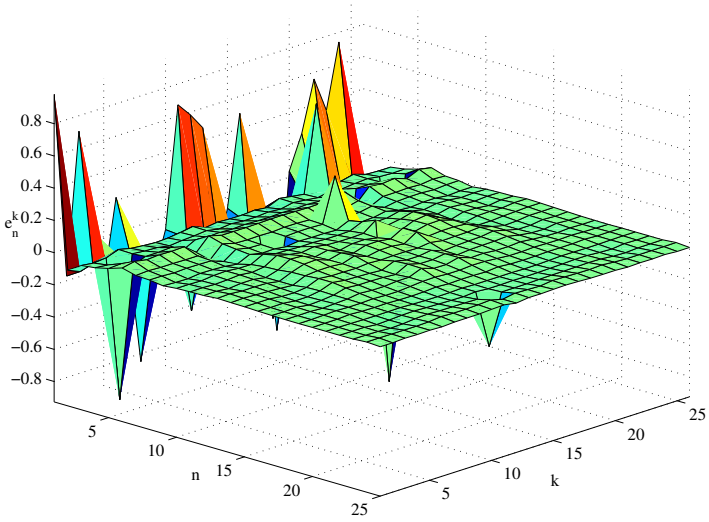

Figure 4.18: Local state error vs. spanwise location and time, for uniform flow, quasi-periodic case, $x/D = 5$, $\Omega = 0.9$

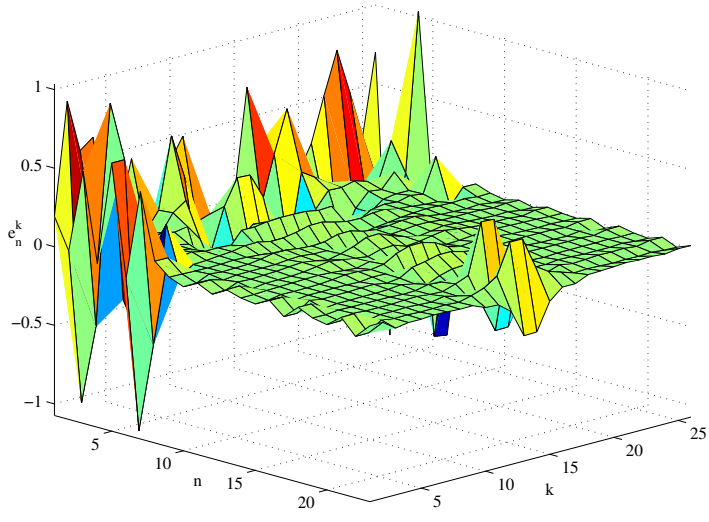

Figure 4.19: Local state error vs. spanwise location and time, for shear flow, lock-on case, $x/D = 5$, $\Omega = 1.0$

Temporal variation of RMS error

The root mean square (RMS) value of the state error, $\|e_n\|$, defined in (3.29), is used as another quantitative measure of estimation. The efficiency of the neural network based self-learning CML is summarized for all the cases in Figure 4.20. The steady state values of $\|e_n\|$ for the uniform flow, lock-on, near wake cases $x/D = 0.5, 1$, uniform flow, quasi-periodic case and the shear flow case are lower for the neural network based self-learning CML compared to the MVLS based self-learning CML (Figure 4.20). For the other cases, the estimation of the two self-learning CML models are comparable.

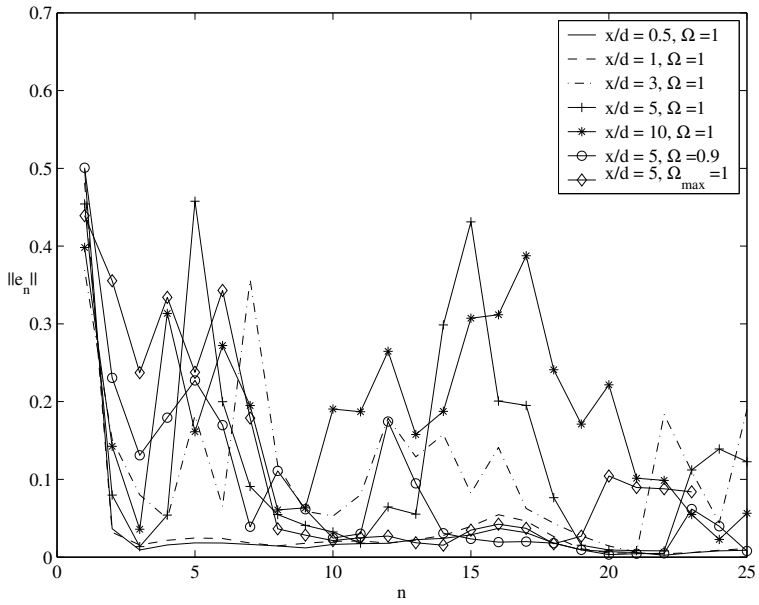

Figure 4.20: Time evolution of the root-mean-square of the state error, $\|e_n\|$, for the self-learning CML.

Chapter 5

Off-line estimation of laboratory wake flows

We have seen that the self-learning CML models based on the MVLS algorithm and on neural networks are quite successful in predicting NEKTAR wake patterns. The NEKTAR simulation study was a proof-of-concept type study to validate the application of the self-learning CML models to estimate wake flow patterns. Therefore, in this chapter we seek to logically extend these estimation techniques to different flow situations in a laboratory wind tunnel. Estimation of experimental wake flow patterns is a pre-requisite to the future goal of development of a low-order self-learning CML model for observer based feedback control of wake patterns. The current focus, however, is the study of various configurations that generate different types of target wake patterns. These target wake patterns are then used for off-line estimation using the self-learning CML models developed in Chapters 3 and 4.

In the off-line estimation technique, the model building exercise need not keep up with the information flow. In other words, parameters related to time such as sampling interval, characteristic times (time period of vortex shedding in our case) are not considered as speed of estimation is not important. This technique is opposed to the on-line estimation method where the computation of the model must be done in such a way that the processing of the measurements from one sample can,

with certainty, be completed during one sampling interval. Identification techniques that comply with the on-line requirement are called *recursive identification methods*, since the measured input-output data are processed recursively (sequentially) as they become available. The techniques developed in Chapters 3 and 4 are also recursive methods, but since the on-line computational requirements are not addressed, we have instead used the term, adaptive estimation method. Later, the results from off-line estimation of wake flow patterns will be used to study the feasibility of on-line estimation in future anticipated studies.

The cross power spectrum method of generation of target wake patterns discussed in Chapter 3 is applied to streamwise velocities measured in the wake. First, the experimental facilities are discussed. Then, the details of the experimental setup are provided. Finally the results of estimation of different target patterns using the self-learning CML models are discussed.

5.1 Experimental facilities and Instrumentation

The experiments were carried out in the WPI AEROLAB low turbulence, low speed, open circuit wind tunnel. A nine blade axial fan, powered by a 180 volt DC, at 9.5 Amps, variable speed motor (maximum of 1750 rpm), is used to create the flow field with airspeed ranges of 0 to 80 mph. The air flows through a 131 x 134 cm honey comb intake, with 0.7 cm cells, through a contraction ratio of 16:1 and into a test section with a cross sectional area of 12 x 12 inch of 45 inches length.

An array of eight hot-wire sensors was used in conjunction with an 8 channel constant temperature anemometry system IFA 300 from TSI. This system consists of a bridge and an amplifier circuit used to control the hot-wire sensors. The output of the IFA 300 system is an analog voltage proportional to fluid velocity. It is fed to an United Electronic Industries WIN30 Analog to Digital data acquisition card, which has a maximum data throughput rate of 1 MHz. The A/D card is inserted into a PC running MS Windows 2000. The TSI ThermalPro software, version 2.20 is used

for data acquisition. Communication between the acquisition software and the IFA cabinet is established using an RS-232C digital interface.

5.2 Experimental setup

An array of 8 TSI hot-wire probes, equally spaced along the spanwise direction were used for measuring the streamwise wake velocities. The experimental setup is shown in Figure 5.1. The probe supports were angled at 45 degrees in order to cause minimal obstruction to the flow. All the 8 probes were held at the same $x/D = 1.9, y/D = 1.22$ location. The uniform distance between adjacent probes was kept at $1\frac{1}{16}$ inches. The diameter of the cylinder was chosen as 0.125 inches. This resulted in freestream Reynolds numbers in the range of $Re = 100$, a range which is applicable for self-learning CML models.

We discuss estimation of 3 different flow structures. First, we estimate rigid-periodic patterns obtained in the wake of a rigid cylinder. Second, we estimate oblique shedding patterns in the wake of a rigid cylinder with endplates. Two discs, each of diameter 2.5 inches with a 0.125 inch hole for the cylinder, were placed close to the tunnel walls. The angle of the discs was suitably varied to obtain the oblique shedding patterns. Third, we estimate a mix of the rigid-periodic and oblique shedding wake patterns in the near wake of a cylinder with end discs.

5.3 Results: Rigid-periodic case

In the first experiment, we consider estimation of periodic patterns in the wake of a rigid stationary cylinder in uniform freestream flow with velocity, $U_\infty = 0.75\, m/s$. Taking the kinematic viscosity for air at a temperature of $20^\circ\, C$, $\nu = 14.9 \times 10^{-6}\, m^2/s$, resulted in $Re = 160$, which is in the laminar vortex shedding range. Once the freestream flow was stabilized, the wake velocity traces were recorded for 1.6384 seconds at a sampling rate 10,000 Hz (sampling period of 0.0001 seconds), see Fig-

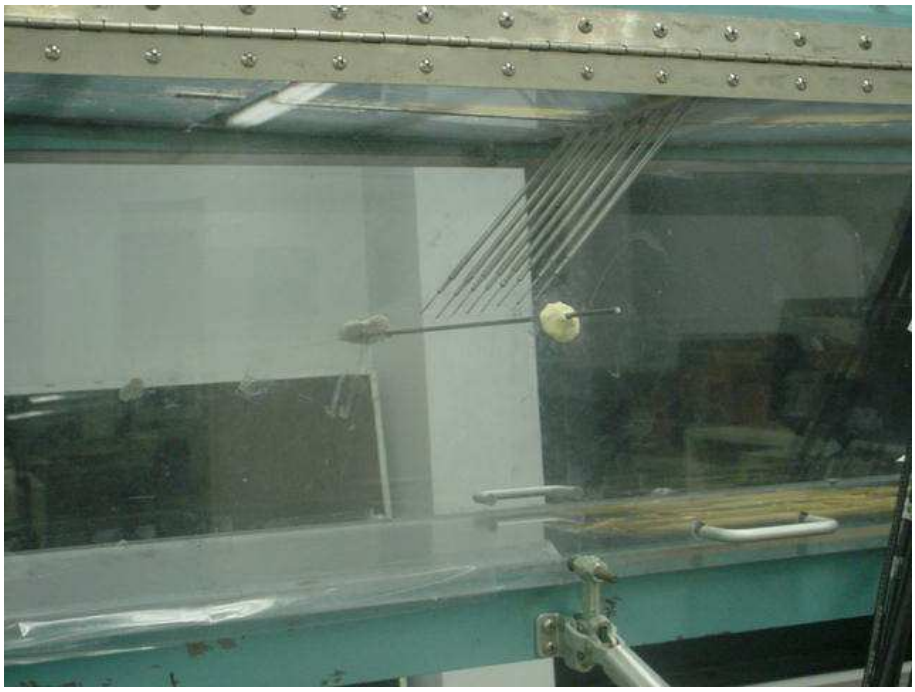

Figure 5.1: Diagram of the experimental setup for velocity measurement.

ure 5.2. The hot-wire signals are mostly periodic, with occasional vortex dislocations (see for example, the fifth and sixth shedding cycles for the third probe, $z/D = 31$). Abrupt changes in amplitude of the local wake velocities are observed at $z/D = 31$ and $z/D = 73.5$ respectively. These features are suggestive of vortex dislocations in the wake. We will attempt to identify these dislocations in observed wake patterns. Power spectra for these velocity traces are shown in Figure 5.3. Peaks in the velocity spectrum are detected at the local shedding frequencies, ranging from 44 Hz to 46 Hz. This resulted in a Strouhal number, $St = f_{so}D/U_\infty = 0.184$, based on the data from the first probe. We use the first probe as reference for the extraction of vortex shedding phase angles from cross-power spectrum as discussed previously for analysis of NEKTAR data.

5.3.1 Self-learning CML based on MVLS algorithm

In this section, we study the effectiveness of the MVLS algorithm based self-learning CML in estimating periodic patterns from laboratory cylinder wake flows. We will first discuss the input parameters used for the estimation model ((3.1), (3.6), (3.10)).

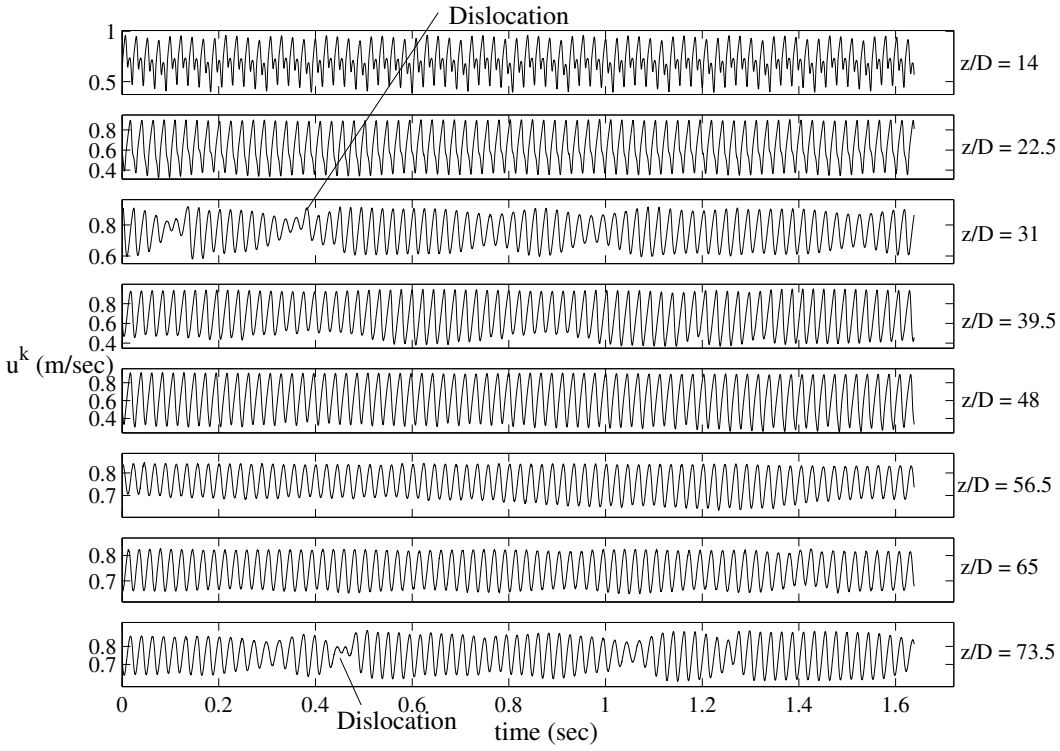

Figure 5.2: Streamwise wake velocity measured using the hot-wire probes.

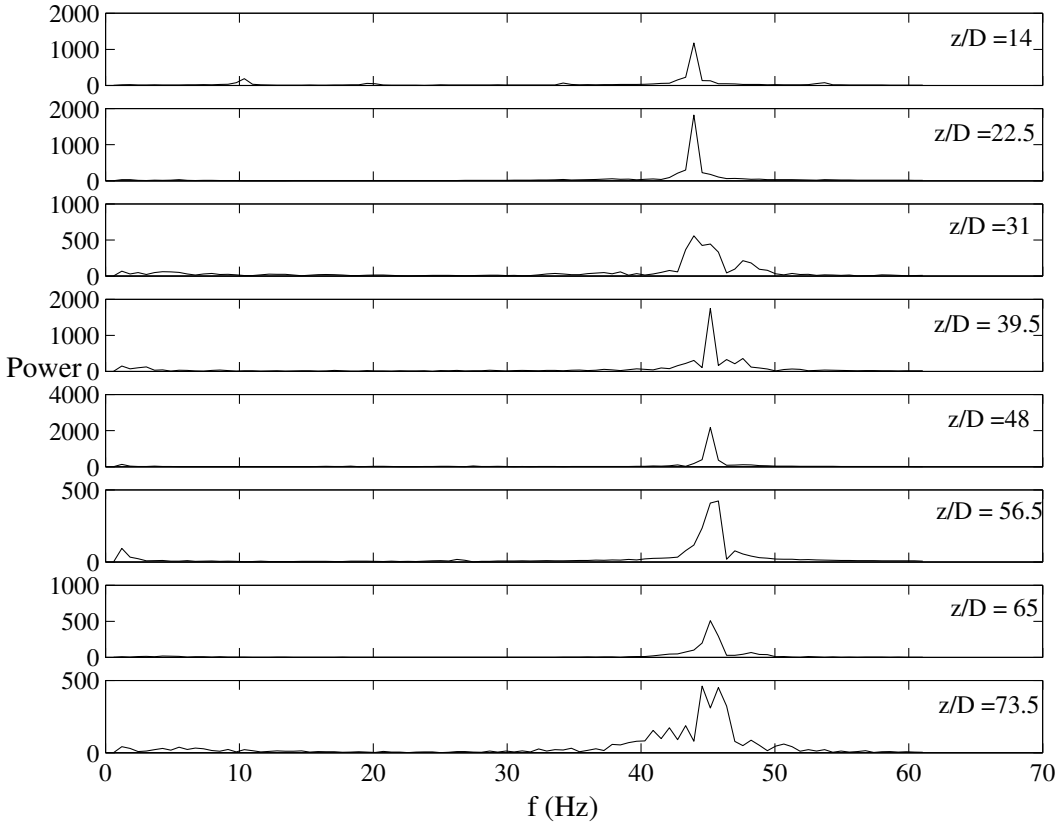

Figure 5.3: Absolute value of the velocity spectrum.

The input weighting matrices, $\mathbf{P}_0$ and $\mathbf{R}$ are diagonal matrices with constant entries P_0 and R respectively. As stated previously, the relevant parameter in the estimation study, P_0/R, was optimized at 0.001. A random initial guess, with random entries from a uniform distribution in the interval $(0.0, 1.0)$, was used for the vortex shedding phase angle, $\widehat{X}_k^1$. The initial guess for the spanwise velocity distribution was uniformly set to zero. In Figure 5.4, we show estimation of wake patterns for $31 \leq n \leq 38$. The periodic wake patterns are estimated with very high accuracy using the MVLS algorithm. The vortex cores in the mid-span are estimated with good accuracy for many shedding cycles. Any deviations from the state, X_n^2, are reduced subsequently using the algorithm. The vortex shedding phase angles, X_n^k, $\widehat{X}_n^k$, used to plot the target and estimated wake patterns, are shown in Figure 5.5. The spatio-temporal evolution of the vortex shedding phase angles, X_n^k, is highly complex. There is no sustained periodicity in the phase angle distribution for $n \leq 23$. The evolution of these transient states is highly complex. However, the MVLS algorithm proves to be highly efficient in estimating these transient states. There are some local errors in estimation, ($n = 5, 6, z/D = 27$ and $n = 47, z/D = 83$), coinciding with formation of vortex dislocations. However, these local errors are subsequently reduced with adaptation.

The state error is used to quantify the accuracy of the estimation. The spatio-temporal evolution of the state error shown in Figure 5.6 provides a quantitative summary of the estimation procedure. We can see spikes in the local state error in the initial stages of estimation, $n = 5$, 6, 16 to 24. However, they quickly settle down values in the range of $(-0.1, 0.1)$. We believe that the large initial values of the state error are due to transient effects. After an interval of periodic patterns, $25 \leq n \leq 40$, efficiently estimated by the MVLS algorithm, further transient effects are seen. However, with progress in the adaptation, these effects are accurately captured. This results in low values of the state error.

We next compare the initial state error, e_1^k, with the state error for n=10, e_{10}^k in Figure 5.7. The initial state error is large because of the random initial guess for the

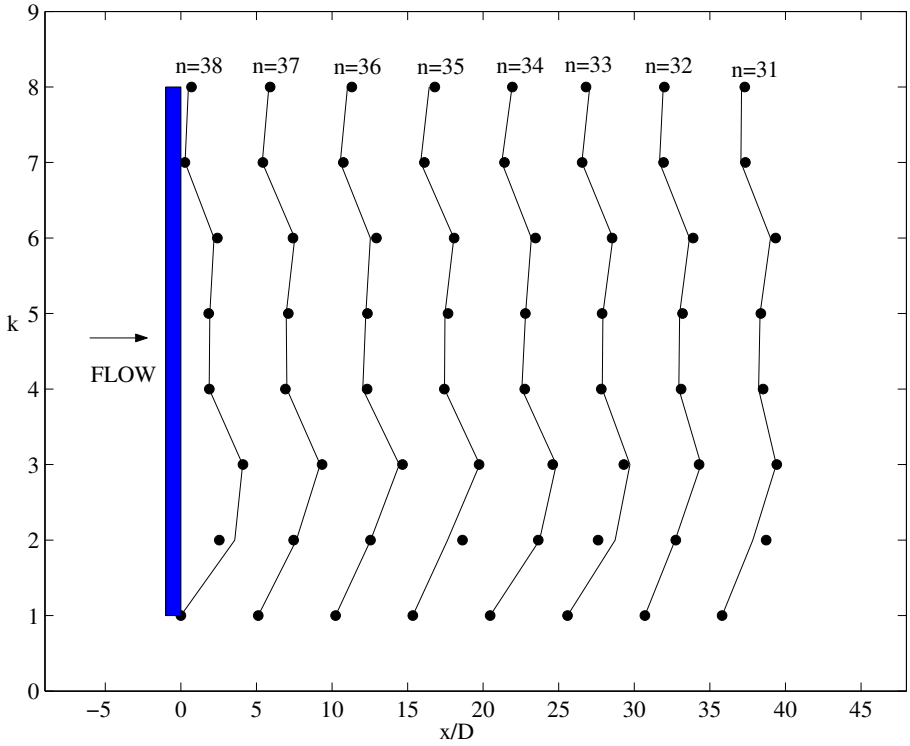

Figure 5.4: MVLS algorithm based estimation of experimental wake patterns for uniform flow over rigid cylinder, $x/D = 1.9, y/D = 1.2, \Omega = 1.0, K_o = 0.0$

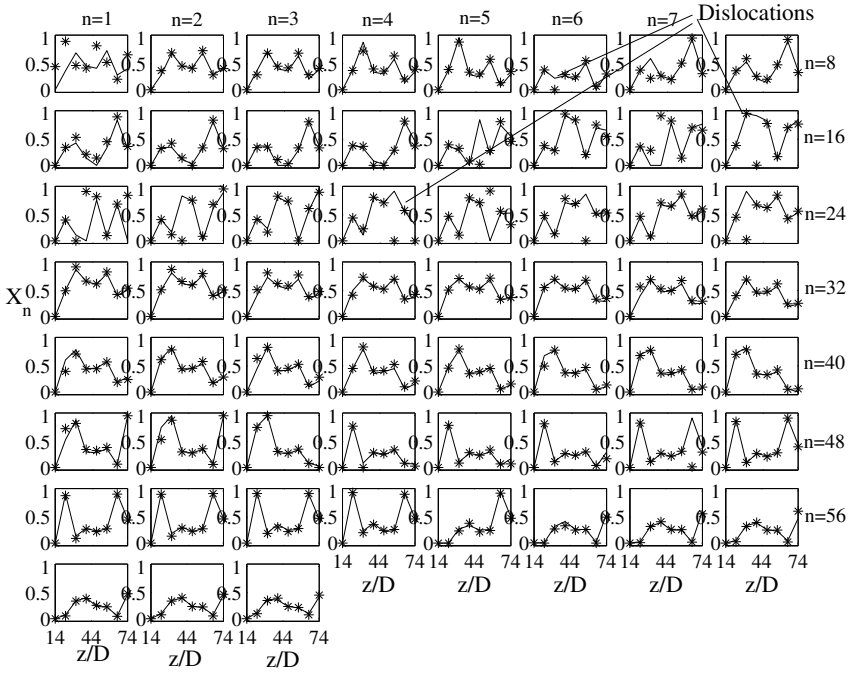

Figure 5.5: Temporal evolution of vortex shedding phase angles for uniform flow over rigid cylinder, $x/D = 1.9, y/D = 1.2, \Omega = 1.0, K_o = 0.0$

self-learning CML. In comparison, low values of e_{10}^k, in the range of $(-0.1, 0.1)$ are obtained.

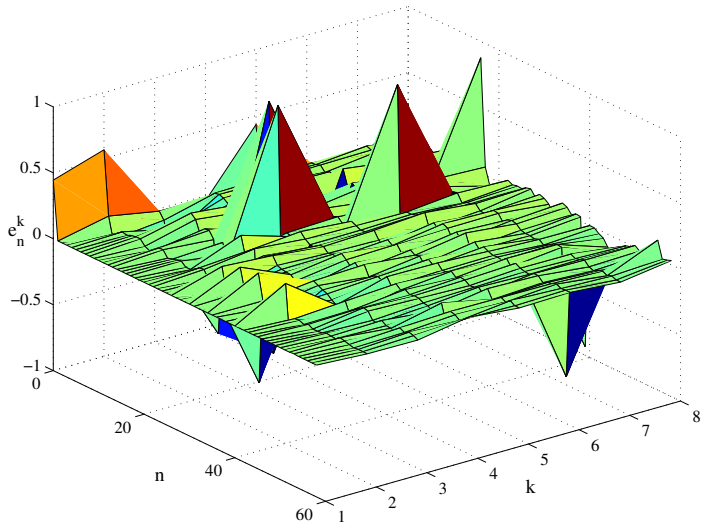

Figure 5.6: 3-d plot of state error, $x/D = 1.9, y/D = 1.2, \Omega = 1.0, K_o = 0.0$

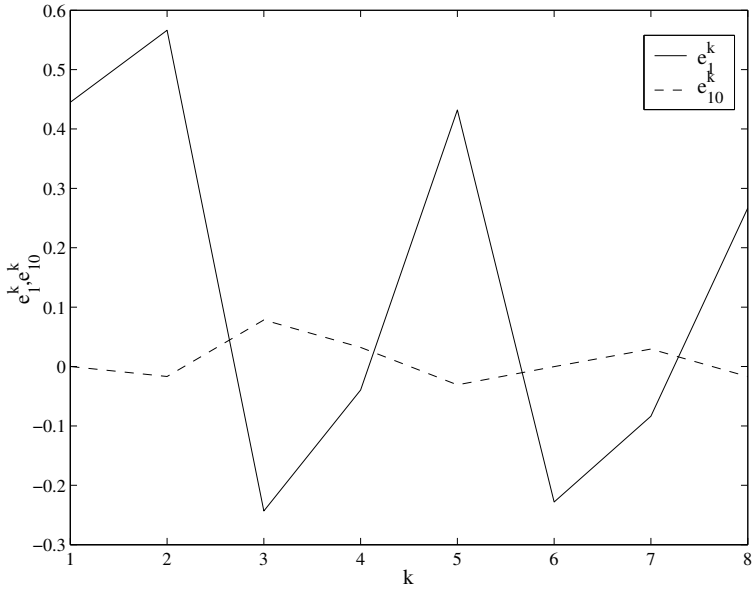

Figure 5.7: Temporal variation of state error, $x/D = 1.9, y/D = 1.2, \Omega = 1.0, K_o = 0.0$

5.3.2 Self-learning CML based on Neural Networks

We will now use the neural network based self-learning CML model developed in Chapter 4 to estimate periodic patterns from experimental cylinder wake flows. In

this manner we can compare the efficiencies of the two self-learning CML models.

The input parameters for the neural network based estimation are first summarized. Radial basis functions are used to represent the neural networks as they were quite successful in the proof-of-concept study in Chapter 4. Nine radial basis functions (i.e. $p = 9$) were found to be optimal for this study. The acceleration parameter, γ_0, was varied in its stable range of 0 to 2 and an optimal value of $\gamma_0 = 1.5$ was obtained. The parameter β_0 was set to 0.001. Zero initial conditions were used for the vortex shedding phase angle distribution, $\widehat{X}_1^k$, and the distribution of neural network weights, $\widehat{Q}_1^k$. The input parameters derived from the wake flow, such as the Re, St etc. remain unaltered for this comparative study.

The estimation of rigid-periodic wake patterns, $31 \leq n \leq 38$, is first shown in Figure 5.8. It is observed that the neural network model is highly efficient in predicting these patterns. However, comparison with Figure 5.4 reveals no significant differences in the efficiency of estimation of the two self-learning CML models.

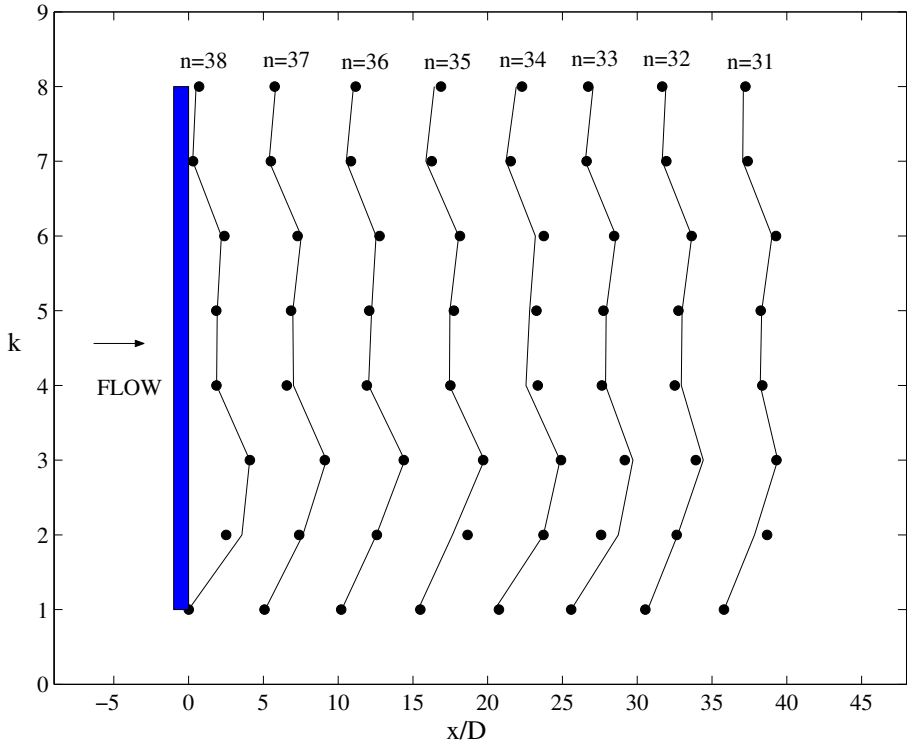

Figure 5.8: Neural Networks based estimation of experimental wake patterns for uniform flow over rigid cylinder, $x/D = 1.9, y/D = 1.2, \Omega = 1.0, K_o = 0.0$

A summary of the estimation of vortex shedding phase angles is shown in Figure 5.9. Most of the initial transient states, $1 \leq n \leq 8$, are accurately estimated. Then the wake becomes highly complex in the range $9 \leq n \leq 24$, due to the formation of vortex dislocations. These states are not predicted accurately by the neural network model. However, in the range $25 \leq n \leq 40$, the wake becomes organized and rigid-periodic patterns are accurately predicted by the neural network based self-learning CML. This range is followed by a second sequence of complex states. The neural network model is found to be more efficient in estimating the second sequence of transients in the range $49 \leq n \leq 58$. In summary, the MVLS algorithm based self-learning CML is found to be better at predicting the wake patterns considered.

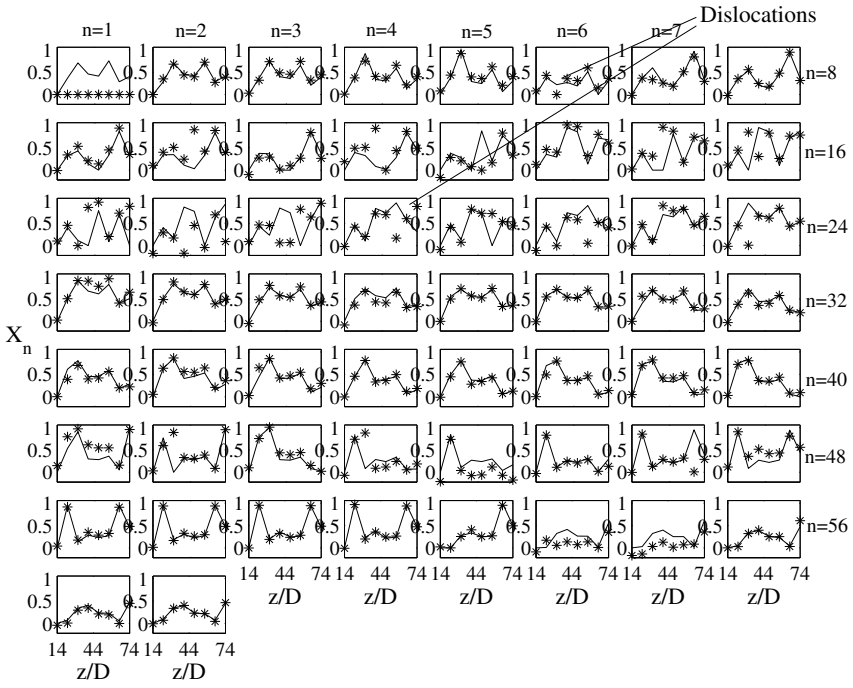

Figure 5.9: Temporal evolution of vortex shedding phase angles for uniform flow over rigid cylinder, $x/D = 1.9, y/D = 1.2, \Omega = 1.0, K_o = 0.0$

A three-dimensional plot of the state error for the neural network estimation is shown in Figure 5.10. As discussed above, large local errors ($|e_n^k| \approx 0.2$) are occasionally obtained in the non-periodic range. However, the neural network adaptation ensures that these errors do not grow unbounded. Although the neural network based self-learning CML is proven to be a stable adaptive estimation scheme, the occurrence

of transient states ensures that the state errors do not converge exponentially to zero. In Figure 5.11 we show that the state error after long time adaptation, say e^k_{50}, is negligible compared to the large initial error.

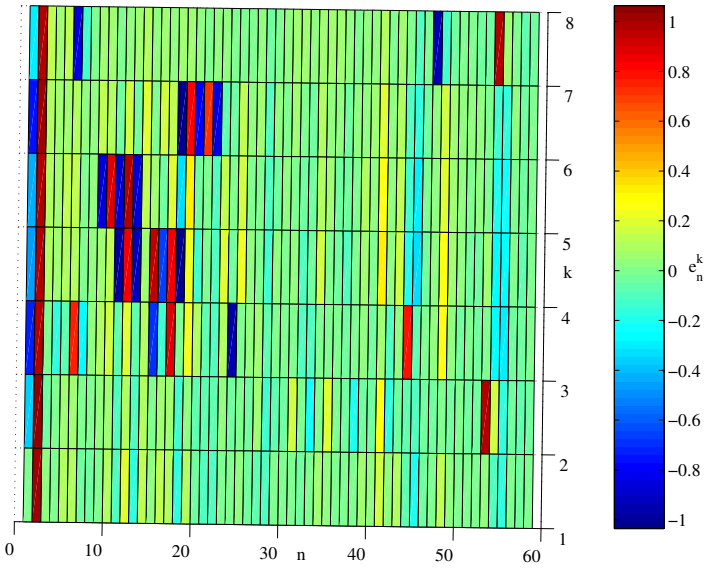

Figure 5.10: 3-d plot of state error, $x/D = 1.9, y/D = 1.2, \Omega = 1.0, K_o = 0.0$

5.4 Results: Oblique shedding

We will now discuss the estimation of oblique shedding patterns in the wake of a rigid stationary cylinder fixed with endplates. Two end discs, each of 2.5 cm diameter, were placed at the ends of the cylinder, close to the tunnel walls. The discs were angled at 14 degrees with respect to the cylinder axis as shown in Figure 5.14. A uniform freestream velocity, $U_\infty = 0.77\, m/sec$ was used for this experiment, resulting in $Re = 162$. The streamwise wake velocities measured by the 8 hot-wire probes are shown in Figure 5.22. The velocity spectrum in Figure 5.13 shows sharper peaks from the rigid-periodic case. The shedding frequency ($f_s = 44.5Hz$) and hence the Strouhal number ($St = 0.184$) are constant throughout the span. The measured velocities are highly periodic and as we will see later, spanwise differences occur only in the form a phase shift resulting in oblique shedding patterns in this case.

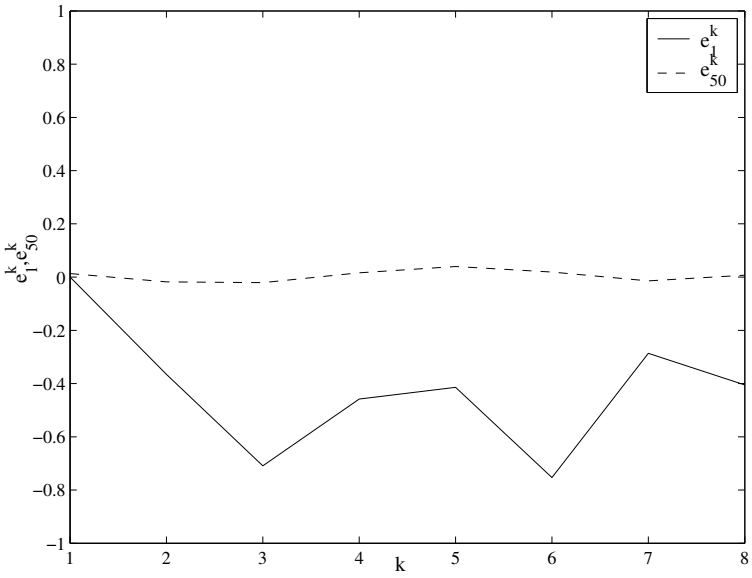

Figure 5.11: Temporal variation of state error, $x/D = 1.9, y/D = 1.2, \Omega = 1.0, K_o = 0.0$

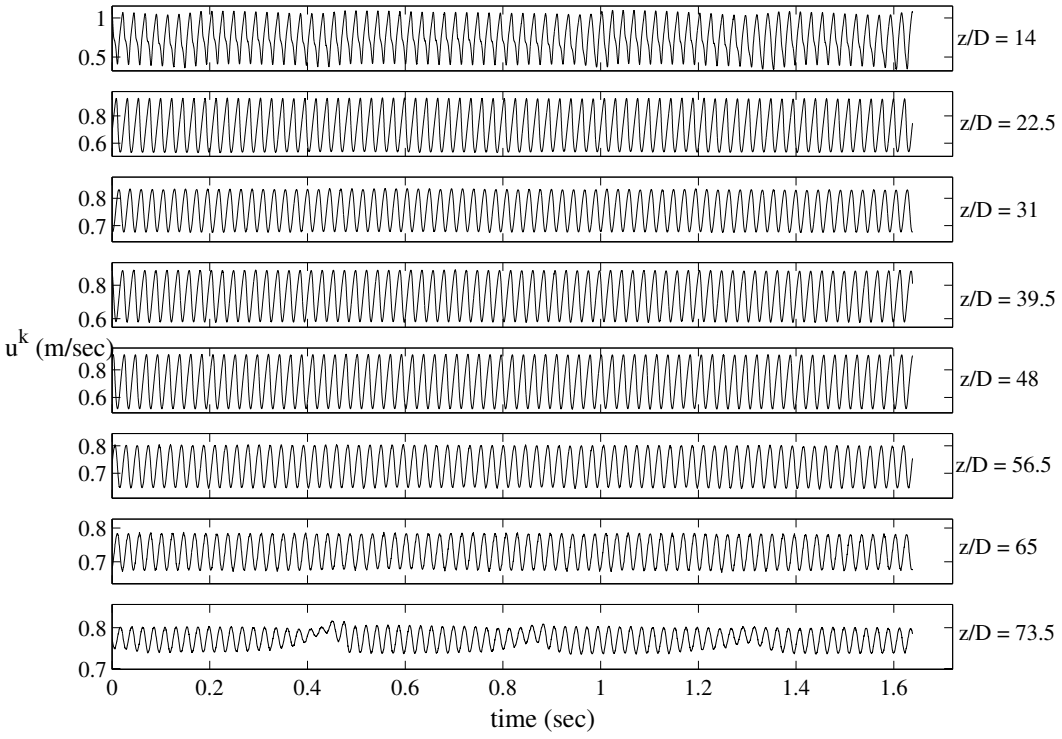

Figure 5.12: Streamwise wake velocity measured using the hot-wire probes.

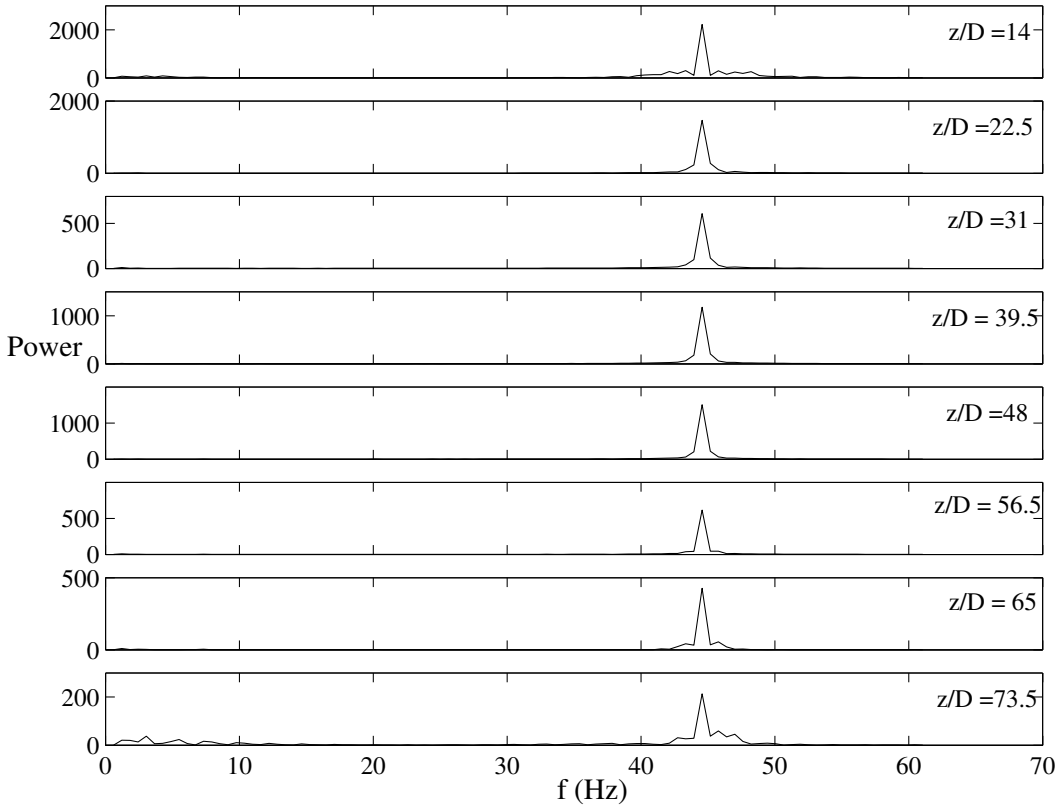

Figure 5.13: Absolute value of the velocity spectrum.

5.4.1 Self-learning CML based on MVLS algorithm

The optimal input parameters for the MLVS algorithm based self-learning CML model remain unchanged from the previous experiment. We use wake patterns 31 to 38 to illustrate the progress of estimation in Figure 5.14. One can clearly see wake patterns shed at an oblique angle with respect to a line drawn parallel to the cylinder axis. Since these patterns are highly periodic, we find that the estimation is highly efficient. The target and estimated vortex shedding phase angles, X_n^k and $\widehat{X}_n^k$, plotted in Figure 5.15 are almost identical. Therefore, the three-dimensional plot of the state error in Figure 5.16 is highly flat with very minimal deviations from the origin. The state error after 10 shedding cycles, e_{10}^k in Figure 5.17 is of the order of 10^{-2}.

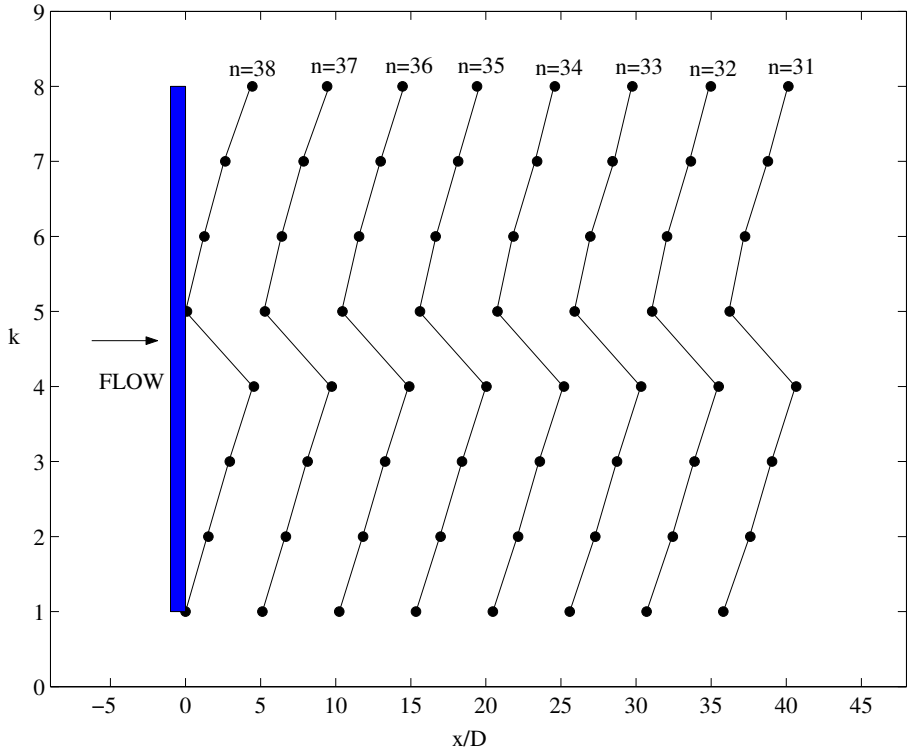

Figure 5.14: MVLS algorithm based estimation of experimental wake patterns for uniform flow over rigid cylinder, $x/D = 1.9, y/D = 1.2, \Omega = 1.0, K_o = 0.0$

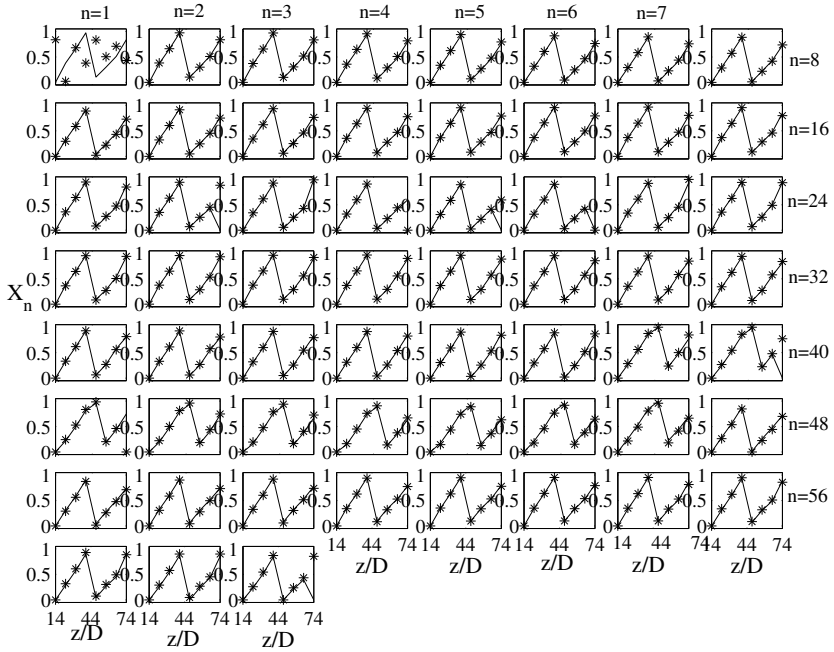

Figure 5.15: Temporal evolution of vortex shedding phase angles for uniform flow over rigid cylinder, $x/D = 1.9, y/D = 1.2, \Omega = 1.0, K_o = 0.0$

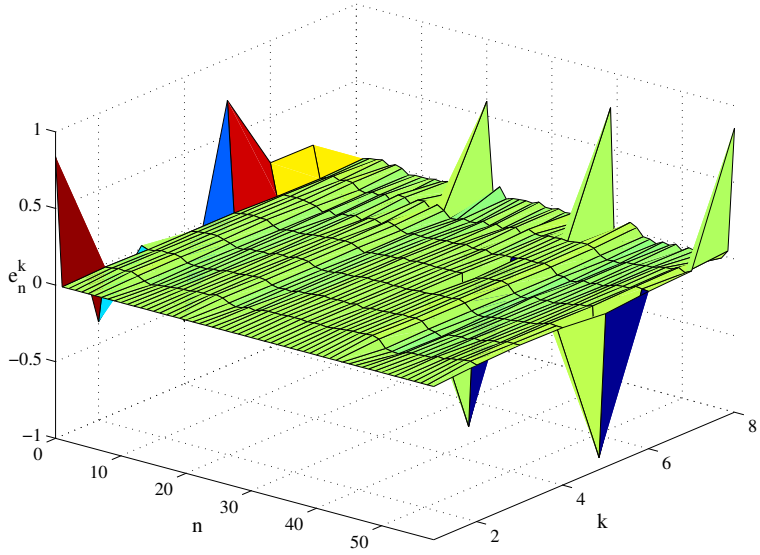

Figure 5.16: 3-d plot of state error, $x/D = 1.9, y/D = 1.2, \Omega = 1.0, K_o = 0.0$

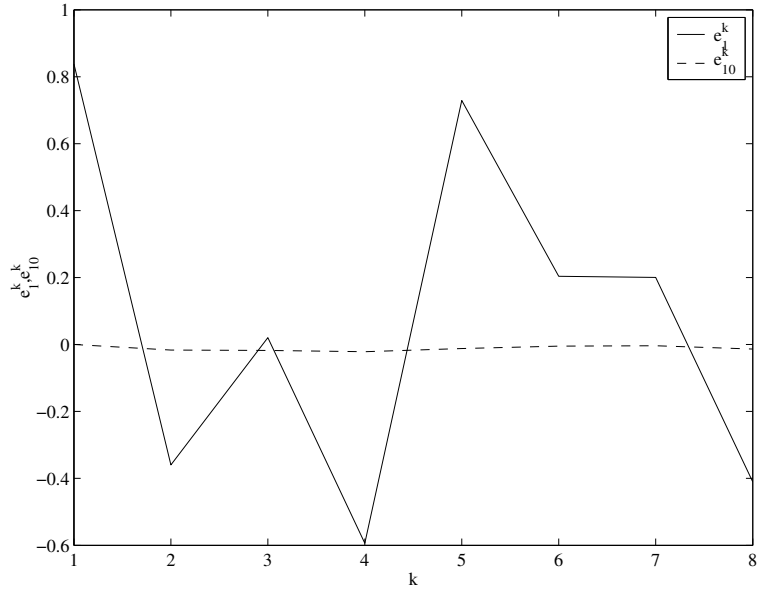

Figure 5.17: Temporal variation of state error, $x/D = 1.9, y/D = 1.2, \Omega = 1.0, K_o = 0.0$

5.4.2 Self-learning CML based on Neural Networks

The neural network based self-learning CML is now used to estimate the oblique shedding patterns. The acceleration parameter is found to be optimal at $\gamma_0 = 1.9$. All the other input parameters and the type of neural network used remain unchanged from the previous section. Observation of wake patterns in Figure 5.18 shows that the neural network based self-learning CML is also highly efficient in predicting oblique shedding patterns. Since the vortex shedding phase angles differ from the wake patterns only by a streamwise linear transformation, the efficiency of estimation is equally reflected in the plot of vortex shedding phase angles in Figure 5.19. The three-dimensional plot of state error in Figure 5.20 shows exponential convergence to zero starting from a high value. The magnitude of state error is higher when compared with the MVLS algorithm based estimation. The state error after 10 shedding cycles, e_{10}^k in Figure 5.21 is of the order of 10^{-2}. In summary, both the self-learning CML models are highly efficient in predicting oblique shedding patterns from wake experiments.

5.5 Results: Mixed type

In the third experiment the flow conditions and the orientation of the endplates are unaltered. However, the position of the endplates along the axis of the cylinder was altered from the second experiment by a distance of approximately $8D$. This resulted in wake patterns that are classified here as a mix of the rigid-periodic and oblique shedding patterns discussed previously. The freestream velocity $U_\infty = 0.76\, m/sec$ giving rise to $Re = 160$. The streamwise wake velocities plotted in Figure 5.22 are highly periodic. Vortex dislocations are identified from the eighth wake velocity trace, between $t = 0.6 sec$ and $t = 0.8\, sec$. Power spectra for the velocity traces are shown in Figure 5.23. Since the Reynolds number for all the experiments (≈ 160) are almost the same, the Strouhal frequencies, $f_{so} = 44\, Hz$, observed in Figure 5.23 are also nearly the same as observed in the first two experiments. However, the position of

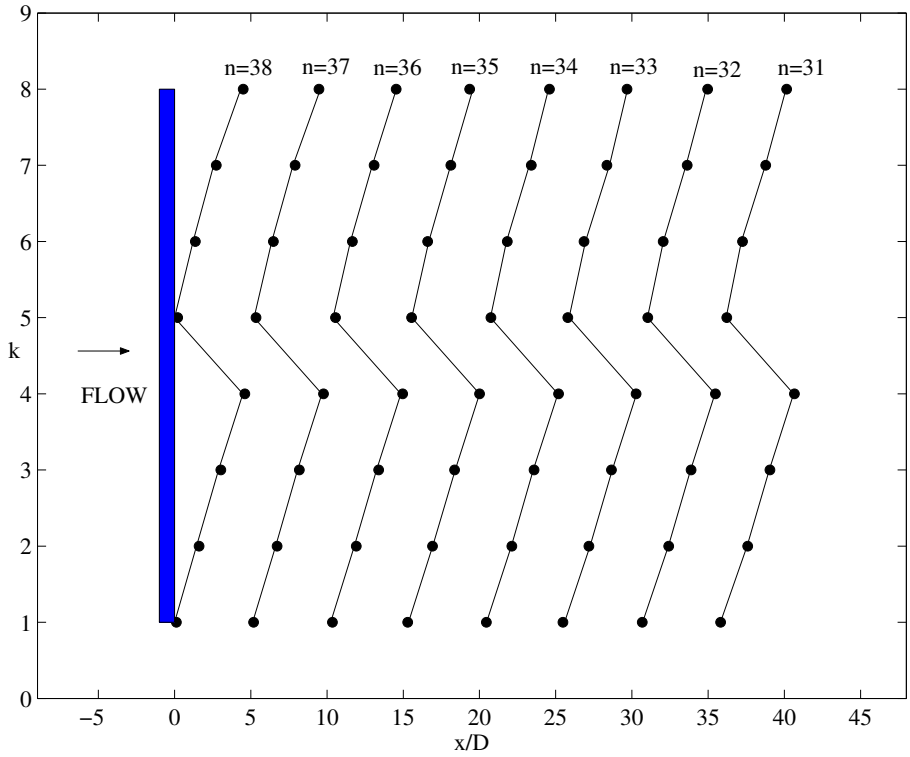

Figure 5.18: Neural network based estimation of experimental wake patterns for uniform flow over rigid cylinder, $x/D = 1.9, y/D = 1.2, \Omega = 1.0, K_o = 0.0$

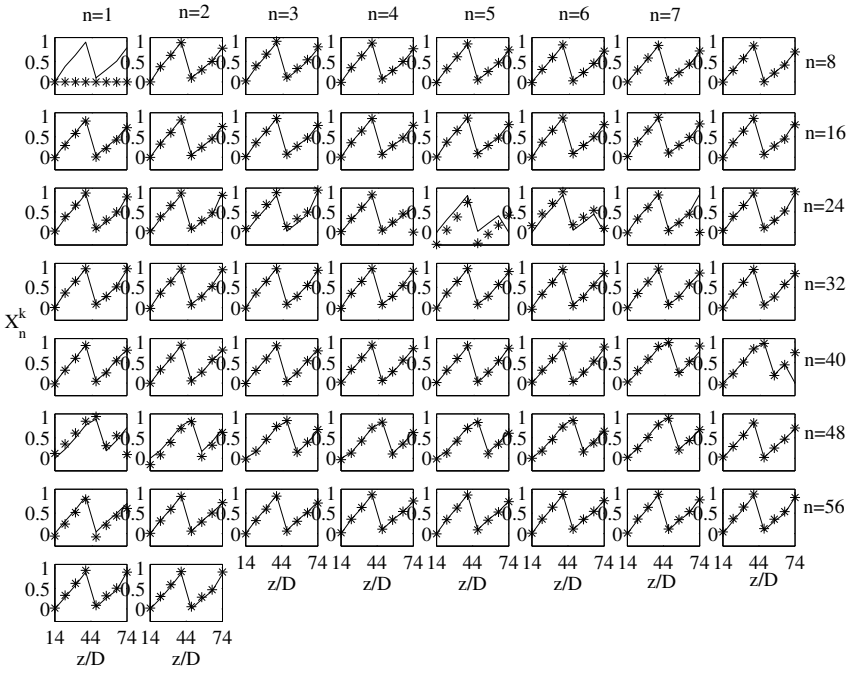

Figure 5.19: Temporal evolution of vortex shedding phase angles for uniform flow over rigid cylinder, $x/D = 1.9, y/D = 1.2, \Omega = 1.0, K_o = 0.0$

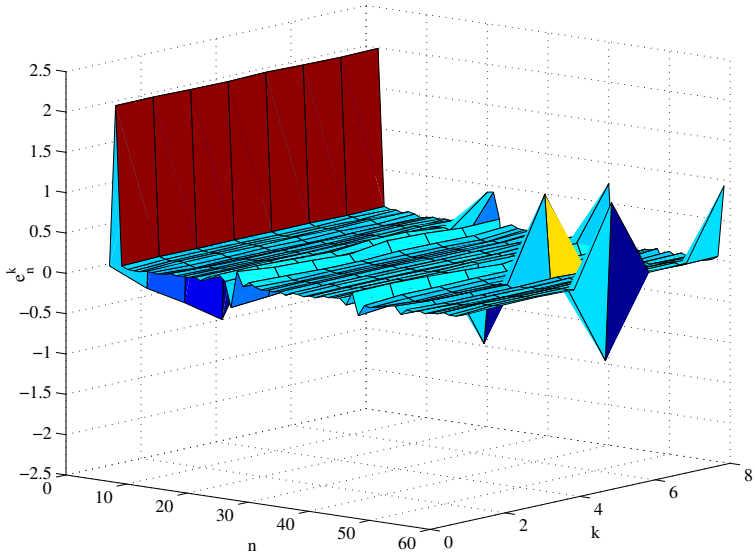

Figure 5.20: 3-d plot of state error, $x/D = 1.9, y/D = 1.2, \Omega = 1.0, K_o = 0.0$

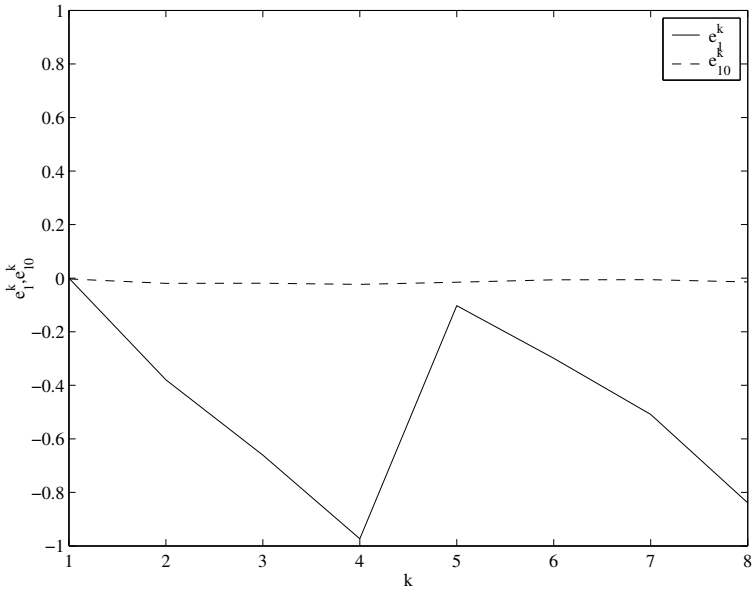

Figure 5.21: Temporal variation of state error, $x/D = 1.9, y/D = 1.2, \Omega = 1.0, K_o = 0.0$

the endplates along the cylinder affects the pattern of shedding in the wake. We will now discuss the estimation of wake patterns from this experiment using the two self-learning CML models.

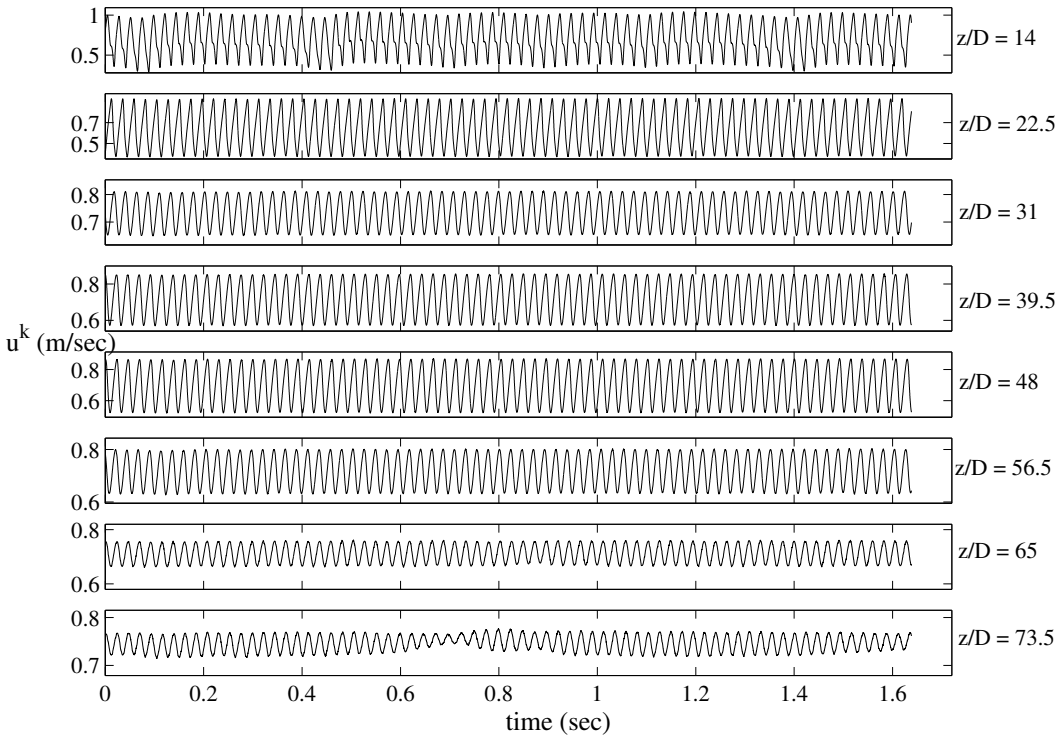

Figure 5.22: Streamwise wake velocity measured using the hot-wire probes.

5.5.1 Self-learning CML based on MVLS algorithm

We have seen previously that the MVLS algorithm is quite successful in estimating wake patterns from experiments. The input parameters for the self-learning CML model for the current experiment are unchanged from the previous two experiments. The estimation of wake patterns, $31 \leq n \leq 38$, are shown in Figure 5.24. The vortex dislocations observed by the eighth probe highlighted in Figure 5.22, are also seen for $n = 31$ to $n = 32$ in Figure 5.24. These vortex dislocations occur intermittently without any periodicity and are therefore very difficult to estimate. However, the self-learning CML model proves to be quite successful in estimating these complex wake structures. One can observe that wake patterns are shed at an oblique angle to an axis parallel to the cylinder axis for one half of the cylinder span. These patterns

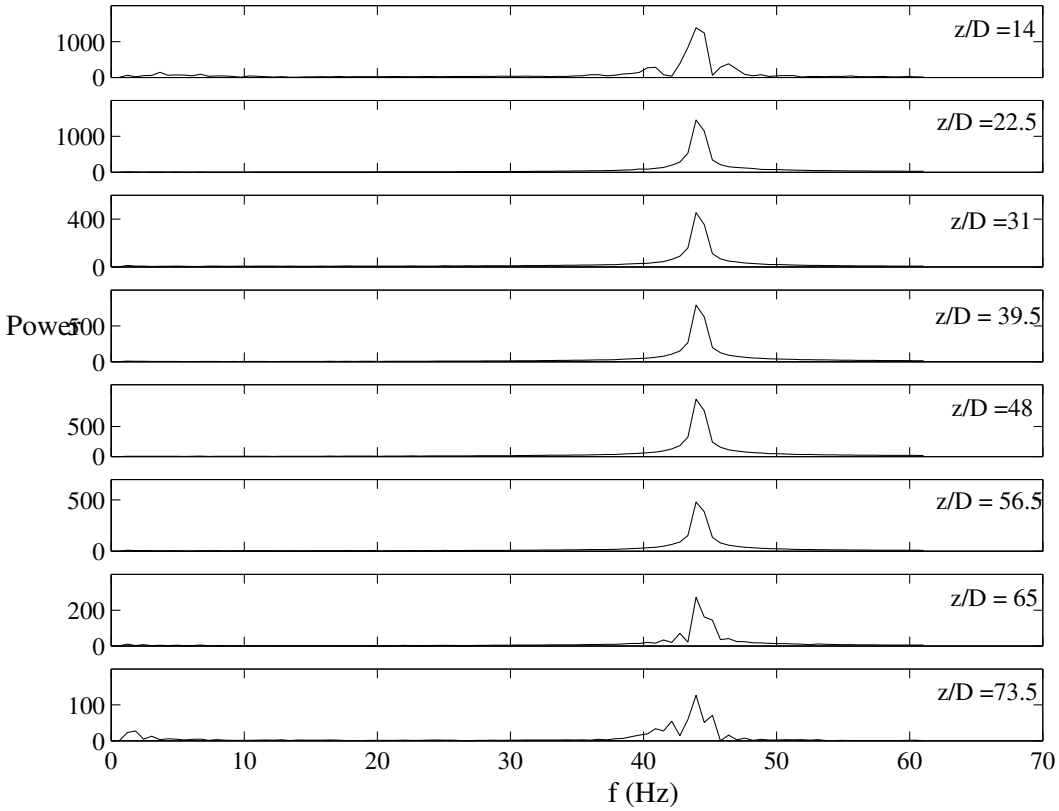

Figure 5.23: Absolute value of the velocity spectrum.

are similar to the ones observed in the second experiment. In the other half of the span, rigid periodic patterns similar to the ones observed in the first experiment, and occasional vortex dislocations are observed. The self-learning CML model accurately estimates these oblique and rigid-periodic wake patterns and their transition along the span.

In Figure 5.25, the vortex shedding phase angle distributions, $X_n^k, \widehat{X}_n^k$ are shown for $n = 1$ to $n = 59$. An initial random distribution of phase angles, $\widehat{X}_1^k$ is used for the estimation model. Both transient and steady states are accurately estimated. The only instance of incorrect estimation is found for $n = 41, 42$, coinciding with the second formation of vortex dislocations. However, even these highly complex transient wake structures are estimated within a couple of shedding cycles. In Figure 5.26, a three-dimensional plot of the state error, $e_n^k = \widehat{X}_n^k - X_n^k$ is shown, giving a quantitative summary of the accuracy of the self-learning CML model. A single spike in the state error is observed near $n = 41$ showing the only instance of incorrect estimation.

Otherwise, the magnitude of state error was of the order of 0.01. A comparison of e_1^k versus e_{10}^k in Figure 5.27 shows two orders of magnitude improvement in estimation from the initial state.

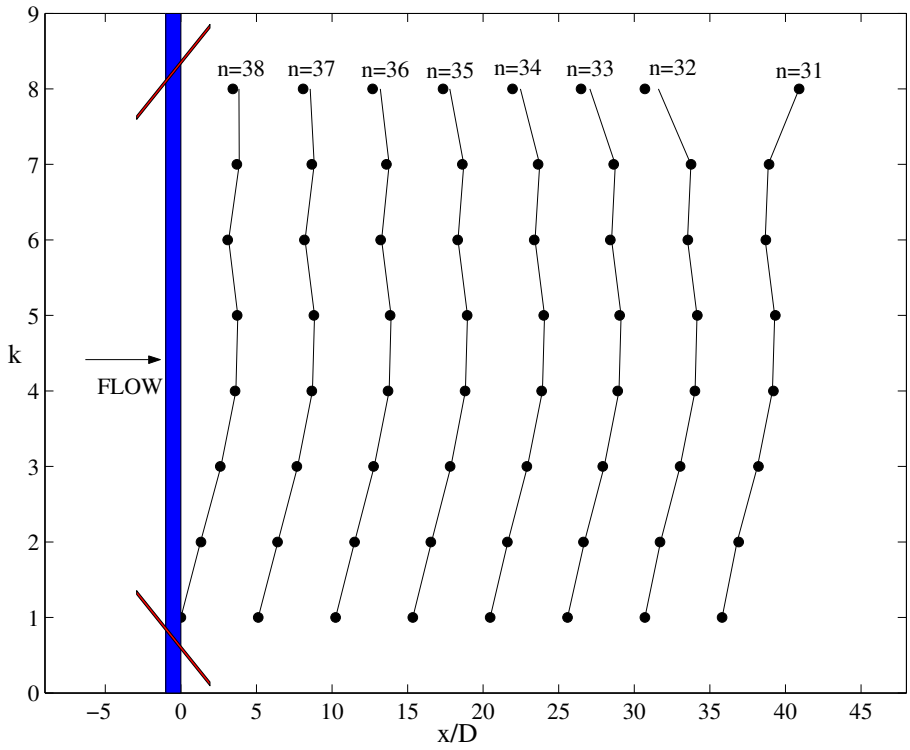

Figure 5.24: MVLS algorithm based estimation of experimental wake patterns for uniform flow over rigid cylinder, $x/D = 1.9, y/D = 1.2, \Omega = 1.0, K_o = 0.0$

5.5.2 Self-learning CML based on Neural Networks

We will now consider neural networks for the estimation of the "mixed type" of patterns. All input parameters except the acceleration parameter (optimal $\beta_0 = 1.9$ here) are the same as considered for the second experiment. In Figure 5.28, we plot wake patterns, $31 \leq n \leq 38$, in order to highlight the formation of vortex dislocations. Both the oblique shedding patterns and the rigid-periodic patterns are estimated accurately by the neural network model. The model is also quite successful in estimating the formation of vortex dislocations. Comparison of the estimation of the neural network based self-learning CML and the MLVS algorithm based self-learning CML (see Figure 5.24) shows that the latter is slightly more accurate in

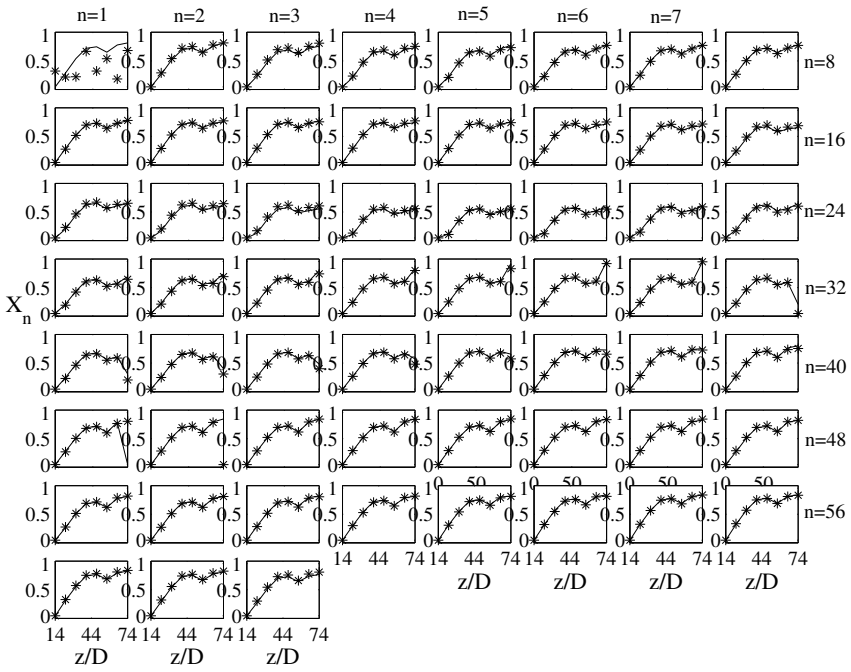

Figure 5.25: Temporal evolution of vortex shedding phase angles for uniform flow over rigid cylinder, $x/D = 1.9, y/D = 1.2, \Omega = 1.0, K_o = 0.0$

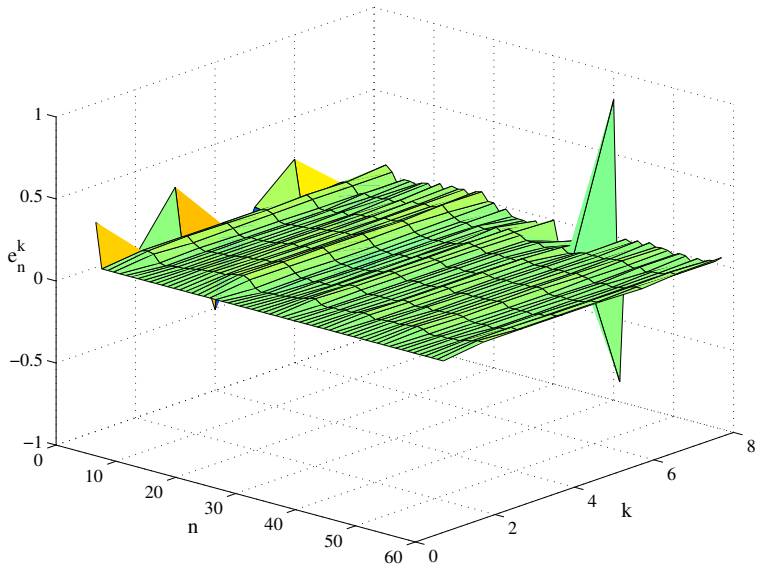

Figure 5.26: 3-d plot of state error, $x/D = 1.9, y/D = 1.2, \Omega = 1.0, K_o = 0.0$

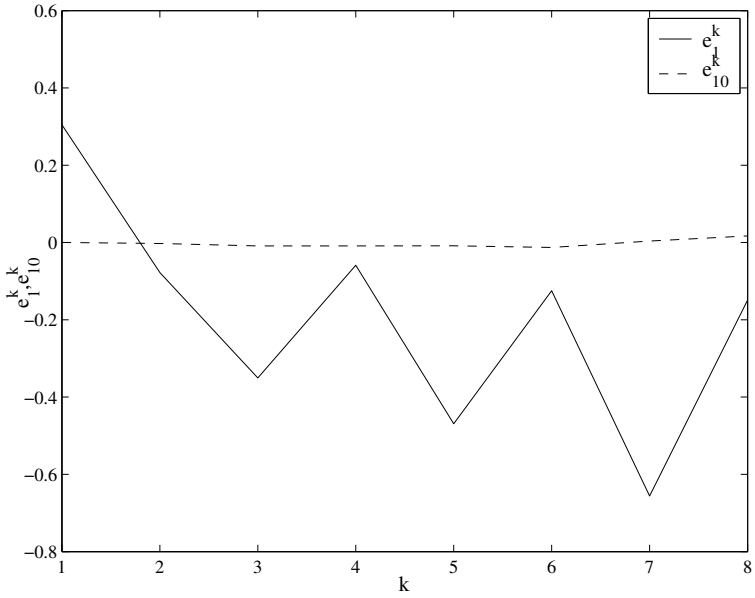

Figure 5.27: Temporal variation of state error, $x/D = 1.9, y/D = 1.2, \Omega = 1.0, K_o = 0.0$

predicting the "mixed type" of patterns.

The temporal evolution of the vortex shedding phase angles, $X_n^k, \widehat{X}_n^k$, is shown in Figure 5.29. An initial guess, $\widehat{X}_1^k = 0$, is used for the neural network model. The "mixed-type" of shedding is estimated within a single shedding cycle. As discussed previously for the MVLS algorithm based self-learning CML, the only instance of incorrect estimation by the neural network model is obtained for the second instance of vortex dislocations near $n = 40$. However, even these highly complex wake structures are estimated within two shedding cycles. We will now present a quantitative summary of the neural network estimation in Figure 5.30. Here, the state error is of the order of 0.01 barring the spike near the second vortex dislocation. Finally, in Figure 5.31 the local distribution of the state error for $n = 10$, e_{10}^k, shows two orders of magnitude improvement in accuracy from the initial estimate.

This study completes a summary of the use of two different self-learning CML models for off-line estimation of wake patterns from experimental wake flows.

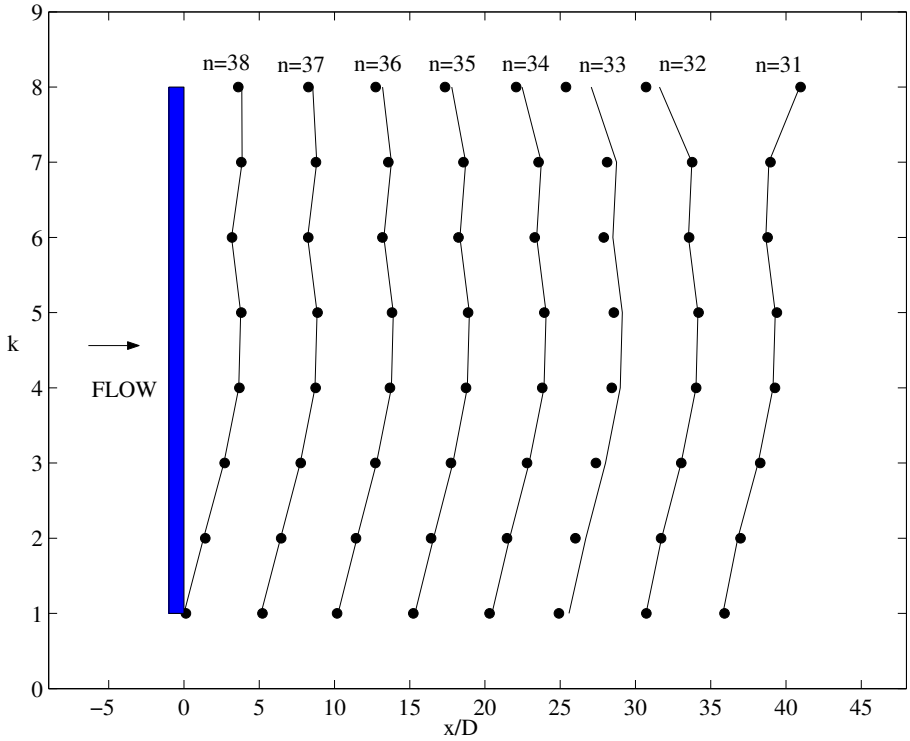

Figure 5.28: Neural Network based estimation of experimental wake patterns for uniform flow over rigid cylinder, $x/D = 1.9, y/D = 1.2, \Omega = 1.0, K_o = 0.0$

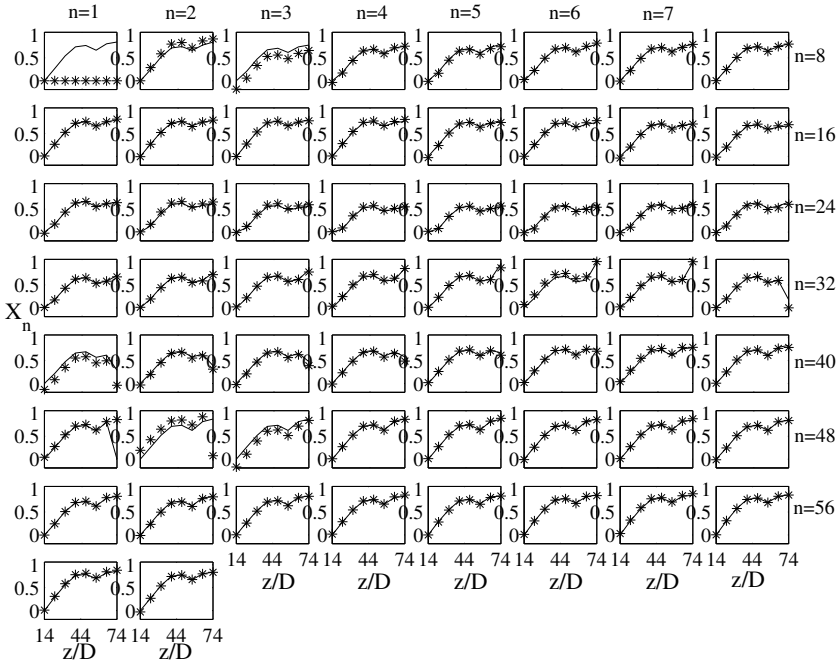

Figure 5.29: Temporal evolution of vortex shedding phase angles for uniform flow over rigid cylinder, $x/D = 1.9, y/D = 1.2, \Omega = 1.0, K_o = 0.0$

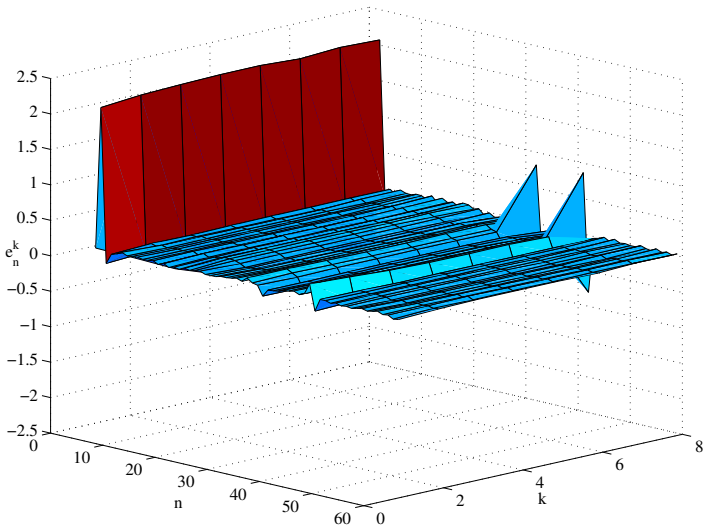

Figure 5.30: 3-d plot of state error, $x/D = 1.9, y/D = 1.2, \Omega = 1.0, K_o = 0.0$

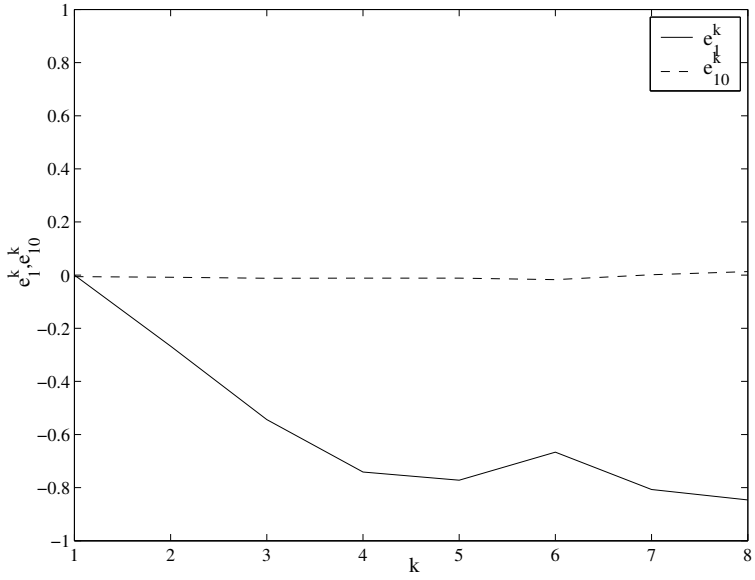

Figure 5.31: Temporal variation of state error, $x/D = 1.9, y/D = 1.2, \Omega = 1.0, K_o = 0.0$

Chapter 6

Control Methodology

In Chapters 2-4, we have established that self-learning CML models can efficiently estimate target wake patterns from numerical simulations and experiments. But for an eventual wake control system, control terms must be added to the CML models to provide feedback control signals to the scheme. In this chapter, we explore different methods of control of the simple CML model in order to achieve desired wake patterns.

The control of wake patterns has both fundamental and practical consequences. It is often possible to obtain a fundamental understanding of fluid dynamic mechanisms at work when a control method is applied. On the practical side, control of wake patterns behind bluff bodies can lead to drag and noise reduction, or altered cable-wake coupling (and hence vibration amplitude) in the case of a flexible cable.

The control of three-dimensional wake patterns in the wake of circular cylinders has been an area of recent focus in experimental work (Williamson, (1989), Hammache and Gharib, (1991)). As in the present work, the goal has often been to modify the complex wake pattern to achieve a vortex shedding pattern oriented in parallel with the cylinder axis.

Numerical studies on vortex shedding suppression based on rigorous control theories are limited due to the complexity of the Navier- Stokes equation. In a recent numerical study, Protas and Styczek (2002) used optimal rotary control of the 2-D cylinder wake at low Reynolds numbers, $Re = 75, 100$, to obtain 7% and 15%

reduction in drag respectively.

Recently, there is an increased interest in the development of control algorithms for simple models of wake flows. Aamo and Krstic (2003) developed a backstepping control method for a semi-discretized Ginzburg-Landau model of vortex shedding. Specific to the present work, addition of control terms into the coupled map lattice constitutes a first step toward use of the CML models in flow control applications for wake flows. The eventual goal is to run the highly efficient CML models with added control terms in parallel with a laboratory wake experiment in which a flexible cable is induced to vibration by an oncoming freestream flow. The primary variable in the CML, the phase of vortex shedding, can be sensed in an experiment through standard hot-film velocity measurement techniques (Davis *et al.*, 2003). As a result, the coupled map lattice studied in this work could model the wake flow in a feedback control system designed to produce desired wake patterns behind the vibrating cable. The present study does not yet address certain practical control issues, such as the method of control actuation for wake forcing, but instead focuses solely on the dynamics of the new coupled map lattice models.

The control of complex behaviors derived from low-dimensional dynamical systems has also been a topic of interest in recent years. For example, "chaos control" techniques first proposed by Ott *et al.* (1990) use occasional proportional logic to stabilize unstable periodic orbits of a chaotic attractor. While the control of unpredictable, chaotic systems seems counter-intuitive at first, the fact that chaotic systems exhibit sensitive dependence on initial conditions means that small amplitude control inputs can have a substantial effect on final system states. Sinha and Gupte (1998) investigated two-dimensional coupled map lattices and targeted spatio-temporal patterns using adaptive control techniques. Several investigators (Singer *et al.*, 1991, Wang *et al.*, (1992), Yuen *et al.*, (1999)) have used control strategies motivated by Ott *et al.* (1990) that are somewhat similar to the proportional control method applied in the present work. These investigations focussed on control of chaos in a thermal convection loop. The desire to explore application of these techniques to the

vortex shedding process using coupled map lattice models is an additional motivation for this work. For comparison purposes adaptive proportional control scheme and discontinuous nonlinear control scheme (Balasubramanian *et al.*, 2002), which will be described in more detail in subsequent discussion, were also applied.

In this chapter, we discuss certain features in the development of three coupled map lattice models where control terms are added (Figure 6.1). The first model is based on occasional proportional control logic and aims to stabilize the unstable periodic orbits of a chaotic attractor (Ott *et al.*, 1990). The second model uses a linear adaptive proportional controller with a spatio-temporal feedback gain. The third model is based on a conditional feedback linearization of the nonlinear coupled map lattice. The resulting linearized CML is controlled using eigenvalue assignment (Rugh, 1995). A summary of the control schemes is given below.

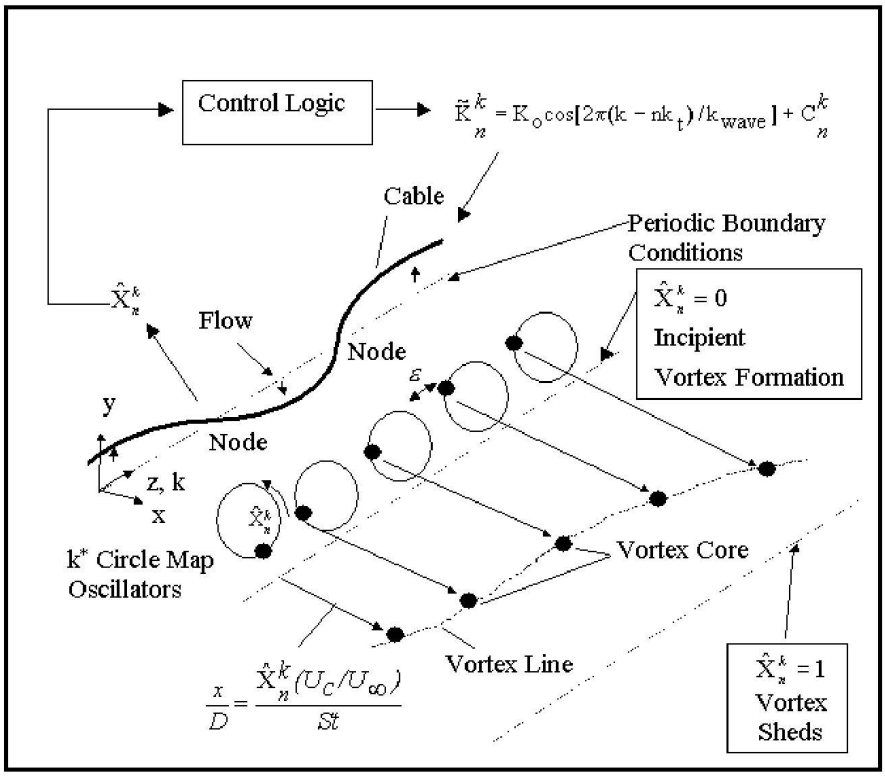

Figure 6.1: Schematic of the coupled map lattice with added control terms.

6.1 Proportional Control

The CML equations (1.7), (1.6) are modified by the addition of a control signal C_n^k to the forcing term K^k, yielding

$$\widetilde{f}_n^k = \widehat{\mathrm{X}}_n^k + \Omega^k - \widetilde{\mathrm{K}}_n^k \sin(\psi_n^k)/2\pi, \tag{6.1}$$

$$\widehat{\mathrm{X}}_{n+1}^k = (1-\epsilon)\,\widetilde{f}_n^k + \epsilon\left(\widetilde{f}_n^{k-1} + \widetilde{f}_n^{k+1}\right), \tag{6.2}$$

where $\psi_n^k = 2\pi\widehat{\mathrm{X}}_n^k - \phi_n^k - \pi/2$, $\widetilde{\mathrm{K}}_n^k = \mathrm{K}^k + \mathrm{C}_n^k$. In comparing (6.1) to (1.6), we note that the phase angle between the vortex shedding event and the cylinder motion, ϕ_n^k, now varies with time since $\widetilde{\mathrm{K}}_n^k$ varies through the C_n^k term. The magnitude of the control signal

$$\mathrm{C}_n^k = \gamma\left(\widehat{\mathrm{X}}_n^k - \overline{\mathrm{X}}^k\right) \quad \text{or} \quad \mathbf{C}_n = \gamma\mathbf{I}\left(\widehat{\mathbf{X}}_n - \overline{\mathbf{X}}\right), \tag{6.3}$$

is proportional to the deviation of the system from the target pattern of vortex shedding $\overline{\mathrm{X}}^k$. The feedback gain γ is constant in time and space .

6.2 Adaptive Proportional Control

This method represents an extension of the proportional control method. Here, each entry of the feedback gain $\widehat{\mathbf{\Gamma}}_n$ is assumed to be different from any other one, and thus through time adaptation of $\widehat{\mathbf{\Gamma}}_n$, the vector $\widehat{\mathbf{\Gamma}}_n = \left[\widehat{\Gamma}_n^1, \widehat{\Gamma}_n^2, \ldots, \widehat{\Gamma}_n^{k^*}\right]^T$ represents a temporally varying vector. Along with (6.1) and (6.2), the following control law is used:

$$\begin{aligned} &\mathbf{C}_n = \mathbf{H}(\widehat{\mathbf{X}}_n)\widehat{\Gamma}_n, \quad \mathbf{H}(\widehat{\mathbf{X}}_n) = \mathrm{diag}\left(\widetilde{f}_n\left(\widehat{\mathbf{X}}_n\right)\right) \quad \text{or} \\ &\mathrm{C}_n^k = \widehat{\Gamma}_n^k \widetilde{f}_n^k(\widehat{\mathbf{X}}_n). \end{aligned} \tag{6.4}$$

In order to determine an update law for the feedback gain $\widehat{\mathbf{\Gamma}}_n$, we define the *state error* $\mathbf{X}$ as

$$\mathbf{X}_{n+1} = \widehat{\mathbf{X}}_{n+1} - \overline{\mathbf{X}}. \tag{6.5}$$

Our goal is to drive the state error to zero in the shortest possible time. We use a multi-variable least squares algorithm to minimize the state error after each timestep. The following equations illustrate the steps in the derivation of the adaptation scheme for the feedback gain $\widehat{\mathbf{\Gamma}}_n$. The feedback gain can be updated by minimizing the cost function

$$\begin{aligned} J_n(\overline{\mathbf{\Gamma}}) &= \frac{1}{2}\overline{\mathbf{\Gamma}}^T\mathbf{P}_0^{-1}\overline{\mathbf{\Gamma}} + \frac{1}{2}\sum_{j=1}^{n}\mathbf{X}_{j+1}^T\widetilde{\mathbf{R}}^{-1}\mathbf{X}_{j+1}, \\ \widetilde{\mathbf{R}}^{-1} &= \frac{\mathrm{diag}\left(\sin(\Psi_n)\right)\mathbf{R}^{-1}\mathrm{diag}\left(\sin(\Psi_n)\right)}{4\pi^2}, \end{aligned} \tag{6.6}$$

where the dummy variable $\overline{\mathbf{\Gamma}}$ is used for analysis purposes only in place of $\widehat{\mathbf{\Gamma}}_n$. The parameters $\mathbf{P}_0^{-1}$ and $\mathbf{R}^{-1}$ are diagonal input weighting matrices and can be varied until optimal values are obtained. The equation

$$\frac{\partial}{\partial\overline{\mathbf{\Gamma}}}J_n(\overline{\mathbf{\Gamma}}) = \mathbf{0} \tag{6.7}$$

provides iteration for $\widehat{\mathbf{\Gamma}}_{n+1}$ with the adaptation proceeding in the direction of decreasing cost function. Next define

$$\begin{aligned} \mathbf{G}(\widehat{\mathbf{X}}_n) &= \frac{\mathrm{diag}(\sin(\Psi_n))\mathbf{H}(\widehat{\mathbf{X}}_n)}{2\pi}, \\ \mathbf{P}_n^{-1} &= \left(\mathbf{P}_0^{-1} + \sum_{j=1}^{n}\mathbf{G}(\widehat{\mathbf{X}}_j)^T\mathbf{R}^{-1}\mathbf{G}(\widehat{\mathbf{X}}_j)\right), \\ &= \left(\mathbf{P}_0^{-1} + \sum_{j=1}^{n}\mathbf{H}(\widehat{\mathbf{X}}_j)^T\widetilde{\mathbf{R}}^{-1}\mathbf{G}(\widehat{\mathbf{X}}_j)\right). \end{aligned} \tag{6.8}$$

The feedback gain adaptation law is then given by

$$\mathbf{P}_n = \mathbf{P}_{n-1} - \mathbf{P}_{n-1}\mathbf{H}(\widehat{\mathbf{X}}_n)^T\left(\widetilde{\mathbf{R}} + \mathbf{H}(\widehat{\mathbf{X}}_n)\mathbf{P}_{n-1}\mathbf{H}(\widehat{\mathbf{X}}_n)^T\right)^{-1}\mathbf{H}(\widehat{\mathbf{X}}_n)\mathbf{P}_{n-1}, \tag{6.9}$$

$$\widehat{\mathbf{\Gamma}}_{n+1} = \widehat{\mathbf{\Gamma}}_n - \mathbf{P}_n\mathbf{H}(\widehat{\mathbf{X}}_n)^T\widetilde{\mathbf{R}}^{-1}\mathbf{X}_{n+1}, \tag{6.10}$$

where $\mathbf{P}_{-1} = \mathbf{P}_0$ is a known input weighting matrix for the state error $\mathbf{X}$. In addition to the techniques discussed in this section, we have used standard adaptive control

techniques (Goodwin and Sin, 1984) including exponential data forgetting, covariance resetting etc.

6.3 Discontinuous Nonlinear Control

In this method the control law is derived to send the state error to rest, so that, as $\mathbf{X}_{n\to\infty} \to \mathbf{0}, \widehat{\mathbf{X}}_{n\to\infty} \to \overline{\mathbf{X}}$. In the case of parallel shedding, $\overline{\mathrm{X}}^k = \eta, \forall\, k = 1, 2, \ldots, k^*$, where η is a real constant. The modified coupled map lattice is written as

$$\widetilde{f}_n^k = \widehat{\mathrm{X}}_n^k + \Omega^k - \widetilde{\mathrm{K}}^k \sin(\psi_n^k)/2\pi, \tag{6.11}$$

$$\widehat{\mathrm{X}}_{n+1}^k = (1-\epsilon)\, \widetilde{f}_n^k + \epsilon \left(\widetilde{f}_n^{k-1} + \widetilde{f}_n^{k+1} \right), \tag{6.12}$$

where $\psi_n^k = 2\pi \widehat{X}_n^k - \phi_n^k - \pi/2$, $\widetilde{\mathrm{K}}_n^k = \mathrm{K}^k + \mathrm{C}_n^k$.

With further manipulation,

$$\mathrm{X}_{n+1}^k = (1-2\epsilon) \left(\mathrm{X}_n^k + u_n^k \right) + \epsilon \left(\mathrm{X}_n^{k+1} + u_n^{k+1} \right) + \epsilon \left(\mathrm{X}_n^{k-1} + u_n^{k-1} \right) \tag{6.13}$$

results, where the input term u_n^k is related to the forcing term $\widetilde{\mathrm{K}}_n^k$ via $u_n^k = \Omega^k - \widetilde{\mathrm{K}}_n^k \sin(\psi_n^k)/2\pi$. We can now write (6.13) in vector form as $\mathbf{X}_{n+1} = \mathbf{A}\left(\mathbf{X}_n + \mathbf{u}_n\right)$ where $\mathbf{X}_n = \left[\mathrm{X}_n^1, \mathrm{X}_n^2, \ldots, \mathrm{X}_n^{k^*}\right]^T$, $\mathbf{A}$ accounts for the spatial coupling and $\mathbf{u}_n = \left[u_n^1, u_n^2, \ldots, u_n^{k^*}\right]^T$. The feedback gain matrix $\mathbf{G}$ is designed using a pole placement (eigenvalue assignment) (Rugh, 1995) technique so that the control input is derived as $\mathbf{u}_n = -\mathbf{G}\mathbf{X}_n$ and the closed loop system becomes $\mathbf{X}_{n+1} = (\mathbf{A} - \mathbf{A}G)\, \mathbf{X}_n$. The model uses a conditional feedback linearization procedure, thereby providing for saturation of the control input using a threshold parameter β. The control input is limited to a threshold parameter α to ensure that the forcing term after control is limited as

shown in (6.15).

$$u_n^k = \begin{cases} -\text{sgn}\left(\mathbf{G}^k\mathbf{X}_n\right) * \min\left(|\mathbf{G}^k\mathbf{X}_n|, \alpha\right) & if|\sin(\psi_n^k)| > \beta \\ \Omega^k - 1 & if|\sin(\psi_n^k)| \leq \beta \end{cases}, \mathbf{G}^k : k^{th}\, row\, of\, \mathbf{G}, \tag{6.14}$$

$$\widetilde{\mathrm{K}}_n^k = \begin{cases} -2\pi\left(u_n^k + 1 - \Omega^k\right)/\sin(\psi_n^k) & if|\sin(\psi_n^k)| > \beta \\ 0 & if|\sin(\psi_n^k)| \leq \beta \end{cases}. \tag{6.15}$$

The control signal C_n^k which drives the error system to rest is then given by

$$\begin{aligned} \mathrm{C}_n^k &= \widetilde{\mathrm{K}}_n^k - \mathrm{K}^k \\ &= \begin{cases} \dfrac{-2\pi}{\sin(\psi_n^k)}\left(1 - \Omega^k - \text{sgn}\left(\mathbf{G}^k\mathbf{X}_n\right) * min\left(|\mathbf{G}^k\mathbf{X}_n|, \alpha\right)\right) - \mathrm{K}^k, & |\sin(\psi_n^k)| > \beta \\ -\mathrm{K}^k, & otherwise \end{cases}. \end{aligned} \tag{6.16}$$

6.4 Results- Control of CML model

The case of uniform flow (Re =100) over a cable oscillating transversely (in $y-z$ plane) to the oncoming flow in standing wave motion is used as the uncontrolled flow in the CML model. The cable mode shape, L/D = 62 and cable amplitude A/D = 0.68 are matched with the parameters in the numerical simulations of Newman and Karniadakis (1996). Other input parameters include $\Omega = 0.99$, $K_o = 0.1$ and $k^* = 41$. Further details will be discussed when the wake patterns for this uncontrolled flow are presented.

In contrast to the other two control methods where energy methods are used to design optimal feedback gain matrices, the simple nature of the proportional control method means that the input feedback gain parameter γ, which is spatially and temporally invariant, must be optimized through a parametric study. The effect of the variation of the feedback gain parameter is shown in Fig. 6.2. In order to determine control effectiveness we define an average deviation of the phase of vortex shedding from the target as

$$\delta = \frac{1}{k^*}\sum_{k=1}^{k^*} |\widehat{\mathrm{X}}^k_{nfinal} - \overline{\mathrm{X}}| \tag{6.17}$$

In the range $0.6 < \gamma < 1.0$, δ is small because the wake is controlled, and periodic patterns similar to the parallel shedding patterns shown in Figure 6.3(b) are obtained. When $\gamma > 1.0$, larger values of δ result because other periodic states away from the target state are activated. After this optimization study, $\gamma = 0.9$ was chosen as the input feedback gain parameter for all presented results using proportional control.

The input parameters for the adaptive proportional control method are $\mathbf{P}_{-1} = \mathbf{P}_0 = 0.01\mathbf{I}_{k^*}, \mathbf{R} = \mathbf{I}_{k^*}$ where $\mathbf{I}_{k^*}$ is the identity matrix of dimension k^*. The main input parameter for the DNL control method is σ_{max}, the maximum eigenvalue of the matrix $(\mathbf{A} - \mathbf{A}G)$. The parameter σ_{max} determines the speed at which convergence to target state is achieved. The eigenvalues of this matrix are distributed randomly in the

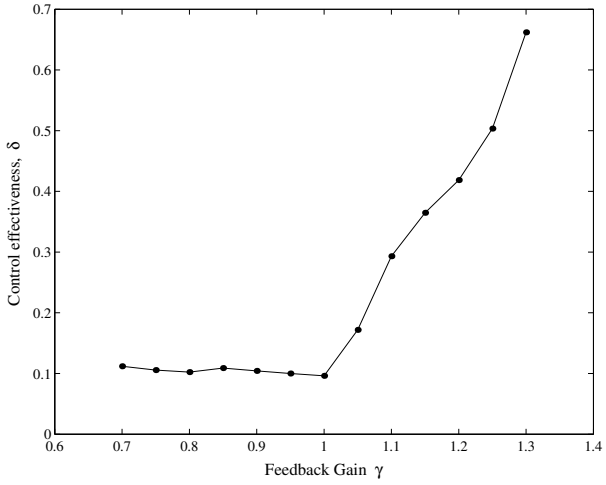

Figure 6.2: Optimization of the feedback gain parameter used in the proportional control signal. Control effectiveness, δ, is defined as the steady state mean deviation of the phase of vortex shedding from the target in (6.16).

circle with radius σ_{max} from 0 to σ_{max}. The parameter σ_{max} lies inside the unit circle of the complex plane. Other input parameters used in the DNL control methods include σ_{max}= 0.9, β= 0.1, α= 0.006. A comparative study of vortex shedding patterns, local dynamics, global dynamics and cable dynamics after application of the three different control methods follows.

6.5 Vortex shedding patterns

The uncontrolled flow case discussed earlier in this section results in vortex dislocations near the cable vibration nodes (Figure 6.3(a)). Vortex shedding patterns from one shear layer are shown. The patterns are viewed by an observer looking in the transverse (y) direction observing the x-z plane (see Figure 1.6). The cable and freestream flow direction (bottom to top) are included to orient the reader. The goal of the control schemes will be to steer the complex wake system to realize ordered, parallel patterns of vortex shedding. It has been shown by Olinger (1998) that parallel (2-D) vortex shedding patterns are predicted by the CML when a rigid cylinder is forced to oscillate in the 1/1 lock-on region (see Figure 6.3(b)). This vortex shedding

pattern serves as the target state ($\overline{\mathrm{X}}^k = \eta = 0.9$) for the control studies.

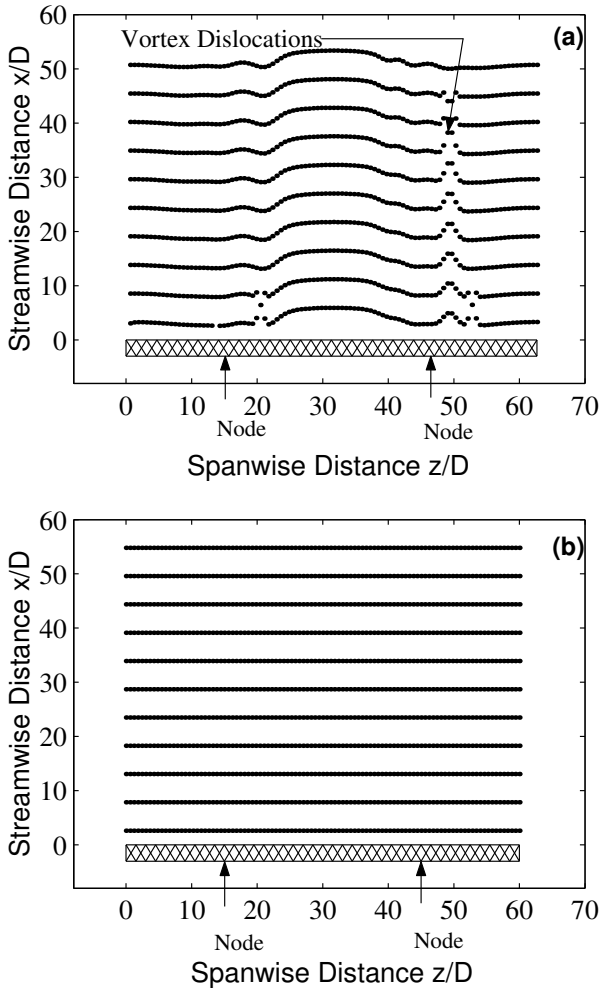

Figure 6.3: (a) Uncontrolled wake pattern showing vortex dislocations, uniform flow, Ω=0.99, K_o=0.1. (b) Parallel shedding patterns used as target state $\overline{\mathrm{X}} = \eta = 0.9$. Rigid cylinder in uniform flow, $\Omega = 0.95, \mathrm{K}^k = 0.9$ (within the lock-on region).

In Figure 6.4(a) proportional control techniques are applied to the uncontrolled flow. Complex wake structures such as the vortex dislocations in Figure 6.3(a) are eliminated and periodic patterns similar to the targeted parallel shedding patterns result after proportional control is activated. The shedding patterns are not precisely parallel but instead resemble the lace-like structures identified by Newman and Karniadakis (1996). We believe this is due to the absence of a spanwise varying feedback gain for proportional control. The application of adaptive proportional control or DNL control seeks to correct this situation.

We have achieved the desired parallel shedding patterns using adaptive proportional control as shown in Figure 6.4(b). When the DNL control signal is activated ordered parallel vortex shedding patterns (Figure 6.4(c)) are achieved. It will be shown in later sections that there is an improvement in targeting accuracy for the DNL method over the proportional control method, and in targeting speed over the adaptive proportional control method.

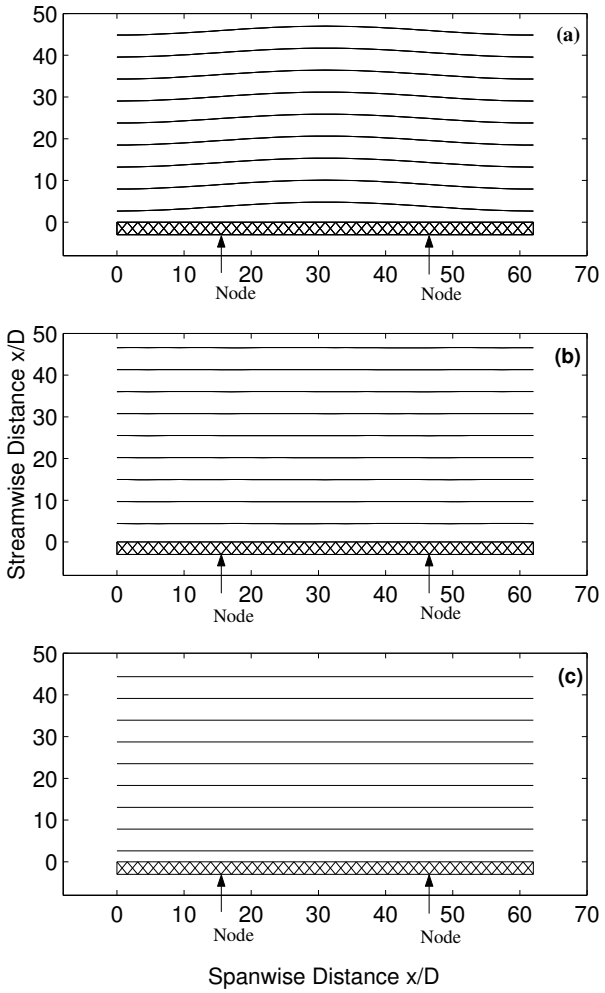

Figure 6.4: (a) Lace-like vortex shedding pattern after proportional control is activated. Ω=0.99, K_o=0.1, k^*=41, L/D=62, Re=100, U_c/U_∞=0.88, ϵ=0.0247, A/D=0.68 at antinode, $\gamma = 0.9$. (b) Parallel (2-D) vortex shedding patterns after adaptive proportional control is activated. Ω=0.99, K_o=0.1, k^*=41, L/D=62, Re=100, U_c/U_∞=0.88, ϵ=0.0247, $A/D = 0.68$ at antinode, $\mathbf{P}_o$=0.01$\mathbf{I}$, $\mathbf{R}$=$\mathbf{I}$. (c) Parallel (2-D) vortex shedding patterns targeted after DNL control is activated. Ω=0.99, K_o=0.1, k^*=41, L/D=62, Re=100, U_c/U_∞=0.88, ϵ=0.0247, A/D=0.68 at antinode, η=0.5, σ_{max}=0.9, β=0.1, α=0.006. Freestream flow direction is from bottom to top for all vortex shedding patterns presented in this paper.

6.6 Local dynamics

The temporal dynamics of a wake can be clearly represented by the successive iterates of the phase of the vortex shedding event at a particular spanwise location, $\widehat{\mathrm{X}}_n^k$. In Figure 6.5(a) we plot the variable $\widehat{\mathrm{X}}_n^{15}$ in case of proportional control, corresponding to a point near the cable midspan i.e. z/D=21.7 and k = 15. The variable $\widehat{\mathrm{X}}_n^{15}$ for the uncontrolled wake ($0 < \mathrm{n} < 600$) exhibits chaotic dynamics with a positive Lyapunov exponent $= 0.118 \pm 0.044$ (Sprott, 1992). The proportional control signal is activated at n = 600. After approximately fifty iterates of the map, $\widehat{\mathrm{X}}_n^{15}$ reaches a steady state value,$\widehat{\mathrm{X}}_{nfinal}^{15}$= 0.3266 consistent with the periodic shedding pattern of Figure 6.4(a). We note that this steady state value varies significantly from the target state $\overline{\mathrm{X}}^k = \eta = 0.9$.

The same variable, $\widehat{\mathrm{X}}_n^{15}$ is then studied using the adaptive proportional control method (Figure 6.5(b)). The adaptive proportional control signal is again activated at n = 600. After approximately one hundred iterations of the map, $\widehat{\mathrm{X}}_n^k$ reaches the target state, $\overline{\mathrm{X}}^k = \eta = 0.9$, within 1% accuracy. This result is consistent with the parallel shedding observed in Figure 6.4(b). The phase dynamics of a spanwise oscillator, $\widehat{\mathrm{X}}_n^{15}$ before and after DNL control activation is studied in Figure 6.5(c). The variable $\widehat{\mathrm{X}}_n^{15}$ reaches the target state of $\overline{\mathrm{X}}^k = \eta = 0.9$ within a few shedding cycles of control activation. There is an improvement in targeting accuracy over the proportional control method and also an improvement in targeting speed and accuracy over the adaptive proportional control method.

The temporal variation of the proportional control signal, C_n^k, at the same spanwise location is shown in Figure 6.6(a) and compared with the adaptive proportional control signal and the DNL control signal in Figure 6.6(b) and Figure 6.6(c) respectively. The magnitude of the adaptive proportional control signal at this spatial location C_n^{15} (Figure 6.6(b)) is less than the required proportional control signal for the same spatial location. The DNL control signal shows an initial spike (Figure 6.6(c)) with the signal magnitude larger than the corresponding adaptive proportional control sig-

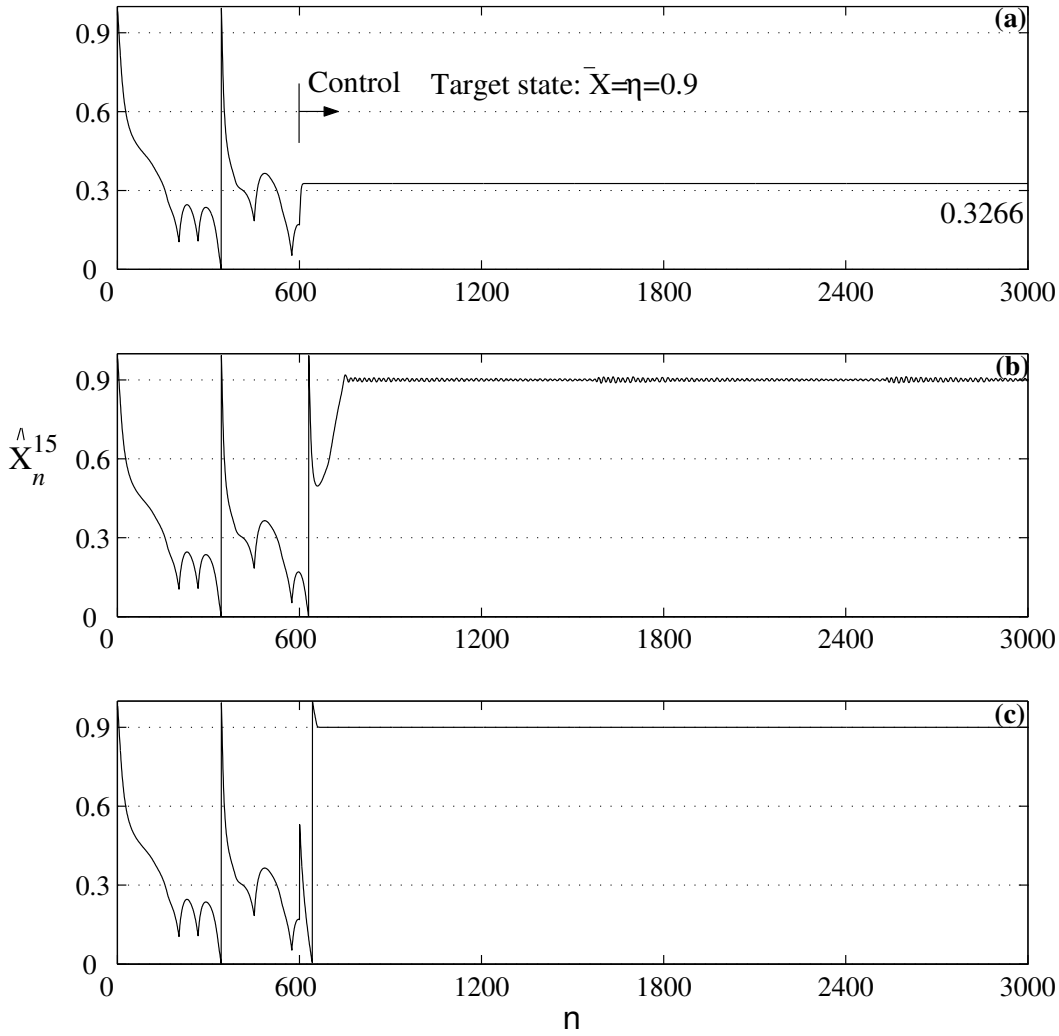

Figure 6.5: Temporal variation of the phase of vortex shedding $\widehat{X}_n^{15}$ at k=15, z/D=21.7. Control turned on at n=600. (a) Proportional control, (b) adaptive proportional control and (c) DNL control.

nal values, but the control signal quickly settles down to a lower constant value once targeting is achieved.

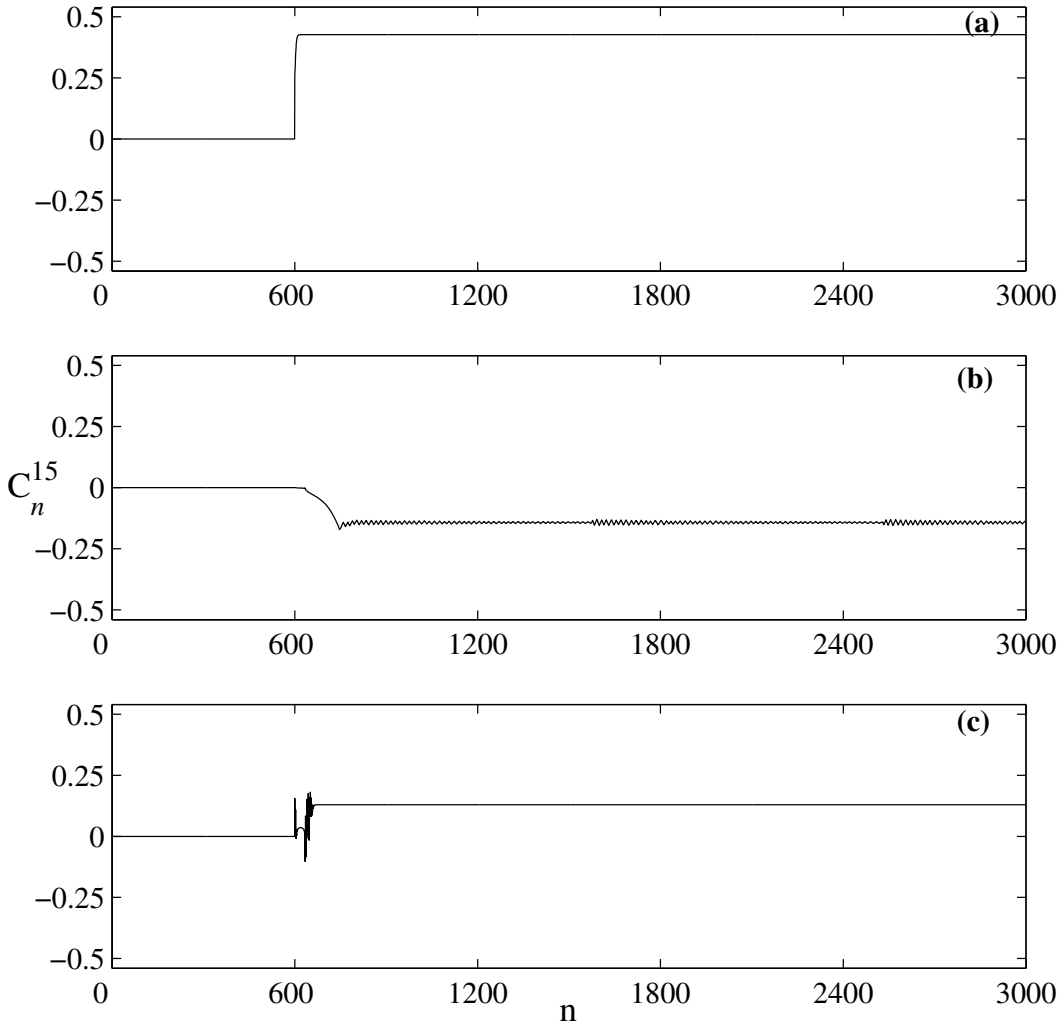

Figure 6.6: Temporal variation of the control signal C_n^{15} at k=15, z/D=21.7. (a) Proportional control, (b) adaptive proportional control and (c) DNL control.

6.7 Global dynamics

The local dynamics has highlighted certain features of the control schemes, however study of the behavior of all k^* oscillators (i.e. the global dynamics) will yield further insight. The targeting accuracy over the spatial domain is studied using the spatial

norm of the phase of the vortex shedding event, $\|\widehat{\mathbf{X}}_n\|$, defined as

$$\|\widehat{\mathbf{X}}_n\| = \sqrt{\frac{1}{k^*}\sum_{k=1}^{k=k^*}(\widehat{\mathrm{X}}_n^k)^2} \tag{6.18}$$

This variable is studied in Figure 6.7(a) for the proportional control case. The variable $\|\widehat{\mathbf{X}}_n\|$ reaches a steady state value, $\|\widehat{\mathbf{X}}_{nfinal}\| = 0.2489$ within a few iterations of control activation. Here *nfinal* = 3000. This value is different from $\widehat{\mathrm{X}}_{nfinal}^k = 0.3266$ (see Figure 6.5(a)), further proving that ordered but not parallel shedding patterns are achieved with the proportional control method. After the adaptive proportional control signal is activated at n = 600, $\|\widehat{\mathbf{X}}_n\|$ reaches the target state, $\overline{\mathrm{X}} = \eta = 0.9$ (Figure 6.7(b)), after a few hundred map iterations. In case of DNL control, the global variable, $\|\widehat{\mathbf{X}}_n\|$, reaches the exact value of $\overline{\mathrm{X}} = \eta = 0.9$ in Figure 6.7(c). These results again indicate that precisely parallel shedding patterns are targeted once control is turned on for these two control cases.

The temporal variation of the spatial norm of the error system variable, $\|\mathbf{X}_n\|$, for the case of proportional control is studied in Figure 6.8(a). The global variable, $\|\mathbf{X}_n\|$, reaches a constant non-zero value indicating that ordered shedding patterns deviating from the targeted parallel shedding patterns are obtained using the proportional control method. The same variable is driven to zero when adaptive proportional control (Figure 6.8(b)) is activated. In case of DNL control (Figure 6.8(c)) the spatial norm of the error system variable, $\|\mathbf{X}_n\|$ is again driven to zero after control is applied, once again confirming the resulting parallel shedding patterns. A dramatic improvement in targeting speed is shown for the DNL technique compared to the adaptive proportional method. The DNL technique achieves control within approximately 100 iterations while the adaptive proportional method requires approximately 1400 iterations.

The spatial norm of the control signal at each timestep, $\|\mathbf{C}_n\|$, represents the energy input used to drive the system to a desired target state. This variable reaches a constant value of 0.3355 in Figure 6.9(a) for the case of proportional control. The

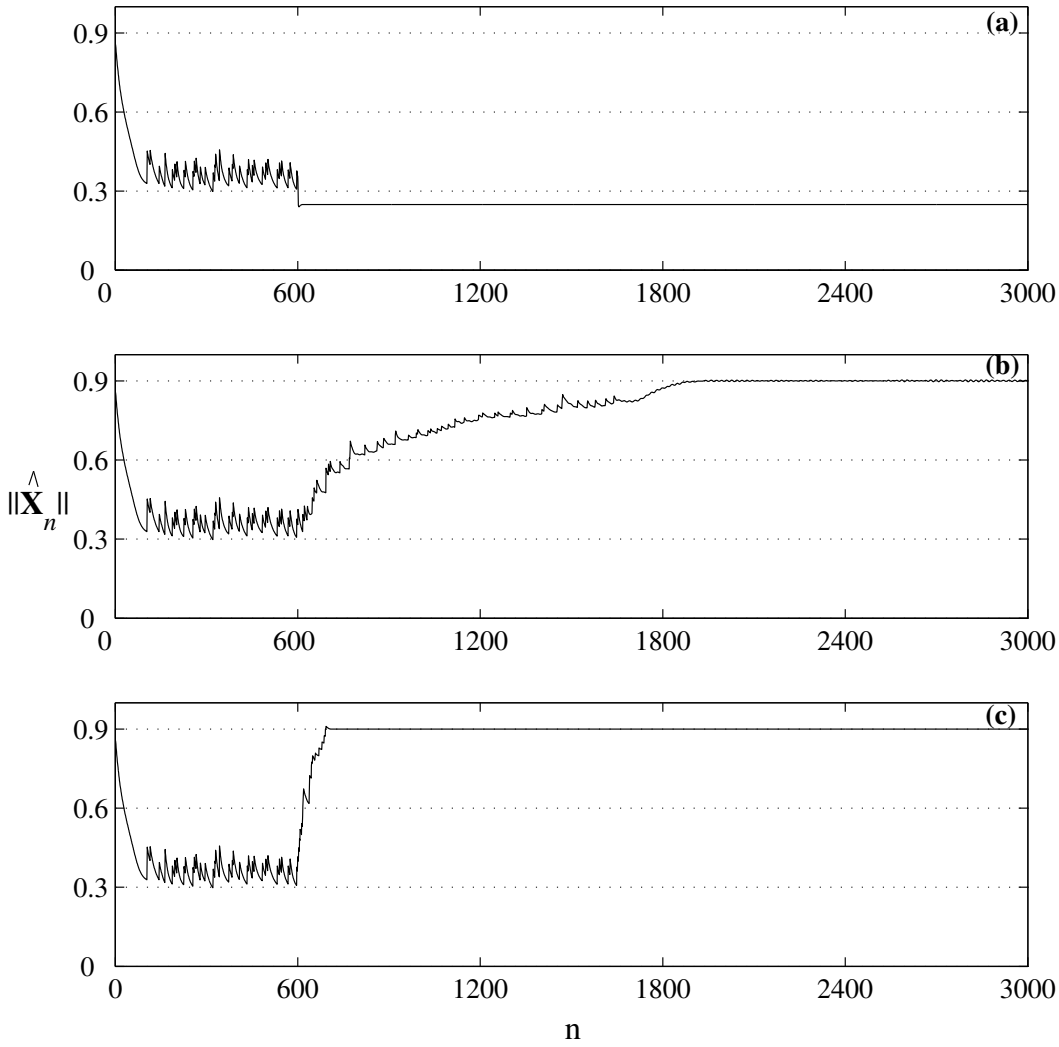

Figure 6.7: Temporal variation of the norm of the system variable $\|\widehat{\mathbf{X}}_n\|$ at k=15, z/D=21.7. (a) Proportional control, (b) adaptive proportional control and (c) DNL control.

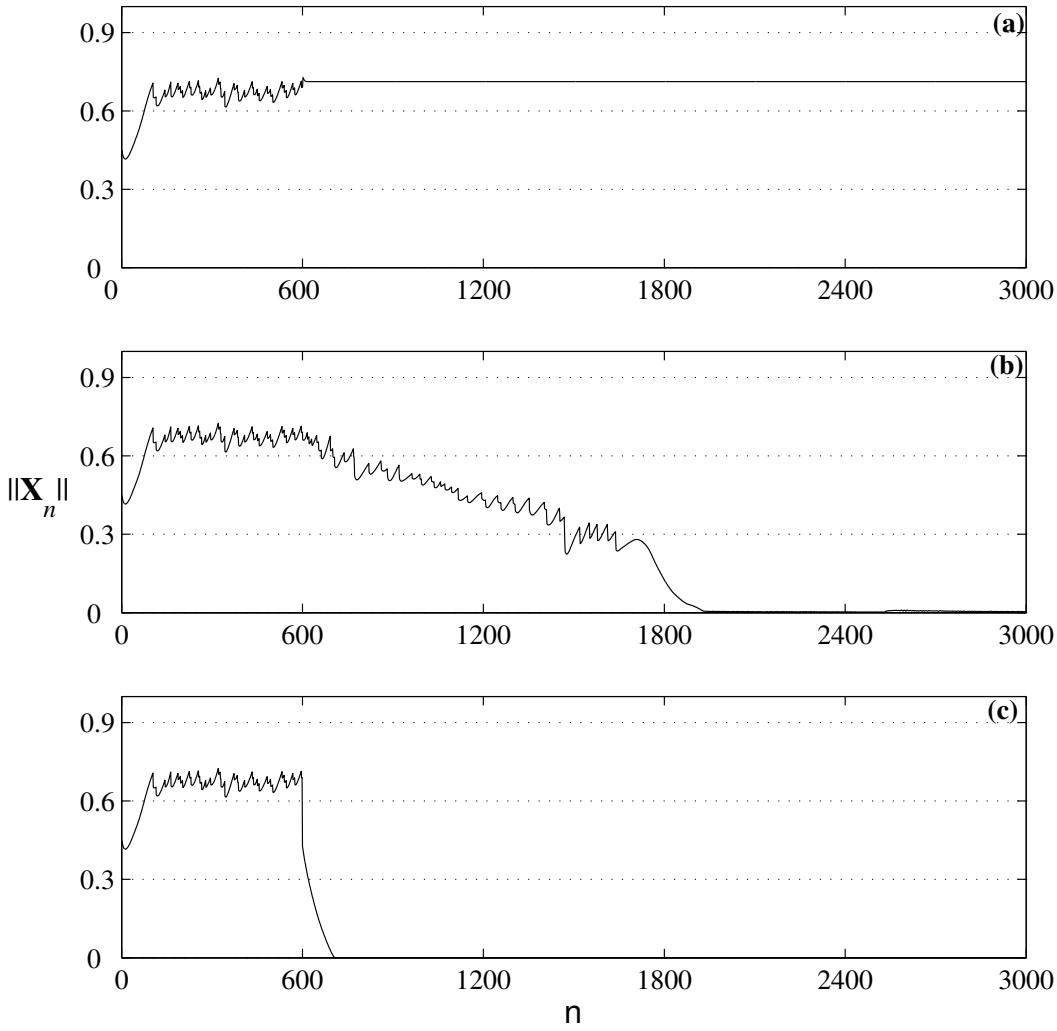

Figure 6.8: Temporal variation of the norm of the error system variable $\|\mathbf{X}_n\|$ at k=15, z/D=21.7. (a) Proportional control, (b) adaptive proportional control and (c) DNL control.

spatial norm of the adaptive proportional control signal $\|\mathbf{X}_n\|$ reaches a value of 0.2146 in Figure 6.9(b), 36% less than the value obtained for the proportional control method. The temporal variation of the norm of the control signal, $\|\mathbf{C}_n\|$, near n =600 in Figure 6.9(c) shows the complexity of the DNL control logic. The steady state magnitude of the norm of the control signal, $\|\mathbf{C}_{nfinal}\|$, was found to be lowest for the DNL logic with a value of 0.0987 (from Figure 6.9(c)). This value is comparable to the amplitude of K_o.

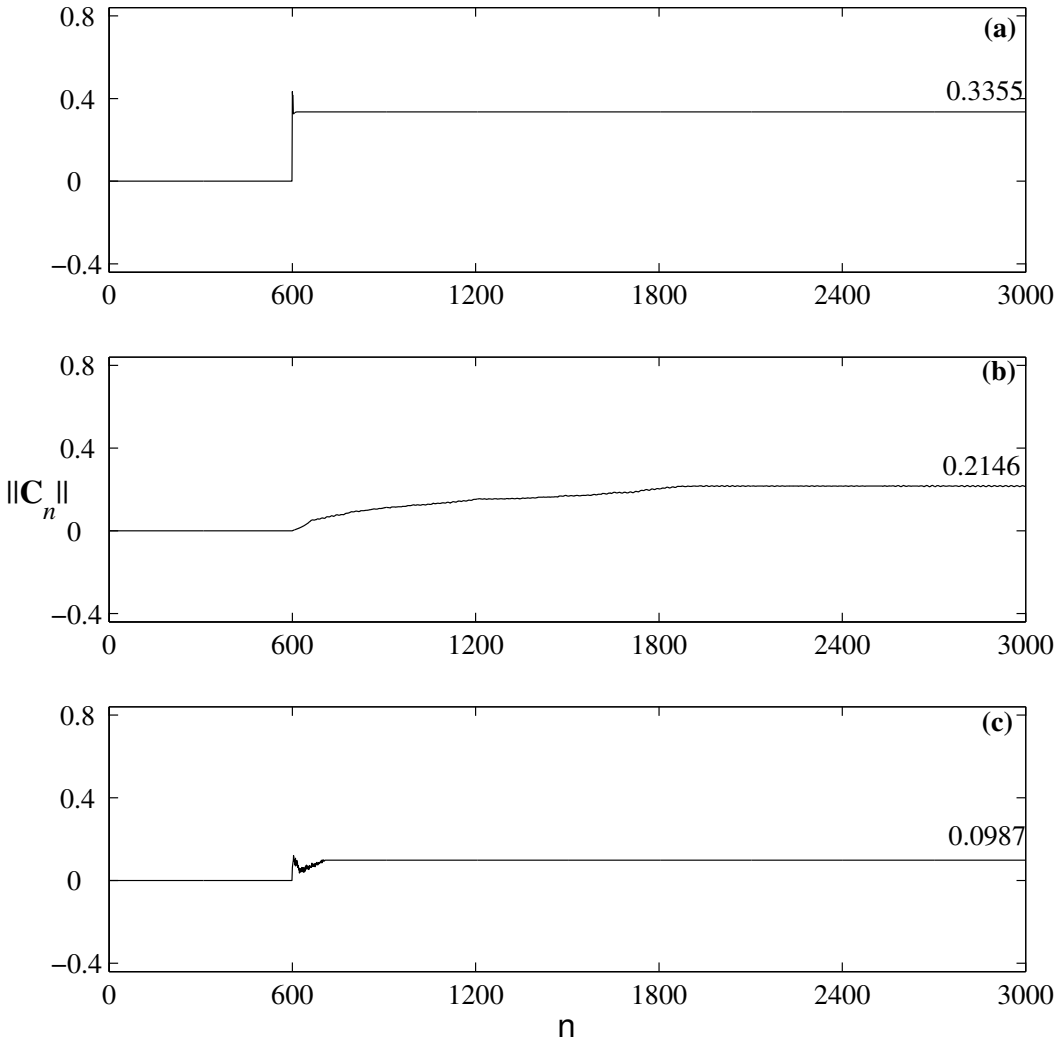

Figure 6.9: Temporal variation of the norm of control signal$\|\mathbf{C}_n\|$ at k=15, z/D=21.7. (a) Proportional control, (b) adaptive proportional control and (c) DNL control.

6.8 Cable dynamics

The previous results have focused on local and global wake dynamics. In this section the cable dynamics are addressed. In Figure 6.10(a) the spatial variation (along the cable span) of the steady state control signal, C^k_{nfinal}, is studied. For the three control methods, a sinusoidal variation in the magnitude of the control signal along the cable span in observed. In Figure 6.10(b) the parameter $\widetilde{K}^k_{nfinal} = K^k + C^k_{nfinal}$, which is analogous to the steady state cable displacement, is presented. Addition of the control signal to the input K^k term results in a constant cable displacement amplitude along the cable span for the adaptive proportional and DNL methods. This implies that the cable oscillates as a rigid cylinder after control is applied. However, a variation in cable displacement along the cable span occurs for the proportional control case. These findings are consistent with earlier results. The adaptive proportional and DNL methods yielded parallel vortex shedding patterns after the control signal was applied as would be expected for flow over a rigid cylinder. The proportional control method yielded periodic, but lace-like, patterns consistent with a variation in cable displacement along the cable span.

To this point the presented results have focused on control for a single flow condition detailed in Figure 6.3. In order to prove the effectiveness of the control techniques over a wider range of flow conditions, a series of model runs varying the frequency ratio Ω and amplitude K_o ($\Omega = 0.99, K_o = 0.1; \Omega = 0.98, K_o = 0.2$ for example) were studied. These values placed the system dynamics just outside of the lock-on region shown in the amplitude- frequency diagram of Figure 6.11 in order to obtain complex wake structures out of the uncontrolled coupled map lattice. The resulting cable displacement $\widetilde{K}^k_{nfinal}$ is plotted against the frequency ratio Ω in the amplitude-frequency diagram of Figure 6.11. A range of values must be plotted for the proportional control case due to the previously discussed variation in cable displacement amplitude for this case (see Figure 6.10(b)). Single data points suffice for the adaptive proportional and DNL cases due to the constant cable displacement for these cases in Figure 6.10(b).

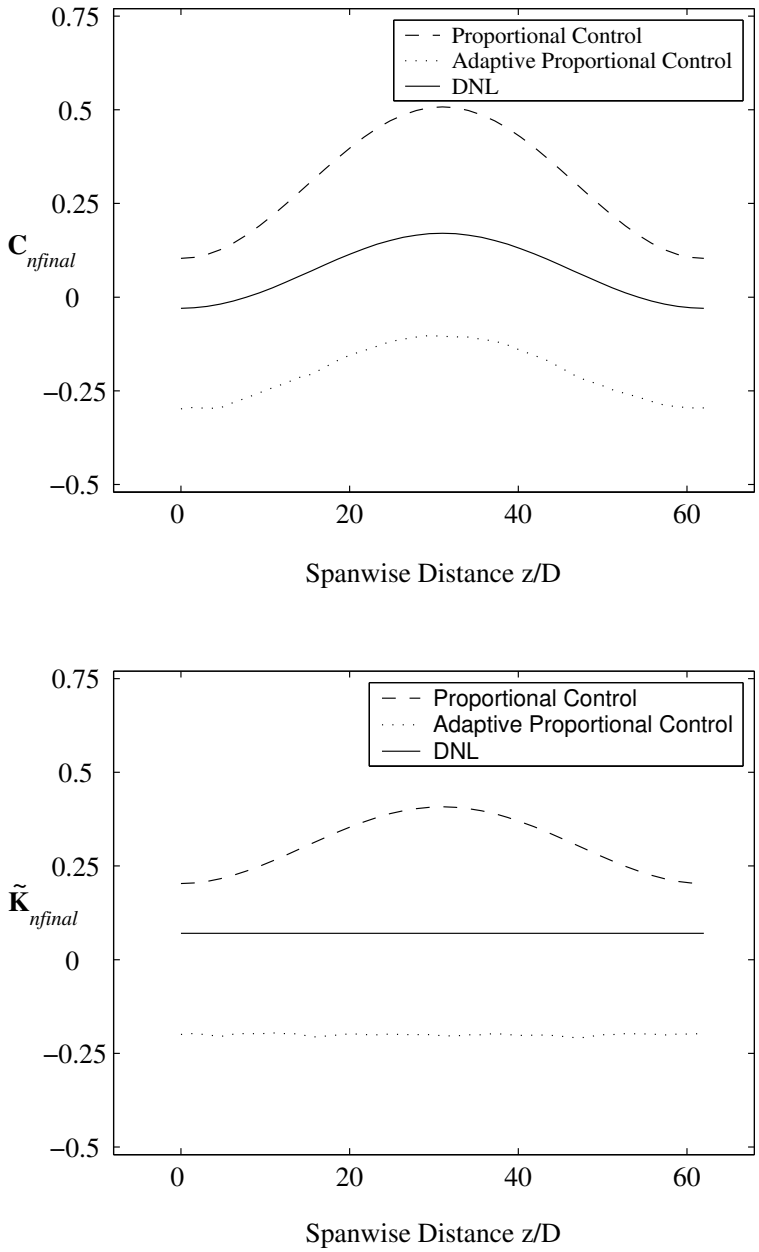

Figure 6.10: (a) Steady state spanwise variation of the control signal, $\mathbf{C}_{nfinal}$. Proportional control (dashed line), adaptive proportional control (dotted line) and DNL control (solid line). (b) Steady state cable displacement $\widetilde{\mathrm{K}}^{k}_{nfinal}$ after control. Proportional control (dashed line), adaptive proportional control (dotted line) and DNL control (solid line)

The solid lines in Figure 6.11 denote the boundary of the 1/1 lock-on region for the temporal circle map in (1.1). It is observed that all three control methods achieve the targeted state by forcing the system into the periodic 1/1 lock-on region of the circle map. The efficiency of the DNL method is highlighted in Figure 6.11. The DNL method incorporates the minimum control signal necessary to drive the system just beyond the boundary of the lock-on region. The other two control methods require larger amplitude control signals that drive the system further into the lock-on region. The largest cable amplitudes are required for the proportional control case consistent with Figure 6.9. Thus, the dynamics of the controlled system can be interpreted from a dynamical systems perspective by correlating the control signal with the behavior of the temporal circle map.

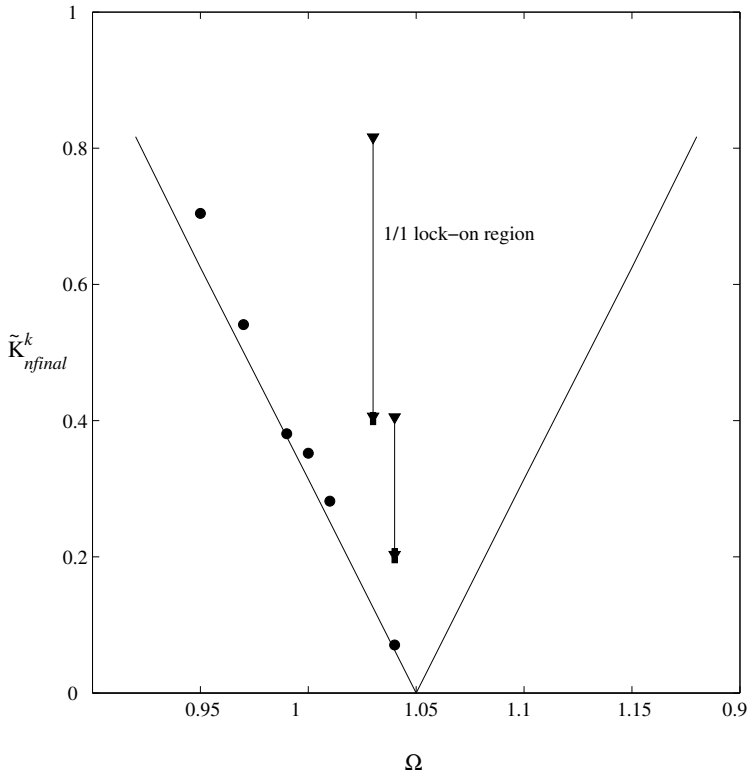

Figure 6.11: Circle map lock-on region showing constant spanwise cable oscillation amplitudes after adaptive proportional (squares) and DNL control activation (circles), and the cable oscillation amplitude range after proportional control (inverted triangles) activation. The cable amplitude after control, $\widetilde{K}^k_{nfinal}$, is driven into the lock-on region consistent with periodic shedding behavior.

6.9 Conclusions

Control terms have been added to a previously developed coupled map lattice (Olinger, 1998). Complex three dimensional vortex shedding patterns predicted by the coupled map lattice, such as vortex dislocations were controlled, and ordered, parallel (2-D) vortex shedding patterns and lace-like patterns were established. Three different control schemes were applied to the coupled map lattice model. The resulting models can be used to compare the control effectiveness of different control schemes. The model based on nonlinear control theory was most effective in controlling the complex wake and targeting parallel shedding patterns predicted by the coupled map lattice. The DNL technique required lower control signal amplitudes than the other two control techniques. The adaptive proportional control method was also effective in controlling the complex wake and targeting parallel shedding patterns. However, this method required larger control signals and longer targeting times to achieve control. A proportional control method was also used to control complex wake structures predicted by the coupled map lattice. However, in this case only periodic lace-like patterns were achieved after control. This limitation of the proportional control method was overcome by designing a spatially (and temporally) adaptive feedback gain matrix for the other two control methods. Finally, the wake structures were correlated to the classical lock-on behavior of the standard circle map using our dynamical systems approach. As discussed earlier, the coupled map lattice models developed are suitable for real-time implementation in future wake experiments with further development. This implementation will be aided by the efficiency of the coupled map lattice models. The CML models require 10^{-2} wall clock seconds per shedding cycle on a Pentium PC, while the numerical simulation of Newman and Karniadakis (1996), for example, requires approximately 10^4 wall clock seconds per shedding cycle on an IBM supercomputer for the same flow.

Chapter 7

Summary, conclusions and future work

A new class of low-order coupled map lattice (CML) models with self-learning features has been developed to estimate wake patterns behind vibrating flexible cables. The self-learning CML models were used to successfully estimate wake patterns from NEKTAR numerical simulations of cylinder wake flows in initial proof-of-concept type studies. Finally, these highly efficient self-learning CML models were applied off-line to estimate wake patterns obtained from laboratory cylinder wake flows. The success of these self-learning CML models means that they could serve as highly efficient flow models in future flow control studies where we would seek to alter the wake to a desired flow pattern. In pursuit of this eventual goal, control terms were added to the basic CML model and desired wake patterns were targeted.

The starting point for this thesis was the basic CML model of Olinger (1998). This model used a series of coupled circle map oscillators along the cylinder span to model vortex shedding patterns in the wake of forced flexible cables. The motivation for the basic CML model was due to the earlier success of Olinger and Sreenivasan (1988) in using a circle map based framework for predicting and organizing wake phenomena of rigid, externally forced cylinders. The basic CML model was shown to model wake phenomena including vortex dislocations, lace-like structures, oblique

shedding etc. However, the limited number of free parameters in the basic CML meant that accurate modeling of complex wake structures observed, for example, in NEKTAR simulations was not possible.

In this thesis, the fundamental non-linear dynamics approach based on circle maps for modeling wake phenomena was retained. The first goal of this thesis was to overcome the limitations of the basic CML model by considering additional vortex dynamics. A new convective-diffusive CML model was developed in this context. In the new convective-diffusive CML model, an additional spanwise velocity parameter can be varied across the cable span. Numerical simulations of the low Reynolds number cylinder wake NEKTAR code were used to first confirm the improved capabilities of the convective-diffusive CML model.

A class of self-learning CML models was established based on the convective-diffusive CML by incorporating adaptive estimation techniques. These techniques involve suitably varying the adjustable parameters of the model in order to progressively reduce the error between the actual and modeled wake data.

First, a self-learning CML model based on the multi-variable least-squares (MVLS) algorithm was developed. In this model, the spanwise velocity distribution is adaptively estimated in order to minimize the difference between the modeled and target wake patterns. We have developed adaptive estimation methods for a multi-variable discrete-time system (convective-diffusive CML) based on minimization of a cost-function with respect to the vector of spanwise velocities. Previous investigators have mainly focused on developing adaptive estimation methods for scalar (single output) discrete-time systems and uncoupled multi-variable discrete-time systems. For these methods, convergence analysis can be preformed easily in order to demonstrate their efficiency and accuracy. For the coupled multi-variable discrete-time system such as the CML, convergence analysis of the adaptive estimation methods had not been previously attempted. For the first time in this thesis, convergence of the MVLS algorithm was addressed by defining a scalar non-negative Lyapunov function which is shown to be non-increasing. This work represents a highly useful and important

original contribution to the field of adaptive parameter estimation, and has applications in adaptive signal processing and adaptive control. In this thesis, the MVLS algorithm was successfully applied in the estimation of wake patterns from numerical simulations and experiments.

A second self-learning CML model based on neural networks was then developed. In this model, the convection of spanwise vorticity is modeled directly using a combination of radial basis function neural networks. The neural network weights are adaptively varied using a combination of a multi-variable normalized least-squares algorithm and a projection algorithm. Convergence of the adaptive estimation scheme was established using Lyapunov methods. The convergence proofs provided in the Appendix represents an extension to the state-of-the art in neural network based adaptive estimation of certain coupled multi-variable discrete time systems.

The self-learning CML models were first used to estimate target wake patterns obtained from the NEKTAR code. In this proof-of-concept study, three different flow situations were considered. The self-learning CML model based on neural networks was found to be slightly more efficient for the uniform flow lock-on near wake cases, $x/D = 0.5, 1$, predicting lace-like flow structures. However, it was found to be less efficient in predicting the transient "M-like" wake structures observed at $x/D = 3$. Highly complex wake structures with decreased spanwise lengths, rapidly changing spanwise lengths and also vortex dislocations were observed in the far wake cases, $x/D = 5, 10$. The neural network model was found to be more efficient whenever the transition in the wake patterns, however complex, was gradual. In other studies, vortex dislocations were observed for the non-periodic wake, $\Omega = 0.9$. Oblique shedding patterns were observed for the sheared freestream flow situation. Both the self-learning CML models were found to be highly accurate in predicting these complex wake structures, with the neural network model performing slightly better. The accuracy of the self-learning CML models was quantified using local and global measures of the state error.

The proof-of-concept study revealed that both the self-learning CML models are

highly efficient for estimation of wake flow patterns. It should be emphasized that the self-learning CML is highly efficient compared to NEKTAR simulations. The self-learning CML requires 10^{-2} wall clock seconds to run on a Pentium PC while the NEKTAR simulation requires approximately 10^4 wall clock seconds per shedding cycle on an IBM supercomputer.

The capabilities of the self-learning CML models were then extended to off-line estimation of wake flow patterns. In this method, the measured wake data is post-processed and the stored wake patterns are made available for estimation using the self-learning models. The cases of uniform flow over a rigid cylinder with and without angled endplates were considered. Three distinct types of patterns, namely rigid-periodic, oblique shedding and "mixed" type, were efficiently estimated by both the self-learning CML models. The first occurrence of vortex dislocations was highly difficult to estimate. However, we believe that these occurrences were rare in the current experiments. If more such instances of vortex dislocations occur, the self-learning CML models would learn from the observed data, and predictions of these highly complex structures would be more accurate.

The shedding frequencies measured in the experiments were approximately 45 Hz. Therefore, the average time period of vortex shedding is approximately 0.02 seconds. The self-learning CML requires approximately 0.006 wall clock seconds per shedding cycle on a Pentium PC. This includes generation of target wake patterns and their estimation. It doesn't include the time required for conversion of hot-wire voltage signals into wake velocities. For the off-line estimation currently pursued, this conversion was performed on a Pentium PC and required approximately 0.05 seconds per shedding cycle. We believe that with improved choices of sampling rates and with the use of simple additional hardware for computation of wake velocities from voltages, the time required for self-learning estimation can be reduced below the time period of vortex shedding. This improvement would allow on-line or real-time estimation of wake flow patterns.

In future, the on-line self-learning CML models would serve as wake models in flow

control experiments. The goal of this work would be to develop an efficient flow control model for targeting desired wake patterns in experiments. Methods developed in this thesis for controlling wake patterns of the simple CML model can similarly be pursued for the self-learning CML models. The future flow control schemes would need to address techniques of control actuation. Current experimental control techniques such as rotary oscillation of the cylinder, transverse oscillation of the cylinder can be explored in the context of the CML. The interfacing of the actuator dynamics to the CML also needs to be studied.

In other studies, with applications to flow control modeling, the techniques of adaptive estimation can be pursued for a self-learning CML modeling a freely vibrating cable-wake interaction.

Bibliography

[1] O.M. Aamo and M. Krstić, *Flow Control by Feedback: Stabilization and Mixing.* Springer, NY, 2003.

[2] P. Albaréde and P.A. Monkewitz, "A model for the formation of oblique shedding and 'chevron' patterns in cylinder wakes," *Physics of Fluids A*, 4(744), 1992.

[3] P. Alstrom and R. Ritala, "Mode locking in an infinite set of coupled circle maps," *Physical Review A*, 35(300), 1987.

[4] G. Balasubramanian. Control of complex cylinder wake structures using coupled map lattices. *MS Thesis, Worcester Polytechnic Institute, Worcester, MA, USA*, 1998.

[5] G. Balasubramanian, D.J. Olinger, M.A. Demetriou, and M.P. Davis, "Development of a self-learning coupled map lattice for modeling cylinder wakes," in *Proc. 2001 ASME Fluids Engg. Division Summer Meeting, Paper Category: F-257, Paper Number: FEDSM2001-18197*, 2001.

[6] G. Balasubramanian, D.J. Olinger, and M.A. Demetriou. Control of a coupled map lattice model for vortex shedding in the wake of a cylinder. *Pramana*, 59(91), 2002.

[7] ——, "Development of a self-learning scheme for modeling cylinder wakes behind flexible cables," *Chaos, submitted*, 2002.

[8] P.W. Bearman, "Vortex shedding from oscillating bluff bodies," *Annual Review of Fluid Mechanics*, 16(195), 1984.

[9] J.E. Bernhardt, J. Mihailovic, C.F. Jines, A. Abouel-fotoh, T.C. Corke, and D.R. Williams, "Instantaneous pressure distribution around an oscillating cylinder," *APS Bulletin*, 41(1779), 1996.

[10] R. Blevins, *Flow Induced Vibrations.* Krieger, FL, 1977.

[11] C. Canuto, M.Y. Hussaini, A. Quarteroni, and T.A. Zang, *Spectral Methods in Fluid Dynamics.* Springer-Verlag, NY, 1996.

[12] M. Davis, M.A. Demetriou, and D.J. Olinger. Low-order modeling of freely vibrating flexible cables. *to appear in Flow, Turbulence and Combustion*, 2003.

[13] M.L. Facchinetti, E. de Langre, and F. Biolley, "Vortex-induced waves along cables," in *Proc. FSI, AE & FIV+N 2002, ASME Intl. Mech. Engg. Congress, Paper Category: Paper Number: FEDSM2002-32161*, 2002.

[14] M.J. Feigenbaum, L.P. Kandanoff, and S.J. Shenker. Quasiperiodicity in dissipative systems. a renormalization group analysis. *Physica D*, 5(370), 1982.

[15] M. Gad-el Hak. Flow control: Passive, active and reactive flow management. *Prentice Hall, Englewood Cliffs, NJ, USA*, 2000.

[16] G.C. Goodwin and K.S. Sin, *Adaptive Filtering, Prediction and Control*. Prentice-Hall, NJ, 1984.

[17] O.M. Griffin and S.E. Ramberg. The vortex-street wakes of vibrating cylinders. *J. Fluid Mech.*, 66(553), 1974.

[18] M. Hammache and M. Gharib. An experimental study of the parallel and oblique vortex shedding from circular cylinders. *J. Fluid Mech.*, 232(567), 1991.

[19] D. Harville, *Matrix algebra from a statistician's perspective*. Springer, NY, 1997.

[20] R.D. Henderson and G.E. Karniadakis, "Unstructured spectral element methods for simulation of turbulent flows," *Journal of Computational Physics*, vol. 122(191), 1995.

[21] C.R. Johnson, *Lectures on adaptive parameter estimation*. Prentice Hall, NJ, 1988.

[22] K. Kaneko, "Spatiotemporal chaos in one and two dimensional coupled map lattices," *Physica D*, 37(60), 1989.

[23] K. Kaneko. Globally coupled circle maps. *Physica D*, 54(5), 1991.

[24] G. Koopman, "The vortex wakes of vibrating cylinders at low reynolds numbers," *Journal of Fluid Mechanics*, 28(501), 1967.

[25] L.D. Landau and E.M. Lifshitz. Fluid mechanics: Course in theoretical physics. *Pergamon, Oxford*, 1959.

[26] J.E. Marsden and M. McCracken. The hopf bifurcation and its applications. *Springer Verlag, New York*, 1976.

[27] P.A. Monkewitz, C.H.K. Williamson, and G.D. Miller, "Phase dynamics of karman vortices in cylinder wakes," *Physics of Fluids*, 8(91), 1996.

[28] D. Newman and G.E. Karniadakis, "Simulations of flow over a flexible cable: A comparison of forced and flow-induced vibration," *Journal of Fluids and Structures*, 10(439), 1996.

[29] ——, "A direct numerical simulation study of flow past a freely vibrating cable," *Journal of Fluid Mechanics*, 344(95), 1997.

[30] D.J. Olinger and K.R. Sreenivasan, "Nonlinear dynamics of the wake of an oscillating cylinder," *Physical Review Letters*, 60(797), 1988.

[31] D.J. Olinger, "A low-dimensional model for chaos in open fluid flows," *Physics of Fluids A*, 5(1947), 1993.

[32] D.J. Olinger, A.B. Chhabra, and K.R. Sreenivasan. The onset of chaos in the wake of an oscillating cylinder: Experiment and the dynamics of the circle map. *Pramana*, 48(2), 1997.

[33] D.J. Olinger, "A low-order model for vortex shedding patterns behind vibrating flexible cables; erratum: A low-order model ... cables[physics of fluids 10(1953), 1998], physics of fluids, 11(1278)." *Physics of Fluids*, 10(1953), 1998.

[34] S. Ostlund, D. Rand, J. Sethna, and E. Siggia, "Universal properties of the transition from quasiperiodicity to chaos in dissipative systems," *Physica D*, 8(303), 1983.

[35] E. Ott, C. Grebogi, and J.A. Yorke. Controlling chaos. *Phys. Rev. Lett.*, 64(1196), 1990.

[36] M.M. Polycarpou, and P.A. Ioannou, "Neural networks as on-line approximators of nonlinear systems," in *Proc. 31st Conference on Decision and Control, Tucson, AZ*, 1992.

[37] B. Protas and A. Styczek. Optimal rotary control of the cylinder wake in the laminar regime. *Phys. of Fluids*, 14(2073), 2002.

[38] M. Provensal, C. Mathis, and L. Boyer, "Bernard-von karman instability: Transient and forced regimes," *Journal of Fluid Mechanics*, 182(1), 1987.

[39] K. Roussopoulos and P.A. Monkewitz, "Nonlinear modelling of vortex shedding control in cylinder wakes," *Physica D*, 97(264), 1996.

[40] W.J. Rugh. Linear system theory. *Prentice Hall, Englewood Cliffs, NJ, USA*, 1995.

[41] H. Schlichting and K. Gersten, *Boundary Layer Theory.* Springer-Verlag, Berlin, 2000.

[42] S.J. Shenker. Scaling behavior in a map of a circle onto itself: Empirical results. *Physica D*, 5(405), 1982.

[43] J. Singer, Y.Z. Wang, and H. Bau. Controlling a chaotic system. *Phys. Rev. Lett.*, 66(9), 1991.

[44] S. Sinha and N. Gupte. Adaptive control of spatially extended systems: Targeting spatiotemporal patterns and chaos. *Phys. Rev. E*, 58(5), 1998.

[45] R. Skop and S. Balasubramanian, "A new twist on an old model for vortex-excited vibrations," *Journal of Fluids and Structures*, 11(395), 1997.

[46] J.C. Sprott. Chaos data analyzer. *Physics Academic Software, Raleigh, NC, USA*, 1992.

[47] K.R. Sreenivasan, P.J. Strykowski, and D.J. Olinger. Hopf bifurcation, landau equation, and vortex shedding behind circular cylinders. *in ASME Forum on Unsteady Flow Separation*, FED 52(1), 1987.

[48] P.K. Stansby, "The locking-on of vortex shedding due to the cross-stream vibration of circular cylinders in uniform and shear flows," *Journal of Fluid Mechanics*, 74(641), 1976.

[49] J.T. Stuart. On the nonlinear mechanics of wave disturbances in stable and unstable parallel flows. part 2: The development of a solution for plane poiseuille flow and for plane couette flow. *J. Fluid Mech.*, 9(353), 1960.

[50] J. Tannehill, D. Anderson, and R. Pletcher, *Computational Fluid Mechanics and Heat Transfer*. Taylor and Francis, PA, 1997.

[51] Y. Wang, J. Singer, and H. Bau. Controlling chaos in a thermal convection loop. *J. Fluid Mech.*, 237(479), 1992.

[52] C.H.K. Williamson. Oblique and parallel modes of vortex shedding in the wake of a circular cylinder at low reynolds numbers. *J. Fluid Mech.*, 206(579), 1989.

[53] C.H.K. Williamson, "Three-dimensional wake transition," *Journal of Fluid Mechanics.*, 328(345), 1996.

[54] D. Yoerger, M. Grosenbaugh, M. Triantafyllou, and J. Burgess. Drag forces and flow-induced vibrations of a long vertical tow cable-part 1: Steady-state towing conditions. *J. Offshore Mech. Arctic Engng*, 113(117), 1991.

[55] P.K. Yuen and H. Bau. Optimal and adaptive control of chaotic convection - theory and experiments. *Phys. of Fluids*, 11(1435), 1999.

Appendix A

Convergence of the neural network based self-learning CML

In this section, we provide proof of convergence of the neural network based self-learning CML.

$$\widehat{\mathbf{Q}}_{n+1} = \mu_{n+1} - \mathbf{I}_{\mu}\frac{(|\mu_{n+1}| - \mathrm{M}_{\theta})}{|\mu_{n+1}|},\ \mathbf{I}_{\mu} = \begin{cases} 1 \text{ if } |\mu_{n+1}| > \mathrm{M}_{\theta} \\ 0 \text{ if } |\mu_{n+1}| \leq \mathrm{M}_{\theta} \end{cases} \tag{A.1}$$

Let us define the parameter estimation error $\zeta_n = \widehat{\mathbf{Q}}_n - \mathbf{Q}^*$ and the Lyapunov function candidate

$$\mathrm{V}(\zeta_{n+1}) = |\zeta_{n+1}|^2 = \zeta_{n+1}^T\zeta_{n+1} = \left(\widehat{\mathbf{Q}}_{n+1} - \mathbf{Q}^*\right)^T\left(\widehat{\mathbf{Q}}_{n+1} - \mathbf{Q}^*\right)$$

$$\mathbf{E}_{n+1} = \overline{\mathbf{W}}(\mathbf{X}_n)\zeta_n - \mathbf{N}_n \tag{A.2}$$

$$\begin{aligned}
|\widehat{\mathbf{Q}}_{n+1} - \mathbf{Q}^*|^2 &= \left(\widehat{\mathbf{Q}}_{n+1} - \mathbf{Q}^*\right)^T\left(\widehat{\mathbf{Q}}_{n+1} - \mathbf{Q}^*\right) \\
&= \left(\mu_{n+1} - \mathbf{I}_{\mu}\frac{(|\mu_{n+1}| - \mathrm{M}_{\theta})}{|\mu_{n+1}|}\mu_{n+1} - \mathbf{Q}^*\right)^T \times \\
&\quad \left(\mu_{n+1} - \mathbf{I}_{\mu}\frac{(|\mu_{n+1}| - \mathrm{M}_{\theta})}{|\mu_{n+1}|}\mu_{n+1} - \mathbf{Q}^*\right) \\
&= (\mu_{n+1} - \mathbf{Q}^*)^T(\mu_{n+1} - \mathbf{Q}^*) - \mathbf{I}_{\mu}\frac{(|\mu_{n+1}| - \mathrm{M}_{\theta})}{|\mu_{n+1}|}\mu_{n+1}^T \times \\
&\quad \left(2\mu_{n+1} - 2\mathbf{Q}^* - \frac{(|\mu_{n+1}| - \mathrm{M}_{\theta})}{|\mu_{n+1}|}\mu_{n+1}\right) \\
&= |\mu_{n+1} - \mathbf{Q}^*|^2 - \mathbf{I}_{\mu}\frac{(|\mu_{n+1}| - \mathrm{M}_{\theta})}{|\mu_{n+1}|}\mu_{n+1} \times \\
&\quad \left(|\mu_{n+1}|^2 - 2\mu_{n+1}^T\mathbf{Q}^* + |\mu_{n+1}|\mathrm{M}_{\theta}\right)
\end{aligned} \tag{A.3}$$

$$
\begin{aligned}
|\widehat{\mathbf{Q}}_{n+1} - \mathbf{Q}^*|^2 &= |\mu_{n+1} - \mathbf{Q}^*|^2 - \mathbf{I}_\mu \frac{(|\mu_{n+1}| - \mathrm{M}_\theta)}{|\mu_{n+1}|}\mu_{n+1} \times \\
&\quad \left(|\mu_{n+1} - \mathbf{Q}^*|^2 + |\mu_{n+1}|\mathrm{M}_\theta - |\mathbf{Q}^*|^2\right) \\
&= |\mu_{n+1} - \mathbf{Q}^*|^2 - \mathbf{I}_\mu \rho_{n+1},
\end{aligned} \tag{A.4}
$$

where

$$
\rho_{n+1} \equiv \frac{(|\mu_{n+1}| - \mathrm{M}_\theta)}{|\mu_{n+1}|} \left(|\mu_{n+1} - \mathbf{Q}^*|^2 + |\mu_{n+1}|\mathrm{M}_\theta - |\mathbf{Q}^*|^2\right).
$$

It can be shown that $\mathbf{I}_\mu \rho_{n+1} \geq 0$. Let $\mathbf{I}_\mu = 1$ otherwise the inequality holds trivially. In this case, $|\mu_{n+1}| > \mathrm{M}_\theta$. By definition, $|\mathbf{Q}^*| \leq \mathrm{M}_\theta$. We have $|\mu_{n+1}|\mathrm{M}_\theta - |\mathbf{Q}^*|^2 > \mathrm{M}_\theta^2 - |\mathbf{Q}^*|^2 \geq 0$. This shows that $\rho_{n+1} > 0$. Hence, $\mathbf{I}_\mu \rho_{n+1} \geq 0$.

$$
\begin{aligned}
|\mu_{n+1} - \mathbf{Q}^*|^2 &= |\zeta_n - \frac{\gamma_0 \overline{\mathbf{W}}(\mathbf{X}_n)^T \mathbf{E}_{n+1}}{\beta_0 + \|\overline{\mathbf{W}}(\mathbf{X}_n)\|^2}|^2 \\
&= \mathrm{V}(\zeta_n) - \frac{\gamma_0}{\beta_0 + \|\overline{\mathbf{W}}(\mathbf{X}_n)\|^2} \left(2\zeta_n^T \overline{\mathbf{W}}(\mathbf{X}_n)^T \mathbf{E}_{n+1} - \frac{\gamma_0 |\overline{\mathbf{W}}(\mathbf{X}_n)^T \mathbf{E}_{n+1}|^2}{\beta_0 + \|\overline{\mathbf{W}}(\mathbf{X}_n)\|^2}\right) \\
&\leq \mathrm{V}(\zeta_n) - \frac{\gamma_0}{\beta_0 + \|\overline{\mathbf{W}}(\mathbf{X}_n)\|^2} \left(2(\overline{\mathbf{W}}(\mathbf{X}_n)\zeta_n)^T \mathbf{E}_{n+1} - \frac{\gamma_0 |\mathbf{E}_{n+1}|^2 \|\overline{\mathbf{W}}(\mathbf{X}_n)\|^2}{\beta_0 + \|\overline{\mathbf{W}}(\mathbf{X}_n)\|^2}\right)
\end{aligned} \tag{A.5}
$$

In the last step we have used the Cauchy Schwarz inequality, $\|\mathbf{AB}\| \leq \|\mathbf{A}\|\|\mathbf{B}\|$. From (A.2) we have,

$$
\begin{aligned}
|\mu_{n+1} - \mathbf{Q}^*|^2 &\leq \mathrm{V}(\zeta_n) - \frac{\gamma_0}{\beta_0 + \|\overline{\mathbf{W}}(\mathbf{X}_n)\|^2} \times \\
&\quad \left(2(\mathbf{E}_{n+1} + \mathbf{N}_n)^T \mathbf{E}_{n+1} - \frac{\gamma_0 |\mathbf{E}_{n+1}\|^2 |\overline{\mathbf{W}}(\mathbf{X}_n)\|^2}{\beta_0 + \|\overline{\mathbf{W}}(\mathbf{X}_n)\|^2}\right) \\
&\leq \mathrm{V}(\zeta_n) - \frac{\gamma_0}{\beta_0 + \|\overline{\mathbf{W}}(\mathbf{X}_n)\|^2} \times \\
&\quad \left(|\mathbf{E}_{n+1}|^2 \left(2 - \frac{\gamma_0 \|\overline{\mathbf{W}}(\mathbf{X}_n)\|^2}{\beta_0 + \|\overline{\mathbf{W}}(\mathbf{X}_n)\|^2}\right) + 2\mathbf{E}_{n+1}^T \mathbf{N}_n\right)
\end{aligned} \tag{A.6}
$$

Define $\alpha_n \equiv \left(2 - \frac{\gamma_0 \|\overline{\mathbf{W}}(\mathbf{X}_n)\|^2}{\beta_0 + \|\overline{\mathbf{W}}(\mathbf{X}_n)\|^2}\right), \overline{\alpha}_n \equiv \frac{\gamma_0}{\beta_0 + \|\overline{\mathbf{W}}(\mathbf{X}_n)\|^2} \alpha_n.$

Note that since $0 < \gamma_0 < 2$, we have $\alpha_n, \overline{\alpha}_n > 0 \, \forall \, n > 1$. Therefore, by completing

the squares we obtain,

$$\begin{aligned}
|\mu_{n+1} - \mathbf{Q}^*|^2 &\leq \mathrm{V}(\zeta_n) - \frac{\gamma_0}{\beta_0 + \|\overline{\mathbf{W}}(\mathbf{X}_n)\|^2} \times \\
&\quad \left(\frac{\alpha_n}{2} |\mathbf{E}_{n+1}|^2 + \frac{\alpha_n}{2} \left(|\mathbf{E}_{n+1}|^2 + \frac{4}{\alpha_n} \mathbf{E}_{n+1}^T \mathbf{N}_n \right) \right) \\
&\leq \mathrm{V}(\zeta_n) - \frac{\overline{\alpha}_n}{2} |\mathbf{E}_{n+1}|^2 - \frac{\overline{\alpha}_n}{2} | \left(\mathbf{E}_{n+1} + \frac{2}{\alpha_n} \mathbf{N}_n \right) |^2 + 2 \frac{\overline{\alpha}_n}{\alpha_n^2} |\mathbf{N}_n|^2.
\end{aligned} \tag{A.7}$$

Now, if we let $\triangle \mathrm{V}_{n+1} \equiv \mathrm{V}(\zeta_{n+1}) - \mathrm{V}(\zeta_n)$ and substitute (A.7) in (A.4), we obtain,

$$\begin{aligned}
\triangle \mathrm{V}_{n+1} &\leq -\frac{\overline{\alpha}_n}{2} |\mathbf{E}_{n+1}|^2 - \frac{\overline{\alpha}_n}{2} | \left(\mathbf{E}_{n+1} + \frac{2}{\alpha_n} \mathbf{N}_n \right) |^2 + 2 \frac{\overline{\alpha}_n}{\alpha_n^2} |\mathbf{N}_n|^2 - \mathbf{I}_\mu \rho_{n+1}, \\
&\leq -\frac{\overline{\alpha}_n}{2} |\mathbf{E}_{n+1}|^2 + 2 \frac{\overline{\alpha}_n}{\alpha_n^2} |\mathbf{N}_n|^2
\end{aligned} \tag{A.8}$$

Let $\overline{\alpha}_o \equiv \inf_n \overline{\alpha}_n$ and let $\alpha_o \equiv \inf_n \alpha_n$. We rewrite (A.8) as:

$$|\mathbf{E}_{n+1}|^2 \leq -\frac{2}{\overline{\alpha}_o} \triangle \mathrm{V}_{n+1} + \frac{4}{\alpha_o^2} |\mathbf{N}_n|^2. \tag{A.9}$$

By summing both sides from $n = 0$ to $n = N - 1$, where N is a finite integer, we have:

$$\begin{aligned}
\sum_{n=0}^{N-1} |\mathbf{E}_{n+1}|^2 &\leq \frac{2}{\overline{\alpha}_o} \left(|\zeta_0|^2 - |\zeta_n|^2 \right) + \frac{4}{\alpha_o^2} \sum_{n=0}^{N-1} |\mathbf{N}_n|^2 \\
&\leq \lambda_1 + \lambda_2 \sum_{n=0}^{N-1} |\mathbf{N}_n|^2, \;\; \lambda_1, \, \lambda_2 > 0.
\end{aligned} \tag{A.10}$$

According to the above equation, in any discrete-time interval $[0, N]$, the "energy" of the prediction error $\mathbf{E}$ is (at most) of the same order as the "energy" of $\mathbf{N}$, that is, the sum of the modeling errors. This points out the relationship between the prediction error and the modeling error. The parameter adaptive law (4.17)- (4.19) guarantees that $\mathbf{E}_n$ and $\widehat{\mathbf{Q}}_n$ are uniformly bounded. If $\mathbf{N} \in l_2$, that is $\sum_{n=0}^{\infty} |\mathbf{N}_n|^2 < \infty$, than $\mathbf{E} \in l_2$ and $\lim_{n \to \infty} \mathbf{E}_n = \mathbf{0}$.